



HAL
open science

Relationship between mechanical parameters and behaviour under external stresses in lipid vesicles with modified membranes.

François Quemeneur

► **To cite this version:**

François Quemeneur. Relationship between mechanical parameters and behaviour under external stresses in lipid vesicles with modified membranes.. Data Analysis, Statistics and Probability [physics.data-an]. Université de Grenoble, 2010. English. NNT: . tel-00615938

HAL Id: tel-00615938

<https://theses.hal.science/tel-00615938>

Submitted on 19 Aug 2011

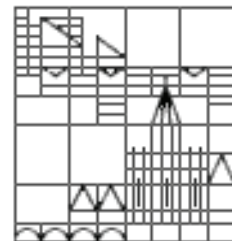
HAL is a multi-disciplinary open access archive for the deposit and dissemination of scientific research documents, whether they are published or not. The documents may come from teaching and research institutions in France or abroad, or from public or private research centers.

L'archive ouverte pluridisciplinaire **HAL**, est destinée au dépôt et à la diffusion de documents scientifiques de niveau recherche, publiés ou non, émanant des établissements d'enseignement et de recherche français ou étrangers, des laboratoires publics ou privés.



UNIVERSITÉ DE GRENOBLE

Universität
Konstanz



THESE

Pour obtenir le grade de

DOCTEUR DE L'UNIVERSITE DE GRENOBLE

Spécialité Physique pour les Sciences du Vivant

Préparée dans le cadre d'une cotutelle entre

L'UNIVERSITE DE GRENOBLE ET L'UNIVERSITE DE CONSTANCE

Arrêtés ministériels : 6 janvier 2005 - 7 août 2006

Présentée et soutenue publiquement par

François QUEMENEUR

le 15 décembre 2010

**Relation entre les paramètres mécaniques et le comportement
sous contraintes externes de vésicules lipidiques à membrane modifiée.**

**Relationship between mechanical parameters and behaviour
under external stresses in lipid vesicles with modified membranes.**

Thèse codirigée par Brigitte PÉPIN-DONAT et par Georg MARET

JURY

M^{me} Patricia BASSEREAU, Directrice de recherche, Institut Curie, Paris	Rapporteur
M. Andres FERY, Professeur de l'Université de Bayreuth	Rapporteur
M. Bertrand FOURCADE, Professeur de l'Université de Grenoble	Président
M. Thomas GISLER, Professeur de l'Université de Constance	Examineur
M. Georg MARET, Professeur de l'Université de Constance	Directeur
M^{me} Brigitte PÉPIN-DONAT, Directrice de recherche, SPrAM/INAC/CEA Grenoble	Directrice
M^{me} Marguerite RINAUDO, Professeur honoraire de l'Université de Grenoble	Invité
M. Carlos MARQUES, Directeur de recherche, Institut Charles Sadron, Strasbourg	Invité

Thèse préparée au sein de l'Institut Nanoscience et Cryogénie du CEA Grenoble,
du Département de Physique de l'Université de Constance
et des Ecoles Doctorales de Physique des Universités de Grenoble et de Constance

Remerciements

Je tiens avant tout à exprimer ma sincère reconnaissance et mes remerciements aux membres du jury pour avoir consacré une partie de leur temps précieux afin d'évaluer mon travail et de s'être déplacés, parfois de très loin, pour assister à la soutenance. Merci à Patricia Bassereau, Andreas Fery, Bertrand Fourcade et Thomas Gisler pour l'intérêt porté à mon travail et pour vos nombreuses remarques qui ont permis l'amélioration de ce manuscrit.

Je voudrais ensuite témoigner toute ma gratitude à mes deux directeurs de thèse, sans qui cette aventure franco-allemande n'aurait pas été possible. Je suis extrêmement reconnaissant envers Brigitte Pépin-Donat de s'être autant investie dans mon travail, m'avoir encouragé et soutenu durant ces quatre années. Je la remercie de sa patience, de sa gentillesse et également de m'avoir transmis ses valeurs scientifiques et humaines. Je remercie également Georg Maret pour m'avoir accueilli dans son équipe et m'avoir fait partager sa passion de la recherche et son honnêteté scientifique. J'ai énormément appris en travaillant avec eux.

Un très grand merci à Marguerite Rinaudo avec qui j'ai énormément appris scientifiquement et humainement tout au long cette thèse. Merci pour ses mille conseils, mis bout à bout, ça compte.

Merci à Carlos Marques, André Schröder et Omar Mertins, avec qui j'ai pris beaucoup de plaisir à travailler et discuter lors de ces semaines très intenses où je vivais dans les sous-sols de l'ICS de Strasbourg.

Toute ma reconnaissance également à Howard Stone pour m'avoir accueilli dans son groupe durant ce trop court été 2006 et m'avoir mis le pied à l'étrier de la microfabrication. Merci pour l'intérêt qu'il a porté à nos objets, et pour sa grande disponibilité en dépit d'un emploi du temps très chargé.

Merci à Catherine Quilliet pour m'avoir fait plonger dans la marmite de " CoQuilliettes " avec sa bonne humeur communicative et son enthousiasme.

Merci à Frédéric Dubreuil pour avoir fait voyager et stresser nos vésicules composites à Bayreuth. J'espère que nous compléterons d'autres carnets de voyage.

Je remercie fortement les trois responsables de l'IRTG, Brigitte, Georg et Joerg Baschnagel, et plus généralement les membres du Collège qui ont fortement contribué au bon déroulement de ma thèse. Merci également à Sabine Lucas pour sa gentillesse et son efficacité; notamment d'avoir su rendre mes nombreux allers-retours entre France et Allemagne beaucoup plus tranquilles en simplifiant les démarches administratives et en rendre cette expérience à l'étranger encore plus facile.

Au cours de ces 4 années, j'ai pu faire de très nombreuses rencontres dans les divers laboratoires ou j'ai séjourné. C'est avec plaisir que je remercie l'ensemble des personnes de mes deux laboratoires de rattachement pour leur accueil chaleureux, et les bons moments que nous avons passés ensemble. Plus particulièrement je remercie les membres du SPrAM du CEA Grenoble, en particulier Jean-Pierre Travers, Peter Reiss et David Djurado pour m'avoir intégré à leurs équipes. Merci aux membres du LEMOH et du CREAB pour avoir fait de cette étape une expéri-

ence très enrichissante. J'adresse aussi de très chaleureux remerciements à Christian Lombard, Mahjoub Fakir et Catherine Pascale pour leur aide technique et leur soutien plus que précieux au quotidien. Merci également à Emmanuel Suraniti, Yoann Roupioz, Roberto Calemczuk et Thierry Livache pour leur aide matérielle et nos nombreux échanges. J'adresse un énorme remerciement à tous les thésards, post-docs et stagiaires du labo, pour ces moments de détente partagés entre deux manips; ils ont contribué à rendre cette expérience encore plus agréable. Merci à Myriam, Emanuela, Nico, Julia, Anastasia, Sandrine, Amman, Clément, Mustapha, Lucia, Pierrot, Virginie, Lorette, Dimitri, Frédéric, Clémence, Elsa, Sudarsan, Chira et Thuy pour votre soutien et je leur souhaite bonne chance pour la suite.

Merci aussi aux membres de l'équipe de Georg Maret au département de physique de l'Université de Constance. Merci à Urs Gasser et Florian Ziese pour les discussions sur l'imagerie confocal et le piégeage optique multiple. Merci à Christian Ortolf, Ina Seifert et Doris Dexler pour leur aide précieuse au quotidien. Merci à Peter, les deux Maryam, Nathan, Corinna, Susan et Christof, pour votre accueil et la bonne ambiance que vous faites régner au labo. J'adresse mes remerciements à Sylvain Mazoyer pour sa sympathie, son enthousiasme et pour les nombreuses Pils que nous avons partagées. Merci aussi à mes 11 colocataires pour nos discussions passionnantes et leur aide précieuse dans un pays dont je ne parlais pas la langue.

Merci également aux membres du CERMAV, tout particulièrement Eric Bayma-Pecit pour son aide précieuse, Bruno Jean pour nos discussions, et les membres du groupe Glycobiologie moléculaire que j'ai côtoyé au cours de mes très nombreuses journées de mesure sur le Zetasizer.

Pour les nombreuses semaines dans l'équipe "Membranes et Microforces" de l'ICS de Strasbourg, j'adresse mes remerciements à Thierry Charitat, Marc Basler, Marie-Laure Hissette, Christopher Haluska et Linda Malaquin et Tatiana Schmatko avec qui j'ai pris beaucoup de plaisir à travailler et discuter.

Un très grand merci aux membres du Stone Group avec qui j'ai passé un très bon été 2006. Je remercie chaleureusement Magalie pour sa patience et sa disponibilité pendant ces quelques mois, menant de front la rédaction de son manuscrit et notre projet commun. Merci à Bill et Jiandi pour votre bonne humeur quotidienne et votre amitié; nous vous attendons pour un petit tour de France.

J'ai pris beaucoup de plaisir à travailler avec Françoise Brochard-Wyart, Clément Campillo, que j'ai retrouvé, et Sébastien Kremer à l'Institut Curie. Je me réjouis de rejoindre ce laboratoire comme post-doctorant.

Toutes les personnes que je viens de citer ont fait de ces 4 années de thèse une expérience exceptionnelle, tant d'un point de vue humain que scientifique. Merci à Amaya et Timo Betz pour leur traduction allemande.

Enfin, je finirai en saluant affectueusement ceux avec qui, j'ai passé du temps à ne pas travailler et qui m'ont beaucoup soutenu durant cette longue étape. Un immense merci à Benoit, Benjamin, Nicolas, Philippe et sa petite famille, Myriam, Emanuela, Cécile et Yoanna pour leur amitié et tous les bons moments que nous avons partagés. Un immense merci à ma famille, mes parents, ma grand-mère ainsi qu'à Laurence, Cendrine et Bruno, pour leur soutien inconditionné. Je termine par une tendre pensée pour Magalie, merci pour sa patience, son soutien, sa présence tout simplement et pour énormément plus ; cette thèse lui est dédiée.

Cette thèse a été effectuée dans le cadre de l'International Research Training Group "Soft Condensed Matter: Physics of Model Systems" entre les Universités de Constance (resp. G. Maret), de Grenoble (Resp. B. Pépin-Donat) et de Strasbourg (Resp. J. Baschnagel). Cette thèse a été financée par l'Université de Constance, ainsi que diverses bourses à la mobilité de la DAAD (Deutscher Akademischer Austausch Dienst (DAAD)), de Université Franco-Allemande (UFA-DFH) et de la région Rhône-Alpes (Bourse Explora'doc). Je suis reconnaissant à ces différents organismes d'avoir cru en mon projet et d'avoir apporté leur soutien au bon déroulement de ces travaux.

Contents

1	Introduction	13
2	Vesicles	19
2.1	From lipids to vesicles	19
2.1.1	Lipids	19
2.1.2	Self-association of lipids in aqueous solution	20
2.1.3	Vesicles	21
2.2	Phase transition of lipid membranes	21
2.2.1	Bilayer structures in fluid, gel and crystalline phases	22
2.2.2	Bilayer structure and lipids mobility	22
2.3	Properties of lipid membranes	23
2.3.1	Membrane permeability	23
2.3.2	Membrane deformation modes	24
2.3.3	Membrane mechanical parameters: effect of the phase transition	27
2.3.4	Membrane tension: definition and role on the bilayer structure	27
2.3.5	Membrane fluctuations	30
2.4	Electrostatics of lipid membranes	30
2.4.1	The electrical double-layer	31
2.4.2	Effects of salt and pH on lipid membrane properties	33
3	From non-charged polymers to polyelectrolytes	35
3.1	Non-charged polymers in solution	35
3.1.1	Gaussian chain model	35
3.1.2	Real chains	36
3.1.3	Semi-flexible polymer chains	37
3.2	Charged polymers (polyelectrolytes) in solution	37
3.2.1	Charge parameter and intrinsic pK	38
3.2.2	Influence of salt concentration on polyelectrolyte conformation	39
3.2.3	Association of oppositely charged polyelectrolytes	42
3.3	Chitosan and derivatives	42
3.3.1	Chitosan structure and properties	42
3.3.2	Chitosan derivatives	43
3.3.3	Complex formation	43
3.3.4	Applications	44
3.4	Hyaluronan and derivatives	44
3.4.1	Hyaluronan structure and properties	44
3.4.2	Hyaluronan derivatives	45
3.4.3	Complex formation	45
3.4.4	Applications	45

4	Vesicle-polyelectrolyte interactions	47
4.1	Generalities on polymer sorption on a surface	47
4.1.1	Amount and conformation of adsorbed polymer	48
4.1.2	Kinetics of polymer adsorption and desorption	50
4.2	Effect of polymer adsorption on the membrane and vesicle structure	51
4.3	Effect of polymer adsorption on membrane properties	52
4.3.1	Mechanical properties	52
4.3.2	Electrostatic properties	52
4.4	Effect of polymer adsorption on vesicle suspension stability	53
4.4.1	Bare vesicle suspension	53
4.4.2	Non-charged polymer coated vesicle suspension	53
4.4.3	Polyelectrolyte coated vesicle suspension	54
4.5	Chitosan and hyaluronan in interaction with lipid membrane	55
4.5.1	Chitosan/lipid membrane	55
4.5.2	Hyaluronan/lipid membrane	56
5	Soft deformable objects under external stresses	57
5.1	Anisotropic depressure: micropipette suction experiments	58
5.2	Isotropic pressure	59
5.2.1	Vesicles: deflation of spherical incompressible shells	59
5.2.2	Deflation of thin spherical shells	62
5.2.3	Red blood cells: membrane-skeleton coupling model	63
5.3	Anisotropic compression: AFM experiments	64
5.3.1	Theory of thin shell deformation	64
5.3.2	Deformation of vesicles using AFM	65
5.4	Flow in non-confined and confined geometries	65
5.4.1	Shear flow	66
5.4.2	Poiseuille flow	68
5.5	Point-acting force: hydrodynamic extrusion of tubes from giant vesicles	72
6	General materials and methods	73
6.1	Preparation of vesicles with membrane in fluid phase	73
6.1.1	Lipids	73
6.1.2	Electroformation of GUVs	75
6.1.3	LUVs preparation by GUVs extrusion	76
6.2	Vesicles coated with polyelectrolytes	76
6.2.1	Polyelectrolytes	76
6.2.2	Incubation of vesicles with polyelectrolytes	78
6.3	PEG treatment of glass substrates	78
6.4	Preparation of GUVs suspension for microscopy observation	79
6.5	Increase of pH, salt and glucose concentrations of the GUVs and LUVs suspensions (so called “pH, salt and glucose shocks”)	79
6.6	Experimental methods for LUVs characterization	79
6.6.1	Spectrofluorimetry: determination of the lipid amount in LUVs	79
6.6.2	ζ -potential and size measurements	80
6.6.3	Isothermal titration calorimetry (ITC)	81
6.7	Experimental methods for GUVs characterization	82
6.7.1	Optical microscopy observations and image analysis	82
6.7.2	ζ -potential measurements	84

6.7.3	Atomic Force Microscopy (AFM)	84
6.7.4	Microfluidic	85
6.7.5	Hydrodynamic extrusion of membrane tethers	87
7	Preliminary study - DOPC membrane, Chitosan and hyaluronan net charge as a function of pH and salt concentration	89
7.1	Net charge of DOPC membrane	89
7.1.1	pH effect	89
7.1.2	Salt effect	91
7.2	Effect of pH on the polyelectrolyte charge density	91
7.3	Conclusion	92
8	Characterization of the coating of DOPC lipid membranes by chitosan and hyaluronan	93
8.1	Direct evidence of chitosan and hyaluronan adsorption on DOPC membranes . .	94
8.2	Characterization of the interactions between chitosan or hyaluronan and DOPC membranes	95
8.2.1	Electrostatic contribution	95
8.2.2	Hydrophobic contribution	99
8.3	Role of polyelectrolyte sorption on the suspension state of LUVs and GUVs . . .	104
8.4	Coverage degree determination	108
8.4.1	From ζ -potential measurements on LUVs	108
8.4.2	From fluorescence measurements on GUVs	109
8.5	Variation of the coverage degree: comparison between chitosan and hyaluronan .	112
8.5.1	Role of the relative membrane/polyelectrolyte net charges	112
8.5.2	Role of the polyelectrolyte molecular weight	113
8.5.3	Conclusions on the chitosan and hyaluronan conformations at the interface	118
8.6	Stability of the polyelectrolyte coating: reversibility of the adsorption?	118
8.6.1	Effect of dilution	118
8.6.2	Effect of pH	121
8.7	Coating of lipid membrane by multilayer of polyelectrolytes	123
8.8	Conclusion	125
9	Study of chitosan- and hyaluronan-coated vesicles behaviors under external stresses	127
9.1	Anisotropic depression: micropipette suction experiments	128
9.2	Osmotic pressure	128
9.2.1	Glucose shocks	128
9.2.2	NaCl shocks	132
9.2.3	HCl or NaOH shocks	135
9.3	Point-acting force: hydrodynamic extrusion of tubes from chitosan-coated vesicles	136
9.3.1	Nanotether extrusion on bare DOPC GUVs	136
9.3.2	Nanotether extrusion on chitosan-coated GUVs	137
9.3.3	Proposed model to describe the tube extrusion from vesicles presenting a membrane asymmetry	139
9.3.4	Interpretation of the experimental results with the membrane spontaneous curvature	142
9.4	Anisotropic compression: AFM experiments	143
9.4.1	Force/deformation of chitosan-coated vesicles	143
9.4.2	Model for result interpretation	144

9.5	Conclusion	146
10	Study of vesicles in gel state under osmotic pressure	149
10.1	Osmotic deflation of DMPC GUVs with membrane in $P_{\beta'}$ gel phase	149
10.1.1	Preparation of spherical DMPC GUVs with membrane in $P_{\beta'}$ gel phase at 15°C	150
10.1.2	Deflation of gel phase GUVs associated with formation of depressions	151
10.2	Numerical simulations of an elastic surface under an isotropic pressure	152
10.3	Comparison between experimental and simulated shapes	155
10.4	Conclusion	158
11	Dynamical deformation of vesicles in fluid state under confined flows	159
11.1	Solution and experimental procedures	159
11.1.1	Sample Solutions	159
11.1.2	Microfluidic devices and video-microscopy	160
11.1.3	Image Analysis	160
11.2	Flow through a narrow capillary	161
11.2.1	Capillary geometry	161
11.2.2	General behavior	162
11.2.3	Velocity profile and transit time of the vesicles	163
11.2.4	Vesicle's dynamic deformation	165
11.2.5	Excess of pressure drop associated with the flow of vesicles in a narrow capillary	168
11.2.6	What about the membrane's motion?	170
11.3	Flow through multiple periodic constrictions	172
11.3.1	Teeth-like geometry	172
11.3.2	General behavior	173
11.3.3	Drift of the vesicles	173
11.3.4	Velocity profile and transit time of the vesicles	175
11.3.5	Vesicle's dynamic deformation	177
11.4	Conclusion	179
12	Conclusion and prospects	181
A	Table units	187
B	Link between isotropic material and 2D model elastic parameters	189
C	Comparison simulations and biological objects	191

Chapter 1

Introduction

Dans l'organisme, les cellules vivantes sont constamment soumises à des stimulations mécaniques résultant à la fois de l'environnement externe et des conditions physiologiques internes [Alberts et al., 2002]. Selon l'intensité, la direction et la distribution de ces stimuli mécaniques, les cellules peuvent répondre de façon très variée [Lim et al., 2006]. A titre d'exemple, les cellules endothéliales soumises à un cisaillement libèrent une hormone qui induit leur rigidification via une réorganisation de leur cytosquelette [Jen et al., 2000]; ou dans le cas de cellules adhérentes sur un substrat, la déformabilité de celui-ci peut modifier leur motilité et leur orientation [Wang et al., 1995].

A ce titre, la compréhension de la réponse mécanique des cellules soumises à des contraintes physiques est une première étape importante pour appréhender la conversion des signaux mécaniques en réponses biologiques et chimiques [Huang and Ingber, 1999].

Bien que les propriétés biologiques et physiques soient réciproquement régulées dans la cellule, il apparaît que les propriétés mécaniques jouent un rôle important dans beaucoup de processus biologiques. En parallèle de l'étude directe du comportement des cellules, il semble donc intéressant de développer et d'étudier des modèles mécaniques de cellules pour comprendre leurs réponses à des contraintes externes. Cette approche permet d'appréhender un processus biologique particulier en étudiant comment des objets biomimétiques répondent à une série de contraintes simulant des situations d'intérêt biologiques (adhésion à un substrat, déplacement dans un écoulement ...) [Liu and Fletcher, 2009].

Les vésicules géantes unilamellaires (GUVs) - membranes sphériques de phospholipides de taille micrométrique [Lipowsky and Sackmann, 1995] - sont considérées comme un modèle simpliste de membranes cellulaires. Cependant leur structure très simple et leur faible résistance aux contraintes externes limitent leur pertinence pour mimer de vraies cellules. Afin d'améliorer leurs propriétés mécaniques, il est possible de modifier soit leur milieu interne soit leur membrane.

Dans ce travail, nous nous sommes intéressés tout particulièrement à la modification de la membrane en utilisant soit la transition de phase des lipides pour obtenir des GUVs présen-

tant une membrane en phase gel, soit en adsorbant des polyélectrolytes (chitosane et acide hyaluronique) sur des membranes fluides. En plus du développement de ces vésicules complexes, notre travail a consisté à étudier le rôle de chacune de ces modifications sur le comportement de ces vésicules soumises à différentes contraintes externes.

Ce manuscrit est composé de douze chapitres distincts. Après une courte introduction, les chapitres 2 et 3 rappellent des généralités sur les vésicules lipidiques et les polyélectrolytes. Puis le chapitre 4 donne un bref aperçu des interactions membrane-polyélectrolyte et de leurs conséquences sur la structure et les propriétés mécaniques des membranes décorées. Dans le chapitre 5, nous proposons une présentation de l'état de l'art sur le comportement d'objets déformables soumis à diverses contraintes externes. Le chapitre 6 détaille les protocoles de préparation de nos vésicules composites ainsi que les techniques expérimentales utilisées. Le chapitre 7 présente les effets du pH et de la concentration en sel sur les charges respectives des vésicules de DOPC, du chitosane et de l'acide hyaluronique. Dans le chapitre 8, nous caractérisons l'interaction entre la membrane lipidique et deux polyélectrolytes. Le chapitre 9 est consacré à l'effet de cette interaction sur le comportement des vésicules décorées soumises à divers contraintes externes, telles que la modification de l'environnement externe (pression osmotique, pH et chocs ioniques), la compression entre deux plans en utilisant la microscopie à force atomique et l'extrusion hydrodynamique de nanotube de membrane. Le chapitre 10 présente les résultats obtenus lors du dégonflement osmotique de vésicules en phase gel. Le chapitre 11 détaille les comportements de vésicules s'écoulant dans deux types de géométries microfluidiques. Nous terminerons par un bilan des résultats obtenus et certaines perspectives ouvertes par ce travail.

○ ○ ○ ○ ○ ○ ○ ○ ○ ○

Living cells in human body are constantly subjected to mechanical stimulations arising from external environment and internal physiological conditions [Alberts et al., 2002]. Depending on the magnitude, direction and distribution of these mechanical stimuli, cells can respond in a variety of ways [Lim et al., 2006]. For examples, the fluid shear stress exerted on endothelial cells in the blood vessels activates hormone release which in turn induces the cell stiffness by rearranging the cytoskeleton [Jen et al., 2000], or tensile stretching of the cell substrate can alter both cell motility and cell orientation [Wang et al., 1995]. Hence, the understanding of how cells mechanically respond to physical loads is an important first step before further investigating how mechanical signals are converted to biological and chemical responses. For example, cell growth, differentiation, migration and even apoptosis are influenced by changes in their shape and structure [Huang and Ingber, 1999].

Beside the fact that biological and physical properties are reciprocally regulated, it appears that the mechanical properties play an important role on many biological processes. Therefore, it is of interest to develop mechanical models of cells to understand how cells respond to external

stresses. This approach may allow to decipher a particular biological process by studying the mechanical response of reconstituted biomimetic objects under controlled conditions (adhesion to a substrate, movement in a flow ...) [Liu and Fletcher, 2009].

Giant Unilamellar Vesicles (GUVs), which are spherical phospholipidic membranes typically on micrometer length-scales [Lipowsky and Sackmann, 1995], are considered as an oversimplified model of cell membranes. Nevertheless their simple structure and their poor resistance to external stresses limit their relevance to mimic real cells. To improve their mechanical properties, either their internal medium or their membrane can be modified.

In this work, we focus on the membrane modification either by using the lipid phase transition to obtain GUVs with membrane in the gel phase, or by coating fluid membranes with polyelectrolytes (chitosan and hyaluronan). In addition to the development of these complex vesicles, our work consisted in studying the role of each one of these modifications on their behavior under various external stresses.

This manuscript is composed of twelve chapters. After a brief introduction, Chapters 2 and 3 recall generalities on vesicles and polyelectrolytes. Then Chapter 4 gives a brief review of the lipid membrane-polyelectrolyte interactions and the consequences on the structure and mechanical properties of the coated membranes. Chapter 5 gives a literature overview on the behavior of deformable objects under the external constraints as applied in this study. Chapter 6 is devoted to materials and methods. Chapter 7 describes the effect of pH and of salt concentration on the net charges of DOPC vesicles, of chitosan and of hyaluronan. In Chapter 8, we characterize the interaction between the lipid membrane and both polyelectrolytes. Chapter 9 is devoted to the effect of this interaction on the behavior of the coated vesicles under the following external stresses: modification of the external environment (osmotic pressure, pH and ionic shocks), compression between two planes using Atomic Force Microscopy and hydrodynamical extrusion of membrane tube. Chapter 10 presents the osmotic shrinkage of vesicles with membrane in the gel phase. The obtained faceted shapes will be confronted with the results of numerical simulations carried out for elastic shells. Chapter 11 details the behavior of vesicles flowing in various microfluidic geometries, before coming to the final discussion and prospects.

○ ○ ○ ○ ○ ○ ○ ○ ○ ○

Einführung

Lebende Zellen im menschlichen Körper sind ständigen mechanischen Reize ausgesetzt, welche durch ihr äußeres Umfeld als auch ihre internen physiologischen Bedingungen ausgelöst werden [Alberts et al., 2002]. Je nach Größe, Richtung und Verteilung dieser mechanischen Reize, können Zellen mit einer Vielzahl verschiedener Möglichkeiten reagieren [Lim et al., 2006]. Zum Beispiel erzeugt die durch den Blutfluss erzeugte Scherung von Endothelzellen der Blutge-

fassen die Freisetzung von Hormonen, welche ihrerseits die Zellsteifigkeit durch Umlagerung des Zellskelets hervorruft [Jen et al., 2000], oder es führt eine Zug-Dehnung des Zell-Substrates zu einer Veränderung sowohl der Zellbewegung als auch der Orientierung [Wang et al., 1995]. Daher ist das Verständnis, wie Zellen mechanisch auf physikalische Belastungen reagieren, ein wichtiger erster Schritt, vor der weiteren Erforschung wie genau mechanische Signale in biologische und chemische Reaktionen umgewandelt werden. So werden zum Beispiel Zell-Wachstum, -Differenzierung, -Migration und selbst -Apoptose durch Veränderungen der äusseren zellulären Form und Struktur beeinflusst [Huang and Ingber, 1999].

Neben der Tatsache, dass biologische und physikalische Eigenschaften wechselseitig geregelt sind, scheint es, als ob die ersten Schritte vieler biologischer Prozessen grossteils von den zellmechanischen Eigenschaften gesteuert werden. Daher ist es von Interesse, mechanische Zellmodelle zu entwickeln, um zu verstehen wie Zellen auf solche äussere Belastungen reagieren. So könnte dieser Ansatz bestimmte biologische Prozesse entschlüsseln, indem es studiert wird wie solche biomimetische Objekte auf kontrolliert erzeugte biologische Situationen reagieren (Adhäsion an einem Substrat, Bewegung in einer Strömung . . .) [Liu and Fletcher, 2009].

Die so genannten "Giant Unilamellar Vesicles" (GUVs) [riesige unilamellare Vesikel], welche aus einer sphärischen Phospholipid-Membran in der Grössenordnung von einigen Mikrometern bestehen [Lipowsky and Sackmann, 1995], werden als ein stark vereinfachtes Modell von Zellmembranen angesehen. Trotz ihres einfachen Aufbaus und ihrer niedrigen Stabilität gegen äussere Belastungen, eignen sie sich als relevantes Modell realer Zellen. Zur Verbesserung der mechanischen Eigenschaften kann entweder ihr internes Medium oder ihre Membran verändert werden.

In dieser Arbeit konzentrieren wir uns auf Veränderungen der Membran, wobei wir entweder den Lipid Phasenübergang nutzen um GUVs mit Membranen in der Gelphase zu erhalten, oder die Membran durch die Beschichtung mit Polyelektrolyten (Chitosan und Hyaluronsäure) modifizieren. Neben der Entwicklung der komplexen Vesikel, bestand unsere Arbeit darin die Rolle jeder dieser Membranveränderungen auf das Vesikelverhalten unter verschiedenen äusseren Belastungen zu studieren.

Dieses Manuskript besteht aus zwölf Kapiteln. Nach einer kurzen Einführung, wiederholen die Kapitel 2 und 3 allgemeine Eigenschaften von Vesikeln und Polyelektrolyten. Dann gibt Kapitel 4 einen kurzen Überblick über die Lipid-Membran-Polyelektrolyt Wechselwirkungen und deren Folgen auf die Struktur und die mechanischen Eigenschaften der beschichteten Membranen. Kapitel 5 enthält eine umfassende Beschreibung der Literatur über das Verhalten verformbarer Objekte unter äusseren Belastungen wie sie in dieser Studie verwendet wurden. Kapitel 6 widmet sich Materialien und Methoden. Kapitel 7 befasst sich mit den Auswirkungen von entweder pH-Wert- oder Salzkonzentrations-Änderungen auf die Nettoladung von DOPC Vesikel, Chitosan und Hyaluronsäure. In Kapitel 8 charakterisieren wir die Wechselwirkung zwis-

chen der Lipidmembran und beiden Polyelektrolyten. Kapitel 9 widmet sich den Auswirkung dieser Interaktion auf das Verhalten der Vesikel unter äußeren Belastungen: Änderung der äußeren Umgebung (osmotischer Druck, pH-Wert und ionische Schocks), Kompression zwischen zwei Ebenen mit Hilfe der Rasterkraftmikroskopie und der hydrodynamischen Extrusion eines Membran-Schlauchs . Kapitel 10 präsentiert die osmotische Schrumpfung von Vesikeln mit der Membran in der Gelphase. Die erhaltenen facettenreichen Formen werden mit den Ergebnissen der numerischen Simulationen elastischer Schalen verglichen. Kapitel 11 beschreibt die Verhaltensweisen von Vesikeln, welche in verschiedenen mikrofluidische Geometrien fließen, bevor man zur abschließenden Diskussion und den möglichen zukünftigen Perspektiven kommt.

Chapter 2

Vesicles

Dans ce chapitre, nous rappelons tout d’abord comment les lipides (qui sont des molécules amphiphiles) s’auto-assemblent en solution pour former des vésicules. Puis, nous discutons l’effet de la température sur la structure et les propriétés des membranes de lipides. Enfin nous présentons l’effet du pH et de la concentration en sel sur les propriétés d’une membrane chargée.



In this chapter, we first remind how the amphiphilic character of lipids allows them to self-assemble in complex structures (from bilayers to vesicles). Secondly, we describe the fluid-gel phase transition before coming to the fluid and gel membrane properties. Finally, we present the effect of salt concentration and pH on charged membrane properties.

2.1 From lipids to vesicles

2.1.1 Lipids

Five main categories of lipids can be distinguished: glycerophospholipids, sphingomyelins, glycolipids, steroids and eicosanoids (for a complete review of the various lipid families refer to [Alberts et al., 2002]). In this study, we only focus on the glycerophospholipids, which are amphiphilic molecules made of an hydrophilic head, composed of a phosphate group and a polar group, connected to two hydrophobic tails by a glycerol group (Figure 2.1a). Depending on the chemical structure of the polar group, the net charge of the phospholipids changes. For example, phosphatidylcholine (PC), phosphatidylethanolamine (PE) and phosphatidylserine (PS) are zwitterionic lipids (carrying both positive and negative charges on the hydrophilic head) while phosphatidic acid (PA), phosphatidylglycerol (PG) and phosphatidylinositol (PI) are negatively charged (Figure 2.1b).

Traditional nomenclature consists in naming the phospholipid as “C_n:m X”, with n the number of carbons on the chain, m the number of unsaturations and X the polar head group. For example, the 1,2-dioleoyl-sn-glycero-3-phosphocholine, commonly named DOPC, has two oleoyl

chains (chain of 18 carbons with one double bond) and a phosphatidylcholine (PC) polar head; the notation is thus diC18:1 PC.

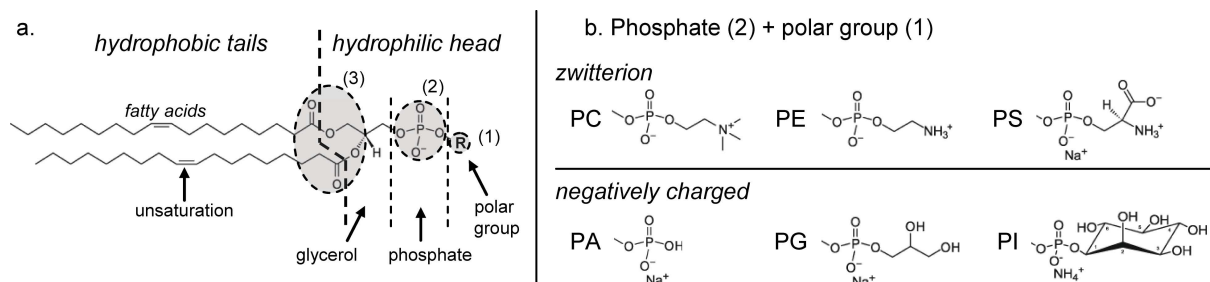


Figure 2.1: (a) Chemical structure of a phospholipid which is composed of a hydrophilic head formed by active sites: a polar group (1), a negative phosphate group (2) and two “carbonyl oxygen” groups (3) which connect the hydrophilic head group and the two hydrophobic tails. (b) Chemical formula of the different polar head groups (1) of the phospholipids: phosphatidylcholine (PC), phosphatidylethanolamine (PE), phosphatidylserine (PS), phosphatidic acid (PA), phosphatidylglycerol (PG) and phosphatidylinositol (PI).

2.1.2 Self-association of lipids in aqueous solution

Above the critical micellar concentration ($\sim 10^{-10}$ M) [Israelachvili, 1992], lipids are not soluble anymore in water and naturally tend to self-assemble in order to limit the contact between hydrophobic tails and water. The formed structures are diverse and essentially governed by geometrical parameters concerning the global shape of the lipid [Israelachvili, 1992, Lipowsky and Sackmann, 1995] (Figure 2.2).

Lipid	Single-chained lipids (surfactants) with large head-group areas: SDS in low salt, ...	Single-chained lipids with small head-group areas: SDS and CTAB in high salt, nonionic lipids, ...	Double-chained lipids with large head-group areas, fluid chains: phospholipids (PC, PE, PS, PA, PG and PI), ...	Double-chained lipids with small head-group areas, anionic lipids in high salt, saturated frozen chains	Double-chained lipids with small head-group areas, nonionic lipids, poly(cis) unsaturated chains, high temperature
Critical packing parameter (V/s^2L_c)	$< 1/3$	$1/3 - 1/2$	$1/2 - 1$	~ 1	> 1
Critical packing shape	cone 	truncated cone 	truncated cone 	cylinder 	inverted truncated cone or wedge
Structures formed	spherical micelles 	cylindrical micelles 	flexible bilayers, vesicles 	planar bilayers 	inverted micelles

Figure 2.2: Some examples of lipid phase structures observed in aqueous solution, based on geometrical arguments concerning the shape of the lipids (adapted from [Israelachvili, 1992]).

In the case of phosphatidylcholine, the sections of the polar head and of the two hydrophobic tails are approximately the same ($\sim 60 \text{ \AA}^2$), which induces, in presence of water, a three dimensional self-closed bilayer structure (assembly of two separate lipid leaflets with a thickness between 3 to 6 nm, depending of the hydrocarbon chain length), named vesicles (Figure 2.3).

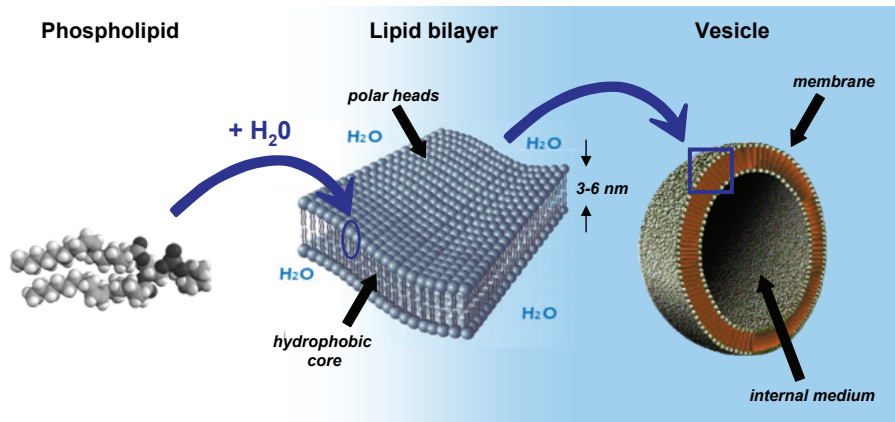


Figure 2.3: In presence of water, lipids self-associate in bilayer structures which tend to close in order to form lipid vesicles.

2.1.3 Vesicles

Depending on the preparation technique used [Walde et al., 2010], it is possible to produce vesicles with different sizes ranging from nanometers to tens of micrometers in diameter. Three main kinds of liposomes are distinguished: Small Unilamellar Vesicles (SUVs; 20 to 100 nm) and Large Unilamellar Vesicles (LUVs; 100 to 500 nm), which are both usually compared to cellular organelles (vesicles of secretion, of transport . . .) [Alberts et al., 2002] and used as protective capsules for biomedical applications [Malmsten, 2003], and Giant Unilamellar Vesicles (GUVs; 0.5 to 100 μm), which are generally studied as over-simple models of biological cells [Lipowsky and Sackmann, 1995] and present the advantage to be directly observable by optical microscopy.

2.2 Phase transition of lipid membranes

When temperature decreases below the main transition temperature T_m , lipid membranes exhibit a structural phase transition from a liquid disordered phase to an ordered solid phase [Luzzati and Husson, 1962]. Table 2.1 reports for several phosphatidylcholine lipids, the effect of the chemical structure (lengths of the hydrocarbon chains and position and number of unsaturation) on the value of T_m .

hydrocarbon	Phosphatidylcholine		Phosphatidylethanolamine	
	lipid	T_m [°C]	lipid	T_m [°C]
saturated	diC12:0 (DLPC)	-1.9	diC12:0 (DLPE)	30.4
	diC14:0 (DMPC)	23.6	diC14:0 (DMPE)	49.3
	diC16:0 (DPPC)	41.3	diC16:0 (DPPE)	62.3
	diC18:0 (DSPC)	54.5	diC18:0 (DSPE)	73.7
unsaturated	C16:0/C18:1c9 (POPC)	-2.5	C16:0/C18:1c9	24.4
	C18:0/C18:1c9 (SOPC)	6.9		
	diC18:1c9 (DOPC)	-18.3	diC18:1c9 (DOPE)	-7.3
	diC18:2c9,12	-55.1	diC18:2	-40.0

Table 2.1: Main transition temperatures for several pure phosphatidylcholine (PC) [Koynova and Caffrey, 1998] and phosphatidylethanolamine (PE) [Koynova and Caffrey, 1994] lipid membrane with different fatty acid chain length and unsaturation.

2.2.1 Bilayer structures in fluid, gel and crystalline phases

X-ray studies have revealed four different structures: one liquid phase denoted as L_α , two ordered gel phases referred to as $P_{\beta'}$ (rippled gel phase) and $L_{\beta'}$ (tilted gel phase) and one crystalline phase called L_c (see Figure 2.4) [Tardieu et al., 1973, Janiak et al., 1979]. Three characteristic temperatures can then be defined: T_m , T_p and T_{sub} .

The transition from fluid to gel to crystalline phase, corresponding to the ordering of the membrane, is associated with a decrease of the surface area and an increase of the bilayer thickness [Rüppel and Sackmann, 1983]. Indeed, in the $P_{\beta'}$ gel phase, periodic corrugations of the membrane have been revealed by several techniques such as electron microscopy [Meyer, 1996] or atomic force microscopy [Kaasgaard et al., 2003], as well as a 20 % decrease of the membrane surface area.

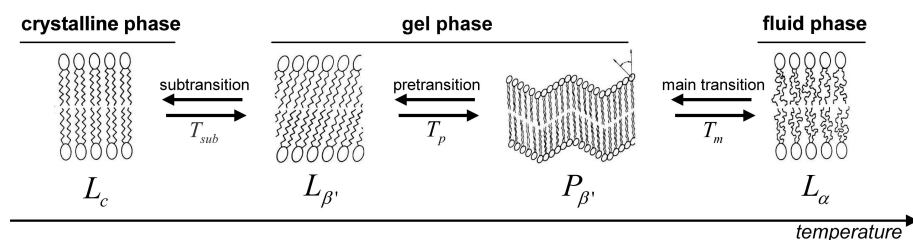


Figure 2.4: Schematic view of structure orientation of phospholipid in the membrane for the different phases: L_α , $P_{\beta'}$, $L_{\beta'}$ and L_c pictures (adapted from [Lipowsky and Sackmann, 1995]); lipids display an increasing order of the chains with decreasing temperature [Janiak et al., 1979].

2.2.2 Bilayer structure and lipids mobility

In the bilayer, phospholipids may exhibit different kinds of movements: rotate around their own axis, diffuse in one leaflet and pass in the other layer (flip-flop mechanism) (see Figure 2.5).

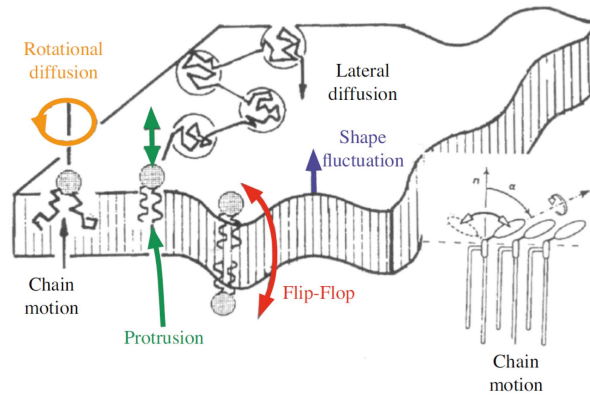


Figure 2.5: Schematic representation of lipid motions in membranes [Charitat et al., 2008].

Within the liquid phase, lipids freely rotate (rotational diffusion time $\sim 10^{-8}$ s [Lipowsky and Sackmann, 1995]) and diffuse along the leaflet (diffusion coefficient \sim few $\mu\text{m}^2/\text{s}$ [Saxton and Jacobson, 1997]). A lipid can thus explore the layer surface of membrane (it belongs to) of a $10 \mu\text{m}$ radius vesicle in few seconds. In the contrary, the transverse diffusion between the two leaflets, are much slower. Usually several days are necessary to exchange half of the phospholipid molecules between the two leaflets [Rothman and Dawidowicz, 1975] and at the scale of usual experiments flip-flop has not to be considered.

When temperature decreases below T_m , the increase of order in the bilayer causes a dramatic loss of the lipid mobility: lateral diffusion coefficient goes from few $\mu\text{m}^2/\text{s}$ in the fluid phase to a value lower than $10^{-3} \mu\text{m}^2/\text{s}$ in the $L_{\beta'}$ gel phase [Cullis, 1976, MacKay, 1981] [Derzko and Jacobson, 1980]. In this case, the lipid explores the layer surface of a $10 \mu\text{m}$ radius vesicle within several hours instead of few seconds in the fluid phase.

In the $P_{\beta'}$ ripple gel phase, heterogeneity in the diffusion coefficients has been observed and interpreted as the co-existence of both L_{α} and $L_{\beta'}$ phases in the membrane [Derzko and Jacobson, 1980]. These results were confirmed by ^{13}C NMR [Davis, 1979] [MacKay, 1981] and EPR [Tsuchida and Hatta, 1988] experiments which show that a fraction of the chains ($\sim 20\%$) remains in a disordered state L_{α} (located in the high curvature domains) and coexists with ordered lipids (linear domains composed of $L_{\beta'}$) [Sun et al., 1996, Rappolt et al., 2000, Heimburg, 2000, de Vries et al., 2005].

2.3 Properties of lipid membranes

2.3.1 Membrane permeability

Molecules exchanges may occur or not through lipid membranes [Balaz, 2009]. Permeability of different molecules through fluid membranes are reported in Figure 2.6. Small polar uncharged molecules (H_2O , urea ...) and hydrophobic molecules (O_2 , CO_2 ...) can diffuse through

the bilayer while lipid membrane is relatively impermeable to larger polar uncharged molecules (such as glucose and sucrose) and ions (H^+ , Cl^- , Na^+ ...).

It has been shown that when undergoing the phase transition, the permeability of the membrane is drastically reduced. The water permeability, in the gel phase, is estimated 50 to 100 times lower than in the fluid phase [Fettiplace and Haydon, 1980, Jansen and Blume, 1995].

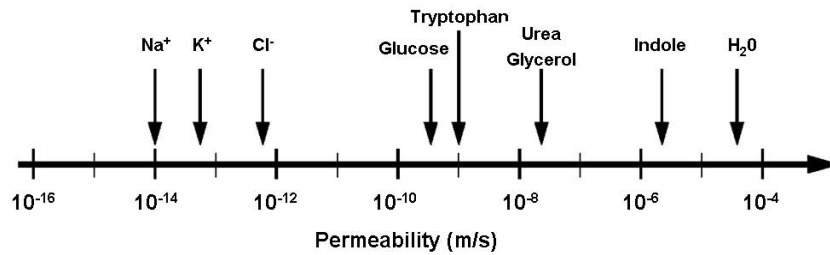


Figure 2.6: Permeability of different molecules through a lipid bilayer in the fluid phase.

It can be taken advantage of the fact that glucose and sucrose molecules cannot cross phospholipid membranes to deflate vesicles. Indeed, if a chemical species is present at different concentrations inside and outside of the vesicle, an osmotic pressure Π applies on the membrane:

$$\Pi = RT \ln\left(\frac{N_{in}}{N_{out}}\right) \quad (2.1)$$

where N_{in} and N_{out} are the number of solute molecules (N_{in}/N_{out} being equivalent to C_{in}/C_{out} , where C_{in} and C_{out} are the solute concentrations of the internal and external media), R is the universal gas constant and T is the absolute temperature. Water molecules will then cross the membrane in order to balance the concentrations allowing us to control the volume of the vesicle at constant total surface area: a controlled modification of the external glucose concentration allows a controlled deflation of the vesicle.

2.3.2 Membrane deformation modes

Because the order of magnitude of the bilayer thickness is very low ($\sim 3-6$ nm) if compared to the vesicle diameter (higher than few hundreds of nanometers for LUVs and GUVs), the membrane can be regarded from a mechanical point of view as an infinitely thin elastic sheet. Assuming that the lipid bilayer is a homogeneous and isotropic material, it can be modeled with an elastic surface [Feynman et al., 1966, Landau and Lifshitz, 1986]. Any strain applied to the membrane may be expressed as a combination of three basic deformations modes illustrated in Figure 2.7: the pure stretch (or compression) (1) and the shear (2) (both in-plane deformations) and the bending (3) (out-of-plane contribution).

Assuming that the deformation is proportional to the applied stress (Hooke's law), mechanical properties of vesicles are described by three elastic parameters: the bending modulus κ , the stretching modulus χ and the shear modulus μ .

In the following, three deformation modes will be explained using these 2D elastic parameters. Relationships with the others (Young modulus and Poisson's ratio) and the link between the 2D and 3D elastic parameters are reported in Appendix B.

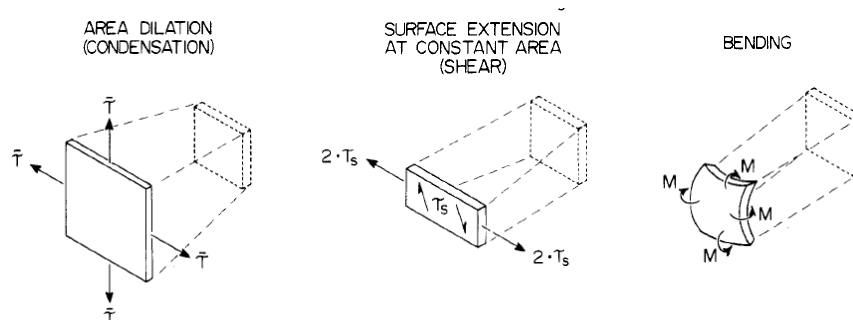


Figure 2.7: Three basic deformation modes for an element of thin surface material [Evans and Needham, 1987].

Stretching deformation

The stretching modulus χ characterizes the cohesion between the lipids of the bilayer. The energy of interaction between phospholipids presents a minimum value for a distance of 1 nm between two successive polar heads; deviation from this distance, by stretching or compression of the membrane (corresponding to change in thickness), costs energy. The energy density $dE_{stretching}$ related to an increase ΔA of the equilibrium surface area A_0 can be written in a quadratic approximation as:

$$dE_{stretching} = \frac{1}{2}\chi \left(\frac{\Delta A}{A_0} \right)^2 \quad (2.2)$$

For example, the stretching modulus of DOPC (diC18:1) membranes in the fluid phase is measured to 260 mN/m by micropipette aspiration experiments [Rawicz et al., 2000].

By comparing the stretching energy (χR^2) with the typical thermal energy ($k_B T$) of the object, for a vesicle of 10 μm radius, it appears that stretching or compression of thermal origin are completely negligible (10 orders of magnitude difference).

Shear deformation

A pure shear strain corresponds to a change of shape in the plane of the membrane at constant surface area. The shear elastic energy per unit surface area $dE_{shearing}$ may be expressed as:

$$dE_{shearing} = \frac{1}{2}\mu(\lambda^2 + \lambda^{-2} - 2) \quad (2.3)$$

where μ is the shear modulus and $\lambda = \frac{L_0 + \Delta L}{L_0}$ is the lateral extension ratio which characterizes the transformation of a square-shaped area element (of length L_0) into a rectangle of length L (leaving the area constant). In the case of fluid membrane, lipids can diffuse freely in the leaflet and relax any stress due to pure shear; so the shear energy of the system can be neglected.

Bending deformation

The third deformation mode accessible for a membrane surface element is the bending mode at constant surface area. The membrane bending can be described by two curvatures: the mean curvature ($C_1 + C_2$) and the Gaussian curvature ($C_1 C_2$), with $C_1 = 1/R_1$ and $C_2 = 1/R_2$ defined in a point of the surface (see Figure 2.8).

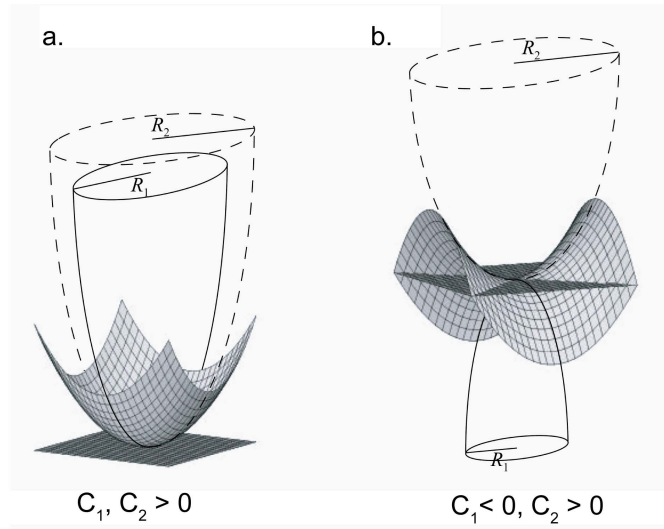


Figure 2.8: Curvatures on a 2D surface. (a) Curvatures of same sign: ellipsoidal form. (b) Curves of opposite sign: saddle form. The length scales R_1 and R_2 denote the radii of curvature [el Alaoui Faris, 2008].

Canham [Canham, 1970] and Helfrich [Helfrich, 1973] introduce the energy density associated to the bending $dE_{bending}$ as:

$$dE_{bending} = \frac{1}{2}\kappa(C_1 + C_2 - C_0)^2 + \frac{1}{2}\kappa_{gaus}C_1C_2 \quad (2.4)$$

where κ is the mean bending modulus, κ_{gaus} is the gaussian bending modulus and C_0 is the spontaneous curvature adopted by the bilayer in absence of external strain.

The total bending energy of the membrane is the integral of $dE_{bending}$ over the whole surface area of the object. The theorem of Gauss-Bonnet shows that the gaussian curvature ($C_1 C_2$), integrated over the total surface of the vesicle, is a topological invariant, so that when the vesicle keeps the same topology (no formation of “handle”), which is our case, the gaussian component of the energy can be neglected.

2.3.3 Membrane mechanical parameters: effect of the phase transition

In the case of DMPC, the different mechanical parameters (stretching modulus χ , shear modulus μ and bending modulus κ) have been evaluated by various techniques in the different membrane phases. It appears that, upon phase transition, the mechanical properties of lipid membranes are dramatically affected. Modifications in these parameters are gathered in Table 2.2.

DMPC $T_m = 23.6^\circ\text{C}$ $T_p = 11-13^\circ\text{C}$	Fluid phase		Gel phase	
	L_α disordered phase 	$P_{\beta'}$ rippled phase 	$L_{\beta'}$ tilted phase 	
χ stretching modulus	240 mN/m [Rawicz et al., 2000]	50– 60 mN/m [Evans and Needham, 1987]	300 mN/m ($L_{\beta'}^*$ at 15°C) [Needham and Evans, 1988] 1 N/m ($L_{\beta'}$ at 4°C) [Evans and Needham, 1987]	
μ shear modulus	-	?	?	
η_s shear surface viscosity	10^{-9} - 10^{-8} N.s/m [Dimova et al., 2000]	?	10^{-3} N/m ($L_{\beta'}^*$ at 15°C) [Needham and Evans, 1988]	
κ bending rigidity	$15k_B T$ [Rawicz et al., 2000]	$75 - 300k_B T^{(a)}$ [Evans and Needham, 1987, Charitat et al., 2008]	$300 - 400 k_B T$ [Charitat et al., 2008]	

(a) Bending moduli of membranes obtained by various techniques at temperatures about $5-8^\circ\text{C}$ below T_m .

Table 2.2: Typical mechanical parameters for DMPC membrane in fluid (L_α) and gel ($P_{\beta'}$ and $L_{\beta'}$) phases.

2.3.4 Membrane tension: definition and role on the bilayer structure

Definition

The last macroscopic parameter, used to describe the membrane, is its tension σ . For a membrane of surface area A and of free energy F , the tension is defined as:

$$\sigma = \frac{\partial(F)}{\partial A} \quad (2.5)$$

The energy density related to the variation of surface area for a tensed membrane is equal to:

$$dE_{tens} = \sigma \frac{\Delta A}{A_0} \quad (2.6)$$

When a pressure difference ΔP exists between the inside and the outside of the vesicle of

radius R , the tension applied to the membrane σ is then expressed by the Laplace's law, as:

$$\Delta P = \frac{\sigma}{2R} \quad (2.7)$$

Vesicles are fragile objects; lipid membranes cannot support high tension such as the vesicle lyses at a weak critical tension σ_{lysis} around 10 mN/m [Olbrich et al., 2000]. Therefore, using the Laplace's Law, the maximal pressure difference supported by a vesicle of 20 μm radius is ~ 100 Pa.

Effect of the tension on the structure of membranes in the gel state

In the Chapter 10, we will show that the phase membrane transition is realized at non-negligible osmotic pressure, which induces a membrane tension. Therefore, we now deal with the effect of membrane tension on the DMPC membrane structure obtained after the fluid-gel phase transition [Evans and Needham, 1987, Needham and Evans, 1988]. We will see that the following bibliographic study allow us to set experimental parameters to get vesicles with the desired gel structure.

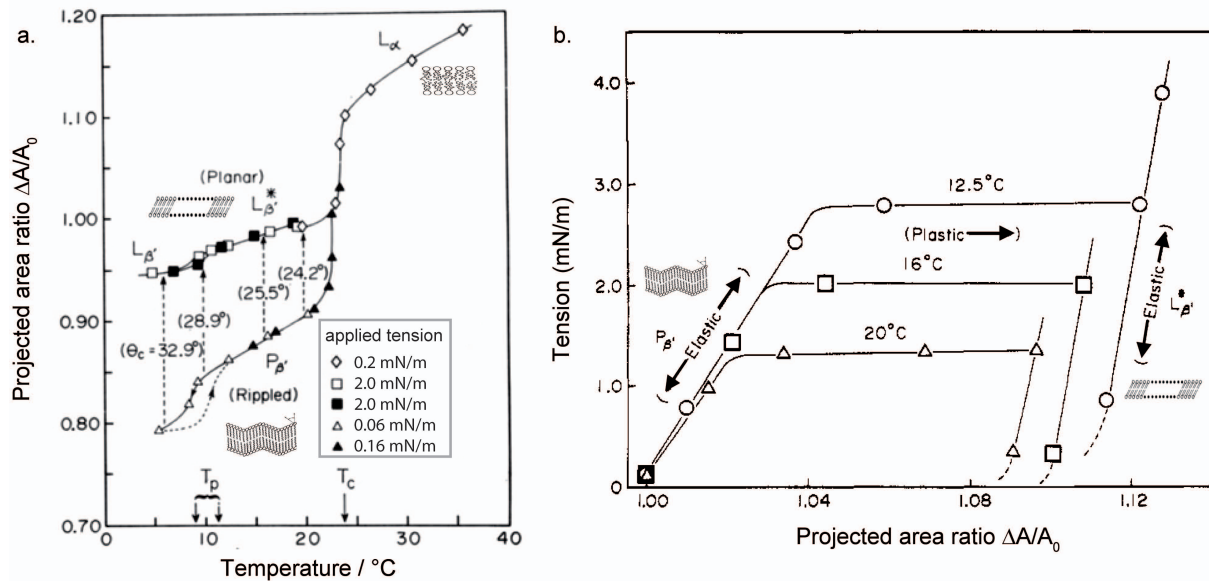
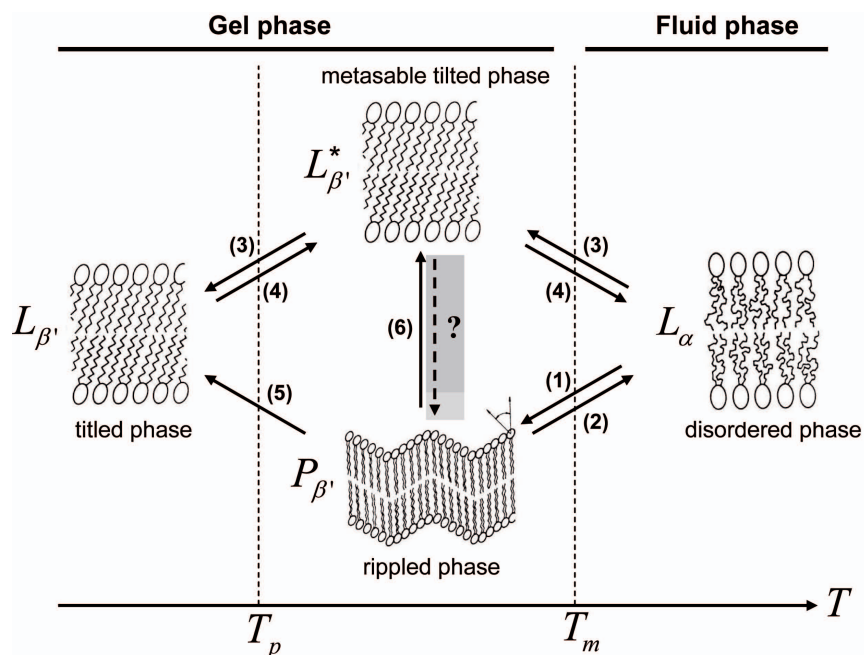


Figure 2.9: (a) The change in surface area ΔA normalized by the initial surface area A_0 of the vesicle, due to a modification in lipid arrangement associated with a temperature change is represented for the three different phases. Heating (solid symbols) and cooling (open symbols) cycles are indicated by different symbols which also refer to different membrane tensions imposed by micropipet suction and reported in the inset. (b) Ripple phase elasticity, yield, and plastic deformation followed by planar phase elasticity for a single vesicle at three different temperatures (adapted from [Needham and Evans, 1988]). Note: for an equivalence between the different units, report to the table in Appendix A.

It was demonstrated, that when the temperature is decreased below T_m , different gel phases are observed depending upon the initial tension applied to the vesicle. Cooling vesicles under zero at very low membrane tension (0.16 mN/m) leads to the $P_{\beta'}$ phase, while moderate or high

tensions (0.2 and 2 mN/m respectively) lead to the $L_{\beta'}^*$ phase, which correspond to the $L_{\beta'}$ phase for temperatures usually associated with the $P_{\beta'}$ phase (Figure 2.9a). Moreover micropipet experiments quantify the loss of surface area associated with the establishment of the two different gel phases ($P_{\beta'}$ and $L_{\beta'}^*$).

Upon successive suction, at fixed temperature, on a vesicle with a membrane in the $P_{\beta'}$ phase, three distinct regimes can be observed (Figure 2.9b). A first regime shows the elastic deformation of the ripple phase. Then, at a critical tension, a plastic expansion related to the irreversible unfolding of the ripple lattice is detected; finally a stiff elastic response to the area expansion due to the lipid compressibility of the planar surface $L_{\beta'}^*$ is observed. When aspiration is stopped, the membrane keeps the $L_{\beta'}^*$ structure and no relaxation transition between the $L_{\beta'}^*$ and $P_{\beta'}$ phase is observed for a temperature between T_m and T_p . These different transitions are summarized in Figure 2.10.



- (1) and (2): variation of temperature under zero or very low tension (0.16 mN/m).
 (3) and (4): variation of temperature under moderate or high tension (0.2 or 2 mN/m).
 (5): at 4°C for several days.
 (6): at fixed temperature, under tension, ripple structure is eliminated.

Figure 2.10: Phase diagram of lipid membranes for DMPC vesicles as function of the stress history (adapted from [Lipowsky and Sackmann, 1995, Evans and Needham, 1987, Needham and Evans, 1988]).

We can note that upon the phase transition, lipid bilayers become significantly more resistant to lysis (σ_{lysis} goes from 2-3 mN/m in L_{α} to 15 mN/m in $L_{\beta'}$). In $P_{\beta'}$, lysis tension is not defined (tension unfolds the ripples leading to $L_{\beta'}^*$).

We will see in section 5.1, that by measuring the membrane tension, it is also possible to evaluate the mechanical parameters of the lipid membrane.

2.3.5 Membrane fluctuations

In fluid phase, the low bending modulus κ (of the order of a couple of $k_B T$) makes of giant vesicles relatively soft objects, which are largely deformable. During experimental observations, vesicles are usually not tensed and undergo large fluctuations at different scales (Figure 2.11a), some being observable by optical microscopy (Figure 2.11b). Fluctuations have been observed a century ago by [Browicz, 1890] in the case of red blood cells and explained in terms of thermal fluctuation around an equilibrium position [Brochard and Lennon, 1975]. The observed area (A_p) does not correspond to the real surface (A) of the vesicle (A_p and A are defined in Figure 2.11a).

Membranes in the gel phase do not exhibit fluctuations due to the high bending modulus κ (of the order of few hundreds of $k_B T$) [Charitat et al., 2008].

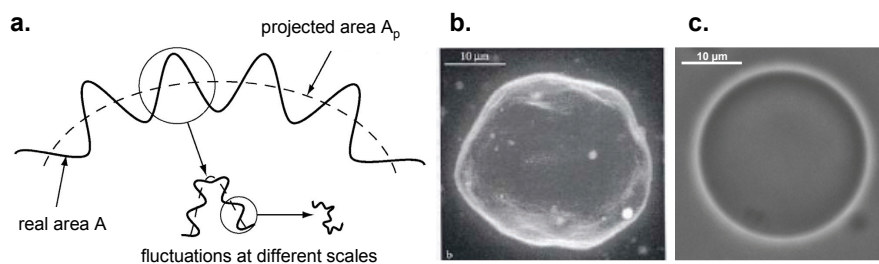


Figure 2.11: *Fluctuations and state of tension of giant vesicles. (a) Schematic representation of the membrane fluctuations at different scales from [Girard, 2004]. A and A_p represents the real area and the projected area, respectively. (b) Soft vesicle observed in fluorescence microscopy: projection of different focal plans, showing broad thermal undulations which crumple the object on several scales (image from [Sandre, 2000]). (c) A tense vesicle observed in phase contrast microscopy exhibits a perfect spherical shape.*

2.4 Electrostatics of lipid membranes

In the previous description, lipid membranes have been regarded as a simple two-dimensional material, neglecting the charges carried by the lipids (see section 2.1.1). However lipid bilayers may be charged, inducing electrostatic contributions to the membrane structural and mechanical properties [Cevc, 1990, Langner and Kubica, 1999].

In the case of phosphatidylcholine lipids, the head group is composed of a quaternary amino group, positively charged whatever the pH, and a phosphate group, which degree of dissociation depends on the pH (see Figure 2.12). Therefore, the net charge of the phosphatidylcholine membrane is positive in acidic conditions ($\text{pH} < 4.0$) (due to quaternary amino groups), equal to zero at $\text{pH} \sim 4.0$ and negative at $\text{pH} > 4.0$ (due to ionization of the phosphate groups and of the carboxylic groups) [Petelska and Figaszewski, 2000]. We stress that, contrary to what is generally considered phosphatidylcholine is a neutral lipid only at $\text{pH} \sim 4.0$; for any other pH value, this lipid must be regarded as a positively or negatively charged lipid.

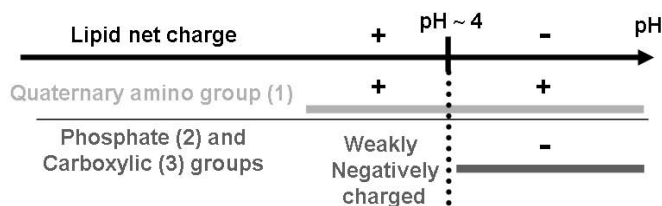


Figure 2.12: Evolution of the phosphatidylcholine lipid net charge with the pH. For an illustration of the different groups, report to Figure 2.1

Like any charged object immersed in an ionic solution, the membrane attracts a cloud of ions forming a diffusive electrical layer, whose properties differ from the bulk. Considering an atomic picture of electrolytes, Helmholtz, Gouy-Chapman, Stern and Graham [Hunter, 1981], have proposed a double layer structure to describe the distribution of ions near a charged surface.

2.4.1 The electrical double-layer

A schematic representation of the electrical double layer is shown in Figure 2.13 for a positively charged surface. In the bulk, *i.e.* far away from the interface, the ions are evenly distributed due to the entropy of mixing. Close to the charged surface, we can distinguish two zones:

- (i) the ***Stern layer***, which is composed of ions specifically adsorb near the surface. This layer is subdivided in two parts: the inner Helmholtz layer composed of a monolayer of chemisorbed dehydrated co-ions (ions of the same sign as those of the surface) and the outer Helmholtz layer formed of hydrated counterions.
- (ii) the ***diffuse layer***, further from the surface, where the distribution of the co-ions and the counterions is determined by both electrostatic interactions with the surface, and the diffusion mechanism due to thermal agitation, which tends to restore the equilibrium with the bulk.

As moving away from the surface, the electrical potential $\Psi(x)$ first increases before decreasing linearly to reach the Stern potential Ψ_S (at the external boundary of the Stern layer corresponding to the Stern plane); then, in the diffuse layer, it decreases exponentially towards zero. The distance from the surface at which the potential equals zero at a given temperature is the Gouy-Chapman length λ_{GC} , defined by the following relation:

$$\lambda_{GC} = (2\pi l_B \Phi)^{-1} \quad (2.8)$$

where Φ is the surface charge density and l_B , the Bjerrum length corresponding to the distance from which the electrostatic energy between two elementary charges e is compensated by the thermal energy $k_B T$:

$$l_B = \frac{e^2}{4\pi\epsilon_r\epsilon_0 k_B T} \quad (2.9)$$

where ε_r and ε_0 are respectively the dielectric constant of the solution and of the vacuum, k_B is the Boltzmann constant and T the temperature. Typically, $l_B = 7.13 \text{ \AA}$ in pure water at $25 \text{ }^\circ\text{C}$.

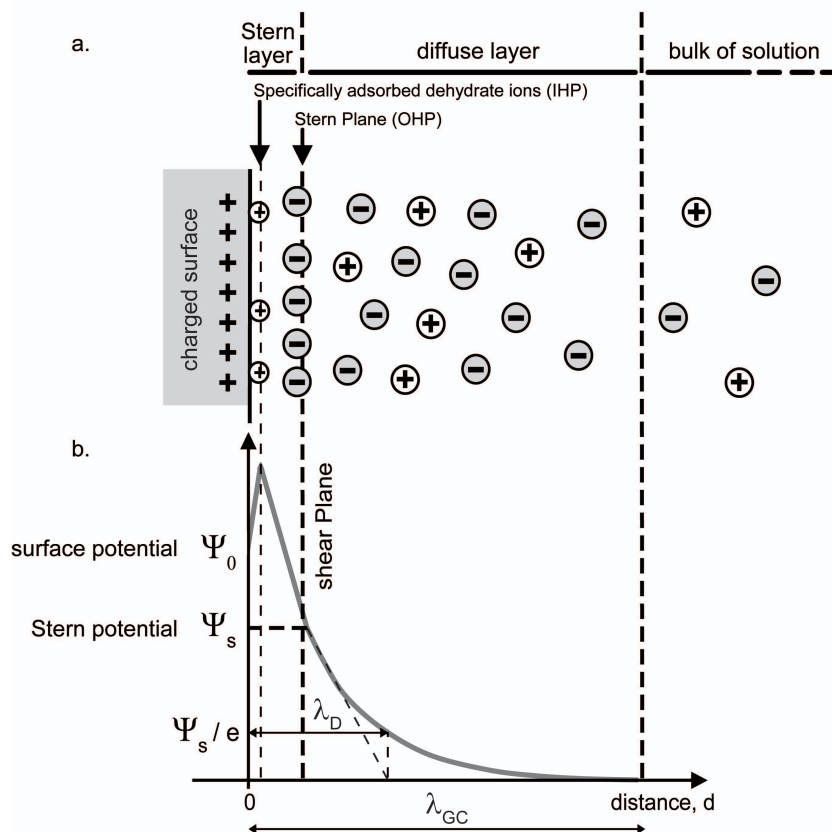


Figure 2.13: (a) Schematic representation of the ion distribution near a charged surface. (b) The potential decreases linearly with the distance to the charged surface, in the Stern layer, and exponentially towards zero, in the diffuse layer. (adapted from [Hunter, 1981]). IHP: inner Helmholtz plane; OHP: outer Helmholtz plane or Stern Plane. (solvent molecules are not represented for clarification).

In this model, the thickness of the diffuse layer seems an essential parameter, making possible to characterize the decrease of the electrical potential. This thickness, called Debye-Hückel length λ_D , depends on the ionic force of the solution and decreases when the ionic force increases. For a given salt containing the various species i of ions, the distance λ_D is defined as:

$$\lambda_D = (4\pi l_B I)^{-1/2} \quad (2.10)$$

where $I = \sum_i z_i^2 c_i$, z_i and c_i being respectively the valence and the concentration of the species i . At this distance, electrostatic interactions are screened in presence of the considered salt. For a solution of 1 mM NaCl concentration λ_D is estimated to 95 \AA .

When particles move in the aqueous medium, due to Brownian motion or sedimentation, only ions contained between the particle surface and the shear plane move with it. The electrokinetic potential on it is defined ζ -potential. The technique used to evaluate it will be presented in the section 6.6.2.

A complete description of this theory is given in [Hunter, 1981, Israelachvili, 1992]. More complex theories have been developed, which take into account interfacial molecular structure, hydration and inter-ionic correlation effects [Langner and Kubica, 1999].

2.4.2 Effects of salt and pH on lipid membrane properties

Structural and mechanical properties of lipid vesicle bilayers are demonstrated to be strongly affected by salts and pH. ζ -potential measurements highlight that salt addition induces the screening of the charged lipids [Winiski et al., 1986], while pH adjusts the membrane charge sign and its charge density. Nevertheless, in both cases, lipids experience a re-organization [Seelig et al., 1987, Sachs et al., 2004], which increases an asymmetry between the two leaflets, thus the spontaneous curvature. This results a modification in the membrane dynamics: changing the lipid mobility [Böckmann et al., 2003] or favoring the flip-flop mechanism [Mui et al., 1995]. Moreover, the electrostatic repulsion between different part of the charged membrane leads to a contribution to the mechanical properties such as stretching and bending moduli [Winterhalter and Helfrich, 1992, Claessens et al., 2004] and tends to rigidify the lipid membrane [Pabst et al., 2007].

These electrostatic interactions can also destabilize the charged membranes, leading from the formation of transient pores [Betterton and Brenner, 1999], changes in the vesicle shapes [Mui et al., 1995, Lee et al., 1999] to the membrane rupture [Diederich et al., 1998] [Shoemaker and Vanderlick, 2002]. Finally, addition of multivalent salt on vesicles suspension involves their aggregation [Sabin et al., 2007] and fusion [Ohki, 1982].

Chapter 3

From non-charged polymers to polyelectrolytes

Après avoir brièvement rappelé des généralités sur les polymères neutres, nous discutons quelques propriétés des polyélectrolytes. Puis nous présentons les deux polymères utilisés pour cette étude: le chitosane et l'acide hyaluronique.

o o o o o o o o o o

In this chapter, after dealing with non-charged polymers, we report some properties of polyelectrolytes. Then we present the two polyelectrolytes used during our study: chitosan and hyaluronan.

3.1 Non-charged polymers in solution

A polymer is composed of repeating structural units of molar mass m_0 , connected by covalent chemical bonds. It is defined by its degree of polymerization DP corresponding to the number of monomeric units in a molecule of a polymer and its molecular weight as $MW = DP \times m_0$.

Various structures of polymer are possible, but we will here focus only on linear ones. We briefly remind some points on Gaussian chain [Flory, 1979] before presenting to the real chain in a solvent [de Gennes, 1979, Kratochvil and Suter, 1989].

3.1.1 Gaussian chain model

Polymer can be first considered as an ideal chain made up with N segments of length b described by a random walk with a Gaussian probability distribution for the chain conformations (Figure 3.1). At each step, the next jump may proceed toward any direction (including the exact superimposition of the preceding monomer) and so on. Only short range interactions along the backbone of the chain are taken into account.

This Gaussian chain is then defined by two characteristic lengths:

- (i) the **mean square of the end-to-end distance** $\langle \vec{R}^2 \rangle$ traducing the separation between the two ends of the polymer chain. This characteristic length corresponds to the unperturbed size of the chain and is equal to $\langle \vec{R}^2 \rangle_0 = Nb^2$.
- (ii) the **radius of gyration** R_g of the chain, assuming that all the masses associated to chain segments are the same, defined as:

$$R_g^2 = \frac{1}{2(N+1)^2} \sum_{i,j=0}^N \langle (\vec{r}_i \cdot \vec{r}_j)^2 \rangle = \frac{1}{6} Nb^2 \quad (3.1)$$

which represents the mean distance from center of mass (O) (see Figure 3.1a).

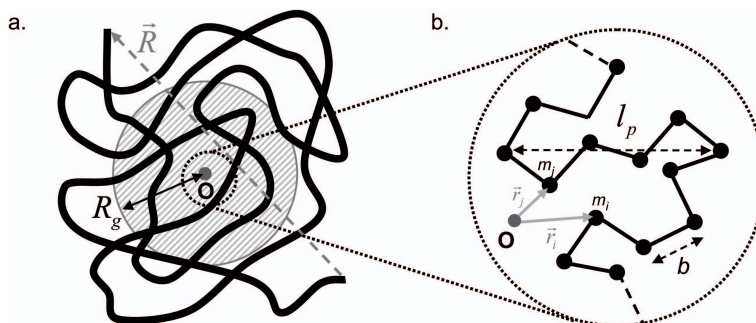


Figure 3.1: A model of polymer chain. The i -th chain segment is defined by its mass m_i and the location vector \vec{r}_i .

The polymer chain behaves like an entropic spring with an elastic Flory energy E written as $E = k_B T \frac{\langle \vec{R}^2 \rangle}{Nb^2}$, for a given end-to-end distance $\sqrt{\langle \vec{R}^2 \rangle}$ [Flory, 1979].

Although the model of the gaussian chain allows the comprehension of important results in the physic of polymers, the real chemical structure and the influence of the solvent are not taken into account. These elements are considered in the real chain model.

3.1.2 Real chains

For a real polymer, the chemical structure imposes restraints on the position of the chain segments ones to each others. Firstly, angles between the neighboring segments are fixed by the atom bonds (*e.g.* 109° for C-C-C chains), then the torsion of the chemical bonds is hindered by a potential energy favoring the minimum energy configurations. Finally, two segments cannot occupy the same space at the same time which introduces an excluded volume. Therefore, these three constraints tend to inflate the real polymer chain and thus increase the two characteristic lengths (end-to-end distance and radius of gyration).

Three kinds of polymer solutions can be discriminated:

- **dilute solution**, when excess of solvent is present, so that interactions between polymer molecules can be neglected for $C < C^*$ (C^* the critical overlap concentration).
- **semi-dilute solution**, when monomers in one chain contact monomers in adjacent chains to form a non-connected network.
- **concentrated solution**, when the polymer chains become highly entangled and their properties approach those of a polymer melt [de Gennes, 1979].

Moreover the solvent affects the chain conformation. In a good solvent, the polymer chain is highly extended to favor the contact with the solvent molecules and presents the maximum swelling ratio in solution. In θ -solvent, for which the excluded volume interactions between the polymer segments are balanced by their attractive interaction, the real polymer chain is equivalent to a gaussian chain ($R_{g,\theta} \propto N^{1/2}$). In bad solvent, monomer-monomer interactions are favored which induce the collapse of the polymer chain. Hence, an expansion factor α_s is introduced to compare these characteristic sizes observed in a given solvent with the θ -conditions. For example, the radius of gyration in a given solvent is equal to $R_g = \alpha_s R_{g,\theta}$. In a given polymer sample, chain lengths can vary over a wide range of molecular masses. The molar-mass dispersity denotes a measure of the dispersion of macromolecular species in a sample of polymer and is defined as the weight-average molecular weight (Mw) divided by the number-average molecular weight (Mn). This parameter has a value equal to or greater than 1.

3.1.3 Semi-flexible polymer chains

The Kratky-Porod worm-like chain model is used to describe the behavior of semi-flexible polymers [Kratky and Porod, 1949]. The central quantity of this model is the persistence length L_p , which is the characteristic length along the chain over which the directional correlation between the segments disappears, *i.e.* its stiffness (see Figure 3.1b). At length scale below L_p , the polymer chain is considered as a rigid rod.

In our work, we focus on charged polyelectrolytes. Therefore in the next section we present how the presence of charges on the polymer chains modifies the results obtained from non-charged polymers.

3.2 Charged polymers (polyelectrolytes) in solution

Polyelectrolytes are macromolecules exhibiting ionizable groups. In polar solvents such as water, these groups can dissociate, leading to charge polymer chain and equivalent amount of counterions in solution. Coulomb interactions are at the origin of a rich variety of properties of polyelectrolyte solutions which are not found in non-charged polymer solutions. Polyelectrolytes play a fundamental role in everyday life being used in a wide-range of technological applications

(dewatering agents, additives to cosmetics . . .) [Hara, 1993] and many of the biopolymers (DNA, hyaluronic acid, proteins) are polyelectrolytes [Alberts et al., 2002].

In contrast with the non-charged polymers whose properties are relatively well understood, polyelectrolytes still raise many questions, from theoretical and experimental point of view. The difficulty comes from the simultaneous action of the short range (excluded volume with electrostatic contribution) interaction between monomers on one chain (present in any polymer) and of the long range (coulombic) interactions. These long range interactions, together with screening effects caused by counterions, introduce new length scales which means that interactions occurs at different distance ranges. This coupling of different length scales leads to a severe influence of local chain properties on the properties of the whole system [Dhont, 2002].

In this part, polyelectrolytes are regarded as a system of punctual charges fixed to a macromolecular chain, suspended in a solution containing counterions distributed around and electrolyte excess (*e.g.* NaCl) (Figure 3.2). “Weak” and “strong” polyelectrolytes are defined as a polymer containing monomer units derived from weak or strong acids (or bases) respectively.

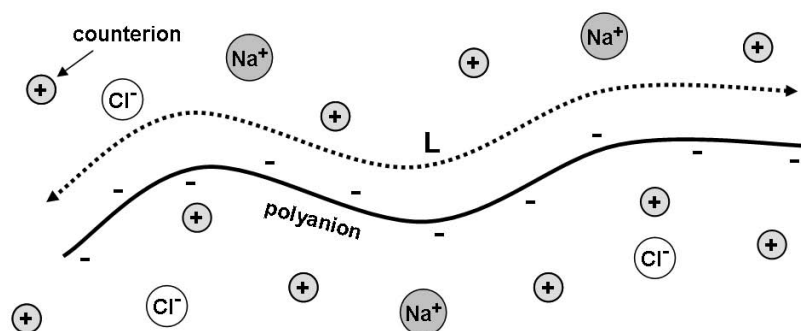


Figure 3.2: Schematic representation of a negative polyelectrolyte of contour length L , surrounded by its counterions and salt ions (Na^+ and Cl^- respectively counterions and co-ions).

3.2.1 Charge parameter and intrinsic pK

In solution, when a small fraction of the monomers is charged, polyelectrolytes are said to be weakly charged and Coulomb interactions interplay with the usual van der Waals interactions; whereas, when they are highly charged (large fraction of charged monomers), Coulomb interactions dominates.

Charge parameter

A dissociated polyelectrolyte chain, including n ionic charges distributed on a polymeric chain of contour length L (end-to-end distance in the maximum extension), is characterized by its charge parameter λ [Lifson and Katchalsky, 1954]. λ compares the mean distance between two successive ionic charged sites of the polymer chains (N/L) and the Bjerrum length l_B , corresponding to the distance over which the electrostatic energy between two charges is exactly

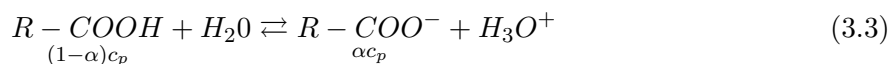
compensated by the thermal energy (see relation 2.9). The charge parameter is defined by:

$$\lambda = \frac{n}{L} l_B \quad (3.2)$$

Intrinsic pK, pK₀

Depending on the “weak” or “strong” character of the polyelectrolyte, its charge may vary or not with pH. For example in the case of “weak polyacids”, charged monomers units are derived from weak acids (e.g COOH units); in solution, only a fraction of the acid groups are dissociated and the degree of dissociation α depends on the pH of the solution. On the contrary, for strong polyacids charged monomers units are derived from strong acids (e.g. with SO₃H units), all monomers are dissociated and global charge is unchanged whatever the pH.

In the case of polyacids with COOH groups (*i.e.* weak polyelectrolytes), the following equilibrium describes the state of ionization in solution:



with α the degree of dissociation and c_p , the total polymer concentration expressed in equivalent per liter as $c_p = [\text{R-COOH}] + [\text{R-COO}^-]$. When sodium hydroxide is added to the polyacid solution to progressively neutralize it, the degree of dissociation $\alpha = [\text{R-COO}^-]/c_p$ can directly be deduced from the pH measurements, and the apparent pK_a of the polyacid is estimated to:

$$pK_a = pH + \log \left(\frac{1 - \alpha}{\alpha} \right) \quad (3.4)$$

Unlike for electrolyte solutions where pK_a is constant and α is function of pH, and depends only on the dissociation constant $K_a = \frac{[A^-][H_3O^+]}{[AH]}$, in the case of polyelectrolytes, pK_a is affected by the intrachain electrostatic potential. To take into account this effect, Katchalsky expressed the pK_a as function of an intrinsic dissociation constant pK₀ of the polyelectrolyte at nil charge density ($\alpha = 0$) and a corrective term $\Delta pK(\alpha)$ due to electrostatic contribution [Katchalsky et al., 1954, Lifson and Katchalsky, 1954]. The pK_a is then given by:

$$pK_a = pK_0 + \Delta pK(\alpha) \quad (3.5)$$

Experimentally, pK₀ is determined by extrapolation of pK(α) for $\alpha = 0$ [Rinaudo, 1974, Milas and Rinaudo, 1997].

pH modification causes a change on the number of ionized and neutral groups.

3.2.2 Influence of salt concentration on polyelectrolyte conformation

The dimensions of polyelectrolytes strongly depend on both the composition of the solvent (dielectric constant and concentrations of the ions) and the polyelectrolyte concentration [Odijk, 1979b, Rinaudo et al., 1997].

In the next paragraphs, we discuss the case of polyelectrolytes in dilute solutions, in the absence and in the presence of salt.

In the absence of salt

A polyelectrolyte chain can be simply modeled, as a set of charged and uncharged segments of length b . This model is not realistic to describe genuine polyelectrolyte solutions, but it serves here to introduce some important concepts relative to charged polymer chains [Barrat and Joanny, 1996].

The polyelectrolyte is considered in this model as a flexible chain of N monomers carrying a total charge fNe (f is the fraction of charged monomers, *i.e.* $(1 - f)N$ monomers are non-charged). The Flory energy E_{Flory} for a chain of size R is composed of a first term which is the elastic energy obtained previously for non-charged chain, and a second term corresponding to the electrostatic energy due to the Nf charges [de Gennes, 1979]:

$$E_{Flory} = k_B T \frac{R^2}{Nb^2} + k_B T \frac{(Nf)^2 l_B}{R} \quad (3.6)$$

The energy minimization with respect to R leads to an equilibrium size:

$$\sqrt{\langle \vec{R}^2 \rangle} \sim N f^{2/3} (l_B b^2)^{1/3} \quad (3.7)$$

This scaling law shows that the overall dimension of the polyelectrolyte increases as $\sqrt{\langle \vec{R}^2 \rangle} \propto N$ in contrast to $\sqrt{\langle \vec{R}^2 \rangle} \propto N^{1/2}$ for the uncharged polymer in θ - condition (see section 3.1). Thus, electrostatic repulsions along the chain tend to swell the polyelectrolyte chain, increasing its global size and inducing locally a much larger stiffness of the chain than in uncharged polymers.

For semi-rigid polyelectrolytes, Odijk has proposed a simple model where the total persistence length L_T of a polyelectrolyte can be written as the intrinsic persistence length L_p (due to natural rigidity of the uncharged chain) and an additional electrostatic persistence length L_e , due to electrostatic repulsion between the charges of the polyelectrolyte [Odijk, 1977]:

$$L_T = L_p + L_e \quad (3.8)$$

Odijk [Odijk, 1977] and Skolnick [Skolnick and Fixman, 1977] show that the electrostatic contribution L_e varied as the square of the Debye-Hückel length λ_D , showing that L_e depends on the screening by salts. This dependence established for DNA [Odijk, 1979a] has been confirmed on hyaluronan by [Berriaud et al., 1998, Buhler and Boué, 2003, Rinaudo, 2009] .

The presence of charges also modifies the radius of gyration R_g obtained previously for non-

charged polymer. An electrostatic expansion factor α_s is introduced to take into account the electrostatic contributions as developed by [Odijk and Houwaart, 1978]. The radius of gyration of a polyelectrolyte $R_{g,PE}$ is thus related to the non-charged chain one by:

$$R_{g,PE} = \alpha_e R_g \quad (3.9)$$

where α_e is an expansion factor related to the electrostatic excluded volume [Reed, 1994]. In absence of salt, all these considerations make the size of a polyelectrolyte in solution much larger than the one of non-charged polymer.

In the presence of salt

As seen before, charges on a linear polyelectrolyte chain will repel each other (Coulomb repulsion), leading to a more expanded chain conformation. If we add a large amount of salt, charges will be screened and consequently polyelectrolyte chain will collapse to a more conventional conformation, similar to a non-charged chain (see Figure 3.3). Hence the electrostatic persistence length L_e is estimated to be related to the salt concentration as $L_e \propto C_s^{-1/2}$.

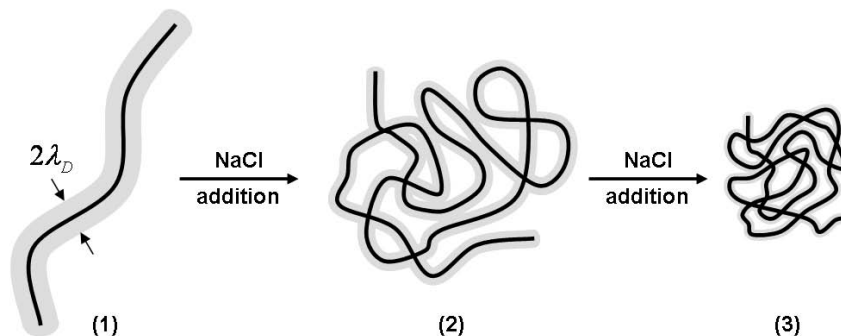


Figure 3.3: Schematic representation of a flexible polyelectrolyte (black line) surrounded by its double layer (Stern and diffuse layers; grey envelope).

When we looked at the chain conformation in the previous paragraphs, we have implicitly assumed that the entropy of mixing was driving the counterions to distribute uniformly in the solution. However when the chain is highly charged, the electrostatic interactions attract the counterions to the oppositely charged polymer chain. The potential, close to the chain, can be so high that for some counterions the entropy of mixing is dominated by the electrostatic attractive energy. Therefore they remain around the polyelectrolyte, reducing the effective charge of the chain compared to the initial (or chemical) charge. This phenomenon is known as counterion condensation [Manning, 1969a, Manning, 1969b].

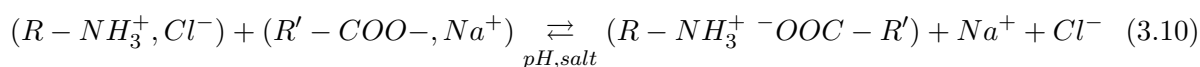
The process of condensation uses a two states model: a part of the counterions are condensed in the close neighborhood along the polyelectrolyte chain forming ion pairs, while the others counterions are free in solution and are submitted to a Debye-Hückel potential (created by the polyelectrolyte) further from the chain. The condensation phenomenon is thus related to

the charge parameter λ characterizing the polyelectrolyte.

When $\lambda < 1$ ($L/n > l_B$), there is no condensation. For $\lambda > 1$ ($L/n < l_B$), counterions associate to the chain, screening a part of the polymer charges such as to reduce λ to the effective value $\lambda = 1$. In this case, the minimum distance between two charges on the chain is the Bjerrum length l_B . Hence the threshold value $\lambda_{Manning}$ is obtained for $L/n = l_B$ ($\lambda = 1$).

3.2.3 Association of oppositely charged polyelectrolytes

When cationic and anionic polyelectrolytes are mixed in solution, a polyelectrolyte complex is formed due to electrostatic interaction between opposite charged groups [Kabanov, 2005]. As example, the reaction between two polyelectrolytes can be described by the following scheme:



The stability of these complexes depends on the properties of both polyelectrolytes (degree of polymerization, degree of ionization for weak polyelectrolytes . . .) and on the solution properties (pH and salt concentration). We can note that, the neutral polyelectrolyte complex is usually insoluble and allows to obtain fibers, films or capsules.

In this study, we will focus on two polyelectrolytes: the chitosan, a positively charged polyelectrolyte in acidic condition ($pH < 6.5$), and the hyaluronan, a negatively charged polyelectrolyte at $pH > 2.5$. These two polyelectrolytes exhibit biocompatibility [Elbert and Hubbell, 1996] and biodegradability properties [Illum and Davis, 1994] [Kogan et al., 2007].

3.3 Chitosan and derivatives

3.3.1 Chitosan structure and properties

Chitosan is a pseudo-natural polysaccharide obtained by deacetylation of chitin extracted from crustaceous shells, cuticles of insects and cell walls of some fungi [Kas, 1997, Rinaudo, 2006]. It is a linear random copolymer of D-glucosamine and N-acetyl-D-glucosamine (Figure 3.4) soluble in acidic conditions ($pH < 6.5$) due to the protonation of the $-NH_2$ functions.

Chitosan sample is characterized by the degree of acetylation DA (fraction of acetylated monomeric units), and the acetyl group distribution along the chain, both dramatically depending on the preparation conditions. The molecular mass of the repeat unit is then $m_0 = 161 + 41 \text{ DA}$ g/mol and the chitosan charge parameter is $\lambda = 1.38(1 - \text{DA})$.

The radius of gyration of the chitosan chain is estimated to R_g (nm) = $0.075 \times M_w^{0.55}$ [Rinaudo, 2006]. The intrinsic persistence length L_p of chitosan is shown to be weakly affected by the DA [Berth and Dautzenberg, 2002]: L_p is estimated to 11 nm ($\text{DA} < 0.25$)

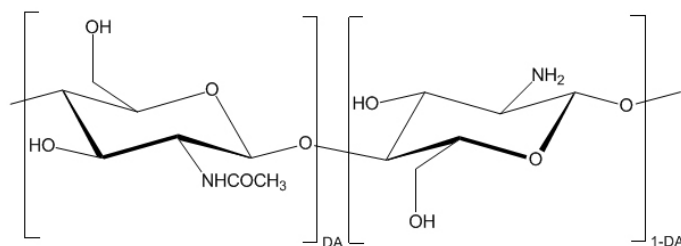


Figure 3.4: Repeat unit of the chitosan, positively charged polymer at $pH < 6.5$ due to the protonation of the amino group ($-NH_2$).

[Brugnerotto et al., 2001, Rinaudo et al., 2005].

The intrinsic pK_0 of the amino group is estimated to 6.0 ± 0.1 [Rinaudo et al., 1999a] [Rinaudo et al., 1999b].

3.3.2 Chitosan derivatives

Chitosan chains can be chemically modified to introduce new properties: solubility at $pH > 7.0$, fluorescence, self-association. Derivatives can be obtained either by non-specific reactions involving the $-OH$ groups on C-3 and C-6 positions or specific reactions of the $-NH_2$ group at C-2 position [Rinaudo et al., 1992].

We only deal here with self association induced by alkylation of chitosan, but many other modifications can be carried out [Rinaudo, 2006]. Alkylated chitosans are amphiphilic polysaccharides with different alkyl chain lengths (C_n from 3 to 14) and controlled degree of substitution DS (usually lower than 0.1 to maintain water solubility in acidic conditions) [Desbrieres et al., 1996]. Alkylated chitosans improve the stability of the air-liquid interface [Desbrieres et al., 1997a] and increase the solution viscosity in acidic conditions due to hydrophobic inter-chain interactions. For the C12 chain length and a $DS = 0.05$, a physical gel is obtained in the presence of slight ionic concentration, resulting from a balance between electrostatic repulsions (due to charged groups) and hydrophobic attraction (due to alkyl chain) [Desbrieres et al., 1996]. The properties of this physical gel depends on salt concentration [Desbrieres et al., 1997b, Rinaudo et al., 2005]. Such hydrophobic associations between alkylated chains can be destroyed reversibly by addition of cyclodextrins [Rinaudo et al., 2005] which are known to complex the alkyl chains [Eli et al., 1999].

3.3.3 Complex formation

In acidic conditions, chitosan forms various complexes with metal ions [Muzzarelli, 1973], with multi-valent cations (higher affinity for divalent cations such as Cu^{2+} , Zn^{2+} or Ca^{2+} ...) [Rhazi et al., 2002], with surfactants (*e.g.* SDS) [Babak et al., 1999], and with synthetic or natural polyanion [Arguelles-Monal et al., 2000, Peniche and Arguelles-Monal, 2001] [Rusu-Balaita et al., 2003], especially, with alginate or hyaluronic acid (HA), where a pH-dependent complex is formed, whose stability depends on the ionic concentration.

3.3.4 Applications

Thanks to its biocompatibility, biodegradability, non toxicity and because it exhibits wound healing properties, chitosan finds many applications in biomedical domains such as surgical sutures, dental implants, encapsulating material . . . [Khor and Lim, 2003, Rinaudo, 2006]. Chitosan also finds applications in many other domains: for example, in agriculture, it serves as stimulant of plant growth, in water and waste treatment, it is used as a flocculant to clarify water, in food and beverages, as preservatives, in cosmetics and toiletries, chitosan maintains skin moisture or treats acne and in biopharmaceutics, it exhibits antiviral and antiphage activities [Pospieszny et al., 1994]. The chitosan is also used as antitumoral, hemostatic or anticoagulant.

3.4 Hyaluronan and derivatives

3.4.1 Hyaluronan structure and properties

Hyaluronic acid (HA) is a linear polysaccharide composed of repeating disaccharide units of β -(1-4)-D-glucuronic acid (GlcA) and β -(1-3)-N-acetyl-D-glucosamine (GlcNAc) (see Figure 3.5), belonging to the glycosaminoglycan family. It is a component of the synovial fluid, cartilage, vitreous humor and extracellular matrices, where it plays important structural and biological roles [Kogan et al., 2007].

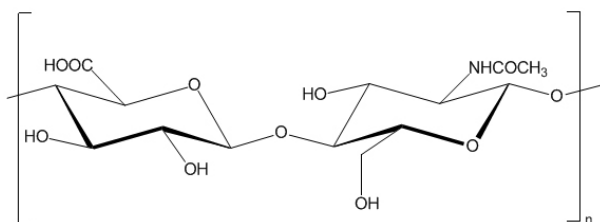


Figure 3.5: Repeat unit of the hyaluronan, anionic polymer at $pH > 2.0$ in relation with dissociation of carboxylic groups ($-COOH$).

The weight-average molecular weight of hyaluronan is evaluated below 10^7 g/mol, and its intrinsic persistence length (L_p) is estimated to 8 nm at 25 °C [Reed, 1994, Berriaud et al., 1998, Kennedy et al., 2002a]. Hyaluronan is a polyelectrolyte which has one carboxylic function per repeat unit. The distance between two ionic sites at complete ionization in salt form is evaluated to 0.98 nm in the extended conformation; the charge parameter is then $\lambda = 0.71$. The molar mass of the repeat unit is $m_0 = 401$ g/mol. The radius of gyration of the hyaluronan chain is estimated to R_g (nm) = $0.054 \times Mw^{0.55}$. Hyaluronan is soluble in water whatever the pH, but it forms a physical gel at $pH \sim 2.5$ by charge repression and H-bonds stabilization [Rinaudo, 2009]. One characteristic of this polyacid is its pK_0 obtained by pH titration of a solution of the hyaluronan acid form. The extrapolation to the null charge ($\alpha = 0$) gives $pK_0 = 2.9 \pm 0.1$ as usually found for poly(carboxylic acid)s in the absence of specific interactions involving the carboxylic groups [Fouissac, 1992].

3.4.2 Hyaluronan derivatives

Hyaluronan chains can be chemically modified to introduce new properties: fluorescence, self assembly by specific or non-specific interactions. Considering the chemical structure of HA, there are three main positions per repeat unit for chemical modification: -OH in C-2 and C-3 positions and -COOH of the glucuronic acid (GlcA); -OH in C-6 position and -NH of the N-acetylglucosamine (GlcNAc) (to a lower extent eventually after partial deacetylation) [Rinaudo, 2008].

3.4.3 Complex formation

As detailed above for chitosan, hyaluronan is able to form various complexes with proteins (*e.g.* collagen) or positively charged polyelectrolytes (polylysine, chitosan . . .) [Rinaudo, 2008].

3.4.4 Applications

Hyaluronan is a highly biocompatible polysaccharide, naturally present in the body, and often used for biomedical applications including viscosupplementation in joint diseases, based on its good viscoelastic properties. Films have also been developed for tissue engineering. Many data are available in [Kennedy et al., 2002b] which concern the biological activity and the biomedical applications of HA. Complexes with polycations are proposed for controlled drug release. Hyaluronan is also used in dermatology and cosmetic industries (preserve tissue hydration), or in drug delivery [Rinaudo, 2008].

Chapter 4

Vesicle-polyelectrolyte interactions

Dans ce chapitre, nous nous concentrons sur l'interaction polyélectrolytes/membrane lipidique et ses conséquences sur les propriétés structurales et mécaniques des membranes décorées. Après avoir rappelé des généralités sur les mécanismes d'adsorption de polymère sur une surface solide, nous discutons la structure de polymère adsorbé sur la surface chargée et des mécanismes possibles de désorption. Nous détaillons ensuite l'effet de l'adsorption de polyélectrolyte sur l'organisation d'une membrane de lipide et sur la structure de la vésicule. Enfin, nous présentons les modifications des propriétés mécaniques des membranes induites par l'adsorption de polyélectrolyte.

o o o o o o o o o o

In this chapter, we focus on the interactions between polyelectrolytes and lipid membranes and their consequences on the membrane structural and mechanical properties. After reporting generalities on the mechanisms of polymer adsorption on solid surface, we discuss the structure of the polymer adsorbed on the charged surface and the possible desorption mechanisms. Then we detail the effect of the polyelectrolyte adsorption on the lipid membrane organization and on the vesicle structure. Finally, modifications of the mechanical properties induced by the polyelectrolyte adsorption are presented.

4.1 Generalities on polymer sorption on a surface

Polymer/surface interactions are controlled by several factors such as: (i) surface properties (e.g., roughness, chemical nature . . .), (ii) polymer properties (e.g. chemical structure, molecular weight and concentration), (iii) nature of the solvent and (iv) the external factors (e.g. temperature, ionic concentration) [Parfitt and Rochester, 1983].

For polyelectrolytes, electrostatic interactions also occur: charge densities of both the surface and the polyelectrolyte, and pH or the salt concentration of the solution have to also be taken into account [Netz and Andelman, 2003].

4.1.1 Amount and conformation of adsorbed polymer

In order to characterize the polymer adsorption on a surface, it is necessary to determine:

- the nature of the interactions.
- the association constant.
- the amounts of adsorbed polymer (coverage degree).
- the conformation of the polymer adsorbed at the surface.
- the structure of the polymer layer on the surface at various scales.

Nature of the polymer-surface interactions

The interactions between polymer and surface can be of different origins depending on the chemical structure of interacting species at local (hydrophobicity, hydrogen bonds) and long range scale (Coulombic association).

Association constant and maximum amount of adsorbed polymer

To determine association constants and maximum amounts of adsorbed polymers, adsorption isotherms are generally drawn. They report the amount of adsorbed polymer on a surface as a function of the polymer concentration free in solution: high adsorption occurs at low concentrations, while for higher concentrations, saturation of the surface is reached (maximum amount of polymer adsorbed, of the order of few $\text{mg}\cdot\text{m}^{-2}$). From these isotherms, the association constant is determined.

Various techniques can be used to determine the quantity of both polymer adsorbed on the surface and free in solution [Fleer et al., 1993] necessary to get the adsorption isotherms.

Conformation of the polymer adsorbed at the surface

The conformation of a polymer changes when it is adsorbed at a surface [Jenkel and Rumbach, 1951]: trains (segments with polymer in contact with the substrate) and loops (segments of polymer not in contact with the surface) are observed (see Figure 4.1).

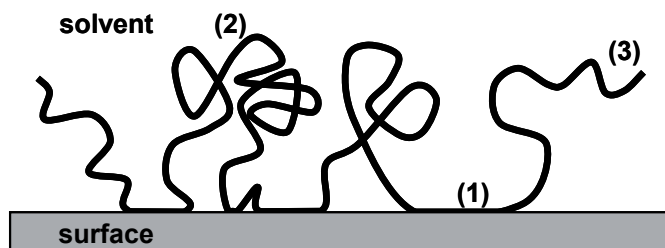


Figure 4.1: Equilibrium conformation of a polymer adsorbed on a surface. (1) “trains” or segments of chains adsorbed flat on the surface. (2) loops and (3) end of the chain free in solution.

The molecular weight dependence of the adsorbed amount of polymer (Γ) gives information on the polymer structure at the surface as proposed by [Perkel and Ullman, 1961]. If Γ is not dependent on Mw, the polymer is assumed to adsorb flat on the surface while a variation of Γ with Mw indicates the presence of trains and loops.

In all the case, polymers with high molecular weight are preferentially adsorbed if compared to lower Mw [Cohen-Stuart et al., 1980].

Dealing with the conformation of polyelectrolytes adsorbed on oppositely charged surfaces:

- at low polymer charge densities, chains are only attached at few surface sites giving rise to extended loops formation (see Figure 4.2a).
- at high polymer charge densities, intra-chain electrostatic repulsions rigidify the chain segments, favoring formation of trains at the surface (see Figure 4.2b).

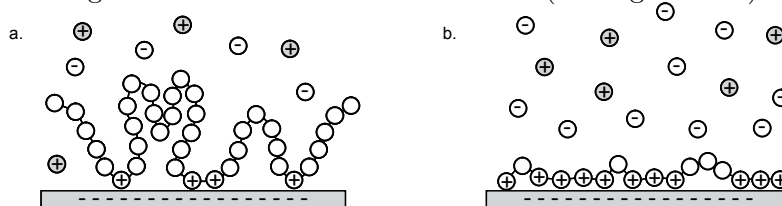


Figure 4.2: Conformation models of polyelectrolytes adsorbed on a charged surface. Different adsorption regimes are predicted with increasing polymer charge density. (a) At low charge density, polyelectrolytes form loops and build a layer in 3D at the neighborhood of the surface and (b) at high charge density, polyelectrolytes are adsorbed flat on the oppositely charged surface (adapted from [Fleer et al., 1993]).

Structure of the polymer layer on the surface

We only deal here with polyelectrolytes, which is the objet of the present work. For charged polymers, a more or less ordered patch-like structure was proposed in the literature [Gregory, 1972] (see Figure 4.3). This patch-like structure consists in a non-uniform distribution of the surface charges, which consist in domains of stuck charged polymer (i.e. with a local charge excess) alternating with domains of bare surface [Dobrynin et al., 2000].

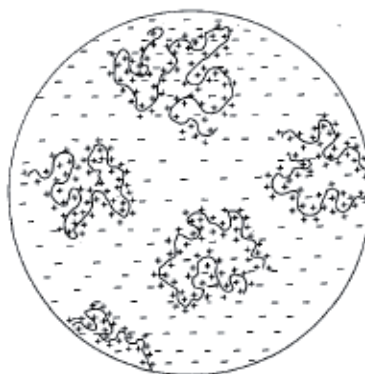


Figure 4.3: Possible arrangement (patch-like) of adsorbed polycations on a particle with low negative surface charge density (from [Gregory, 1972]).

4.1.2 Kinetics of polymer adsorption and desorption

The polymer adsorption and desorption can be regarded as a three-step process [Nylander et al., 2006] shown in Figure 4.4:

- The **mass transport** towards the surface (A) generally involves both convection and diffusion processes, which are well known (hydrodynamic and Fick's laws) [Hoogeveen et al., 1996].
- The **attachment to the surface** (B) is less understood, as it involves diffusion of the polymer over a repulsive barrier created by the already adsorbed polymer chains [Geffroy et al., 2000].
- The **rearrangement at the surface** (C) consists in conformation changes and motion of segments of the adsorbed chain over the surface, in order to minimize the polymer chain free energy [Samoshina et al., 2005].

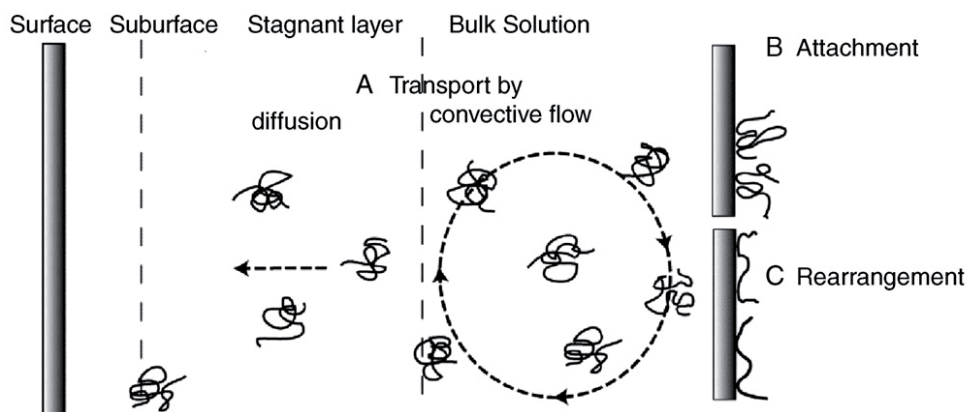


Figure 4.4: Three-step process of polymer adsorption: (A) Transport from the bulk to the surface, (B) attachment to the surface and (C) rearrangement in the surface layer (adapted from [Nylander et al., 2006]).

Polymer adsorption

The first step (A) controls the adsorption process up to 75% of the maximum adsorbed amount of polymer is reached, then the second step (C) becomes rate determining [Fleer et al., 1993, Schneider et al., 1996]. The rearrangement processes (C) take place on much longer timescale than the two first steps: adsorbed polymer chains can be kinetically trapped at the interface in non-equilibrium states [O'Shaughnessy and Vavylonis, 2005], as illustrated in Figure 4.5.

Polymer desorption

The reversibility of the polymer adsorption has been extensively investigated either by varying the experimental conditions (e.g. variation of the polymer concentration in solution [Pefferkorn et al., 1985], variation of pH or salt concentration) or by following the exchange between free and adsorbed polymers in relation with the chain lengths [Dijt et al., 1994]. The rate of desorption is therefore found as mass transport-limited [Dijt et al., 1992].

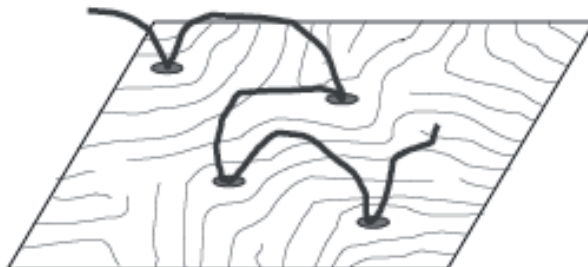


Figure 4.5: Conformation of a chain arrived lately on the surface (black line). The limited number of free adsorption sites on the surface forces the chain to form loops (adapted from [Gromer, 2007]).

For polyelectrolytes adsorbed on oppositely charged surface, the mechanism of desorption is mainly controlled by electrostatic interactions and consequently by charge density of the polymer and of the surface, and by the salt concentration [de Ven, 1994, Hoogeveen et al., 1996, Samoshina et al., 2005].

We have previously considered the adsorption of polyelectrolyte on a solid charged surface, nevertheless fluid lipid membranes are deformable materials where lipids can move freely (see section 2.2.2). The mobility of the lipids in fluid membrane accelerates the equilibration of the polyelectrolyte-lipid complex contrary to membrane in gel state which is “similar” to solid surface [Clausen-Schaumann and Gaub, 1999].

We now address the question of the effect of the polyelectrolyte adsorption on lipids organization and membrane properties.

4.2 Effect of polymer adsorption on the membrane and vesicle structure

At the nanometric scale, the polyelectrolyte coated membrane structure consist in polyelectrolyte rich domains coexisting with bare membrane domains [Yaroslavov et al., 2009] (i.e. the patch-like domains discussed just before); adsorbed polyelectrolyte may induce local lipid crystallization [Feng et al., 2004].

At the micrometric scale, polyelectrolyte coating can lead to changes in the global vesicle structure [Tribet and Vial, 2008]. It can for example induce membrane invaginations [Angelova and Tsoneva, 1999], buds formation [Kim and Sung, 2001], pore opening, membrane ruptures with reorganization in multilamellar structure [Vial et al., 2005, Luan and Ramos, 2007, Lee et al., 2006], or the vesicle disintegration [Majoros et al., 2005].

4.3 Effect of polymer adsorption on membrane properties

4.3.1 Mechanical properties

Adsorption of polymer on lipid membrane modifies its mechanical parameters. For example, neutral or charged polymers of the same sign than the membrane induced a decrease of its bending modulus (of few $k_B T$) [Brooks et al., 1991, Clément and Joanny, 1997], while, when polyelectrolytes and membranes are of opposite charge, the adsorption tends to rigidify the vesicle membrane, increasing it by a few $k_B T$ [Shafir and Andelman, 2007]. Only few studies report experimental determination of the mechanical parameters for lipid membranes coated by polyelectrolytes.

4.3.2 Electrostatic properties

Effect of non-charged polymer adsorption on the double-layer structure

Adsorption of polymer affects the double-layer structure as illustrated in Figure 4.6a. When a non-charged polymer is adsorbed at the surface of a particle, the structure of the electrical double layer at the object surface is modified as presented in the Figure 4.6b. Three main modifications are observed:

- changes in surface charge density by ionization of surface groups or adsorption/desorption of ions.
- displacement of ions adsorbed at the inner Helmholtz plane (IHP) due to the presence of polymer trains adsorbed at the surface.
- changes in the thickness of the diffuse layer.

As a consequence, the presence of non-charged polymer loops forces the shear plane to shift further out from the surface, at a distance corresponding approximately to the thickness of the adsorbed polymer layer. Hence ζ -potential decreases and does not coincide anymore with the Stern potential [Varoqui, 1982].

When polyelectrolytes are adsorbed at the surface of oppositely charged surface, it causes its charge neutralization [Bonekamp et al., 1987]. Upon further addition of polyelectrolytes, charge inversion occurs (Figure 4.6c) Such charge inversion has been recently evidence for polyelectrolyte-coated liposomes (DPPG/poly(L-lysine) [Volodkin et al., 2007] or DOTAP/poly-acrylate [Cametti, 2008]).

This inversion is at the origin of the formation process of polyelectrolyte multilayers which consists in depositing alternatively polycations and polyanions [Decher, 1997].

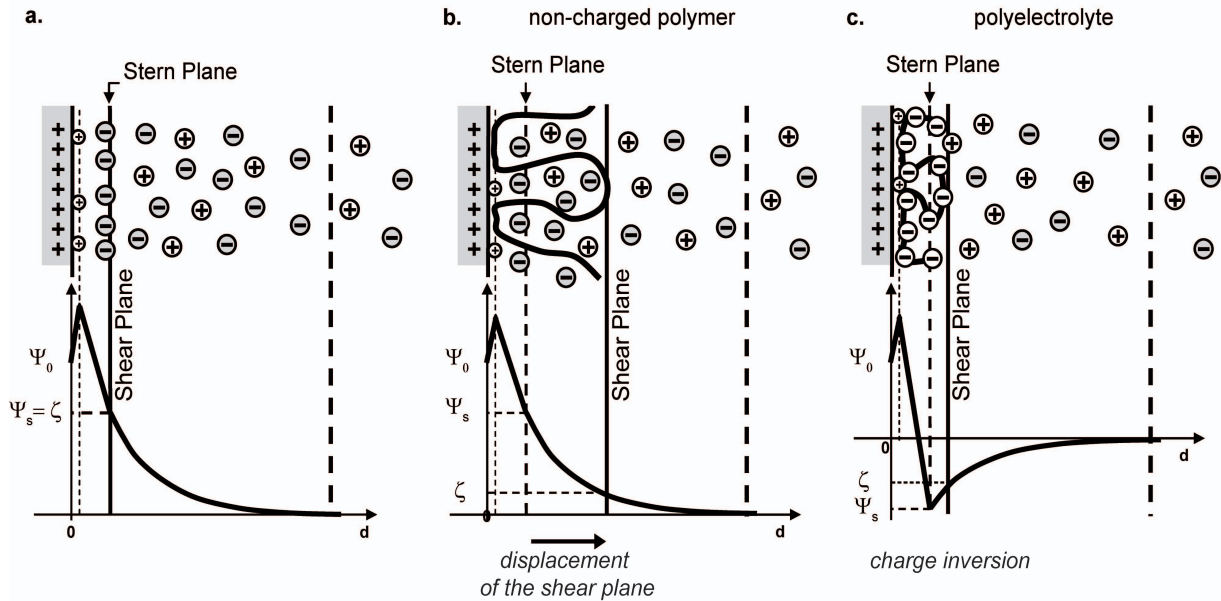


Figure 4.6: Schematic representation of the structure of the electrical double layer in (a) absence and in presence of adsorbed non-charged polymer (b) or polyelectrolyte (c).

4.4 Effect of polymer adsorption on vesicle suspension stability

4.4.1 Bare vesicle suspension

For bare vesicles, the DLVO (Derjaguin, Landau, Verwey, and Overbeek) theory [Evans and Yeung, 1994] allows a good approach of the stability of liposome suspensions by comparing the attractive van der Waals (close range: ~ 15 nm) and the repulsive electrostatic interactions.

In the case where electrostatic forces dominate, the objects stay isolated in solution, whereas if the van der Waals interactions govern the system, the particles aggregate. This latter effect is known as flocculation.

4.4.2 Non-charged polymer coated vesicle suspension

In this case, HVO (Hesslink, Vrij and Overbeek) theory [Hesslink et al., 1971] has to be used instead of DLVO because steric repulsions due to the adsorbed polymer has to be taken into account.

Indeed, when two particles coated with polymer get close to each other, the interpenetration of the polymer loops induces an increase of the free energy, causes an increase of the distance between the two particles, and hence the stabilization of the suspension.

However, in some cases, the presence of long polymer chains can induce flocculation by creating a polymer “bridge” between two particles. This effect increases with the polymer molecular weight and the particle concentration.

4.4.3 Polyelectrolyte coated vesicle suspension

For adsorption of polyelectrolytes with low charge densities (loops formation), the HVO model is pertinent to discuss the suspension stability.

For polymer with higher charge densities (flat adsorption), the DLVO model seems more appropriate, but experimentally flocculation is observed [Pefferkorn, 1995] which can not be explain within the frame of this model.

This flocculation can be explained within the frame of the extended DLVO model proposed by [Velegol and Thwar, 1984], which takes into account the attraction between oppositely charged patches of two approaching vesicles. These patches are respectively the bare membrane and the polyelectrolyte rich domains of the “patch-like” structure of the coated membrane just previously described.

An interesting point is that flocculation is avoided when a large excess of polyelectrolyte is added to the liposome aggregate suspension [Volodkin et al., 2007, Cametti, 2008] (Figure 4.7a). It is interpreted as follows, when the global net charge of the vesicles equal zero, aggregates reach a maximum finite-size. Additional adsorption of polyelectrolyte causes the overcharging effect with inversion of the net charge [Bordi et al., 2009] of the polyelectrolyte-coated surface and the degree of aggregation decreases to form isolated decorated vesicles. Presence of salt increases the polyion concentration region where aggregates are formed (Figure 4.7b).

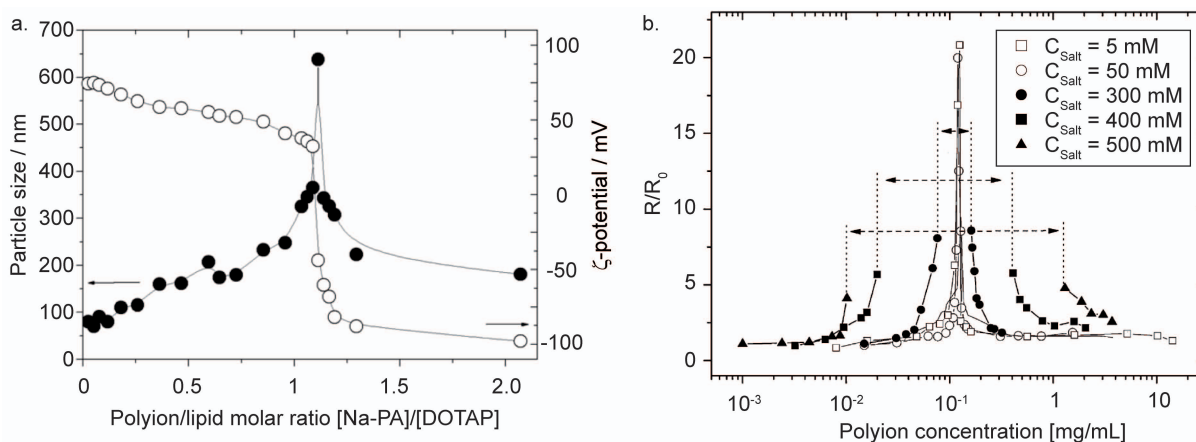


Figure 4.7: (a) Particle diameter (solid disks) and ζ -potential (open disks) of NaPA-DOTAP complexes as a function of the polyion/lipid molar charge ratio parameter (adapted from [Bordi et al., 2009]). (b) The average radius R/R_0 of liposome clusters as a function of NaPA polyion concentration for different NaCl concentrations. The arrows mark the boundaries of the polyion concentration ranges where the samples are unstable and flocculation occurs. These regions widen with the increase of the salt concentration (adapted from [Cametti, 2008]).

4.5 Chitosan and hyaluronan in interaction with lipid membrane

4.5.1 Chitosan/lipid membrane

It was shown that chitosan interacts with the lipid membrane. This interaction has been proven to be primarily of electrostatic origin [Henriksen et al., 1994] between phosphate groups of phosphatidylcholine polar head and ionized amino groups of chitosan [Mertins et al., 2010]. Recently, the additional contribution of hydrogen bonding and hydrophobic interactions, due to the chemical structure of chitosan (*e.g.* -CH groups on the glucose cycle [Mazeau and Vergelati, 2002]), have been proposed by [Pavinatto et al., 2010] to justify the higher bioactivity of chitosan than other polycations.

Adsorption of chitosan on the membrane induces changes of molecule organization [Elsabee et al., 2009]. The local order reduction of the 2D packing of acyl chains in the DPPC bilayer initially in the gel state was highlighted [Mertins et al., 2008], leading to the increase of the lipid mobility in the membrane [Fang et al., 2003, Fang and Chan, 2003]. Concerning the effect of chitosan adsorption on the membrane mechanical properties, no quantitative values of the elastic parameters have been proposed so far. Nevertheless, two observations give a trend. Firstly, chitosan coating seems to induce a decrease of the thermal fluctuations of coated fluid membrane, which is attributed to an increase of the bending rigidity by [Mertins et al., 2008]. Secondly, the study of the chitosan interaction with DPPC Langmuir monolayers shows a reduction of the in-plane elasticity [Pavinatto et al., 2010]; this effect increasing with the lipid charge density, thus electrostatic interactions.

Finally, it was shown that chitosan coating enhances the drug entrapment efficiency [Guo et al., 2003] by decreasing the membrane permeability [Henriksen et al., 1997] [Filipovica-Grci et al., 2001] and stabilizes the coated liposome suspension increasing their storage and their resistance to surfactants [Mady et al., 2009]. Chitosan being biocompatible and biodegradable, and acting as a bioadhesive, such coated liposomes may be considered as new protective capsules for drug formulations. As example, they are proposed for oral [Thongborisute et al., 2006], ocular [Zhang and Wang, 2009], nasal [Ding et al., 2007] or cutaneous applications [Perugini et al., 2000].

Although these published studies discuss various techniques to prepare chitosan-coated vesicles and describe a number of physico-chemical tests aimed at elucidating interaction origin, stability and leakage behavior, no information has been presently reported quantifying the efficiency of chitosan-coating, determining the molecular architecture at the membrane interface or estimating the membrane mechanical parameters. We will discuss these different points in this manuscript.

4.5.2 Hyaluronan/lipid membrane

As for the chitosan, the interaction between hyaluronan and lipid membrane is mainly of electrostatic origin [Taglienti et al., 2006], but less study reports information on this complex, in spite of the numerous biomedical and industrial applications of hyaluronan.

Chapter 5

Soft deformable objects under external stresses

Dans ce chapitre est présenté le comportement d'objets déformables soumis à cinq contraintes externes différentes: une dépression locale (aspiration en micropipette), une contrainte isotrope (différence de pression osmotique), une compression entre deux plans parallèles (microscopie à force atomique, AFM), une force ponctuelle appliquée pour extruder un tube de membrane et un écoulement confiné.

Bien que nos études concernent des vésicules, nous étendons cet état de l'art aux capsules élastiques et aux globules rouges, afin de présenter les généralités nécessaires pour comprendre les résultats obtenus sur des vésicules à membranes modifiées. Les propriétés mécaniques et structurelles des objets, déterminées à partir des comportements observés, sont également discutées pour chacun des cinq types de contraintes.

○ ○ ○ ○ ○ ○ ○ ○ ○ ○

In this chapter, we present the behavior of deformable objects submitted to five different external stresses: local depressure, isotropic constraint (such as a pressure difference between the inside and the outside), compression between two parallel planes, local point-acting force applied in order to pull off a lipid tether and flow. Despite the fact that our studies concern vesicles, we extend this review to elastic capsules and red blood cells, in order to introduce generalities necessary to understand the results we have obtained on vesicles with modified membranes. The mechanical and structural properties of the objects, retrieved from their behaviors, are also discussed for each external stress.

While numerous techniques exist to probe the (macroscopic) rheological properties of suspensions containing deformable objects, there is a limited number of tools to analyze mechanical properties of micron-sized particles on the single-colloid level. In the following, we give a brief overview of five techniques used during this work.

5.1 Anisotropic depressure: micropipette suction experiments

This technique consists in the suction of a deformable object (e.g. vesicles [Kwok and Evans, 1981], living cells [Hochmuth, 2000], ...) into a thin capillary, as illustrated in Figure 5.1. For example, suction experiments on GUVs allow the determination of various physical parameters of the lipid membrane, such as permeability [Olbrich et al., 2000], tension, viscosity or elasticity.

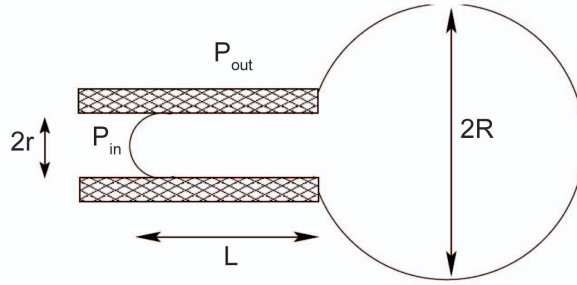


Figure 5.1: Schematic of a GUV partially aspirated in a micropipette (adapted from [Fa, 2003]). The different parameters measured during the experiment are presented.

Micropipette aspirations experiments consist in measuring increase of the surface area ($\frac{A-A_p}{A}$), as a function of the applied difference of pressure (Figure 5.2a) converted to tension σ by the Laplace law, as:

$$\sigma = \frac{P_{out} - P_{in}}{2} \frac{r}{1 - \frac{r}{R}} \quad (5.1)$$

where R and r are respectively the vesicle and inner capillary radii.

The increase in area is then related to the membrane tension as:

$$\frac{A - A_p}{A} \simeq \frac{k_B T}{8\pi\kappa} \ln\left(\frac{\sigma}{\sigma_0}\right) + \frac{\sigma - \sigma_0}{\chi} \quad (5.2)$$

Two regimes can be discriminated [Rawicz et al., 2000]:

- a first regime (low suction) where an exponential variation of the tension is observed as a function of surface area expansion. It corresponds to the unfolding of the membrane fluctuations. The bending modulus κ of the membrane is determined from the slope in a semi logarithmical representation of the tension versus the apparent area expansion (see Figure 5.2b).
- a second (higher suction), the tension is proportional to the apparent area expansion and the slope gives directly the stretching modulus χ (see Figure 5.2c).

Typically, membrane surface areas can be expanded about 2 to 5 %, but beyond this value, the membrane opens hydrophilic pores [Zhelev et al., 1994, Sandre et al., 1999] and the vesicle lyses at a critical tension σ_{lysis} around 10 mN/m [Olbrich et al., 2000] for fluid membrane.

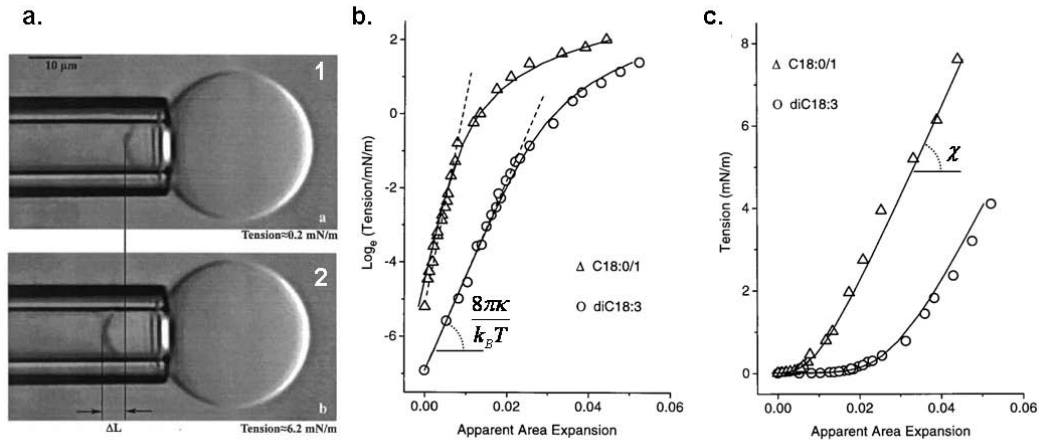


Figure 5.2: Examples of a typical micropipette experiment realized to determine the membrane rigidity κ and stretching modulus χ of vesicles with membrane in the fluid state. (a) Snapshots of a vesicle area expansion tested under low (1) or high (2) tensions. The change in projection length ΔL is proportional to the change in apparent surface area ΔA . (b) Semi logarithmical plot of tension versus apparent area expansion. The slope of the linear fit (dashed lines) in the first part of the curve corresponding to very low tensions yield the elastic bending modulus κ . (c) Linear plot of tension versus apparent area expansion. The linear second part of the curve corresponding to high tensions gives the stretching modulus χ (adapted from [Rawicz et al., 2000]).

5.2 Isotropic pressure

In this part, we focus on the shape transformations of vesicles, elastic thin shells and red blood cells under an external pressure induced for example by changing the osmotic conditions.

Actually, membranes and shells being permeable, water or small molecules can diffuse across them in response to an osmotic difference between the inner compartment and the outside medium which results in a decrease of the object volume. The reduced volume V_R is then defined as the volume V of the deflated object over the volume of the sphere of same surface area S :

$$V_R = \frac{V}{\frac{4}{3}\pi S^{2/3}} \quad (5.3)$$

We limit this review to deflation of deformable objects which do not change of topology, i.e. no transition from sphere to torus, no Gaussian bending energy.

5.2.1 Vesicles: deflation of spherical incompressible shells

Vesicles with fluid membranes

In a first approach, equilibrium shapes can be calculated by simply considering the incompressible lipid membrane as an elastic surface without explicit reference to the material structure

and it is described by the bending energy integrated on the whole surface:

$$H_{Helfrich} = \frac{\kappa}{2} \iint_S (C_1 + C_2 - C_0)^2 dA \quad (5.4)$$

The phase diagram, shown in Figure 5.3, reports the shapes of lowest bending energy as function of the volume-to-area ratio (V_R) and the dimensionless spontaneous curvature $c_0 = R_0 C_0$ (R_0 is the characteristic size of the vesicle) [Seifert et al., 1991]. Four types of axisymmetric shapes are observed depending of the deflation and C_0 : the prolate-dumbbell shapes, the pear-shaped vesicles, which are intimately related to the budding process, the oblate-discocyte shapes and the stomatocytes.

This model is relevant to describe a large panel of the deflated vesicle shapes, experimentally observed, nevertheless it does not illustrate the non-axisymmetric shapes such as the starfish-like shapes [Wintz et al., 1996]. Therefore, it is restrictive to describe the membrane just as a structure-less two dimensional surface; the molecular structure must be retained.

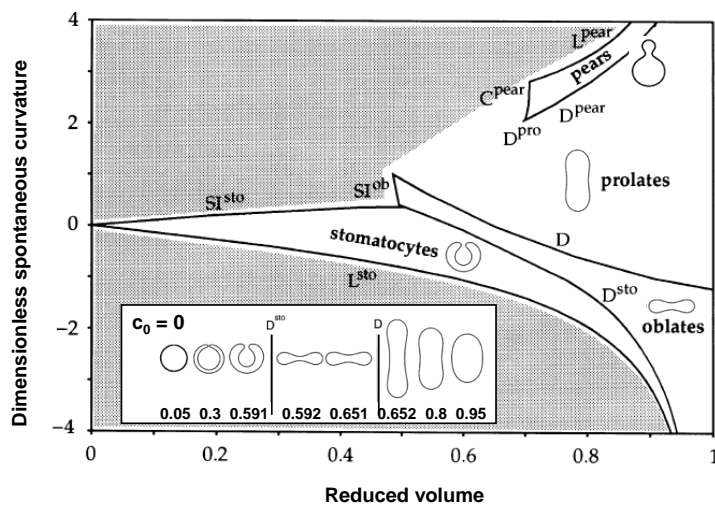


Figure 5.3: Phase diagram of the spontaneous-curvature model shows the shapes of minimal curvature energy as a function of the dimensionless spontaneous curvature c_0 and of the reduced volume V_R . The regions where the prolate/dumbbell, pear-shaped, oblate/discocyte and stomatocyte have lowest energy are separated by transition lines. The line C_{pear} denotes a continuous transition. All other transitions are discontinuous. The lines L^{sto} and L^{pear} correspond to limit shapes with infinitesimal neck. Beyond the lines SI^{ob} and SI^{sto} self-intersecting states occur. In the shaded area, the shape of lowest energy has still to be determined. The inset presents the shapes obtained for $C_0 = 0$. (adapted from [Seifert et al., 1991, Lipowsky and Sackmann, 1995]).

The Area Difference Elasticity (ADE) model takes into account the bilayer architecture by adding a non-local bending energy term corresponding to the stretching of one lipid leaflet relative to the other one [Waugh et al., 1992, Miao et al., 1994]. Hence the relevant parameters determining vesicle shapes are the reduced volume V_R and the effective differential area, $\overline{\Delta a_0}$ i.e. the preferred curvature of the membrane.

$$H_{ADE} = \frac{\kappa}{2} \iint_S (C_1 + C_2 - C_0)^2 dA + \frac{\bar{\kappa}}{2} \frac{\pi}{Ad^2} (\Delta A - \Delta A_0)^2 \quad (5.5)$$

The resulting shape phase diagram is shown in Figure 5.4a, where minimal energy shapes are depicted for each parameter region, now describing the non-axisymmetrical shapes (Figure 5.4b).

Transitions from these various shapes are observed in particular budding process (see Figure 5.4c) leading to fission and formation of a daughter vesicle corresponding to the lowest energy conformation. We can notice that this phase diagram may be explored in the vertical direction in particular by modification of the pH [Lee et al., 1999] or the ionic concentration [Tanaka et al., 2002] of the outer medium which modifies the spontaneous curvature and the bending rigidities, acting on $\overline{\Delta a_0}$.

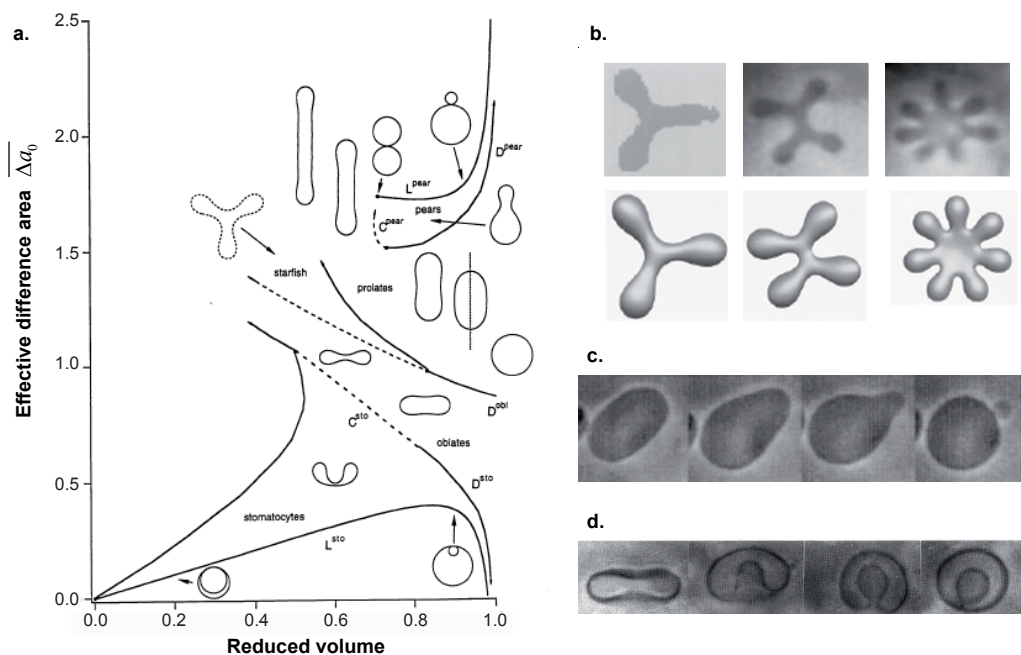


Figure 5.4: (a) The phase diagram of the ADE model shows the lowest-energy shapes as a function of the effective difference area, $\overline{\Delta a_0}$, i.e. the preferred curvature of the vesicles, and of the reduced volume V_R (e.g. spheres correspond to $V_R = 1$) [Döbereiner, 2000]. (b) Starfish-like shape vesicles observed by phase contrast microscopy (top) and theoretically calculated (bottom) [Wintz et al., 1996]. (c) Budding transition from prolate to pear, followed by the formation of a daughter vesicle [Käs and Sackmann, 1997] (d) Transition discocyte-stomaocyte [K.Berndl et al., 1990].

Vesicles with fluid membranes in interaction with polymers

Shapes obtained under osmotic depression for coated vesicles are, for a large part (e.g invaginations or budding processes), well described with the ADE model.

Few recent publications combine to the Helfrich curvature energy (Eq. 5.4) and the self-consistent-field theory for polymers to determine the shapes of the decorated vesicles as well as the segment distributions of the anchored chains [Wang et al., 2005, Guo et al., 2009].

Vesicles with gel phase membranes

Deflated shapes obtained for vesicles with the membrane in the gel phase are at the best of our knowledge not actually reported in the literature. Only some publications seem to report the presence of “facets” on these vesicles without giving any explanation [Antunes et al., 2009].

As mechanical and rheological properties of membranes in the gel phase drastically differ from those in the fluid state (see section 2.3.2), their effect on the shapes of deflated vesicles remains to be addressed.

5.2.2 Deflation of thin spherical shells

If now we consider that the homogeneous and isotropic material is compressible, the free energy consists in both a bending and an in-plane contribution:

$$H_{elastic\ shell} = \iint_S \left(\frac{\kappa}{2} (C_1 + C_2 - C_0)^2 + \frac{1}{2} \epsilon_{ij} K_{ijkl} \epsilon_{kl} \right) dA \quad (5.6)$$

where ϵ_{ij} and K_{ijkl} are respectively the 2D strain tensor and the elasticity tensor [Ben-Amar and Pomeau, 1997].

The balance between the stretching and the bending energies is characterized by the dimensionless Föppl-von Karman number $\gamma = \frac{Y_{2D} R^2}{\kappa}$, where R is the initial radius of the object and Y_{2D} is the 2D Young modulus [Lidmar et al., 2003]. This term scales as $(\frac{R}{d})^2$, where d is the shell thickness, in the case of thin shells where $d \ll R$.

When an external isotropic pressure is applied on the elastic shells, they first deflate keeping a spherical shape, then above a critical pressure $P_c \propto Y_{3D} (\frac{d}{R})^2$ [Landau and Lifshitz, 1986], they become unstable and buckle by inversion of a spherical cap with a characteristic length \sqrt{Rd} , forming a cup-like shape (Figure 5.5a). This buckling process is a first-order transition (Figure 5.5b).

This buckling instability has been experimentally observed for polyelectrolyte capsules under osmotic pressure [Gao et al., 2001] and for porous shells (e.g. drops containing polymer or colloidal suspension) by evaporating or dissolving the enclosed medium [Pauchard and Couder, 2004, Marty and Tsapis, 2008, Quilliet et al., 2008] (see examples in Figure 5.5c).

Although the formation of a single depression is energetically more favorable than creation of multiple depressions, few published results report observations of multiple depressions [Pauchard and Allain, 2003, Tsapis et al., 2005] (see Figure 5.5d).

Therefore, the number of depression depends on the relative shell thickness (R/d) (see Figure 5.5e), nevertheless, no study correlates this number with the elastic parameters and no shape diagram is available (i.e. equivalent to the ADE shape diagram).

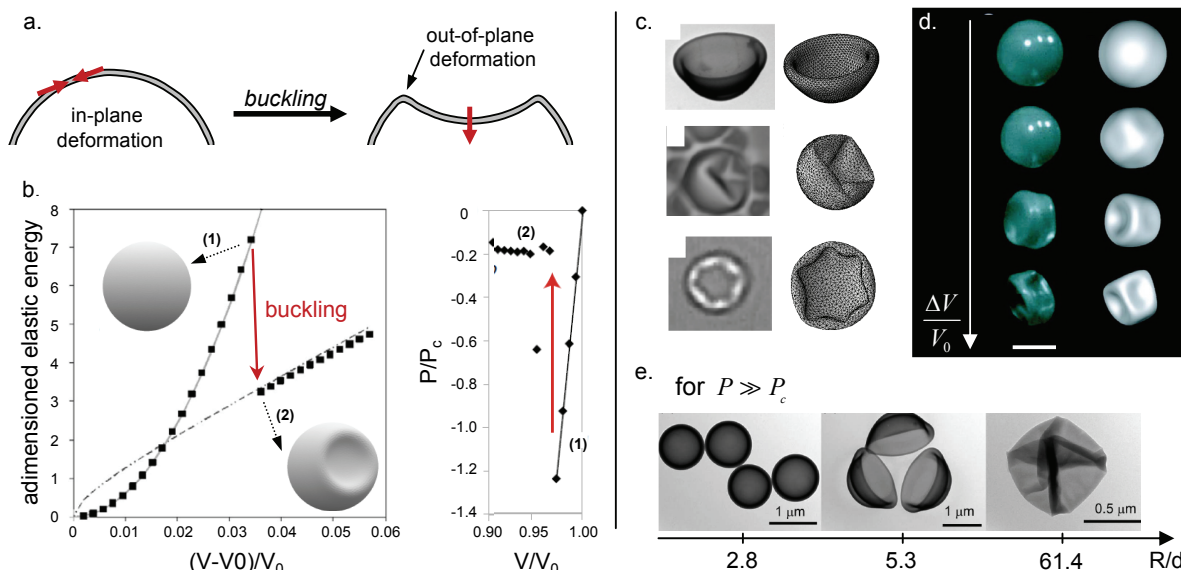


Figure 5.5: (a) Schematic of the buckling instability. (b) Elastic energy, non-dimensionalized by κ , of a shrinking shell initially unstrained ($C_0 = 1/R$) (adapted from [Quilliet et al., 2008]) and the inner pressure normalized by the critical pressure P_c , when the volume is decreased (adapted from [Marmottant et al., 2010]). (c) and (d) Comparison of deflated shell shapes observed experimentally and simulations using the free energy of Eq 5.7: (c) PDMS shells adapted from [Quilliet et al., 2008] and (d) Time sequence of the drying of a droplet filled with a colloidal suspension adapted from [Tsapis et al., 2005]. (e) Effect of the relative shell thickness (d/R) on the final deflated shapes of PDMS shells (TEM micrographs adapted from [Zoldesi, 2006]).

5.2.3 Red blood cells: membrane-skeleton coupling model

Deflation shapes of red blood cells are reported in [Betticher et al., 1995]. The membrane of these cells is a composite structure made of a fluid lipid bilayer closely associated with an 2D elastic network of spectrin [Mohandas and Evans, 1994]. Hence, the lipid membrane resists to bending deformations but has no shear resistance while the skeleton is comparatively soft but resists both stretch and shear deformations.

In order to describe the various deformations of red blood cells (see Figure 5.6a), Wortis and coworkers have extended the ADE model by adding an elastic contribution of the anchored skeleton [Lim et al., 2002, Mukhopadhyay et al., 2002], as:

$$H_{RBC} = H_{ADE}(\kappa) + H_{mem-skeleton}(\chi, \mu) \quad (5.7)$$

We notice that the bending contribution of the skeleton is neglected in this model because estimated two orders of magnitude smaller than that of the bilayer (i.e $\kappa_{skeleton} \sim \chi_{skeleton} \times (\text{thickness})^2$). Figure 5.6b reports the obtained RBC shape diagram and compare simulations and experiments. An extended review on the RBC shapes is proposed in [Lim et al., 2008].

A comparison of experimental and simulated shapes may allow to determine the elastic

parameters of the objects. For example, Young modulus of polyelectrolytes capsules were determined by this method ($Y_{3D} \sim$ few hundreds MPa) and confirmed by AFM experiments [Vinogradova, 2004].

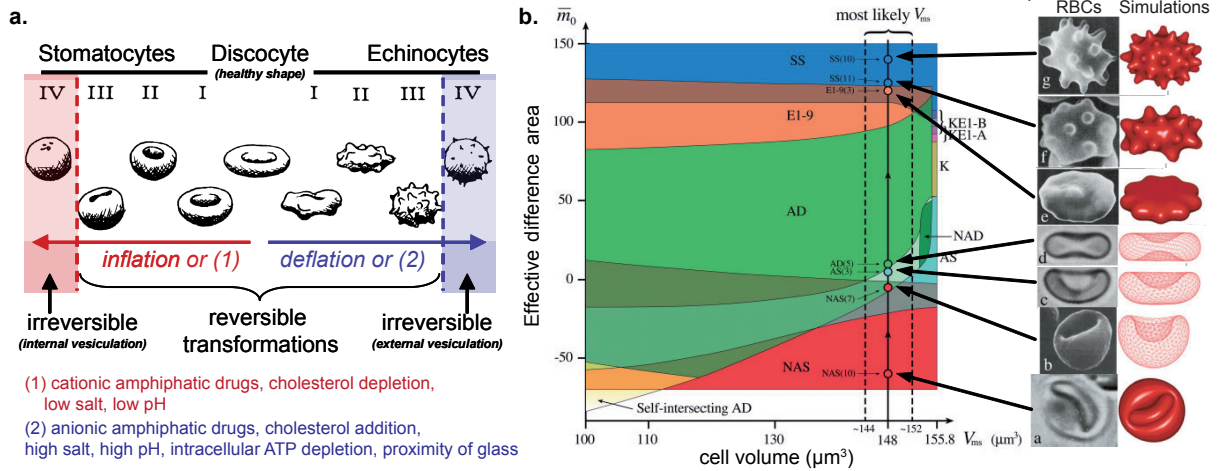


Figure 5.6: (a) RBC shape transformation sequence determined experimentally (adapted from [Betticher et al., 1995]). (b) Shape diagram of lowest-energy shapes as a function of the effective difference area, i.e. the preferred curvature of the RBC composite membrane, and of the cell volume). Only in the “most likely” region does the sequence of predicted shapes agree with the experimental sequence of shape transformation (adapted from [Lim et al., 2008]).

5.3 Anisotropic compression: AFM experiments

Micrometric deformable objects were studied by atomic force microscopy (AFM) using a colloidal probe [Ducker et al., 1991]. In this case, the studied object is compressed between the colloidal particle glued on the tip and the substrate. An observation of capsule shape modification is performed simultaneously with the compression using various kinds of optical microscopies [Lulevich et al., 2004, Dubreuil et al., 2003].

This method allows to distinguish between different regimes in load-deformation profiles and to study the permeability, elasticity and plasticity of deformable objects.

Two reviews introduce the recent development of both theoretical models and experimental techniques to investigate the deformation behavior of deformable objects by AFM and therefore to examine their mechanical and interfacial properties in quantitative manner [Liu, 2006, Fery and Weinkamer, 2007]. We will only report few points interesting for our study (Chapter 9).

5.3.1 Theory of thin shell deformation

We always consider elastic shells of isotropic material with $d \ll R$ such as it can be modeled by an elastic surface; the deformation of the shell being either an in-plane stretching and shear or an out-of-plane bending. Depending on which of these deformation modes are most important

and are allowed, different theories have been developed [Liu, 2006].

We will only discuss here the model proposed by [Lulevich et al., 2004], where the drainage of water through the shell is neglected and the volume does not change on the short timescale of the AFM experiments.

To relate the relative deformation ε to the change in the capsule radius, they further assume that, for small deformations, the shape of the capsule remains spherical excepted in the contact regions. Then, for a small ε , volume conservation requires:

$$R = R_0 \left(1 + \frac{\varepsilon^2}{2}\right) + O(\varepsilon^3) \quad (5.8)$$

where R is the final radius of the capsule.

From the elastic energy (Eq. 5.4), they express the force response f of the system as the sum of the bending and the stretching contributions:

$$f = \frac{\pi}{\sqrt{2}} Y_{2D} d \varepsilon^{1/2} + 2\pi \frac{Y_{2D}}{1 - \nu_{2D}} R_0 \varepsilon^3 \quad (5.9)$$

where d is the thickness, Y_{2D} the 2D Young modulus and ν_{2D} the 2D Poisson's ratio of this shell. We notice that the stretching contribution is radius dependent in this model.

The relative bending and stretching forces ($\frac{f_{stretching}}{f_{bending}} = \frac{2\sqrt{2}}{1-\nu_{2D}} \frac{R_0}{d} \varepsilon^{5/2}$,) can be modulated either changing the shell thickness d (at fixed R) or by changing the relative deformation ε

5.3.2 Deformation of vesicles using AFM

The rare AFM experiments on vesicles are always realized on SUVs or LUVs (i.e. diameter < 500 nm). Liang and coworkers highlight for EggPC SUVs (fluid membrane; 50 nm), that inclusion of cholesterol increases the Young modulus and the bending rigidity of one order of magnitude [Liang et al., 2004], with values in agreement with micropipette experiments on GUVs [Evans and Rawicz, 1990]. Delorme and Fery evaluate for DPPC LUVs (120 nm) in gel phase, the bending rigidity to 330 ± 50 $k_B T$ [Delorme and Fery, 2006], in agreement with results reported in Table 2.2 and highlight a discontinuity in their deformation behavior, attributed to a buckling transition [Landau and Lifshitz, 1986].

5.4 Flow in non-confined and confined geometries

Understanding the dynamical behavior of deformable objects in a flow presents both fundamental (e.g. blood rheology apprehension) and biomedical engineering interests (e.g. lab-on-chip technologies).

This section is a non-exhaustive review on behaviors of vesicles, capsules and red blood cells in shear flow, without boundaries or in presence of a wall, and the Poiseuille flow. Various theoretical and experimental works reported in the literature have allowed us to better understand the results report in the Chapter 11. We only consider low Reynolds number flows ($\text{Re} = \frac{\rho LU}{\eta} \ll 1$, where ρ and η are the density and the dynamic viscosity (Pa.s) of the fluid in motion, respectively; L is the characteristic length of the system and U the speed of the object), so that inertial effects can be neglected in front of the viscous ones.

5.4.1 Shear flow

Shear flow refers to the laminar flow of a viscous fluid in the space between two parallel plates, one of which is moving relative to the other, as illustrated in Figure 5.7a. The shear rate is defined as $\dot{\gamma} = \frac{dV_x}{dy}$, where V_x is fluid speed and y the distance to the stationary wall, and is constant in simple shear flow. The shear flow can be decomposed in both elongational and rotational contributions (Figure 5.7b).

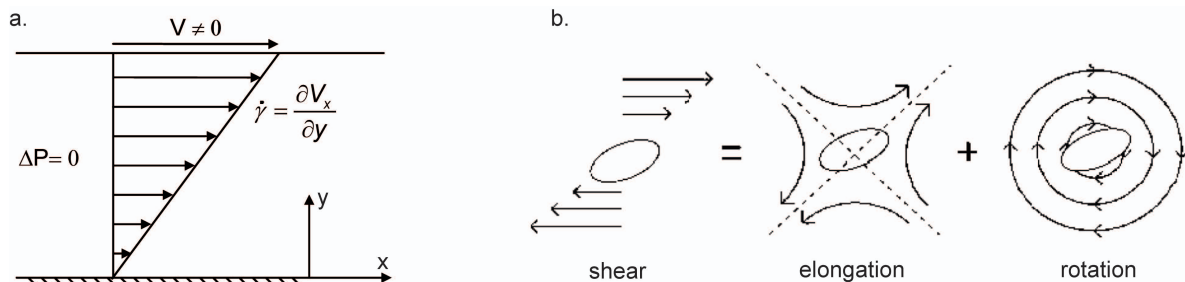


Figure 5.7: (a) Shear flow of fluid between a moving upper plate and a stationary lower plate (Couette flow). (b) Schematic representation of the velocity field decomposition in elongational and rotational contributions.

Vesicles, capsules and red blood cells subjected to a simple shear flow, exhibit various dynamical motions [Messlinger et al., 2009], depending on the flow parameters (shear rate $\dot{\gamma}$, outer fluid viscosity η_{out}) and on the particle properties (inner fluid viscosity η_{in} , shell (membrane) viscosity η_{mem} , elastic moduli, and reduced volume V_R).

Objects far from the walls

Far from the walls, fluid vesicles exhibit two distinct steady regimes when the viscosity ratio λ increases [Keller and Skalak, 1982]. First, at low viscosity contrast $\lambda = \eta_{in}/\eta_{out}$, the vesicle adopts a steady orientation and its membrane rotates around its internal fluid (tank-treading regime, Figure 5.8a line 3). Then, when the viscosity ratio λ increases, the vesicle flips similar to a rigid body (tumbling regime, Figure 5.8a line 1). In both cases, the ellipsoidal shapes remain unchanged and only the vesicle orientation, compared to the flow direction, changes [Kantsler and Steinberg, 2005, Mader et al., 2006].

An unsteady motion, corresponding to the tumbling - tank-treading transition, has been recently highlighted when the shear rate is increased (Figure 5.8a line 2) [Kantsler and Steinberg, 2006]. In this regime, the vesicle's long axis undergoes an oscillation (or vacillation) around the flow

direction, while the shape executes a breathing motion.

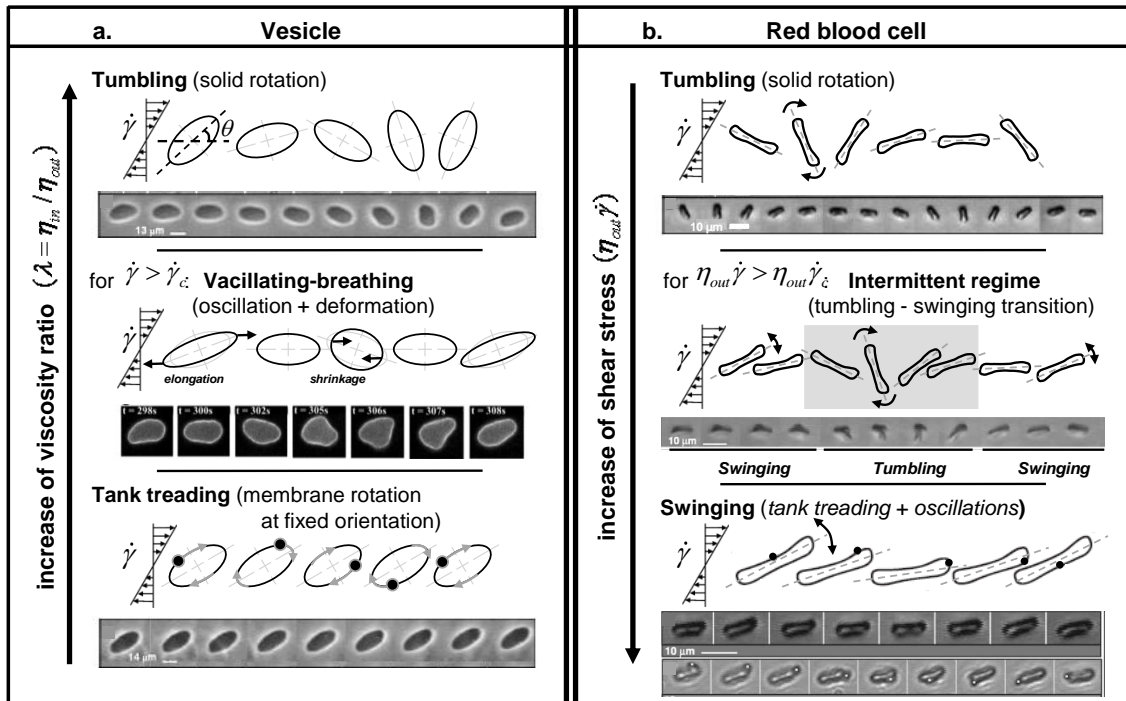


Figure 5.8: Dynamical states of vesicles (a) and red blood cells (b) in a shear flow. Differences in their behaviors are observed depending on the viscosity ratio and the shear stress. Optical microscopy images and sketches are adapted from [Abkarian et al., 2007, Skotheim and Secomb, 2007, Abkarian et al., 2008, Deschamps et al., 2009].

The behavior under flow described above changes when the objects exhibit shear elasticity (e.g. red blood cells) [Bagchi and Kalluri, 2009]. In this case the classical tank treading motion is associated with an oscillation of the inclination (Figure 5.8b line 3), depending of the applied shear stress ($\eta_{out}\dot{\gamma}$) [Abkarian et al., 2007, Skotheim and Secomb, 2007]. Such swinging regime has also been detected in elastic protein-coated drop [Erni et al., 2005] and elastic capsules [Chang and Olbricht, 1993, Walter et al., 2001].

We now deal with flow in presence of walls; this case is of high interest in physiological conditions [S.P. Sutera, 1993].

Object near a wall

In this case, deformable objects are repelled from the wall due to a hydrodynamic lift force creating a particle-depleted region near the wall (Figure 5.9a). Olla [Olla, 1997a, Olla, 1997b] calculated the drift undergone by a fluid deformable ellipsoid and obtained an expression for the drift velocity given by:

$$v_{drift} = \beta \frac{\dot{\gamma} R^3}{h^2} \quad (5.10)$$

where $\dot{\gamma}$, is the applied shear rate, R is the radius of the sphere of the same volume as the ellipsoid, h the distance between the wall and the particle, and β is a dimensionless param-

ter dependent on the orientation of the tank-treading particle and its shape (i.e reduced V_R), and consequently is also related on the viscosity ratio λ between the object and the suspending medium. The lateral migration is defined as the movement perpendicular to the wall.

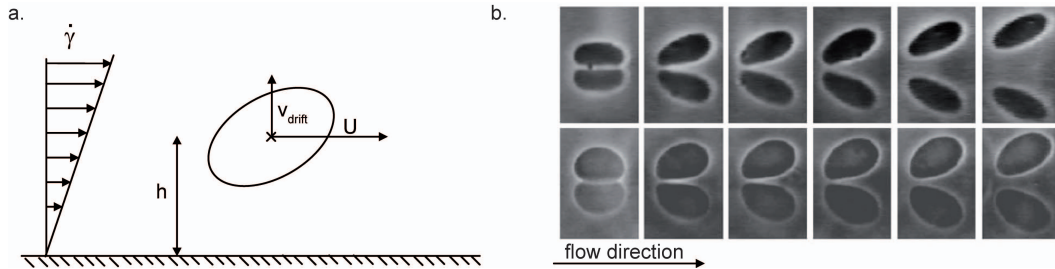


Figure 5.9: *Drift of deformable objects submitted to a shear flow near a wall. (a) Definition of the parameters. (b) The lift force pushes the vesicles away from the wall [Abkarian and Viallat, 2005]. Each row of pictures represents the deformation of one vesicle for a different flow rate. We can note that we distinguish the vesicle and its reflection on the substrate.*

This formula is found for vesicles [Abkarian et al., 2002, Callens et al., 2008] [Messlinger et al., 2009] and red blood cells [Fischer and Schmid-Schönbein, 1977, Secomb, 2003] in tank-treading motion near a wall. Above a critical λ , objects tumble and no more shift from the wall.

5.4.2 Poiseuille flow

Plane Poiseuille flow is the steady state flow between two stationary parallel plates where the flow is driven by an imposed pressure gradient between the inlet and the outlet of the channel (Figure 5.10).

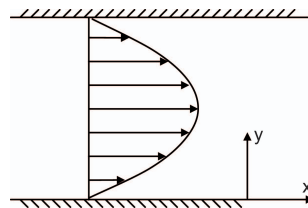


Figure 5.10: *Schematic representation of a Poiseuille flow*

The recent development of microfluidic techniques allows the investigation and the manipulation of individual objects in confined geometries (i.e. micrometric distance between the two walls).

Lateral migration in Poiseuille flow

Lateral migration is reported for vesicles [Coupier et al., 2008] and red blood cells [Secomb et al., 2007] in microchannels where interactions with the walls cannot be neglected.

In the case of vesicles, the movement toward the center of the channel is attributed to a

combined effect of the walls and of the curvature of the velocity profile. Like for shear flow, the viscosity contrast is always the key parameter of the migration (i.e. tank-treading-tumbling transition) [Kaoui et al., 2008, Danker et al., 2009]. The dependency of the drift velocity scales as $1/h^2$, as previously reported in presence of a single wall (see Eq 5.10).

This transverse migration is responsible for concentrating the particles at the channel center and creating an object-free layer near the wall (e.g., application for the blood plasma separation [Faivre et al., 2006]).

We now consider the case where objects and channels exhibit similar sizes.

Deformable objects in confined geometries

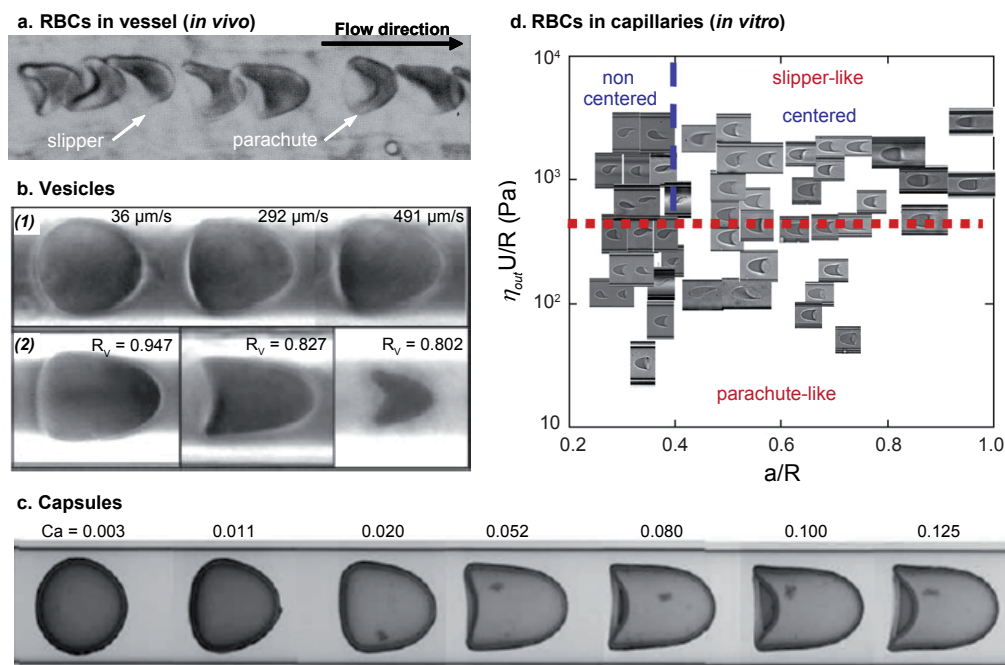


Figure 5.11: Steady shapes adopted by vesicles, capsules and red blood cells flowing in capillaries. (a) Shapes of RBCs *in vivo* in a capillary of width $w = 7 \mu\text{m}$. Most of the cells show the parachute-like shape; the cell on the left shows the slipper-like shape [Skalak and Branemark, 1969]. (b) Shape of vesicles from [Vitkova et al., 2004]. (1) Deformation of one vesicle (radius $a_0 = 20.2 \mu\text{m}$, $V_R = 0.983$, $\lambda = 0.71$) at increasing velocities ($U = 36, 292, 491 \mu\text{m/s}$). (b): Other types of shapes observed in the experiment (the corresponding parameters are $a_0 = 20.9, 18.8$ and $8.7 \mu\text{m}$; $V_R = 0.947, 0.827$ and 0.802 ; $\lambda = 0.80, 0.67$ and 0.40 ; $U = 219, 541$ and $505 \mu\text{m/s}$). Scale: the picture height is about $50 \mu\text{m}$. (c) Stationnary shapes of capsules for a non-dimensional particle size for $2a_0/W=0.81$, where W is the diameter of the capillary tube and for different capillary numbers from [Risso et al., 2006]. (d) Phase diagram of RBC shapes as a function of the external shear stress $\eta_{out} U/R$ and the non-dimensional particle size a/R [Abkarian et al., 2008].

As they flow through the *in vivo* microcirculation, red blood cells deform to fit the smallest capillaries dimensions (Figure 5.11a). *In vitro*, for capillaries with diameter comparable to the cell size, it is shown that vesicles [Vitkova et al., 2004] (Figure 5.11b), capsules [Risso et al., 2006, Lefebvre et al., 2008] (Figure 5.11c) and red blood cells [Secomb et al., 1986] align with the

flow axis and adopt a steady bullet- or parachute-like shape depending on their reduced volume, their velocity and the viscosity contrast. Moreover, for high fluid speed, red blood cells also exhibit a non-axisymmetric slipper-like shape, whose equilibrium position is not always on the centerline, and depends on the confinement [Abkarian et al., 2008] (Figure 5.11d). We notice that the last experimental result is in contradiction with numerical results which argue the transition from the slipper to the parachute can occur when the RBC velocity increases [Noguchi and Gompper, 2005, Kaoui et al., 2009].

The formation of slipper-like shape for vesicle has been recently observed by [Noguchi et al., 2010], and it remains to be investigated.

Deformation dynamic through a pore

Few studies of the transient shapes adopted by deformable objects crossing a pore have been reported. The sequence of deformation of a capsule entering, going through and exiting a close fitting channel has been observed experimentally by [Risso et al., 2006] (Figure 5.12a) and theoretically by [Quéguiner and Barthès-Biesel, 1997] (Figure 5.12b). Barthès-Biesel and co-workers calculated the capsule velocity and the excess of pressure associated with its motion in a cylindrical pore as a function of its position (see Figures 5.12c and 5.12d); the pressure drop amplitude depends on the capsule volume and the viscosity contrast [Diaz and Barthès-Biesel, 2002].

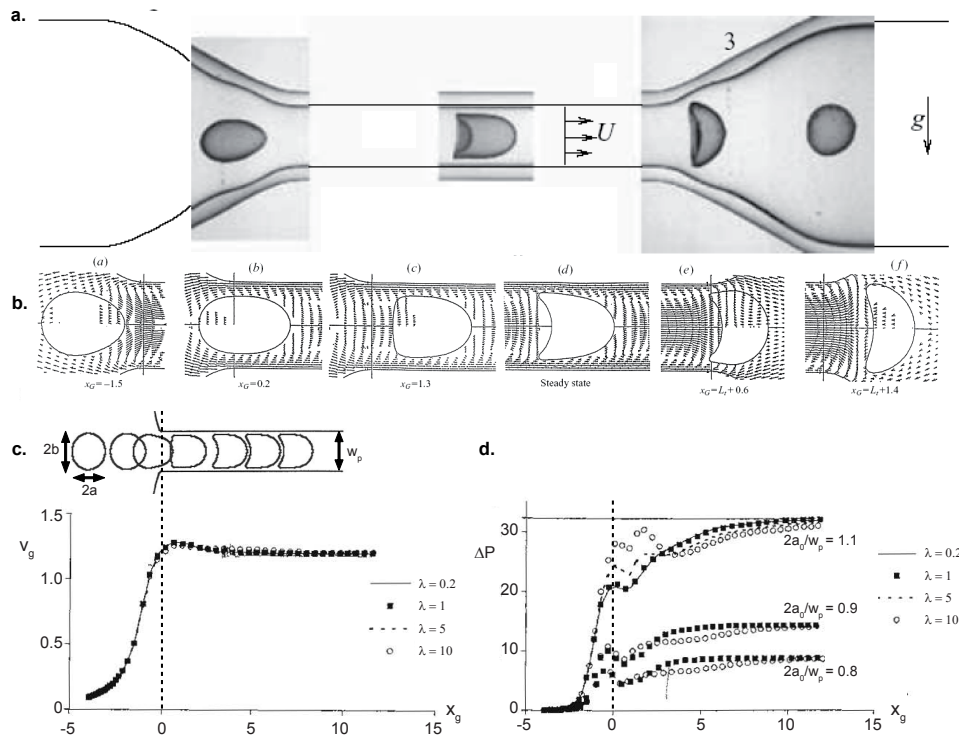


Figure 5.12: (a) Dynamical deformation of capsules flowing in a constriction [Risso et al., 2006]. (b) Flow field and sequence of deformation of a capsule for a confinement $2a_0/w_p = 0.8$ (w_p the pore width and $a_0 = (ab^2)^{1/3}$ the equivalent radius of the capsule) [Quéguiner and Barthès-Biesel, 1997]. Evolution of the center of mass velocity (c) and pressure drop (d) of an elastic capsule through a geometrical constriction, for different viscosity contrasts λ and confinement [Diaz and Barthès-Biesel, 2002].

Simultaneous measurements of the dynamical deformation of the red blood cells (Figure 5.13a) and the variation of the pressure drop produced by their motion in the channel (Figure 5.13b) are reported by [Abkarian et al., 2006]. They show that the pressure drop depends on the cell volume [Faivre et al., 2006]. The comparison of healthy RBCs with rigidified cells (treated with glutaraldehyde) also highlights that the excess pressure drop associated with the passage of a rigidified cell is both higher in intensity and broader in time, which reveals a slower deformation of the modified cell relative to that of a healthy cell for the same flow environment. Finally, using this differential manometer, they estimate the membrane lysis tension of red blood cells to 0.4 psi (Figure 5.13c) in good agreement with the values obtained by micropipette experiments (0.6 psi) [Mohandas and Evans, 1994]. One advantage of this microfluidic approach is that many cells can be examined in relatively short time, as compared to the micropipette technique.

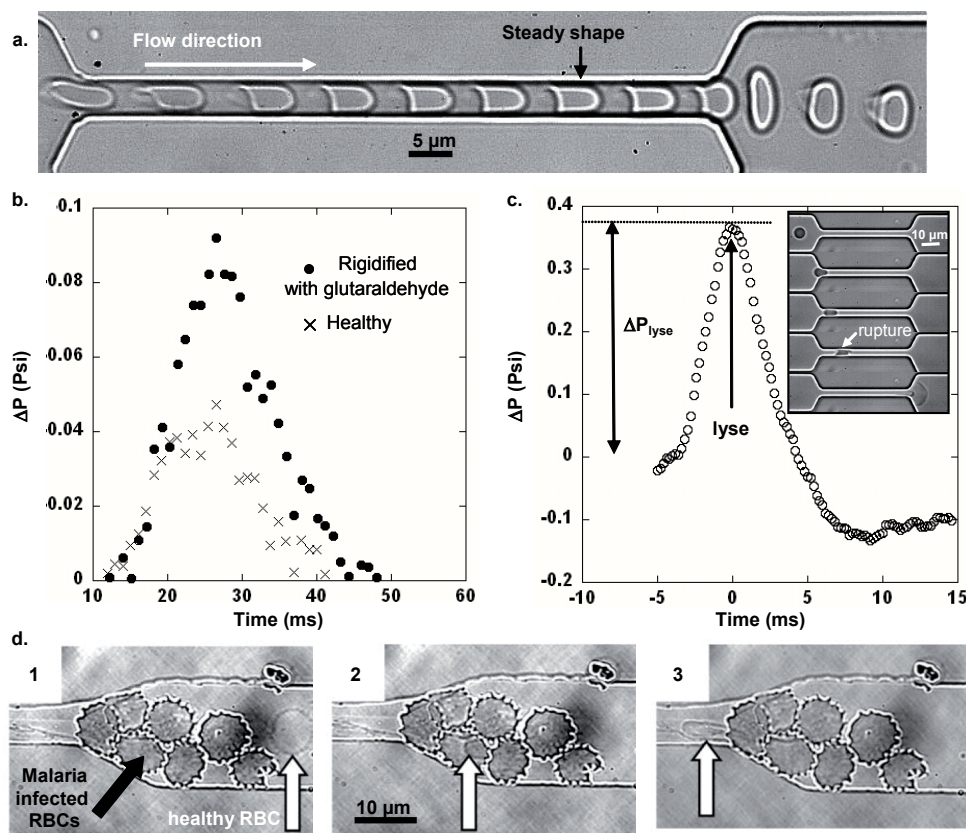


Figure 5.13: Time-lapse sequence of deformation of a healthy RBC flowing in a close-fitting $100 \mu\text{m}$ long channel (time lapse of 10 ms). (b) Pressure drop versus time for different conditions characterizing the state of the RBCs; the driving pressure is 5 psi . (c) Pressure drop associated with the burst of the cell in the channel; inset: Sequence of deformation and lyse of an inflated red cell (adapted from [Abkarian et al., 2006, Faivre et al., 2006, Abkarian et al., 2008]). (d) A video sequence showing the passage of an healthy RBC through a blockage formed by infected cells (adapted from [Shelby et al., 2003]).

The consequence of some diseases is the modification of the mechanical properties of the red blood cells which modifies their deformability, affecting their behavior under flow. As example, we can cite the morphologies anomalies of the RBC due to alcoholism or the malaria which

rigidifies and deforms the RBC. In the case of the malaria (see Figure 5.13d), infected RBCs not deform to enter in the constriction, while a healthy one can slip between the infected RBC and flow in the pore [Shelby et al., 2003], illustrating the effect of the cell mechanical properties on their behavior under flow.

To conclude, we notice that, very few publications report the determination of the mechanical parameters of deformable objects from their behavior under flow in confined geometries [Lefebvre et al., 2008]. In this work, we report such a study on bare vesicles with the aim to optimize confined geometries allowing the estimation of the mechanical properties of objects in a suspension.

5.5 Point-acting force: hydrodynamic extrusion of tubes from giant vesicles

A point-force acting on the fluid membrane of a living cell or an artificial vesicle is known to give rise to the extraction of thin bilayer tubes from the membrane [Waught and Agre, 1982]. A large panel of tether-pulling experiments have been reported using mechanical micropipette manipulation [Evans and Yeung, 1994], optical tweezers [Dai and Sheetz, 1999], electrical micro-electrode manipulation [Karlsson et al., 2001] or hydrodymanical flow [Evans and Yeung, 1994] [Heinrich and Waugh, 1996] and allow an accurate determination of the mechanical (e.g. bending modulus, membrane viscosity) or structural (e.g. membrane-cytoskeleton coupling, lipid mobility) membrane parameters [Derenyi et al., 2007].

In this work we use the hydrodymanical flow technique: a vesicle punctually attached to a needle is first submitted to a constant flow, below a threshold velocity U_c , the vesicle is only slightly deformed, while above U_c , a membrane tube is extruded; the length $L(t)$ increases up to a stationary length L_∞ . Then, the flow is stopped, the tube retracts and $L(t)$ decreases to 0. This technique allows to study both membrane tube extrusion and retraction dynamics [Rossier et al., 2003, Borghi et al., 2003b]. The static model to the dynamics of membrane tube formation will be reported in section 9.3.1.

Chapter 6

General materials and methods

Dans ce chapitre, nous présentons les protocoles utilisés pour préparer les différents types de vésicules, et nous décrivons brièvement les techniques expérimentales employées pour les étudier.

o o o o o o o o o o

In this chapter, we present the protocols used to prepare the different sorts of vesicles and we describe briefly the experimental techniques used to study these samples. We first detail the chemicals and the protocols of preparation specific to each type of composite vesicles. Then, the protocol used to apply controlled osmotic, pH or salt shocks on GUVs is reported. Finally, some background information are provided on the methods applied to characterize respectively LUVs and GUVs.

6.1 Preparation of vesicles with membrane in fluid phase

6.1.1 Lipids

Vesicles with fluid lipid membrane used in this work, are prepared from the 1,2-dioleoyl-sn-glycero-3-phosphocholine (18:1 PC (cis), DOPC, Mw = 786.15). It is a zwitterionic phospholipid with two chains of 18 carbons having one unsaturation per each carbon chain (see Figure 6.1a). The main transition temperature (T_m) is evaluated to -18.3 ± 3.6 °C [Koynova and Caffrey, 1998].

Two different fluorescent phospholipids can also be added to label the DOPC fluid membranes: the 1-Oleoyl-2-[12-[(7-nitro-2-1,3-benzoxadiazol-4-yl)amino]dodecanoyl]-sn-Glycero-3-phosphocholine (18:1-12:0 NBD PC, Mw = 882.09), with a nitrobenzoxadiazole fluorescent group (NBD) (excitation/emission: 460/534 nm) on one tail, or the 1,2-dioleoyl-sn-glycero-3-phosphoethanolamine-N-(Lissamine Rhodamine B Sulfonyl (ammonium salt) (18:1 Liss Rhod PE, Mw = 1,301.73), a zwitterionic phospholipid, labeled on the polar head with a rhodamine group (excitation/emission: 557/587 nm) (see Figure 6.1b). The degrees of fluorescent labeling in weight are respectively 1/50 w/w for the 18:1-12:0 NBD PC and 1/80 w/w for the 18:1 Liss Rhod PE.

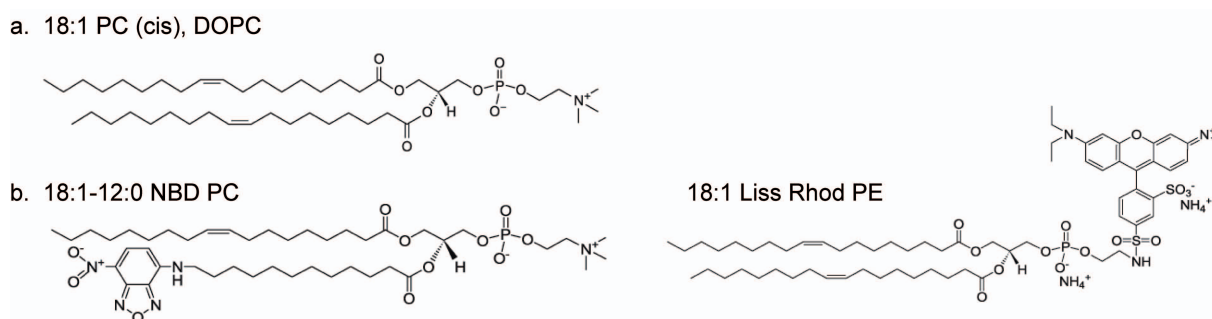


Figure 6.1: Chemical structures of the lipids used to prepared vesicles with fluid membranes. (a) DOPC, the main component of the fluid membrane and (b) fluorescent labeled phospholipids used in this work (from <http://www.avantilipids.com>).

Vesicles with membrane in gel phase are prepared with the 1,2-Dimyristoyl-*sn*-Glycero-3-Phosphocholine (14:0 PC, DMPC, Mw = 677.94), a phospholipid with two saturated chains of 14 carbons (see Figure 6.2). Its main transition temperature is evaluated to 23.6 ± 1.5 °C [Koynova and Caffrey, 1998]. Fluorescent labeling is obtained by addition of 1-Myristoyl-2-[12-[(7-nitro-2-1,3-benzoxadiazol-4-yl)amino]dodecanoyl]-*sn*-Glycero-3-Phosphocholine (14:0-12:0 NBD PC, Mw = 828.00), a phospholipid labeled with a nitrobenzoxadiazole fluorescent group (NBD) (excitation/emission: 460/534 nm) on one tail. The degree of fluorescent labeling is 1/50 w/w.

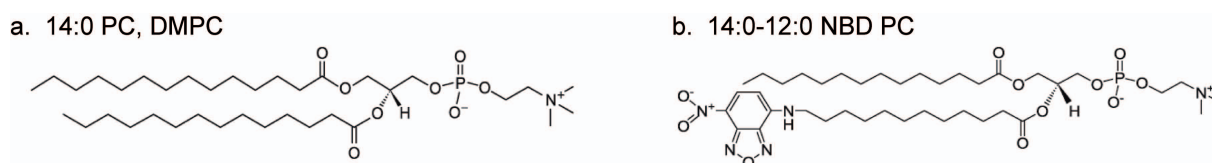


Figure 6.2: Chemical structures of the lipids used to prepared vesicles with gel membranes: DMPC, the main component of the membrane and 14:0-12:0 NBD PC, a fluorescent labelled phospholipid (from <http://www.avantilipids.com>).

These different lipids are purchased from Avanti Polar Lipids and dissolved separately as received in a chloroform/methanol solution (9/1 v/v) at 10 mg/mL. Lipid mixtures are then prepared at a total concentration of 2 mg/mL and kept at -20 °C until used for the vesicles preparation.

A simple mixing of lipid and water doesn't result in spontaneous formation of unilamellar vesicles. Two different protocols are applied to produce the vesicles used in this work: the electroformation technique to prepare Giant Unilamellar Vesicles (GUVs, diameter > 0.5 μ m) [Angelova and Dimitrov, 1987] and the extrusion of GUVs through a filter to obtain Large Unilamellar Vesicles (LUVs, 100 nm < diameter < 500 nm) [Hope et al., 1985].

6.1.2 Electroformation of GUVs

This technique consists in hydrating a dry film of lipids under an alternate electric field to form vesicles, which are in majority unilamellar, with a size distribution ranging from 1 to 50 μm .

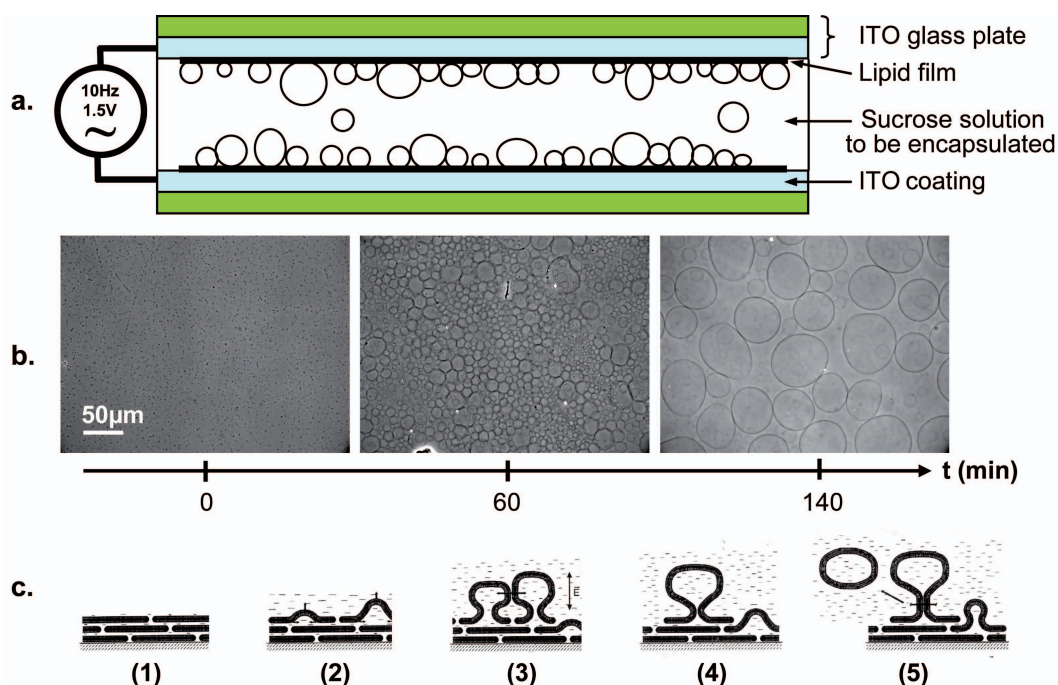


Figure 6.3: (a) Schematic representation of the cross section of the electroformation chamber. (b) Formation and growth of vesicles as function of time observed by phase contrast microscopy. (c) Possible mechanism of GUV formation (adapted from [Luisi and Walde, 2000]).

The standard electroformation protocol consists in the following steps:

1. **Deposit of a film of lipids:** approximately 80 μL of lipid solution (2 mg/mL in chloroform/methanol) are spread on two Indium Tin Oxide (ITO) coated glass plates (5 cm x 5 cm). Lipid-coated glass plates are then dried in a vacuum chamber for at least 1 hour to remove the organic solvent.

2. **Preparation of the electroformation chamber:** the ITO glass plates are placed with the coated sides facing each other and are held at a distance of 1 mm by a thin Teflon spacer. The formed chamber is hermetically closed with a sealing paste after the injection of 2.5 mL of the 200 mM sucrose solution to encapsulate (Figure 6.3a).

3. **Formation and growth of vesicles:** a sinusoidal AC voltage of 200 mV amplitude and 10 Hz frequency is then applied. It induces periodic electroosmotic displacement of the aqueous medium near the electrodes which pulls off the lipid layers from the surface and allows to form mushrooms (sketches 1 and 2 in Figure 6.3b). The swelling of these mushrooms is induced by increasing, step by step, the voltage between 200 mV and 1.5 V and controlled by optical mi-

crosscopy (ITO plates are optically transparent: thickness of the ITO coating ~ 125 nm). During the process of electroformation, the growth of the swelled mushrooms is induced by the fusion between close elements which lead to form a new one of bigger size (Figure 6.3b sketches 3 and 4 and sequence Figure 6.3c). Then the AC frequency is lowered to 4 Hz for 10 minutes to close the mushrooms, separate them from the ITO glass plates and form spherical vesicles in solution [Luisi and Walde, 2000] (Figure 6.3b sketch 5).

4. **Collect and storage of the vesicles:** at the end of this process, the swelling chamber is gently emptied, to avoid to shear the vesicles. The GUVs suspended in the sucrose solution are then stored at 4°C and protected from the light, in the case of fluorescent labeling.

6.1.3 LUVs preparation by GUVs extrusion

The LUVs are obtained by extrusion of a suspension of GUVs produced by electroformation, through a 0.2 μm filter (Acrodisc[®] Syringe Filter 0.2 μm HT Tuffryn[®] membrane), as illustrated in Figure 6.4). LUVs prepared in these conditions are unilamellar [Hope et al., 1985, Nayar et al., 1989] with diameters of 200 ± 10 nm. It is of interest to prepare LUVs from the GUVs solution, to obtain a suspension of LUVs with the same lipid composition.

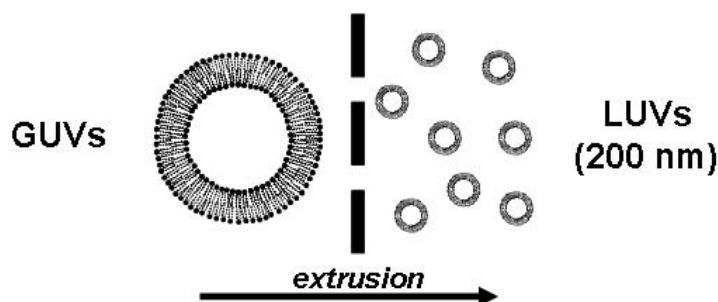


Figure 6.4: Schematic representation of a GUV extrusion through pores of a filter to form LUVs.

Depending on the experiments, GUVs and LUVs can be suspended in an external solution containing HCl, NaOH and NaCl at controlled concentrations allowing to reach desired pH and salt conditions.

6.2 Vesicles coated with polyelectrolytes

6.2.1 Polyelectrolytes

Initial polyelectrolytes

Two different pseudo-natural polyelectrolytes have been used to coat the vesicles:

- Chitosan (CHIT) is a positively charged polyelectrolyte. For our experiments, we have used four different chitosans, with various weight-average molecular weights (Mw) and degree

of acetylation (DA). Chitosan, $M_w = 5 \times 10^4$ and $DA = 0.04$, is provided by Primex; $M_w = 1.49 \times 10^5$ and $DA = 0.15$ is purchased from Sigma-Aldrich; $M_w = 2.25 \times 10^5$ and $DA = 0.05$ is obtained from Far East crabs shells by Mullagaliev [Rinaudo et al., 2005] and $M_w = 5 \times 10^5$ and $DA = 0.20$ is purchased from Kitomer (Marinard, Canada).

- Hyaluronan (HA) is a negatively charged polyelectrolyte. For our experiments, we have used five different hyaluronan, with various weight-average molecular weights: $M_w = 1.14 \times 10^4$, 4.1×10^4 , 1.95×10^5 , 6.63×10^5 and 1.8×10^6 , purchased from ARD (Pomacle, France).

The chemical structures of the two types of polymers are presented in Figures 3.4 and 3.5.

Fluorescent labeling of the polyelectrolytes

In order to both observe the chitosan or hyaluronan decoration on vesicles by fluorescence microscopy and quantify the polymer adsorption, we have labeled these two polyelectrolytes with fluorescent probes:

- **Chitosan labeled with fluorescein** (CHIT-Fluo): 1 g of chitosan ($M_w = 5 \times 10^5$) is dispersed in 40 mL of distilled water and dissolved by addition of 60 mL of 0.1 M HCl; 25 mL of dried methanol are added before introduction of 50 mL of a solution of MeOH containing 52 mg of fluorescein isothiocyanate (FITC from Fluka). After being stirred during 3 hours at room temperature, the mixture is diluted with water up to a final volume of 600 mL. The solution is neutralized with a 0.1 M NaOH solution to $pH \sim 7$. The fluorescent chitosan precipitate is filtrated, washed with an ethanol/water 70/30 (v/v) mixture until obtention of a clear filtrate and finally dried at room temperature.
- **Hyaluronan labelled with rhodamine** (HA-Rhod): 1 g of HA ($M_w = 6.63 \times 10^5$) is dissolved under stirring in 100 mL of 0.02 M NaCl and the pH is controlled at 6.1. Then 50 mL of methanol are added under stirring and directly after, 50 mg of tetramethylrhodamine B isothiocyanate (purchased from Sigma-Aldrich) dissolved in 50 mL of methanol are added too.

The degree of labeling is determined from the fluorescence intensity of diluted solutions of the free fluorescent probe compared with the fluorescence of a diluted solution of the labeled polysaccharides. It is found to be around 1 rhodamine per 25 disaccharide units (or 50 sugar units) for hyaluronan and 1 fluorescein per 60 sugar units for chitosan. These low percentages are chosen in order to minimize changes of physical properties of polyelectrolytes and lipid membrane assemblies by labeling.

Alkylated polyelectrolytes

The initial polyelectrolytes, chitosan ($M_w = 2.25 \times 10^5$, $DA = 0.05$) and hyaluronan ($M_w = 6.63 \times 10^5$) are also chemically modified to introduce hydrophobic alkyl groups randomly along their backbones.

- **Alkylated chitosans** are prepared by a direct reductive amination reaction [Desbrieres et al., 1996], using the different aldehydes [Rinaudo et al., 2005]. The chitosan derivatives obtained exhibit a low degree of alkylation of 0.05 but with different alkyl chain lengths: C6, C10, and C12. The reference of the polymers will indicate the length of the alkyl chain (n carbon chain) as CHIT-Cn.
- **Alkylated hyaluronan** is prepared by reacting aldehydic chain (1-decanal: C10) with the adipic dihydrazide derivative (HA-ADH). The alkylated hyaluronan (HA-C10) used has a degree of alkylation of 0.08; it was provided by ARD (Pomacle, France) [Creuzet et al., 2006].

Polyelectrolyte solutions

Solutions of hyaluronans (HA, HA-Rhod and HA-C10) are prepared at 0.4 g/L by dissolving the polymer in 200 mM sucrose solution in water at pH = 6.0, while similar dissolution of cationic chitosan (CHIT, CHIT-Fluo and CHIT-Cn) requires addition of a stoichiometric amount of HCl on the basis of -NH₂ content in the chitosan to reach a final pH of 3.5. Polyelectrolyte solutions are stirred for a night at room temperature, until complete solubilization. Then they are diluted down to 0.1 to 0.01 g/L in a 200 mM sucrose solution in water, at adjusted pH (3.5 or 6.0) and NaCl concentrations.

6.2.2 Incubation of vesicles with polyelectrolytes

Incubation of LUVs and GUVs is made at room temperature for at least 30 minutes in polyelectrolyte water solution of concentrations ranging between 0.01 and 0.1 g/L. The technique allows the preparation of vesicles with polyelectrolytes only present on the external part of the lipid membrane.

6.3 PEG treatment of glass substrates

Glass substrates of the observation chambers are covered with a hydrophilic polymer, poly(ethylene glycol) (PEG) grafted covalently according to the protocol given by [Zhang et al., 1998], in order to avoid its interaction with GUVs or polyelectrolytes. The procedure is the following:

1. **Glass slides are washed** with a “Piranha” solution for 30 minutes. This very oxidant mixture activates the silicium oxide on the surface of the glass and helps the silanization. Then, glass plates are washed 3 times with distilled water, then twice with methanol.

2. **Silanization:** glass slides are left for a night in a mixture of 43 mL of methanol, 2 mL of distilled water, 400 μ L of acid acetic and 1 mL of 3-MercaptoPropylTrimethoxySilane at 95 % (Sigma-Aldrich) (Figure 6.5a). This amount of silane allows to cover approximately 50 cm². The glass plates are then washed with methanol, dried with argon and baked 10 minutes at 120 °C.

3. **PEG treatment:** once cooled, glass plates are placed during few hours at room temperature in a aqueous solution with 0.14 mg of Mal-PEG (methoxypolyethylene glycol-maleimide, Mw = 5000, Sigma-Aldrich) (Figure 6.5b) per cm² of glass to be treated. The maleimide function reacts with the mercapto function of silane already grafted. The glass plates are finally washed with distilled water, dried with argon and stored under vacuum until used.



Figure 6.5: Chemical structures of the (a) 3-(MercaptoPropyl)TrimethoxySilane, (b) methoxypolyethylene glycol-maleimide.

6.4 Preparation of GUVs suspension for microscopy observation

In order to easily observe the GUVs by inverted optical microscopies, we induce their sedimentation by decreasing the density ratio between external and internal media. Therefore, a volume V of the GUVs with similar internal and external sucrose water solution of concentration C is added to a volume $9V$ of glucose water solution at the same concentration C . In addition, the difference between the refractive index of internal sucrose and external glucose water solutions allows vesicle observations by phase contrast microscopy.

6.5 Increase of pH, salt and glucose concentrations of the GUVs and LUVs suspensions (so called “pH, salt and glucose shocks”)

Shocks are imposed by successive injection of 5 μL of HCl, NaOH, glucose or NaCl water solutions at different initial concentrations (ranging between 10^{-3} to 1 M) so that pH is adjusted between 1.5 to 12 and NaCl and glucose concentrations between 1 mM to 500 mM, in the vesicle suspension. The small volumes are injected to limit the convection.

In the case of confocal microscopy observations, injections have to be made through a 0.8 μm filter in order to reduce the vesicle displacement generated by the convection, as proposed by [Bernard et al., 2002].

6.6 Experimental methods for LUVs characterization

6.6.1 Spectrofluorimetry: determination of the lipid amount in LUVs

Lipid amount contained in LUVs can not be directly deduced from the amount of lipids involved in GUVs electroformation because lipids may be lost during the electroformation process

and the GUVs extrusion through the filter. To evaluate the lipid quantity in the solution, a fixed amount of fluorescent labeled lipids is mixed with DOPC (respectively in a weight ratio of 1/50 for the 18:1-12:0 NBD PC and 1/80 for the 18:1 Liss Rhod PE) and fluorescence intensity measurements on vesicle suspensions are performed with a Perkin-Elmer Luminescence Spectrometer LS50B, at 20 °C.

Assuming that no free lipids are present in solution and using to an appropriate calibration, the fluorescence intensity measurements are converted in a lipid quantity contained in the vesicle membranes. This determination is systematically made on our LUVs samples.

For our preparation protocols of GUVs and LUVs, we have evaluated that, typically, GUV suspensions contain only 1/6 to 1/3 of the total lipid amount initially deposited on the ITO glass plates for the electroformation and that extrusion induces an additional loss of 30 to 40 %.

In the following, we will assume that the amount of lipids included in the external leaflet of the lipid membrane represents one-half of the total lipids.

6.6.2 ζ -potential and size measurements

Measurements on vesicles suspensions (total concentrations of lipid ranging between 3 and 5×10^{-3} mg/mL) are performed at 20 °C with a commercial Zeta-sizer (Zetasizer NanoZS, Malvern, France). With the apparatus, both size and ζ -potential of LUVs in suspension are measured.

The size of LUVs is determined by dynamic light scattering (DLS) experiments.

ζ -potential is estimated from the displacement of the LUVs in presence of an electric field E . When E is applied on an electrolytic solution, charged particles are attracted towards the electrode of opposite charge sign while viscous forces acting on the particles tend to oppose this movement. When equilibrium is reached between these two opposing forces, the particles move with constant velocity v . The electrophoretic mobility U_e , defined as v/E , is related to the ζ -potential by the Henry relationship:

$$U_e = \frac{2\epsilon_r\epsilon_0\zeta}{3\eta} f(a/\lambda_D) \quad (6.1)$$

where η is the viscosity of the external solution, ϵ_r and ϵ_0 are respectively the permittivities of the solution and of the vacuum, a the particle radius and λ_D the Debye length. The Henry function $f(a/\lambda_D)$ depends on the particle shape and ranges for a sphere from 1 (Huckel limit: $a/\lambda_D \ll 1$) to 3/2 (Smoluchowski limit: $a/\lambda_D \gg 1$) [Hunter, 1981]. LUVs being considered as spherical particles with an electrical double layer smaller than their radius in our experimental conditions, the relation 6.1 then becomes the Smoluchowski relationship:

$$U_e = \frac{\epsilon\epsilon_0\zeta}{\eta} \quad (6.2)$$

Experimentally, the ζ -potential is calculated from the liposome mobility measured from an electrophoretic light scattering (ELS) experiment made with a voltage applied of 40 V. Values of ζ -potential are averaged over fifteen repeated measurements and given with an accuracy of ± 2 mV. This technique detects only vesicles with diameters lower than 10 μm .

For each ζ -potential measurement, the following protocol is repeated: a given volume of solution (HCl, NaOH, NaCl or polyelectrolyte) is added to the liposome suspension; after homogenization by stirring and 30 minutes at rest, we inject 1 mL of this mixture in the Zetasizer Nano Cell and the ζ -potential is measured. After each measurement the whole solution is collected from the cell and reintroduced into the bulk solution (to keep a nearly constant volume of solution) before the addition of the next volume of solution. Those steps are repeated as many times as necessary.

6.6.3 Isothermal titration calorimetry (ITC)

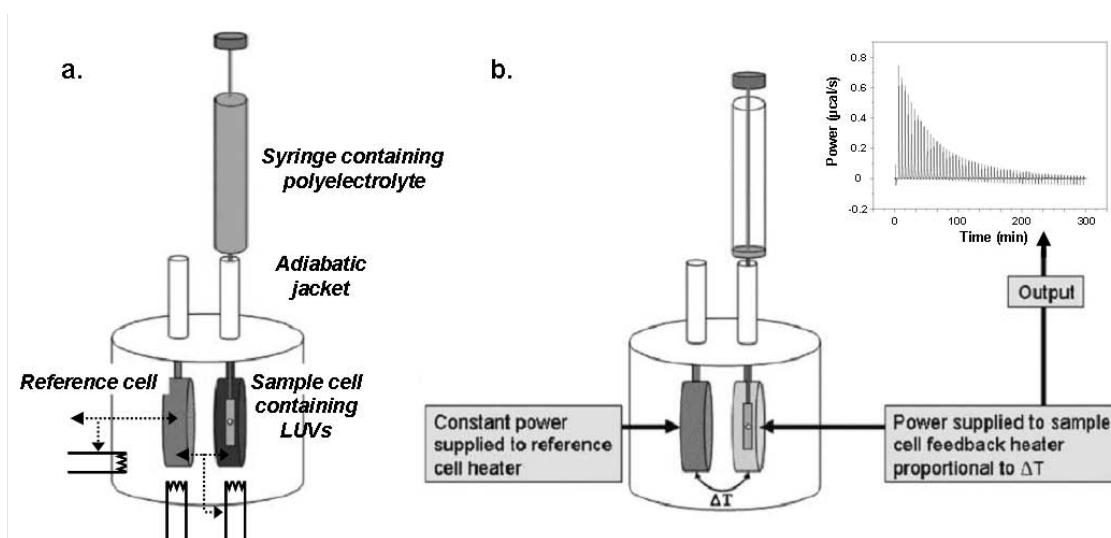


Figure 6.6: Schematic representation of an Isothermal Titration Calorimeter. (a) Both working and reference cells are kept at the same temperature via a differential electrical feedback system (dotted lines) in an adiabatic environment. (b) When an injection is made, the change in heat associated with binding (endothermic or exothermic) results in a change in temperature in the sample cell. A change in power (heat/s) is required to return the cells to identical temperatures (T) (i.e., $\Delta T = 0$). This change in power is recorded as a series of injections is made as presented in the inset (adapted from [Ladbury, 2004]).

ITC is a quantitative technique allowing the measurement of the association constant (K), enthalpy changes (ΔH), and binding stoichiometry (n) of the molecule-molecule interaction in solution. The microcalorimeter is composed of two identical cells of same volume: a reference cell containing the solvent and a sample cell containing the suspension of LUVs (Figure 6.6a), surrounded by an adiabatic jacket (no heat exchange). The polyelectrolyte solution is contained in a motorized syringe allowing precise injections (± 0.1 μL) in the sample cell. When interactions occur, a temperature difference appears between the two cells. The energy required

to equilibrate the two cells is measured. The amount of heat produced for each injection is calculated by integration of the area under each individual peaks by the instrument software, after taking into account the dilution (Figure 6.6b).

ITC measurements are realized at 20 °C using a Microcal VP-ITC titration microcalorimeter (Northampton, MA). LUVs suspension (0.2 mM lipid concentration in the LUV suspension) and chitosan (6.135 mM monomeric concentration) are prepared in 200 mM sucrose water solution at both pH (3.5 and 6.0). The measurement of adsorption enthalpy of chitosan on LUVs is performed in a cell containing 1.447 mL of the LUV suspension, by 60 injections of 5 μ L of the chitosan solution at a constant 300 rpm stirring rate. Each injection is performed over a period of 3 seconds. The heat is measured for up to 300 seconds before the subsequent injection takes place.

6.7 Experimental methods for GUVs characterization

6.7.1 Optical microscopy observations and image analysis

Optical microscopy techniques

Different techniques are used for this study:

- **Phase-contrast microscopy** transforms refractive index differences in contrast differences. Hence, vesicles filled with a sucrose solution and immersed in a glucose solution appears dark on a bright background (Figure 6.7a). One disadvantage of this technique is that the presence of a bright halo around the interfaces may hinder the size measurements of the objects.
- **Fluorescence microscopy** consists in irradiating the sample with a desired and specific band of wavelengths, and observe light emitted by the fluorescent molecules. The interest of this technique is to allow the observation of the space and temporal distribution of marked molecule in the sample. A typical fluorescent microscopy observation of a vesicle's membrane is shown in Figure 6.7b. Nevertheless, with this technique, the whole sample is excited, the resulting fluorescence does not only come from the focal plane: a parasite background signal is also observed.
- **Laser scanning confocal microscopy** is a fluorescence technique which, contrary to classical Fluorescence microscopy, consists in a punctual illumination and by a detection through a pinhole in an optically conjugate plane in front of the detector to eliminate out-of-focus parasite signal. As only light punctually produced by fluorescence very close to the focal plane can be detected, the image resolution, particularly in the sample depth direction, is much better than that of widefield microscopes. However as much of the light from sample fluorescence is blocked at the pinhole this increased resolution is at the cost of decreased signal intensity so long exposures are often required. A typical confocal microscopy

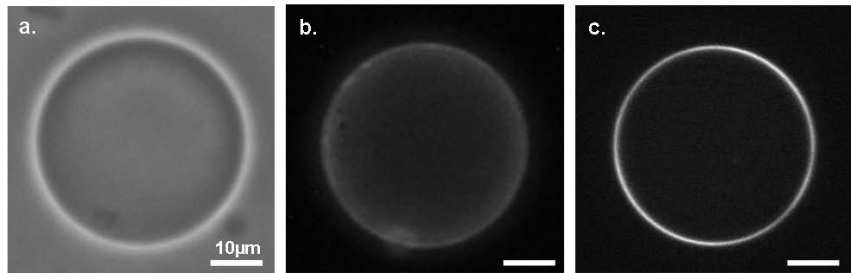


Figure 6.7: Observations of a vesicle in the equatorial section by different optical microscopy techniques: (a) phase contrast, (b) fluorescence and (c) confocal microscopy.

observation of a vesicle is shown in Figure 6.7c. Confocal laser scanning microscopy is also a valuable tool to obtain high resolution images and allows three dimensional imaging.

Video and image analysis

Video: movies of the behavior of GUVs under stresses are recorded with two types of cameras depending on the time scale of the observed events: for relatively “slow” events (vesicle deflation, extrusion of tether ...), a simple CCD camera allows us to obtain a real-time image (typically 25 fr.s^{-1}) while for faster events, such as objects flowing in a microfluidic device with typical velocities of the order of magnitude of a centimeter per second or fast-confocal imaging, the use of a high-speed camera able to recording with frame rates up to 10000 fr.s^{-1} is required.

Image analysis: once recorded and digitized, all the images are treated using different analysis softwares. The most commonly used software are Image J and Matlab (MathWorks).

Quantitative measurement of fluorescence

Two different quantitative methods are used to measured the fluorescence quantity emitted either by a global vesicle or by a point of the membrane:

1. **Global fluorescence emitted by a vesicle:** we measure the total amount of fluorescence emitted by a vesicle as proposed by [Mertins et al., 2009]: on a picture of fluorescence, we define a square with a length L so that the vesicle is inscribed inside, as shown in the Figure 6.8a.

We evaluate the vesicle mean intensity I_{mean} in this square as:

$$I_{mean} = \frac{1}{L^2} \sum_{i=1}^L \sum_{j=1}^L I_{ij} \quad (6.3)$$

where I_{ij} is the intensity of the pixel of coordinates (i,j) . We also measure the average intensity of the background (i.e. outside the vesicle) $I_{background}$, this intensity is considered as a constant in any point of the image. Finally the quantity of fluorescence F emitted by the vesicle is defined

as:

$$F = (I_{mean} - I_{background})L^2 \quad (6.4)$$

where $I_{background} L^2$ is the correction term corresponding to the background fluorescence.

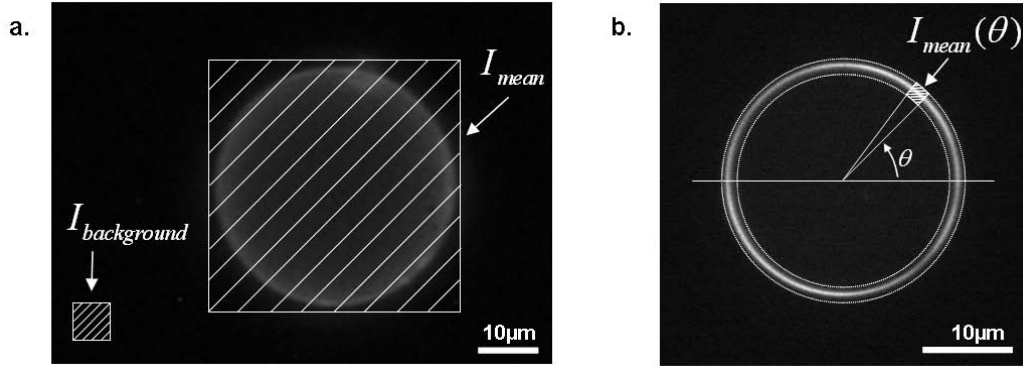


Figure 6.8: Principle of the fluorescence measurements. (a) the total fluorescence emitted by a vesicle and (b) fluorescence emitted by a point of the membrane.

2. Measurements of the fluorescence emitted by a point of the membrane: we also perform confocal fluorescence measurements along the membrane contour to detect the presence of eventual heterogeneities in the membrane. In this case, images are analyzed with the ImageJ plug-in “Azimuthal Average”. We apply a recent published procedure [Carvalho et al., 2008, Campillo et al., 2009]: the profiles along the membrane contour (i.e. for 360°) are obtained by measuring over a 10 pixels wide ring-shaped region around the membrane (Figure 6.8b).

We deduce the mean fluorescence intensity along the GUV membrane contour (I_{mean}) and its standard deviation (σ) for each GUV. In order to compare the different GUVs, we calculate the ratio σ/I_{mean} , which represents the heterogeneity of the membrane, over several GUVs. The lower the ratio σ / I_{mean} , the more homogeneous is the composite membrane. The azimuthal fluorescence intensity is corrected for a \sin^2 and \cos^2 angular modulation, which originates from the polarization of the laser [Carvalho et al., 2008, Sandre, 2000, Haluska et al., 2008].

6.7.2 ζ -potential measurements

Zeta potential measurements are made on GUVs of size lower than $10 \mu m$ following the protocol previously described for LUVs.

6.7.3 Atomic Force Microscopy (AFM)

In order to investigate the deformability of polyelectrolyte coated vesicles, we use an Atomic Force Microscope (Molecular-Force Probe (MFP) 3D AFM (Asylum Co, Santa Barbara, USA)) mounted on an inverted optical microscope. The cantilever (CSC 38, Micromash, Estonia) spring constant k is measured before each experiments via the thermal noise method

[Hutter and Bechhoefer, 1993]. The glass sphere (radius = $30 \pm 1 \mu\text{m}$) is glued (UHU Plus endfest 300) [Ducker et al., 1991] on the cantilever and is centered above the GUVs with an accuracy of $\pm 0.5 \mu\text{m}$, using the optical fluorescence observations. A schematic of the experiment is presented in Figure 6.9.

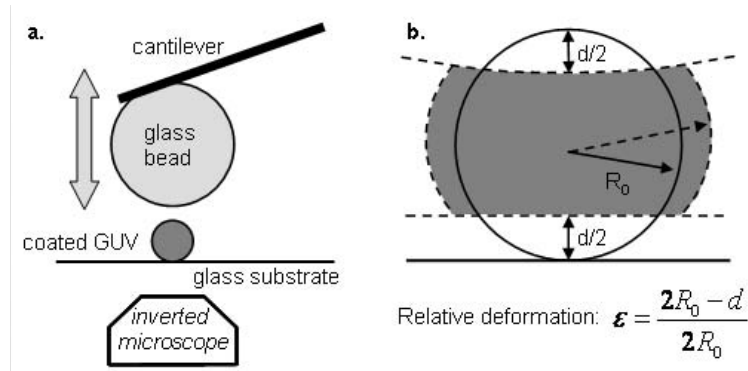


Figure 6.9: (a) A schematic sketch of a colloidal probe AFM setup used for the giant vesicle compression. The GUV is immobilized on a flat substrate and is compressed by a large colloidal particle (the particle diameter is large as compared to the vesicle), which is glued to an AFM-cantilever. The cantilever is integrated into the AFM setup. The optical microscope below allows high-resolution imaging of the contact zone. (b) Deformation of the coated vesicle under compression (dotted lines).

Deformation is measured as a function of the load applied and in the same time, the GUV is observed by fluorescence microscopy. The force is determined from the cantilever deflection δ via $F = k\delta$. The relative deformation ϵ is defined as $\epsilon = (2R_0 - d) / 2R_0$ (Figure 6.9b), where R_0 is the radius of the non-deformed vesicle determined optically and d is indentation defined as the difference between the imposed displacement of the cantilever and its deflection.

6.7.4 Microfluidic

Fabrication of microfluidic channel

Microfluidic devices are made in Poly(Dimethylsiloxane)(PDMS) with the techniques of soft lithography and replica molding [Macdonald et al., 2000]. PDMS present many advantages as to be optically transparent, malleable and to be sealed easily and irreversibly to itself or to glass substrates after an exposition to plasma treatment.

To obtain microfluidic channel, we first draw the geometry of interest with a computer-aided design software (Clewin) and print the design on a transparency by a high-resolution commercial image setter. This transparency serves as the photomask for the photolithography process: it is placed on a silicon wafer beforehand spin-coated with a thin layer (between 6 and $200 \mu\text{m}$) of photoresist polymer (SU-8) and exposed to UV light (Figure 6.10a). The design formed of cross-linked SU-8 is then developed to form the positive mold: channels of interest appear as ridge. The liquid PDMS (Dow Corning) is poured into a petri dish over the positive mold (Figure 6.10b) and cured in an oven at 65°C for 1 hour. The replica is then peeled from the mold and access holes for the channels are punched out of the cured layer with a truncated 20G needle.

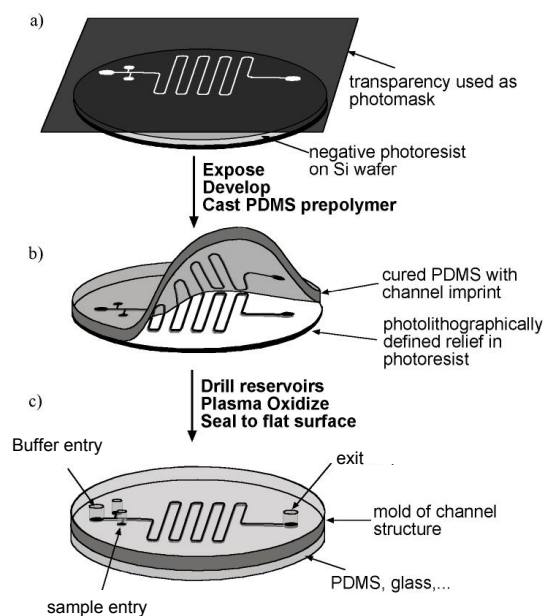


Figure 6.10: *Fabrication steps of a PDMS microfluidic device (www.gmwgroup.harvard.edu).*

The PDMS device can be next sealed irreversibly to a cover glass or to another blank piece of PDMS (Figure 6.10c) after activation by a plasma treatment during 90 seconds (Plasma cleaner PDC-32G, Harrick plasma).

Flow in a microfluidic channel

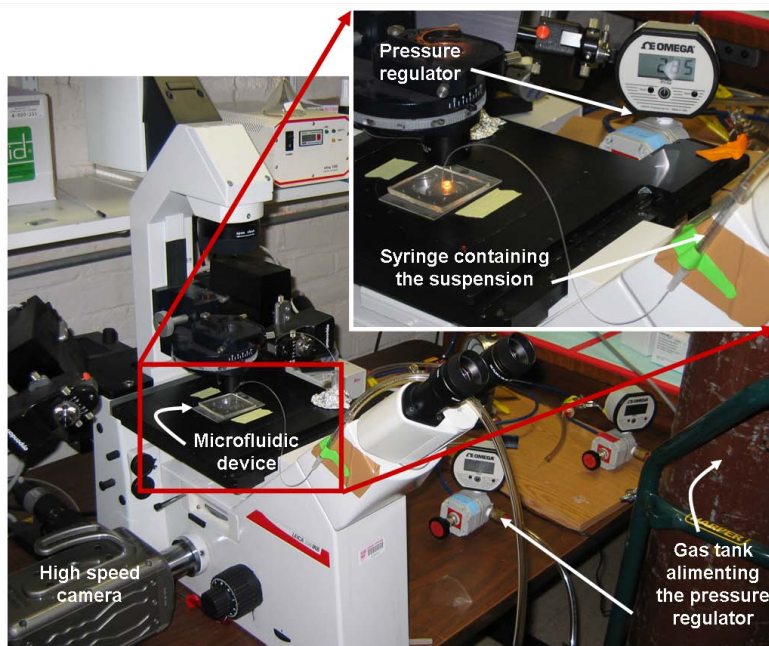


Figure 6.11: *The pressure-driven set-up shows a gas bottle providing the gas to a pressure regulator in order to push the fluid in the syringe [Favre, 2006].*

Several methods exist to generate a flow of fluid in the microfluidic devices such as a pressure gradient, a syringe pump or an electric field. In our experiments, the fluids are driven by static

pressure, producing a Poiseuille flow profile. The figure 6.11 shows the experimental set-up of a microfluidic system activated by the pressure. The suspension of objects is loaded in a syringe tube and connected to a compressed air tank through custom adapters. PE 20 tubes are used to connect the syringe needle to the input hole of the device. Pressure applied to the needle is controlled by a regulator (Bellofram Type 10) with a sensitivity of 5 mPsi and measured using test gauges (Wika) with a resolution of 150 mPsi

This method is distinct from flow-rate driven pumping since the use of specified pressures sets up the corresponding flow rates.

6.7.5 Hydrodynamic extrusion of membrane tethers

Extrusions of membrane tethers on chitosan-coated vesicles are realized with the setup previously developed in the group of F. Brochard-Wyart (Institut Curie, Paris). Micro-rods are made from glass capillaries using a horizontal laser pipette puller (P-2000, Sutter Instrument Co.) and by breaking off the tips with a micro forge at the desired diameter (1-5 μm). Tips are immersed in a 0.1 % w/v poly(L-lysine) solution (Sigma Diagnostic Inc.) for few minutes before use. Poly(L-lysine) is a positively charged polyelectrolyte and it is known that bare GUV membranes are slightly negatively charged. This allows the vesicle to stick to the rod through the electrostatic forces. Although chitosan-coated vesicles are positively charged, this protocol works which can be explained by the existence of nanometric “bare” domains on the coated membrane.

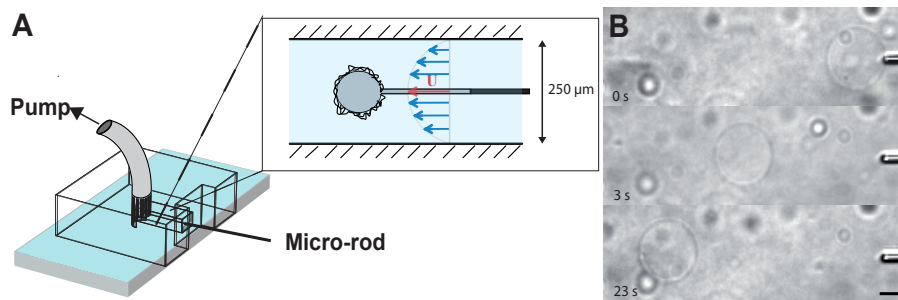


Figure 6.12: (a) *Experimental setup: chamber consisting in a micro-channel imprinted in PDMS stuck on a glass slide. Zoom: schematic representation of a vesicle anchored to a micro-rod inside the channel subjected to the flow.* (b) *Video micrographs of tube extrusion sequence from vesicle under a hydrodynamic flow. The tube is attached to the extremity of a poly(L-lysine)-coated glass micro-rod. The scale bar represents 15 μm .*

The flow chamber is made from a channel-shaped piece of PDMS sheet stuck on a clean glass cover slide. The channel (section $\sim 150 \times 10^3 \mu\text{m}^2$, length 1 cm) is filled with a 200 mM glucose solution ($\eta = 10^3 \text{ Pa}\cdot\text{s}$). The chitosan-coated vesicles are suspended in a reservoir connected to the end of the channel, where the micro-rod is introduced (Figure 6.12a). A vesicle is picked up with the tip of the poly(L-lysine)-coated micro-rod and brought in the channel. The micro-rod is placed in the center of the channel, to avoid wall effects and minimizes uncertainty on velocity in the Poiseuille flow inside the channel. The other end of the channel is connected to a syringe

that withdraws the liquid at a given velocity. In this geometry, the Poiseuille flow velocity ranges from 0 to few 1000 $\mu\text{m/s}$ and the Reynolds number is very small ($\text{Re} \ll 1$). A step of flow velocity U is applied (Figure 6.12b). When U reaches a threshold value U_{C_0} , the vesicle is stretched and a tube is extracted. Stepwise increases of flow velocity U can be applied.

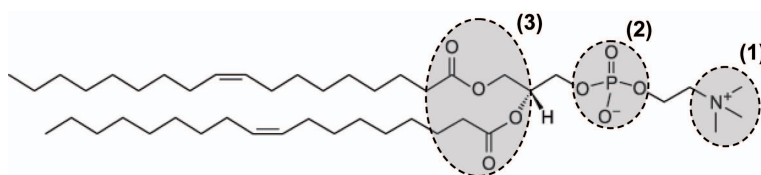


Figure 7.1: Structure of the 1,2-Dioleoyl-*sn*-glycero-3-phosphocholine (DOPC) with the following active sites: the polar head group with a positive quaternary amino group (1), a negative phosphate group (2), and two “carbonyl oxygen” groups (3), which connect hydrophilic head group and the two hydrophobic tails.

When pH of the LUV suspension solution is decreased by addition of HCl, the ζ -potential increases, and equals zero (isoelectric point, IEP) around $\text{pH} \sim 4.0$ in good agreement with [Petelska and Figaszewski, 2000]. Then the ζ -potential becomes positive and reaches finally a constant value of +16 mV at $\text{pH} \leq 3.0$. Actually, under pH decreases, the dissociation of the phosphate acid and carboxyl groups is repressed, and the positive contribution of the quaternary amino group is increased.

When the pH is increased by addition of NaOH, ζ -potential decreases from -23 mV at $\text{pH} = 6.0$, to a constant value of -32 mV for $\text{pH} \geq 7.5$. Then the ζ -potential decreases very slightly, reaching a kind of plateau. The slight reduction of the plateau value is interpreted in terms of the complete dissociation of the phosphate and carboxyl groups of the lipids (the quaternary amino group charge being unchanged whatever the pH).

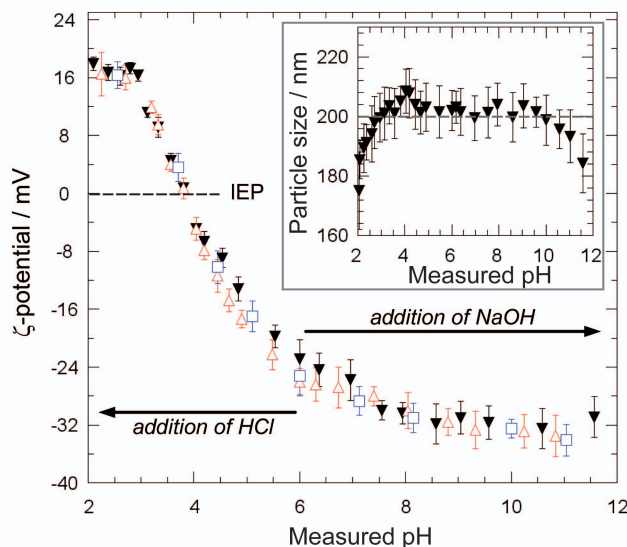


Figure 7.2: ζ -potential variation of bare DOPC LUVs as a function of pH, without fluorescent labeling (solid black triangles) or including fluorescent probes: 18:1 Liss Rhod PE lipids in a weight ratio 80:1 (open red triangles) or 18:1-12:0 NBD PC lipids in a weight ratio 50:1 (open blue squares). Isoelectric point (IEP) is obtained whatever the fluorescent labeling around $\text{pH} = 4.0$. Inset shows the particle size of DOPC LUVs upon pH variation.

We also demonstrate in Figure 7.2 that the ζ -potential variation is the same for fluorescein (18:1-12:0 NBD PC) or rhodamine (18:1 Liss Rhod PE) labeled lipids, whatever the pH, showing that the net charge of the zwitterionic DOPC membrane is not modify by the labelling. These

results are in agreement with previously published data [Portet et al., 2009].

In addition, inset of figure 7.2 shows that size of non-labeled bare vesicles remains constant in the accuracy limit between $2.5 < \text{pH} < 11.0$. For extreme pH values (out of this range), size decrease is attributed to osmotic deflation [Sabin et al., 2006].

In the following studies, the pH value will be adjusted either at $\text{pH} = 6.0$ or at $\text{pH} = 3.5$ to obtain respectively LUVs with negatively or positively charged zwitterionic membranes.

7.1.2 Salt effect

When NaCl concentration increases at fixed pH in the solution of the LUV suspension, Figure 7.3a shows that ζ -potential increases in presence of NaCl at $\text{pH} = 3.5$ and at $\text{pH} = 6.0$ from the initial value to a plateau reached for $[\text{NaCl}] \sim 6 \times 10^{-3} \text{ M}$, due to possible association with some counterion with polar heads [Sabin et al., 2006]. For both pH, the total variation of ζ -potential ($\Delta\zeta_{max}$) is around +20 mV.

The particle size variation upon NaCl addition, detailed in Figure 7.3b, confirms the interpretation given previously for pH modifications: the excess of concentration induces an osmotic deflation of the liposomes.

To sum up, salt and pH shocks studies:

- confirm that the charge density of DOPC zwitterionic membrane is strongly dependent on the pH and sensitive to salt concentration.
- show that bare DOPC LUVs suspension is stable in a broad range of pH, even at the isoelectric point (no aggregation occurs).
- confirm that a monovalent salt does not induce aggregation of DOPC LUVs in agreement with published results for PC lipids [Garcia-Manyes et al., 2005, Sabin et al., 2006].
- show that the fluorescent labeling of the DOPC membrane by 18:1-12:0 NBD PC or 18:1 Liss Rhod PE does not modify the ζ -potential value, indicating that the small amount of labeled lipids added does not affect the net charge of the zwitterionic membrane.

7.2 Effect of pH on the polyelectrolyte charge density

Potentiometric and conductimetric titrations realized previously on chitosan [Rinaudo et al., 1999b] and hyaluronan [Fouissac, 1992] allow us to determine their degree of ionization at $\text{pH} = 3.5$ and 6.0 . At $\text{pH} = 6.0$, hyaluronan is strongly negatively charged (100 % of the carboxyls groups are ionized) and chitosan is partially positively charged (40 % of the amino groups are protonated). At $\text{pH} = 3.5$, only 25 % of the hyaluronan carboxyls groups are ionized while in chitosan, 100 % of the amino groups are protonated.

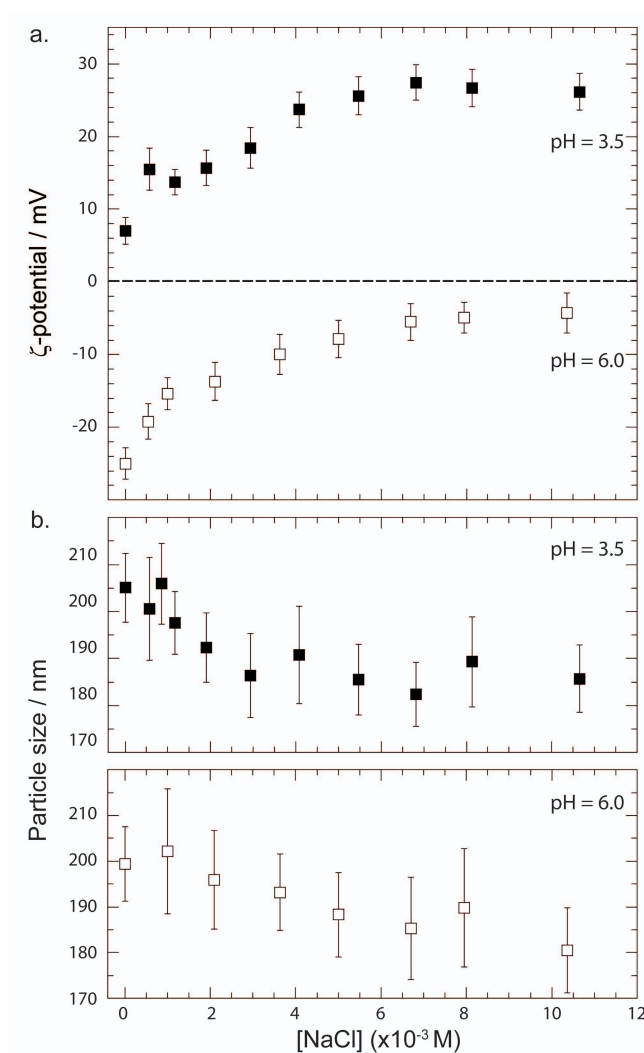


Figure 7.3: Variations of (a) ζ -potential and (b) particle size of DOPC LUVs as a function of NaCl concentration at pH = 6.0 (open squares) and pH = 3.5 (solid squares).

7.3 Conclusion

With the two pH situations (3.5 and 6.0), we can screen all the scenarios of relative membrane and polyelectrolyte charges as summed up in Table 7.1.

	Chitosan		Hyaluronan	
	pH = 3.5	pH = 6.0	pH = 3.5	pH = 6.0
Ionization of the polyelectrolyte (PE)	100 % NH_3^+	40 % NH_3^+	25 % COO^-	100 % COO^-
Net charge of the membrane	positive $\zeta = + 7 \text{ mV}$	negative $\zeta = - 23 \text{ mV}$	positive $\zeta = + 7 \text{ mV}$	negative $\zeta = - 23 \text{ mV}$
membrane/PE charges	+ / +	- / +	+ / -	- / -

Table 7.1: Effect of pH on the net charge of chitosan, hyaluronan and DOPC membrane. pH allows to screen all the situations combining positively or negatively charged membrane and polyelectrolyte.

Chapter 8

Characterization of the coating of DOPC lipid membranes by chitosan and hyaluronan

Ce chapitre est consacré à une caractérisation détaillée de l'adsorption du chitosane et de l'acide hyaluronique sur les membranes zwitterioniques de DOPC en utilisant diverses techniques expérimentales sur des LUVs (mesures de mobilités électrophorétiques, isotherme de titration calorimétrique) ou sur des GUVs (microscopies optiques). Après avoir démontré l'adsorption du chitosane et de l'acide hyaluronique sur les membranes de lipide, nous discutons l'origine de l'interaction, mesurerons le degré de couverture en fonction de la quantité de polymère ajouté en solution et caractériserons la conformation des polyélectrolytes sur la surface des membranes. Puis, nous prouvons que l'adsorption de polyélectrolyte affecte faiblement la structure de la membrane. En conclusion, nous étudions la stabilité de cette décoration lorsque la concentration en polymère en solution est diminuée par dilution et lors de chocs de pH; puis nous détaillons la formation des multicouches de polyélectrolyte sur les membranes de lipide.

○ ○ ○ ○ ○ ○ ○ ○ ○ ○

This chapter is devoted to an extensive characterization of the adsorption of chitosan and hyaluronan on zwitterionic DOPC membranes using various experimental techniques on LUVs (electrophoretic mobilities measurements, isothermal calorimetric titration or electron paramagnetic resonance observations) or GUVs (optical microscopy observations).

After demonstrating the adsorption of chitosan and hyaluronan on lipid membranes, we discuss the origin of the interaction, quantify the coverage degree as a function of the polymer added and characterize the polyelectrolyte conformation at the membrane surface. Then, we show that polyelectrolyte adsorption weakly affects the membrane structure. Finally, we study the stability of this coating under the dilution of the polymer concentration in solution and pH shocks, before coming to the formation of polyelectrolyte multilayers on lipid membranes.

8.1 Direct evidence of chitosan and hyaluronan adsorption on DOPC membranes

GUVs are incubated in solutions of chitosan or hyaluronan at $\text{pH} = 3.5$ and 6.0 and observed by confocal imaging. These two pH values are chosen in order to screen various scenarios of relative net charges of membrane and polyelectrolyte (see Table 7.1). Lipids and polyelectrolytes are labeled with different fluorescent probes, so that it is possible to visualize independently the lipid membrane and the polyelectrolyte coating of a same vesicle (see Figure 8.1).

As expected, polyelectrolytes adsorb on the oppositely charged membrane. More surprisingly, they also adsorb on lipid membrane of the same charge sign. In both cases, the whole surface of the vesicle looks homogeneously covered by polyelectrolytes without noticeable modification of GUVs shape or integrity of its lipid membrane. Only few heterogeneities are observed for chitosan coating (and not for the membrane) at $\text{pH} = 6.0$ which may be attributed to adsorption of chitosan aggregates formed in solution because of its low solubility at this pH .

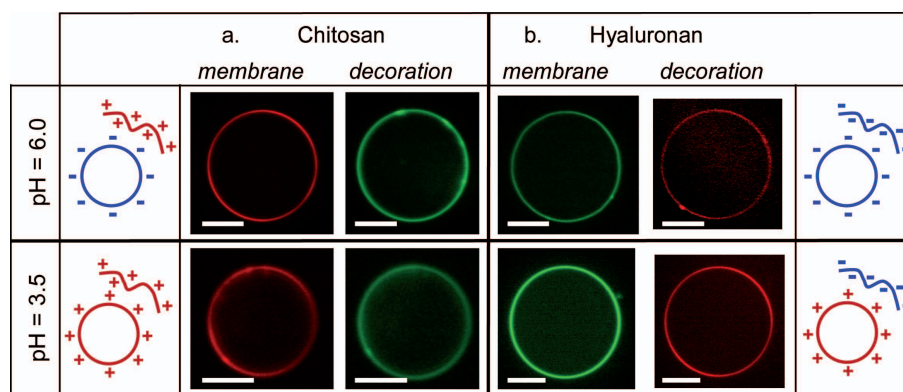


Figure 8.1: Fluorescence confocal observations of a chitosan ($M_w = 5 \times 10^5$, $DA = 0.20$) and a hyaluronan ($M_w = 6.63 \times 10^5$) coated GUVs incubated either at $\text{pH} = 3.5$ or at $\text{pH} = 6.0$. For the same GUV, we visualize successively the lipid membrane and the polyelectrolyte coating. The scale bars represent $10 \mu\text{m}$. For each pH , sketches showing the membrane and the polyelectrolyte charge signs are reminded (see Table 7.1).

A quantitative study of the azimuthal fluorescence profiles (see section 6.7.1) of the non-coated membrane (as reference) and of chitosan and hyaluronan coated GUVs at $\text{pH} = 3.5$ or 6.0 , averaged over twenty GUVs (Figure 8.2), confirms lipid membrane and polyelectrolyte coating homogeneity at the micrometric scale.

Direct comparison of coverage degrees is not possible from measurements of fluorescence intensities shown in Figure 8.1 because optical recording parameters are not constant (laser intensity, camera exposure time) but adjusted to obtain optimal contrast. Moreover, fluorescence efficiencies of fluorescein and rhodamine are pH -dependent [Haugland, 2005]. We will estimate the degree of coverage in section 8.4.

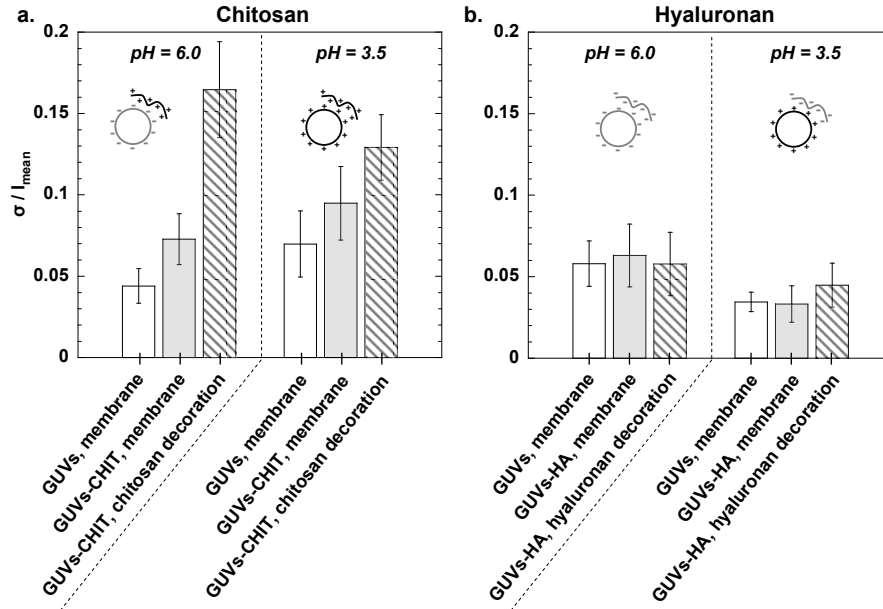


Figure 8.2: Analysis of the heterogeneities of vesicles coated with chitosan (*Chit-Fluo*) (a) or hyaluronan (*HA-Rhod*) (b) at $pH = 6.0$ and 3.5 . The ratio between the standard deviation of the signal of fluorescence and the average intensity (σ/I_{mean}) is given for each polyelectrolyte and each pH , for the membrane of vesicles before (white columns) and after coating (dimmed columns) and for the adsorbed layer of polyelectrolytes (hatched columns). Insets present cartoons of the respective charge signs of the membrane and polyelectrolytes as a function of the pH .

8.2 Characterization of the interactions between chitosan or hyaluronan and DOPC membranes

In order to determine the origin of interactions (electrostatic or/and hydrophobic) between chitosan, hyaluronan and DOPC membranes, we have observed the effect of various parameters on ζ -potential of LUVs upon addition of polyelectrolyte in their suspensions. We stress that free polymer chains, if alone in solution, are not revealed by ζ -potential measurements.

8.2.1 Electrostatic contribution

Starting with the assumption that this interactions are mainly of electrostatic origin, we have chosen to represent the added polyelectrolyte as the molar ratio of ionized groups (NH_3^+ and COO^- for chitosan and hyaluronan respectively), over accessible lipids of the outer lipid layer (lipid out). In the following, these molar ratio will be referred as R_{CHIT} and R_{HA} .

Effect of the respective membrane/polyelectrolyte net charges on ζ -potentials variation upon polyelectrolyte addition on LUVs suspensions

Four different cases of relative membrane and polyelectrolyte net charges are considered and imposed by pH , as previously presented in Figure 8.1.

Figure 8.3 presents at $pH = 3.5$ and 6.0 , the variations of the ζ -potential of LUVs observed in presence of chitosan and hyaluronan respectively, as a function of the added molar ratio R .

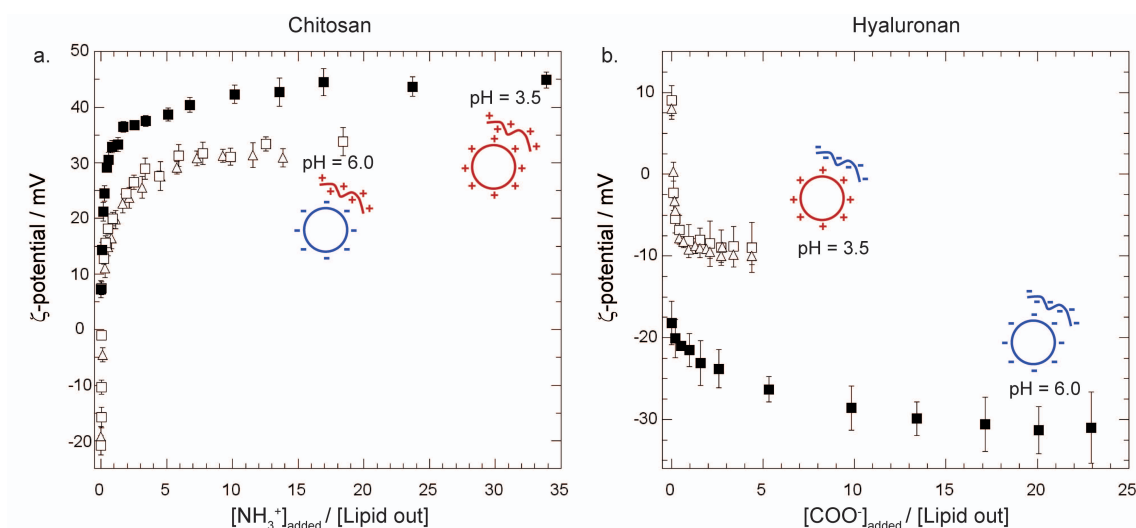


Figure 8.3: Variation of ζ -potential of the LUVs (DOPC + 18:1 Liss Rhod PE, 80/1 w/w) in presence of (a) chitosan or (b) hyaluronan as a function of the molar ratio of added polyelectrolyte ionized groups (NH_3^+ and COO^- for chitosan and hyaluronan respectively) over accessible lipids on the external leaflets of the membrane at pH = 3.5 and 6.0. Data are obtained with (a) chitosan ($M_w = 5 \times 10^5$, $DA = 0.20$) at pH = 3.5 (solid squares) and at pH = 6.0 (open squares) and chitosan labeled with fluorescein (Chit-Fluo, $M_w = 5 \times 10^5$) at pH = 6.0 (open triangles), and (b) hyaluronan ($M_w = 6.63 \times 10^5$) at pH = 3.5 (open squares) and at pH = 6.0 (solid squares) and hyaluronan labeled with rhodamine (HA-Rhod, $M_w = 6.63 \times 10^5$) at pH = 3.5 (open triangles). Solid or open signs are used when the charge signs of the membrane and polyelectrolytes are respectively the same or opposite, as detailed in the sketches for each pH.

Data obtained with native polyelectrolytes and fluorescent labeled ones (used for the confocal microscopy observations) are compared for both chitosan and hyaluronan.

Upon addition of polyelectrolyte in the LUVs suspension, ζ -potential evolutions present the same general trend: a sharp linear variation at for low polymer addition, then a smooth evolution before reaching a constant value in large excess of polymers.

For chitosan (Figure 8.3a), ζ -potential varies from -21 mV to +34 mV at pH = 6.0 and from +7 mV to +45 mV at pH = 3.5; the plateau values being obtained for a molar ratio $[\text{NH}_3^+]/[\text{lipid out}] \sim 5$ at pH = 6.0 and 10 at pH = 3.5. For hyaluronan (Figure 8.3b), ζ -potential varies from -18 mV to -31 mV at pH = 6.0 and from +8 mV to -10 mV at pH = 3.5. The plateau values are reached for a molar ratio $[\text{COO}^-]/[\text{Lipid out}] \sim 15$ at pH = 6.0 and 0.6 at pH = 3.5.

In these 4 cases, ζ -potential measurements are reproducible and are not modified when the concentration of the added polyelectrolyte solution ranges between 0.01 and 0.1 mg/mL, at a given molar ratio.

Moreover, we do not observe any change in ζ -potential variation when chitosan and hyaluronan are labeled with fluorescent groups (section 6.2.1).

The following conclusions can be drawn from these experiments:

- Chitosan or hyaluronan interact with the membrane, whatever their respective charge signs: a large variation of ζ -potential is observed in the various cases (we stress that experiments

8.2. CHARACTERIZATION OF THE INTERACTIONS BETWEEN CHITOSAN OR HYALURONAN AND

being performed at fixed pH and salt concentration, this variation can only be attributed to the adsorption of polyelectrolytes).

- The presence of the ζ -potential plateau suggests a limit of polyelectrolyte adsorption on the membrane. This behavior reflects the overcharging effect with formation of an electrostatic barrier limiting further adsorption
- For polyelectrolyte and lipid membrane of opposite net charges, polyelectrolyte adsorption induces charge inversion of the polyelectrolyte-coated liposomes. We will discuss this point in the section 8.3.
- The difference in molar ratio to reach the ζ -potential plateau value for chitosan and hyaluronan depends of their respective charge with regard that of the membrane.

Effect of the respective membrane/polyelectrolyte net charges on the interaction enthalpy of LUVs upon polyelectrolyte addition

Calorimetric titration experiments are performed at pH = 3.5 and 6.0 in order to further study the interaction between DOPC lipid membrane and chitosan ($M_w = 2.25 \times 10^5$, $DA = 0.05$). Figure 8.4 presents the variation of enthalpy $\Delta H_{NH_3^+}$ expressed in kcal per mole of injected NH_3^+ , as a function of R_{CHIT} at both pH values.

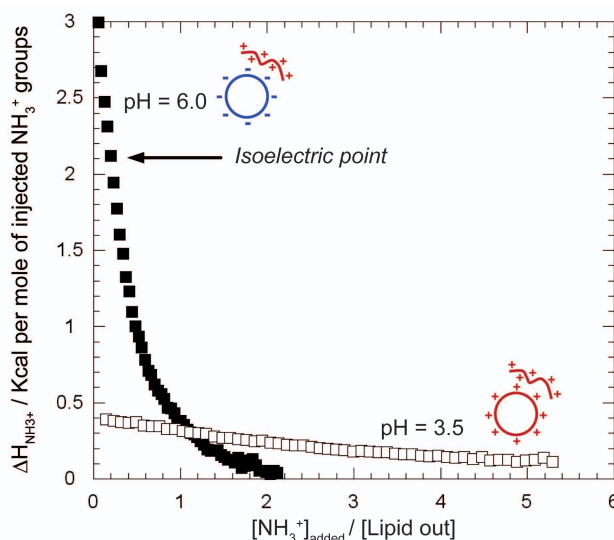


Figure 8.4: Influence of the membrane and chitosan net charges on the interaction energy upon polyelectrolyte adsorption. The evolution of the molar enthalpy is shown as a function of the molar ratio $[NH_3^+]/[lipid\ out]$ for $M_w = 2.25 \times 10^5$ at pH = 3.5 (open symbols) and pH = 6.0 (solid symbols).

At pH = 6.0, when oppositely charged chitosan and membrane interact, a large enthalpic effect occurs. Upon further additions, enthalpic variations decrease progressively and tend to very small values for $[NH_3^+]/[lipid\ out] > 2.2$, corresponding to the ζ -potential plateau when coated membrane and polyelectrolyte are both positively charge. This behavior reflects the overcharging effect with formation of the electrostatic barrier limiting further adsorption. We notice that

this value ($[\text{NH}_3^+]/[\text{lipid out}] \sim 2.2$) is much larger than 0.18 obtained at the isoelectric point.

At $\text{pH} = 3.5$, the enthalpic effect still exists indicating that interaction still occurs although both membrane and chitosan are initially positively charged. Nevertheless, it is dramatically lower than at $\text{pH} = 6.0$ and decreases very smoothly indicating that the limit of fixation should be obtained for much larger excess of chitosan as observed for ζ -potential measurements (Figure 8.3a). This shows that positive chitosan amino groups interact with negative groups present on the membrane even if a long range electrostatic repulsion exists between globally positive membrane and positive chitosan.

Role of ionic strength on polyelectrolyte/LUVs membrane interaction as observed by ζ -potential measurements

In order to confirm the electrostatic interaction between polyelectrolyte and zwitterionic membrane, ζ -potential measurements are performed with hyaluronan in the presence of 5 mM NaCl and compared with the results previously obtained in the absence of salt at $\text{pH} = 3.5$ and 6.0 (see Figure 8.3b).

Figure 8.5 shows that the presence of 5 mM NaCl modifies the ζ -potential variation upon polyelectrolyte addition in two different ways: either by delaying the plateau apparition for membrane and polyelectrolyte of opposite charge sign (Figure 8.5a) or by allowing to reach the plateau for lower amount of added polyelectrolyte, when membrane and polyelectrolyte exhibit the same charge sign (Figure 8.5b).

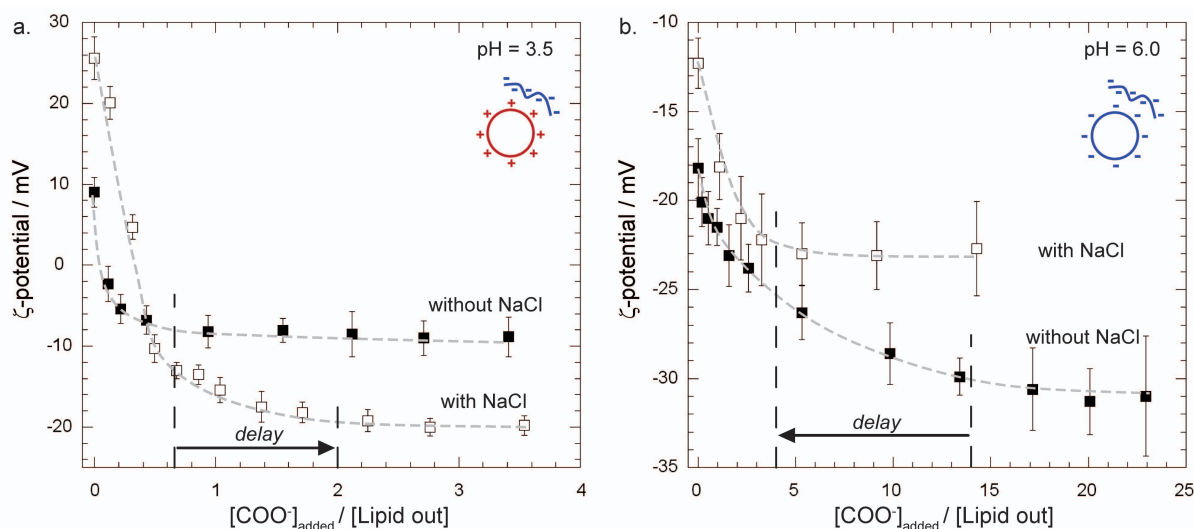


Figure 8.5: Variation of ζ -potential of LUVs (DOPC + 18:1 Liss Rhod PE, 80/1 w/w) at $\text{pH} = 3.5$ (a) and $\text{pH} = 6.0$ (b) upon addition of hyaluronan ($M_w = 6.63 \times 10^5$) expressed by the molar ratio $[\text{COO}^-]/[\text{lipid out}]$, in absence (solid squares) or in presence (open squares) of external salt (5 mM NaCl). Dotted lines are added to guide the eye and have no physical meaning.

We interpret these results in terms of screening effect : by decreasing the Debye-Hückel

8.2. CHARACTERIZATION OF THE INTERACTIONS BETWEEN CHITOSAN OR HYALURONAN AND

length, salt reduces the electrostatic interactions (both attractive and repulsive) between the polyelectrolyte and membrane, which favors polyelectrolyte adsorption on membranes of same charge sign and delays adsorption on oppositely charged membranes. This behavior is also verified with chitosan in presence of 5 mM NaCl at pH = 3.5, as reported later in Figure 8.10. These results further confirm the electrostatic origin of the chitosan- or hyaluronan-zwitterionic DOPC membrane interaction.

We now address the question of the existence of hydrophobic interaction. Actually, polysaccharides exhibit a hydrophobic character due to the -CH groups present on the glucose cycle [Mazeau and Vergelati, 2002]. In particular, fluorescence spectroscopy measurements with pyrene (a small hydrophobic molecule) have revealed the formation of intermolecular aggregates in chitosan solution involving the appearance of hydrophobic domains able to solubilize pyrene molecules [Philippova et al., 2001]. We now try to reveal eventual hydrophobic contributions on the chitosan and hyaluronan adsorption on DOPC membrane.

8.2.2 Hydrophobic contribution

The hydrophobic part inherent to both polysaccharide itself being difficult to probe experimentally, our approach consists in chemically modifying chitosan and hyaluronan chains by grafting alkyl chains of different length (6, 10 or 12 carbons), as detailed in section 6.2.1. Hence by making longer the hydrocarbon chain, the hydrophobic character of the modified polyelectrolytes is increased [Rinaudo et al., 2005].

We now study the role of the alkylation on the polyelectrolyte-lipid membrane interaction by focusing on chitosan ($M_w = 2.25 \times 10^5$, $DA = 0.05$). Same results were obtained for hyaluronan (HA-C10) at pH = 3.5 and 6.0 [Quemeneur et al., 2008].

Thereafter, difference between the measured ζ -potential and the ζ -potential value of the bare lipid membrane is considered ($\Delta\zeta$ -potential) in order to get independent from the initial state of the membrane and easily compare the different samples.

Effect of hydrophobic modification on the polyelectrolytes/LUV membrane interaction observed by ζ -potentials measurements

The effect of the alkyl chain length grafted on chitosan on the ζ -potential variation is first observed at pH = 3.5 (see Figure 8.6). Measurements are performed with the same protocol for the four different samples: homogenization after injection of the chitosan or Chit-Cn, incubation during 30 minutes before the first ζ -potential measurement. We remind that, at pH = 3.5 and for low ionic concentration, electrostatic repulsions between polycationic chains are stronger than the hydrophobic attraction between their alkylated grafted chains [Rinaudo et al., 2005].

Figure 8.6a presents the variations of the $\Delta\zeta$ -potential and particle size of LUVs upon progressive addition of unmodified chitosan ($M_w = 2.25 \times 10^5$, $DA = 0.05$) and modified chitosans

(Chit-C n ; alkyl chains: C6, C10 and C12) at pH = 3.5; they are expressed as a function of the molar ratio of chitosan repeat units over accessible lipids included in the external leaflet ($[\text{repeat units}]/[\text{lipid out}]$) in order to consider all saccharide units.

First of all, we observe that adsorption of unmodified chitosan or Chit-C12 induces a similar increase of the LUV diameter (\sim few nm), corresponding to the thickness of the polyelectrolyte layer. These results object to published results which claim that alkylation of chitosan induces a drastic increase of the LUVs size (\sim few tens of nm) due to the formation of multilamellar vesicle structure [Lee et al., 2006]. Therefore, the present comparison between unmodified and alkylated chitosan experiments is relevant to probe the polymer adsorption mechanism.

Secondly, whatever the polyelectrolyte (Chit or Chit-C n), ζ -potential variations display the same general trend: a sharp linear increase for the molar ratio $[\text{repeat units}]/[\text{lipid out}] < 3$, then a smooth variation before reaching a constant value equal to + 48 mV in each case for large excess of polyelectrolytes. Nevertheless, we observed that the plateau gets delayed as the alkyl chain gets longer.

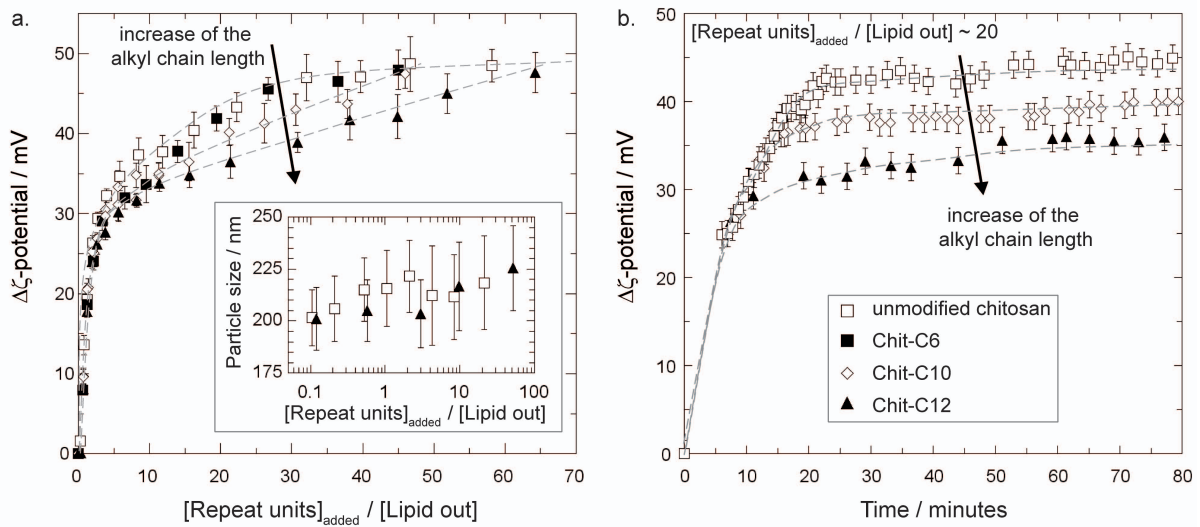


Figure 8.6: Influence of alkyl chain length on $\Delta\zeta$ -potential of LUVs (DOPC + 18:1 Liss Rhod PE, 80/1 w/w) at pH = 3.5 versus (a) the molar ratio $[\text{repeat units}]/[\text{lipid out}]$ and (b) time (prepared at fixed $[\text{repeat units}]/[\text{lipid out}] \sim 20$), for chitosan modified with different alkyl chain lengths: unmodified chitosan ($M_w = 2.25 \times 10^5$, $DA = 0.05$; open squares), Chit-C6 (solid squares), Chit-C10 (open diamonds), and Chit-C12 (solid triangles). Dotted lines are added to guide the eye and have no physical meaning. Inset in (a) shows the size evolution as a function of the added molar ratio for the unmodified chitosan and Chit-C12.

The following conclusions can be drawn:

- ζ -potential plateau value is independent of alkyl chain lengths grafted on chitosan which confirm that electrostatic interaction mechanism mainly governs the chitosan adsorption.
- A delay to reach the plateau is observed with alkylated chitosans and depends of the alkyl chain length, which can be interpreted in two ways:

8.2. CHARACTERIZATION OF THE INTERACTIONS BETWEEN CHITOSAN OR HYALURONAN AND

- (i) a competition between electrostatic polyelectrolyte adsorption on lipid bilayer and hydrophobic auto-association in solution (which depends on the alkyl chain length)
- (ii) a decrease of the polyelectrolyte diffusion rate due to the presence of alkyl chains, which induces that the points presented in Figure 8.6a, could be obtained out of equilibrium and thus irrelevant.

In order to discriminate between these two assumptions, we observe the variation of the ζ -potential as a function of time (see Figure 8.6b) of LUVs incubated with chitosans (unmodified, C10 and C12) at a ratio of [repeat units]/[lipid out] ~ 20 . After the chitosan injection, ζ -potential increases and reaches after 30 minutes the steady value previously shown in Figure 8.6a, for all the chitosans (either unmodified or alkylated). Taking into account, that all the experimental measurements, are performed after 30 minutes of incubation, we can conclude that all the data points reported in Figure 8.6a correspond to measurements performed at equilibrium. Consequently the competition between adsorption of the polyelectrolytes on the lipid membranes (i.e. mainly electrostatic interaction) and auto-association of the alkylated derivatives in solution (i.e. hydrophobic interaction) is responsible for the delay to reach the plateau in ζ -potential (Figure 8.7).

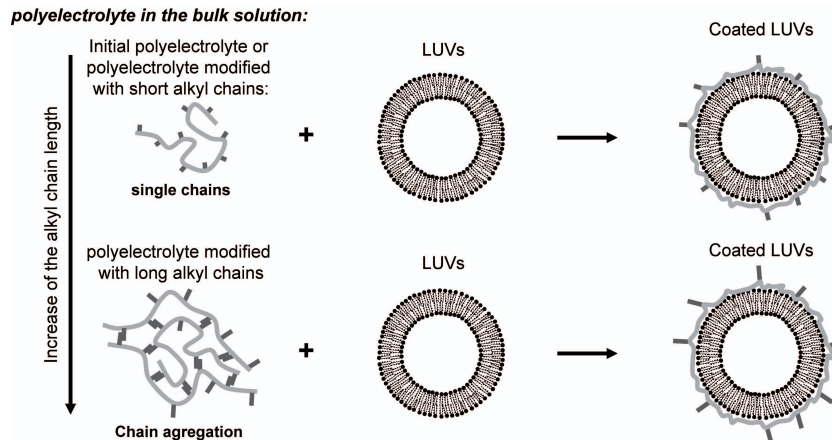


Figure 8.7: Schematic of the interaction of alkylated chitosan with LUVs

Such association between alkylated chitosan, depending on the alkyl chain length, was already reported in the literature [Rinaudo et al., 2005], evidencing that the longer the alkyl chains are, the more important the hydrophobic self-associations are in solution. Authors demonstrate that the polyelectrolyte self-association could be tuned either by addition of cyclodextrins (where inclusion of hydrophobic alkyl chains can occur) which suppresses a large part of the alkyl/alkyl associated domains or by a salt addition which favors hydrophobic association due to the screening of electrostatic interchain repulsions.

Taking these results into account, we now study the influence of cyclodextrin and salt additions to further confirm the role of alkylated chitosan auto-association on the observed ζ -potential evolution.

Influence of β -Cyclodextrins (β -CD) on the alkylated chitosan/lipid interaction observed by ζ -potentials measurements

The competitive effect between alkyl chains auto-association in solution and polyelectrolyte adsorption on the lipid membrane is first probed by reducing the hydrophobic auto-association using the alkyl chain inclusion into cyclodextrin cavities.

Cyclodextrins are cyclic oligosaccharides composed of a hydrophobic cavity able to complex hydrophobic substances and a hydrophilic outer character leading to their water solubility; they are commonly used to complex alkyl chains and surfactants [Eli et al., 1999] (see Figure 8.8). Used β -Cyclodextrins (β -CD) are kindly provided by Roquette (Lestrem, France).

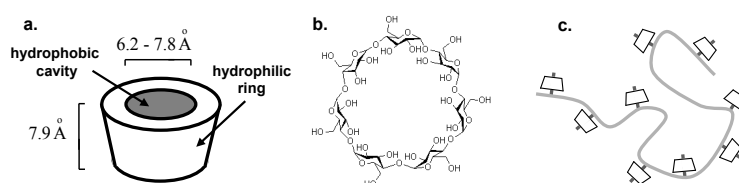


Figure 8.8: (a) Schematic and (b) chemical structure of β -Cyclodextrin. (c) Sketch of the complexation between the chitosan alkyl chains and the β -Cyclodextrin.

In Figure 8.9, we compare the variation of the ζ -potential of LUVs in presence of a solution of Chit-C12 containing stoichiometric amount of β -CDs with respect to alkyl chains, with those previously obtained for unmodified chitosan and Chit-C12 in absence of β -CDs (see Figure 8.6a).

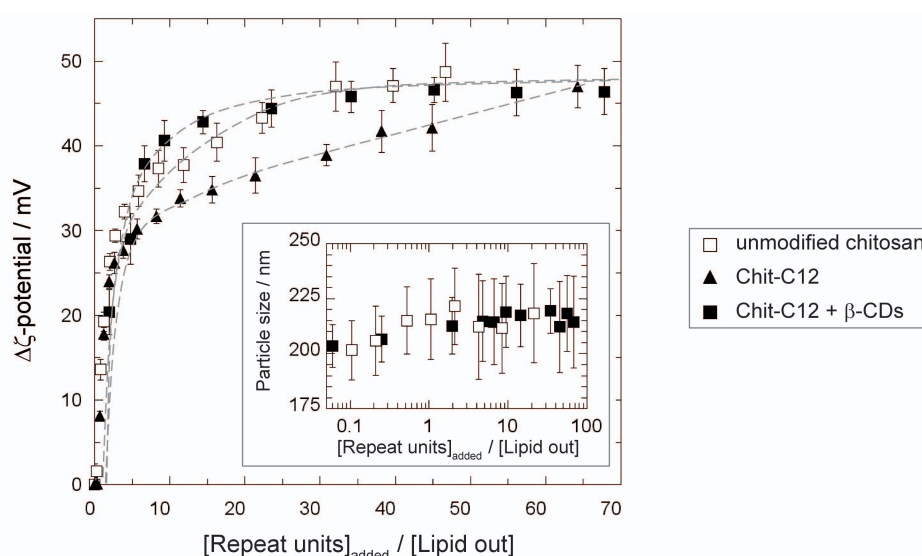


Figure 8.9: Normalized ζ -potentials of LUVs (DOPC + 18:1 Liss Rhod PE, 80/1 w/w) at $pH = 3.5$ as a function of the molar ratio $[\text{repeat unit}]/[\text{lipid out}]$ for different chitosan systems: unmodified chitosan ($M_w = 2.25 \times 10^5$; open squares), Chit-C12 (solid triangles), and Chit-C12 in presence of β -cyclodextrins (solid squares). Dotted lines are added to guide the eye and have no physical meaning. Inset shows the size evolution as a function of the added molar ratio for the unmodified chitosan and Chit-C12 in presence of β -cyclodextrins.

8.2. CHARACTERIZATION OF THE INTERACTIONS BETWEEN CHITOSAN OR HYALURONAN AND

These experiments reveal that:

- In this conditions, contrary to literature which reports that β -CDs extract lipids from the membrane which could result in its dissolution [Ohtani et al., 1989], LUVs are not dissolved by β -CDs associated to chitosan alkyl chains (see inset Figure 8.9), even for a large ratio corresponding to 0.5 β -CDs per accessible lipid head.
- The addition of β -CDs (i.e. the suppression of the alkyl/akyl association in solution) favors the alkylated-chitosan adsorption on the membrane surface, reducing the amount of added repeat units necessary to reach the plateau, as far as the quantity obtained for the unmodified chitosan.
- The same maximum amount of chitosan (related to $\Delta\zeta$, see section 7.4) is adsorbed on LUVs whatever the conditions (unmodified chitosan, Chit-C12 or Chit-C12/ β -CD).

These observations are in good agreement with our previous conclusion claiming that the main mechanism of interaction between chitosan and phospholipid bilayers is of electrostatic origin.

Influence of salts on the alkylated chitosan-lipid interaction observed by ζ -potentials measurements

The competitive effect between alkyl chains auto-association in solution and polyelectrolyte adsorption on the lipid membrane is now probed by studying the role of salt addition. Figure 8.10 shows the variation of the ζ -potential of liposomes as a function of the amount of added chitosans (unmodified and Chit-C12) in absence and in presence of 5 mM NaCl.

These results show that NaCl addition increases the delay before reaching the plateau value for the alkylated chitosan, which is interpreted in terms of charge repulsion decrease between chitosan chains in solution due to the salt charge screening. In good agreement with our previous assumption (i).

Both studies of β -cyclodextrin and salt addition on adsorption of chitosan and alkylated derivatives point out the influence of hydrophobic aggregation in solution and seem to exclude the hydrophobic anchoring of the alkylated chain in the investigated zwitterionic lipid bilayer at the considered polyelectrolyte concentration. These results are in agreement with the suggested conclusion of a published paper [Ercelen et al., 2006] in which the thermal transition of neutral membrane (DMPC, zwitterionic lipid) is reported to be unmodified upon alkylated chitosan interaction.

To sum up, these results

- confirm the interaction between chitosan or hyaluronan and zwitterionic DOPC membranes and highlight a stronger affinity in the case of opposite net charges.

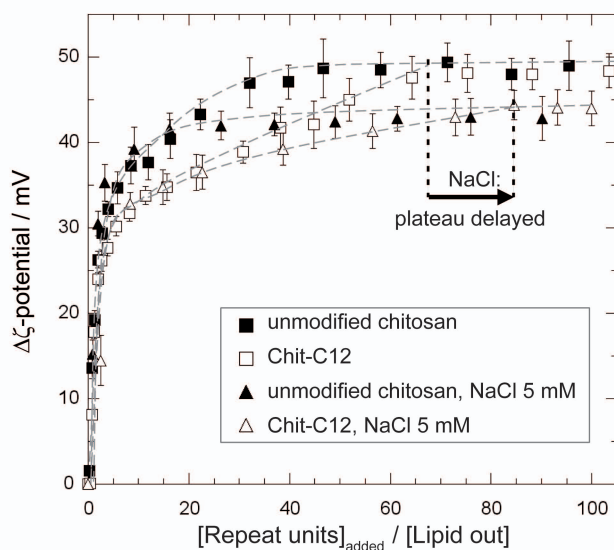


Figure 8.10: Normalized ζ -potentials of LUVs (DOPC + 18:1 Liss Rhod PE, 80/1 w/w) at pH = 3.5 as a function of the molar ratio [repeat unit]/[lipid out] for different chitosan systems: unmodified chitosan ($M_w = 2.25 \times 10^5$; solid squares), Chit-C12 (open squares) in absence of NaCl, unmodified chitosan ($M_w = 2.25 \times 10^5$; solid triangles), Chit-C12 (open triangles) in presence of NaCl 5 mM. Dotted lines are added to guide the eye and have no physical meaning.

- show that the presence of salt modifies this affinity, favoring the adsorption of polyelectrolytes on membranes of same charge or delaying the adsorption for oppositely charged membranes.
- reveal that alkylation of both polyelectrolytes does not change their maximum amount adsorbed on the liposomes which indicates that the hydrophobic contribution does not affect the interaction.

These three points highlight the **electrostatic origin** of the interactions between DOPC membranes and chitosan or hyaluronan. Nevertheless hydrogen-bonds and hydrophobic interactions can not be excluded during the adsorption process [Pavinatto et al., 2010]; in particular when membrane and polyelectrolyte exhibit the same charge sign.

Therefore, we now focus on the polyelectrolyte adsorption on lipid membrane of opposite charge sign.

At the isoelectrical point (IEP, ζ -potential = 0), since a charge inversion (or overcharging) is observed (see Figure 8.3), where repulsive forces between particles are repressed (see section 4.4); we now address the question of the suspension stability of coated vesicles as a function of the added polyelectrolyte.

8.3 Role of polyelectrolyte sorption on the suspension state of LUVs and GUVs

The variation of LUVs ζ -potential and size are observed as a function of progressive addition of chitosan on DOPC membrane at pH = 6.0 (Figure 8.11a). We observe that upon first addi-

8.3. ROLE OF POLYELECTROLYTE SORPTION ON THE SUSPENSION STATE OF LUVS AND GUVS10

tions of the positively charged chitosan, the negative net charge of the vesicle is progressively decreased and tends towards zero. The isoelectric point occurs at $[\text{NH}_3^+]/[\text{lipid out}] \sim 0.18$ and corresponds to the neutralization of the global negative charge of the lipidic vesicles.

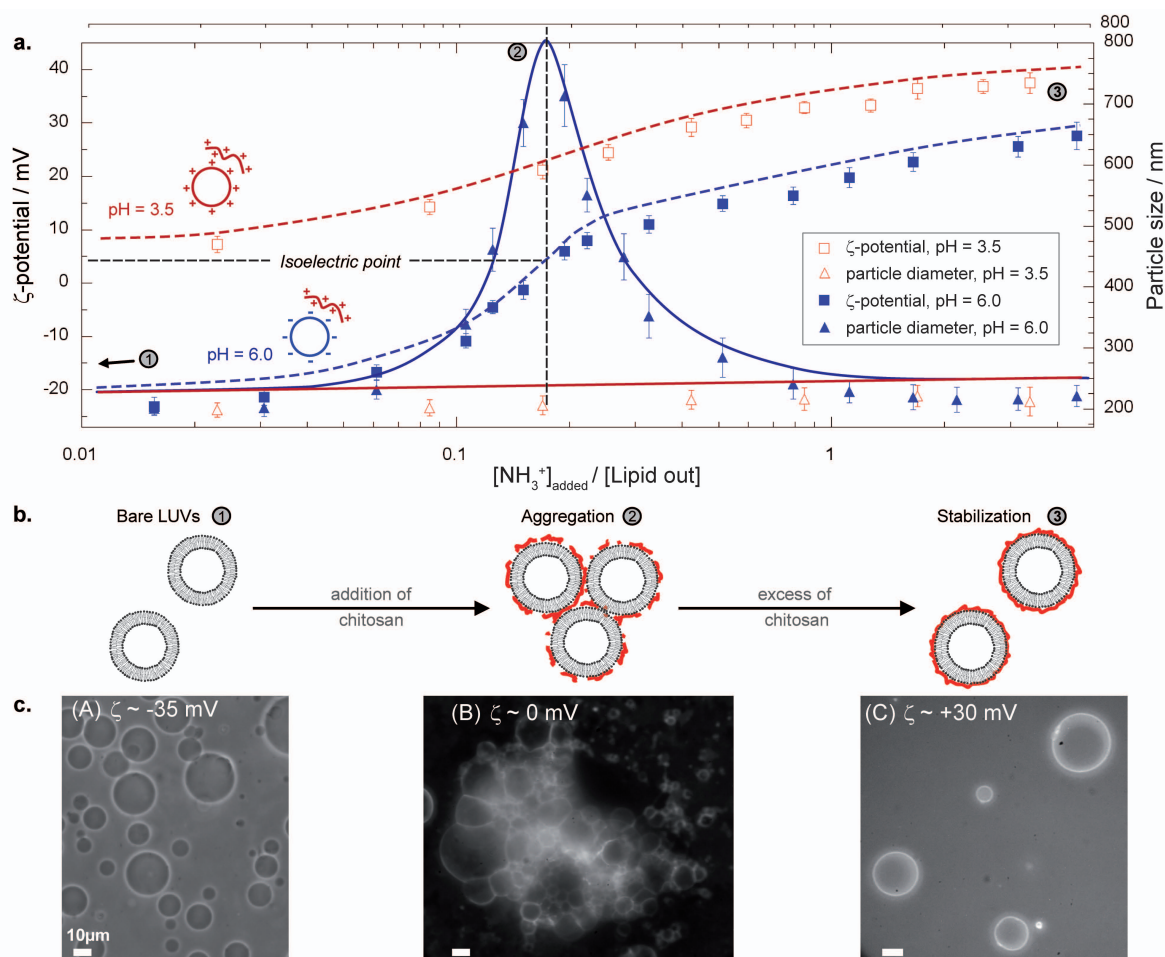


Figure 8.11: (a) Variation of the ζ -potential (squares) and the particle diameter (triangles) of LUVs upon addition of chitosan, expressed by the molar ratio $R = [\text{NH}_3^+]/[\text{lipid out}]$ at $\text{pH} = 6.0$ and $\text{pH} = 3.5$. Open or solid signs are used when the initial charge signs of the membrane and polyelectrolytes are respectively the same or opposite, as detailed in the sketches for each pH . Lines are added to guide the eye and have no physical meaning. (b) Schematic LUVs suspension structure for three different cases of chitosan addition: (1) isolated bare LUVS when no chitosan is added, (2) LUVS aggregation when chitosan addition corresponds to the isoelectric point of the LUVs (ζ -potential = 0) and (3) isolated chitosan-coated LUVs when chitosan addition corresponds to coating saturation. (c) Similar aggregation-dissociation process is highlighted by microscopy observations on DOPC GUVs incubated, at $\text{pH} = 6.0$, with chitosan at different molar ratios R : (A) $R = 0$ (bare GUVs, ζ -potential ~ -35 mV), (B) $R \sim 0.18$ equivalent to the isoelectric point, and (C) $R \sim 5$ (ζ -potential $\sim +30$ mV) corresponding to the maximum of coating. The scale bars represent 10 μm .

From light scattering data, it is clearly shown that a maximum in size of particles present in solution for the partially chitosan-coated vesicles is obtained at the isoelectric point. We observe finite aggregates (absent in the case of bare vesicles - see Figure 7.2 inset) with a maximum size around 800 nm (i.e. average diameter of aggregates/average diameter of vesicles

around 4) without any observed flocculation over few hours. Such aggregation phenomenon was previously reported for similar systems (DPPG/poly(L-lysine) [Volodkin et al., 2007] or DOTAP/polyacrylate [Cametti, 2008]).

Upon addition of excess of chitosan, we observe that adsorption still occurs but LUVs aggregates are progressively dissociated with charge inversion to finally obtain isolated positively charged LUVs exhibiting the same dimension than that of vesicles in the bare state. Further increasing the polyelectrolyte/particle ratio, the chitosan excess does not adsorb anymore on the LUVs and remains “freely” dissolved in solution, contributing to the overall ionic strength of the solution.

Similar LUVs aggregation-desaggregation processes have been observed with hyaluronan at $\text{pH} = 3.5$ (in both cases, membrane and polyelectrolyte have opposite charge sign). For hyaluronan, the maximum aggregates size obtained at the isoelectric point (for a ratio $[\text{COO}^-]/[\text{lipid out}] = 0.11$) is around 900 nm for $M_w = 6.63 \times 10^5$ (i.e. average diameter of aggregates/average diameter of vesicles around 4.5).

The aggregate dissociation is attributed to an overcharging of the vesicles upon further addition, causing electrostatic repulsion.

In our study, the concentration of polyelectrolyte at the adsorption plateau corresponds to the complete dissociation of aggregates allowing studying of isolated chitosan or hyaluronan-coated vesicles.

Schematic structures of the vesicle suspension for different polyelectrolyte additions are presented in Figure 8.11b:

- state (1) corresponds to initial isolated bare vesicles.
- state (2) to aggregated coated vesicles at the isoelectric point.
- state (3) to isolated highly coated vesicles.

This particles association-dissociation mechanism results from the equilibrium between long range repulsion and short range attraction, all of electrostatic nature in good agreement with a patch-like structure assumed for the coated membrane, as previously presented in section 4.4.

The same aggregation-desaggregation phenomenon were interestingly obtained for GUVs suspension upon addition of chitosan: Figure 8.11c shows the direct observation of bare GUVs (A), GUVs aggregation at isoelectric point (B) and isolated highly coated GUVs (C) (corresponding to the ζ -potential plateau), which result from aggregate dissociation. The interesting conclusion is that, in excess of chitosan, coated vesicles are isolated allowing to test their intrinsic physico-chemical properties in Chapter 9.

In order to limit the aggregation process and to easily prepare suspension of isolated coated vesicles, we also verify that ζ -potential and size measurements obtained for a molar ratio higher than 2 by a single addition or successive additions of polyelectrolyte solution are identical. Therefore, GUVs will be directly incubated at the desired concentration in a single step.

On the contrary and as expected when experiments are performed at $\text{pH} = 3.5$, where both bare vesicles and chitosan are positively charged, adsorption is demonstrated by ζ -potential variation but without any vesicle charge inversion nor vesicle aggregation upon addition of chitosan due to the increase of the net charge leading to stabilization of the suspension (see Figure 8.11a).

Finally, the possible influence of the vesicle size on polyelectrolyte sorption is investigated by studying the ζ -potential variation of LUVs (200 nm) and GUVs ($\sim 5 \mu\text{m}$) as a function of added chitosan ($M_w = 5 \times 10^5$, $DA = 0.2$) at $\text{pH} = 6.0$ (Figure 8.12). We remind that zetasizer only detects particles ranging between 5 nm to $10 \mu\text{m}$, and consequently no quantification of the GUV aggregation was obtained by this technique.

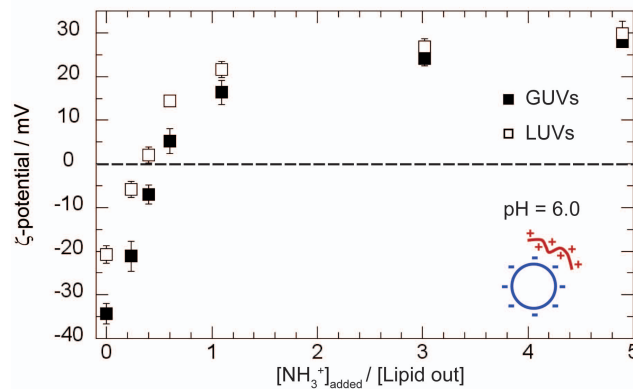


Figure 8.12: ζ -potentials variation at $\text{pH} = 6.0$ of LUVs (open squares) and GUVs (solid squares) as a function of the added chitosan amount ($M_w = 5 \times 10^5$, $DA = 0.20$) expressed by the added molar ratio $[\text{NH}_3^+]_{\text{added}} / [\text{lipid out}]$ (ionized chitosan amino groups over accessible lipids of the membrane).

For bare and slightly coated GUVs, the negative ζ -potential is larger than that of LUVs. Nevertheless, this results is not ascribed to an influence of vesicle size on polyelectrolyte sorption but interpreted in terms of GUVs deformation due to the electric field [Dimova et al., 2009]. Actually, because of their large size, GUVs are deformed to prolate-like shape with a lower friction than the spherical corresponding vesicles and then, they present a larger mobility for the same surface charge state. An interesting point is that for higher amount of added chitosan (roughly corresponding to the ζ -potential plateau), ζ -potential of LUVs and GUVs become similar which seems to indicate that, at maximum coating, deformation of coated GUVs decreases likely due to a membrane stiffness increase. This interpretation will be confirmed by the AFM experiments reported in section 9.4.

These results highlight that:

- Adsorption of chitosan or hyaluronan on oppositely charged vesicles induces successively

formation of aggregates upon low polymer coating, followed by aggregates dissociation and stabilization of isolated coated vesicles with comparable size to the bare ones, in excess of polyelectrolyte.

- The vesicles size (in a range from nm to μm) does not play any role on the adsorption and in particular on the maximum polyelectrolyte coating.
- Studies of polyelectrolyte-coated GUVs behaviors under various external stresses have to be realized on isolated objects with a high polyelectrolyte coating.

We finally remark that these finite-size liposome clusters open interesting perspectives for biotechnological applications, such as “multi-compartments” vectors obtained from the assembly of several different vesicles in a single cluster and which could be employed for simultaneous and independent multi-drug delivery at the same location as proposed by [Bordi et al., 2009].

8.4 Coverage degree determination

In this section, we focus on the adsorption of chitosan at $\text{pH} = 6.0$, and discuss the quantification of the adsorbed polyelectrolyte amount from ζ -potential measurements on LUVs and from fluorescence microscopy observations on GUVs.

8.4.1 From ζ -potential measurements on LUVs

Both polyelectrolyte and lipid exact concentrations in solution are required to establish the isotherm of adsorption. Since, lipid concentrations cannot be directly deduced from the amount of lipids involved in GUVs electroformation (see section 6.6.1), we determine by *in situ* fluorescence measurements, the amount of lipids involved in the membranes of LUVs and assume that no free lipids are present in solution.

For polyelectrolyte, it is necessary to determine both the concentration of free polymer in solution (C_{eq}) and the amount adsorbed on the membrane (Λ). We assume, as usually, that upon addition of very small amounts of polyelectrolyte into a vesicle suspension (with a membrane of opposite charge), the polyelectrolyte is fully adsorbed on the liposomes and that the variation of ζ -potential is related to the amount of ionized groups (i.e. NH_3^+ and COO^- for chitosan and hyaluronan respectively) fixed on the membrane. In a first approach, this allows the calculation of the amount of polyelectrolyte adsorbed taking into account the protonation degree (controlled by pH) and acetylation degree (DA) in the case of chitosan. The amount of chitosan adsorbed on the zwitterionic membrane is expressed in mass of polymer per unit surface of external membrane (assuming an area-per-lipid head of 0.725 nm^2) [Petrache et al., 2004].

Figure 8.13 shows the amount of chitosan ($M_w = 5 \times 10^5$, $\text{DA} = 0.20$) adsorbed at $\text{pH} = 6.0$ on the zwitterionic membrane, obtained from the ζ -potential measurements reported in Figure 8.3a; the molar ratio of repeat unit (one sugar unit for chitosan, see Figure 3.4) adsorbed per

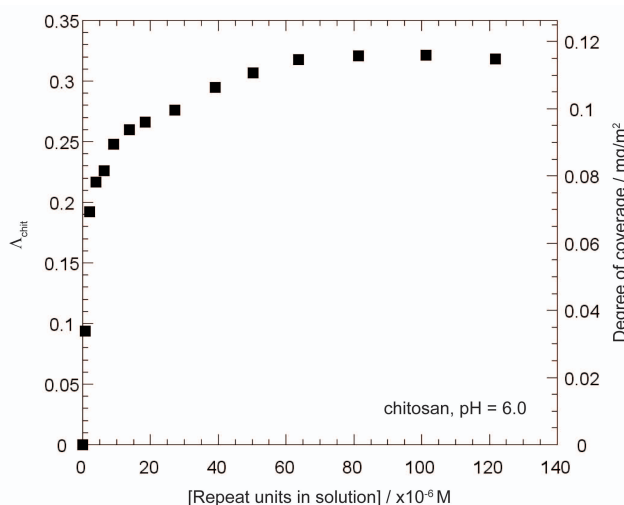


Figure 8.13: Amount of chitosan ($M_w = 5 \times 10^5$, $DA = 0.2$) adsorbed at $pH = 6.0$ on LUVs (DOPC + 18:1 Liss Rhod PE, 80/1 w/w) expressed as the molar ratio Λ_{chit} (repeat units adsorbed per lipid polar head in the external leaflet) versus the repeat unit concentration of free polyelectrolyte in solution at equilibrium ($\times 10^{-6}$ M). Grey line is added to guide the eye and have no physical meaning. The correspondence is imposed between the molar ratio Λ_{chit} and the degree of coverage. We notice that the isoelectric point corresponds to a coverage degree of 0.048 mg/m^2 .

accessible lipid (Λ_{chit}) and the degree of coverage are presented as a function of the repeat unit concentration of free polymer in solution, at equilibrium.

Hence, the maximum degree of coverage is evaluated to approximately 0.12 mg/m^2 for chitosan at $pH = 6.0$, according to typical values obtained for polymers adsorbed on attractive surfaces [Fleer et al., 1993].

8.4.2 From fluorescence measurements on GUVs

We now study the polyelectrolyte adsorption on GUVs by quantifying the fluorescence emitted by the coating via optical microscopy observations [Mertins et al., 2009]. These experiments, realized in the group of Carlos Marques (Institut Charles Sadron, Strasbourg), consist in measurements of the fluorescence intensity-per-unit surface (F/S) emitted by the chitosan coating on isolated GUVs, at different polymer concentrations.

GUVs are incubated at $pH = 6.0$ with a fluorescein-labeled chitosan ($M_w = 1.49 \times 10^5$, $DA = 0.15$ [Mertins et al., 2009]) at different concentrations and observed by fluorescence microscopy. Because the used fluorescence filter of the microscope does not allow discriminating the membrane and the polyelectrolyte fluorescent emissions (contrary to previous confocal microscopy observations, shown Figure 8.1), vesicles are prepared with unlabeled DOPC to observe only the chitosan coating.

The fluorescence intensity F emitted by the chitosan coating is evaluated over about forty isolated coated vesicles for each polymer concentration by the method described in the section 6.7.1 and plotted as a function of the measured vesicles area S . The Figure 8.14a illustrated these

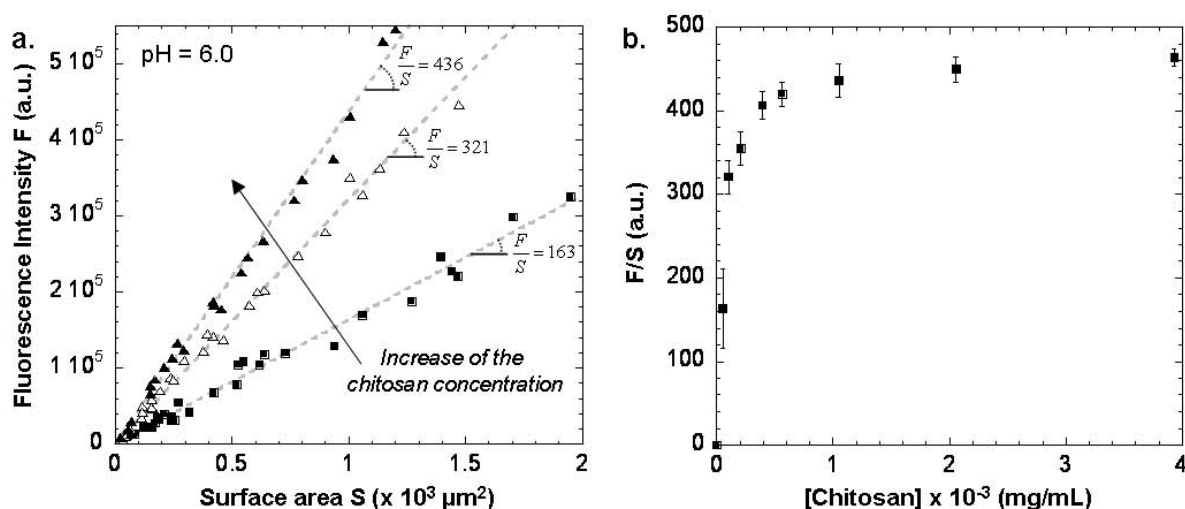


Figure 8.14: (a) Fluorescence intensity F as a function of the vesicle surface area S for three different chitosan concentrations used to incubate the GUVs: 5.3×10^{-5} (solid squares), 10.5×10^{-5} (open triangles) and 5.6×10^{-4} mg/mL (solid triangles). From further discussion, the estimation of F/S dependence at the isoelectric point is shown by the solid line. (b) Fluorescence intensity-per-unit surface F/S as a function of the total chitosan concentration added in the GUVs suspension. Error bars account for the different error sources due to background determination and accuracy of the intensity integration.

results with three different chitosan concentrations (one located around the isoelectric point and the other in larger concentration); a linear relationship between the fluorescence intensity F and the area S is observed at each polymer concentration, showing that chitosan is adsorbed at the membrane surface.

The fluorescence intensity-per-unit surface F/S is then plotted as a function of the amount of chitosan added to the GUV suspension (Figure 8.14b). The amount of polymer-per-unit bilayer surface (F/S) presents the classical trend previously observed in ζ -potential measurements: a sharp increase, and then a smooth variation before reaching a constant value for large excess of chitosan. Nevertheless these data cannot be directly transformed into an “adsorption isotherm” because the amount of adsorbed chitosan and the lipid exact concentration cannot be measured.

In order to relate F/S to a degree of coverage, we have assumed that the adsorption process of chitosan on DOPC membrane is the same for LUVs and GUVs at a given pH, the F/S plateau value ($472 \text{ a.u./}\mu\text{m}^2$) obtained for GUVs is then correlated to the maximum adsorbed amount of chitosan (0.12 mg/m^2) beforehand determined on LUVs (Figure 8.13). It allows to convert the fluorescence measurement on GUVs into degree of coverage as reported in Figure 8.15a.

This calibration makes possible to compare our results obtained for GUVs coated with chitosan by our method and other published results on GUVs electroformed directly from an inverse phase precursor containing a mixture of DOPC and chitosan developed in the group of C. Marques [Mertins et al., 2009]: starting from an inverse phase of droplets of aqueous chitosan solution dispersed in the majority organic solvent containing the lipids and then applied the classical electroformation protocol. In this way, the adsorbed chitosan is present on the internal

8.5 Variation of the coverage degree: comparison between chitosan and hyaluronan

In order to further characterize the interaction between zwitterionic DOPC membranes and chitosan or hyaluronan, we now study the variation of the maximum adsorbed polyelectrolyte amount as a function of various parameters: respective charge sign and molecular weight (Mw).

8.5.1 Role of the relative membrane/polyelectrolyte net charges

Figure 8.16a presents the coverage degrees deduced from ζ -potential measurements reported in Figure 8.3 as a function of the polyelectrolyte concentration free in the suspension for similar molecular weights (i.e. chitosan $M_w = 5 \times 10^5$ and hyaluronan $M_w = 6.63 \times 10^5$) at pH = 3.5 and 6.0.

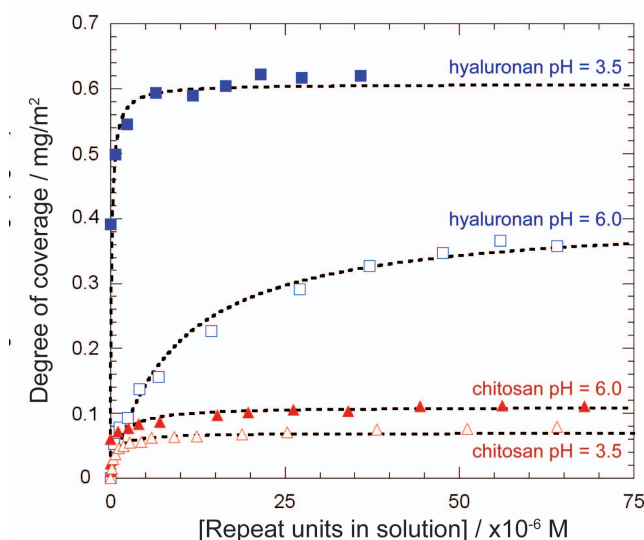


Figure 8.16: Degree of coverage for chitosan ($M_w = 5 \times 10^5$, $DA = 0.20$; triangles) and hyaluronan ($M_w = 6.63 \times 10^5$; squares) as function of the repeat unit concentration of polyelectrolyte free in solution at pH = 3.5 and 6.0. Open or solid signs are used when the charge signs of the membrane and polyelectrolytes are the same or opposite respectively. The dotted lines are added to guide the eye and have no physical meaning.

These data reveal that:

- The maximum coverage degree by both polyelectrolytes is obtained for very low polymer concentrations, showing the high affinity of chitosan or hyaluronan with DOPC membrane.
- The highest coverage degree is observed when both polyelectrolytes and membrane are oppositely charged.
- The degree of coverage is always larger for hyaluronan than for chitosan.

8.5. VARIATION OF THE COVERAGE DEGREE: COMPARISON BETWEEN CHITOSAN AND HYALURONAN

The maximum amount of sugar units adsorbed per lipid (Λ_{sat}) and the degree of coverage obtained for chitosan ($Mw = 5 \times 10^5$, $DA = 0.20$) and hyaluronan ($Mw = 6.63 \times 10^5$) at both pH are reported respectively in Tables 8.1 and 8.2.

8.5.2 Role of the polyelectrolyte molecular weight

Coverage degree of substrates by polymers may vary as a function of polymer structure and molecular weight depending on whether polymers adsorb flat or form trains and loops at external membrane surface [Fleer et al., 1993]. Previously, ζ -potential variation of DOPC vesicles upon chitosan and hyaluronan addition was interpreted in terms of amount of polyelectrolyte charges adsorbed and, consequently, in terms of degree of coverage. Therefore, in order to get information on the conformation of polyelectrolyte adsorbed on vesicles, we now study ζ -potential variation of liposomes as a function of chitosan and hyaluronan molecular weights.

Chitosan adsorption

Firstly, three chitosan samples of different molecular weights and acetylation degrees are used: $Mw = 5 \times 10^4$ ($DA = 0.04$), 2.25×10^5 ($DA = 0.05$), and 5×10^5 ($DA = 0.20$). Figure 8.17 presents, at $pH = 3.5$ and 6.0 respectively, the variation of the $\Delta\zeta$ -potential of liposomes observed in presence of the three chitosans as a function of the added polymer amount expressed by the molar ratio $[NH_3^+]_{added} / [lipid\ out]$ which accounts for acetylation degree.

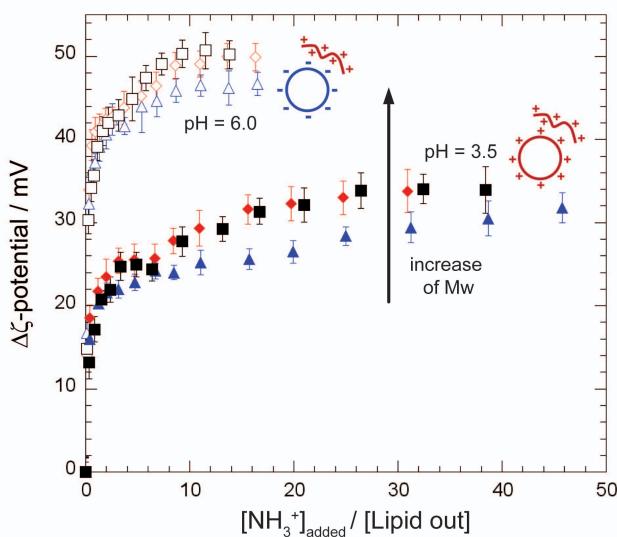


Figure 8.17: Influence of the chitosan molecular weight (Mw) on the variation of the ζ -potentials of LUVs at $pH = 3.5$ (solid symbols) and $pH = 6.0$ (open symbols). The evolution of the normalized ζ -potential is shown as a function of the added molar ratio $[NH_3^+]_{added} / [lipid\ out]$ (ionized chitosan amino groups over accessible lipids of the membrane) for 3 different Mw : 5×10^4 (triangles), 2.25×10^5 (diamonds), and 5×10^5 (square).

For all chitosan molecular weights, ζ -potential variation displays the same general trend as

previously observed. Figure 8.17 shows that, for both pH values (3.5 and 6.0), the maximum value of ζ -potential (i.e. $\Delta\zeta_{max}$) observed at the plateau only slightly varies with Mw : i.e. the total amount of ionized chitosan amino groups fixed on the lipid membrane, at a given pH, is nearly independent on the molecular weight.

At pH = 6.0 (negative membrane/positive polyelectrolyte), curves of ζ -potential variation as a function of added chitosan are superimposed for the three chitosans molecular weights; plateau values ($\Delta\zeta_{max} \sim +50$ mV) are obtained for the same ratio $[\text{NH}_3^+]/[\text{lipid out}] > 5$. These results are in good agreement with a flat adsorption of chitosans with a thickness of the adsorbed layer which does not displace significantly the shear plane.

At pH = 3.5 (positively charged membrane and polyelectrolyte), a larger amount of chitosan (highly soluble because fully protonated), which slightly depends on Mw, is necessary to get the plateau ($\Delta\zeta_{max} \sim +33$ mV): $[\text{NH}_3^+] / [\text{lipid out}] \sim 15$ for the higher molecular weights (Mw = 2.25×10^5 and 5×10^5) but $[\text{NH}_3^+]/[\text{lipid out}] \sim 45$ for Mw = 5×10^4 . These results may be interpreted in terms of looser interactions when polyelectrolyte and membrane have the same charge sign. In the case of the low molecular weight chitosan we suggest that it adsorbs flat on the surface due to its high charge density and its stiffness (contour length around 10 times L_p) while interacting with the negative charges on the membranes. Dealing with higher molecular weight chitosans, they stick on the surface as charged worm-like chains causing higher local charge density at the interface; then saturation occurs more rapidly.

From ζ -potential values, we get the maximum amount of adsorbed chitosan expressed as Λ_{sat} (maximum molar ratio of adsorbed chitosan monomeric units and lipid out) and the coverage degree (see section 8.4.1). Table 8.1 gives Λ_{sat} and coverage degrees determined for the different molecular weights at pH = 3.5 and 6.0. As expected, larger adsorption occurs at pH = 6.0 than at pH = 3.5 whatever the molecular weight.

pH	Mw (g/mol)	Λ_{sat} (± 0.01)	Coverage degree (mg/m ²)
3.5	5×10^4	0.20	0.07
	2.25×10^5	0.22	0.08
	5×10^5	0.22	0.08
6.0	5×10^4	0.30	0.11
	2.25×10^5	0.32	0.12
	5×10^5	0.32	0.12

Table 8.1: Influence of molecular weight and pH on maximum amount of adsorbed chitosan on DOPC vesicles expressed as Λ_{sat} (maximum molar ratio of chitosan monomeric units over lipid out) and related coverage degrees (see section 8.4.1).

Taking into account that fluorescent microscopy observations reveal a homogeneous coverage (Figures 8.1 and 8.2), chitosan-coated surface of the vesicle may be regarded as a homogeneous patch-like layer formed of domains of chitosan chains adsorbed flat on the interface. The surface

8.5. VARIATION OF THE COVERAGE DEGREE: COMPARISON BETWEEN CHITOSAN AND HYALURONAN

covered by these domains represents 10 % of virtual monolayer formed by side-by-side monomer compact coverage assuming chitosan monomeric occupies an area of 0.25 nm^2 .

Hyaluronan adsorption

Adsorption of five hyaluronan samples ($M_w = 1.14 \times 10^4$, 4.1×10^4 , 1.95×10^5 , 6.63×10^5 and $1.8 \times 10^6 \text{ g/mol}$) is only studied at $\text{pH} = 3.5$ where membrane and hyaluronan are oppositely charged; Figure 8.18 shows variations of normalized $\Delta\zeta$ -potential as function of the added amount of hyaluronan.

Contrary to chitosan results, the total variation of ζ -potential ($\Delta\zeta_{max}$) is strongly dependant on the molecular weight: higher the molecular weight, larger is the $\Delta\zeta_{max}$.

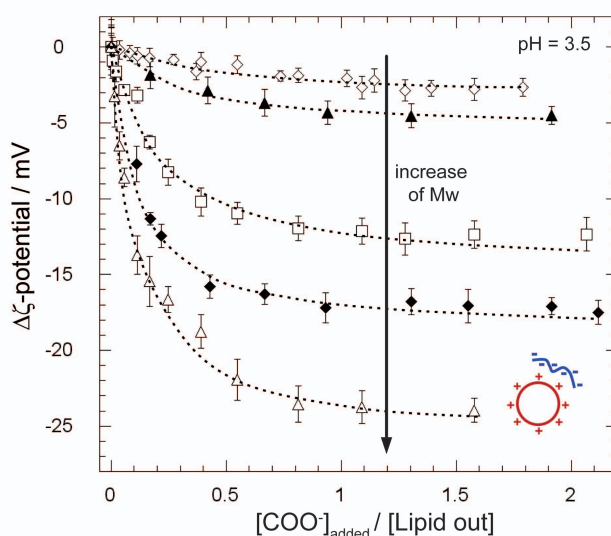


Figure 8.18: Influence of the hyaluronan molecular weight (M_w) on the variation of the ζ -potentials of LUVs DOPC + 18:1 Liss Rhod PE, 80/1 w/w) at $\text{pH} = 3.5$. The evolution of the normalized ζ -potential is shown as a function of the added molar ratio $[\text{COO}^-]_{\text{added}} / [\text{Lipid out}]$ for 5 different M_w : 1.14×10^4 (open diamonds), 4.1×10^4 (solid triangles), 1.95×10^5 (open squares), 6.63×10^5 (solid diamonds) and 1.8×10^6 (open triangles).

From ζ -potential values, we determine the maximum amount of adsorbed hyaluronan expressed as Λ_{sat} (maximum molar ratio of adsorbed hyaluronan repeat units over lipid out) and the coverage degree (see section 8.4.1). Table 8.2 gives Λ_{sat} and coverage degrees determined for the different molecular weight at $\text{pH} = 3.5$. The degree of coverage of hyaluronan is much larger than for chitosan and varies strongly with molecular weight at $\text{pH} = 3.5$.

Taking into account that fluorescent microscopy observations reveal a homogeneous coverage (Figures 8.1 and 8.2), and that the adsorption depends on M_w , the external surface of hyaluronan-coated vesicles may be regarded as a homogeneous distribution of coated domains composed of trains and loops with an average low density in polyelectrolyte monomeric units. Exception may occur for the lowest molecular weight which behaves as a stiff molecule with

pH	Mw (g/mol)	Λ_{sat} (± 0.04)	Coverage degree (mg/m ²)
3.5	1.14×10^4	0.12	0.11
	4.10×10^4	0.21	0.19
	1.95×10^5	0.51	0.47
	6.63×10^5	0.71	0.65
	1.80×10^6	0.97	0.90
6.0	6.63×10^5	0.41	0.36

Table 8.2: Influence of molecular weight at $pH = 3.5$ on maximum amount of adsorbed hyaluronan on DOPC vesicles expressed as Λ_{sat} (maximum molar ratio of hyaluronan repeat units and lipid out) and related coverage degrees (see section 8.4.1).

a contour length of 3 Lp. Actually, assuming a monolayer formed by side-by-side repeat unit compact coverage (0.5 nm^2 each disaccharide), the maximum degree of hyaluronan coverage should be equal to 1.34 mg/m^2 . Of course, such a model of repeat units stacking to form a dense monolayer is unrealistic; the degree of coverage given in Table 8.2 for the highest molecular weight (much larger in this case than for chitosan) is of the same order of magnitude than that expected from this unrealistic model. This further confirms the presence of hyaluronan loops and trains at the surface of vesicle. We are aware that loops formation may displace the shear plane and leads underestimation of ζ -potential values and then, of Λ_{sat} and the coverage degree [Varoqui, 1982].

Interpretation on the chitosan and hyaluronan conformation difference at the membrane surface

In order to explain this difference of conformation, we can first consider the chemical structure of both polyelectrolytes (see Figure 8.19).

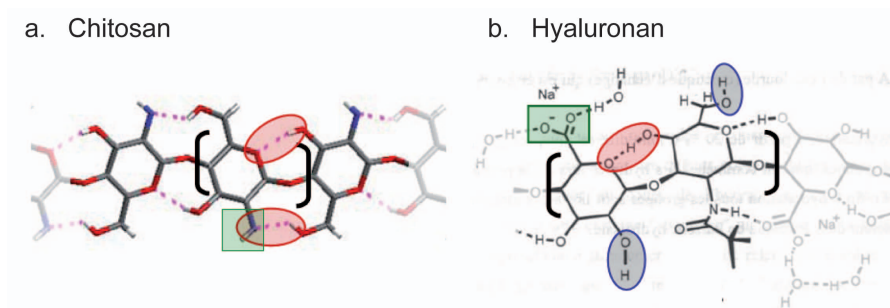


Figure 8.19: Chemical structures of (a) chitosan (adapted from [Rinaudo, 2006]) and (b) hyaluronan (adapted from [Haxaire, 2000]). H-bonds, free -OH groups and -COOH or NH_3^+ -groups are highlighted.

If we first look at the hydrogen-bonds, we can see that they are more numerous in the case of chitosan, which implies a higher rigidity of the chains illustrated by a higher persistence length: 11 nm for chitosan [Brugnerotto et al., 2001, Rinaudo et al., 2005] and 8 nm for hyaluronan [Reed, 1994, Berriaud et al., 1998, Kennedy et al., 2002a]. Then by looking at the hydroxyl,

8.5. VARIATION OF THE COVERAGE DEGREE: COMPARISON BETWEEN CHITOSAN AND HYALURONAN

carboxyl and amino groups which interact with water molecules, we can notice that they are more numerous in the hyaluronan. This can explain its higher water solubility than chitosan. Therefore than hyaluronan tends to be more extended in solution.

Moreover, considering that the charge parameter λ , which is basically related to the charge density (3.2.1), is equivalent for both polyelectrolytes (≈ 0.3 and 0.2 for chitosan at $\text{pH} = 6.0$ and hyaluronan at $\text{pH} = 3.5$ respectively), we can conclude that the adsorbed chain conformations mainly depend on the polymer chemical structure.

Competition between high and low molecular weights of hyaluronan

Polymers with high molecular weights have been demonstrated for a long time to preferentially adsorb on charged surfaces than those with lower molecular weight [Cohen-Stuart et al., 1980]. In our case, it was only possible to confirm the larger adsorption of highest molecular weights for hyaluronan using ζ -potential measurements. Actually, these experiments do not allow to clearly discriminating between various molecular weight for chitosan (similar ζ -potential variation).

We wonder now the role of a partial coating with low molecular weight polyelectrolyte on the adsorption of high molecular weight chains of hyaluronan. Hence we partially coat the membrane with the low molecular weight hyaluronan ($M_w = 1.14 \times 10^4$) up to $\Lambda = 0.07$ and we observe exactly the same ζ -potential variation as observed in the previous experiment (Figure 8.20) which points out the good reproducibility of the measurements. Then, when we reach a ratio $[\text{COO}^-]/[\text{lipid out}] = 0.7$ added, we stop adding hyaluronan of $M_w = 1.14 \times 10^4$ and add progressive amounts of hyaluronan with higher molecular weight ($M_w = 1.8 \times 10^6$).

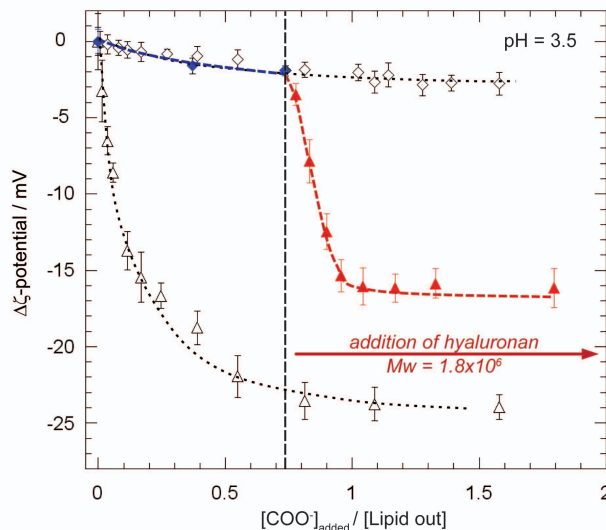


Figure 8.20: Influence of a partial coating by a low molecular weight ($M_w = 1.14 \times 10^4$, solid blue diamonds) on the adsorption of a high molecular weight ($M_w = 1.8 \times 10^6$, solid red triangles) on liposomes. The evolution of the normalized ζ -potential is compared with previous results obtained for $M_w = 1.14 \times 10^4$ (open diamonds) and 1.8×10^6 (open triangles) in (a). The dotted lines are added to guide the eye and have no physical meaning.

We observe a sharp decrease of the ζ -potential indicating an additional adsorption of the hyaluronan of higher molecular weight. Nevertheless, in excess of high hyaluronan molecular weight, ζ -potential does not reach the expected value of -25 mV ($\Lambda_{sat} = 0.97$) obtained previously for $M_w = 1.8 \times 10^6$ alone. We interpret this result assuming that hyaluronan fraction of low molecular weight remain adsorbed and is not displaced by the higher molecular weight hyaluronan in the time scale of our experiments (few hours). The remaining available surface limits the adsorption of the high molecular weight hyaluronan.

8.5.3 Conclusions on the chitosan and hyaluronan conformations at the interface

- For both polyelectrolytes, fluorescence microscopy shows that a homogeneous layer is adsorbed at the micrometric scale. The structure of this polymeric layer at the nanometric scale is made of charged domains where polyelectrolyte adsorbed flat (chitosan) or forms loops and trains (hyaluronan) on the basis of the molecular weight dependence.
- The polyelectrolyte conformation at the vesicle surface is controlled by both the persistence length and the polymer affinity for the solvent.
- With chitosan, whatever the molecular weight, in excess of polymer, the coated vesicle presents always highly positively charged.
- With hyaluronan, on the opposite, in excess of polyelectrolyte, the negative global charge of the coated vesicles is dependant on its molecular weight.

8.6 Stability of the polyelectrolyte coating: reversibility of the adsorption?

At this point, we have discuss mechanism of adsorption and estimate a coverage degree for both polyelectrolytes at equilibrium (i.e at a given polymer concentration in solution). We now address the question of coating stability under modification of the bulk conditions such a decrease of the polymer concentration or change of the pH value. Do polyelectrolytes desorb?

8.6.1 Effect of dilution

We first address the question of adsorption reversibility: is the adsorbed polymer, desorbed when its concentration free in the external solution is modified by addition of pure solvent? We will only consider the chitosan coating at $\text{pH} = 6.0$.

Electrophoretic mobility measurements on LUVs are not well-adapted to estimate the stability of chitosan coating versus wide dilutions, because we are obliged to work on samples with a total lipid concentration ranging between 3 and 5×10^{-3} mg/mL, which limits the range of

observable dilutions. Therefore we study chitosan desorption on GUVs by quantifying the fluorescence emitted by the coating via optical microscopy observations as presented in section 8.4.2.

Before studying the effect of the dilution, the stability of the polymer attachment at the membrane surface is observed as function of time. Figure 8.21a illustrates for the three different chitosan concentrations, previously used in Figure 8.14a, that the chitosan remains adsorbed to the DOPC membranes for at least 4 days. The experiments are performed on selected isolated coated GUVs even in the range of the isoelectric point ($F/S \sim 180$). These results are in agreement with an aging experiment realized on a chitosan-coated LUV suspension by ζ -potential measurements (Figure 8.21b). Similar observations were also reported by Mertins on their chitosan-coated GUVs (prepared from the inverse phase precursor) [Mertins et al., 2009]. Therefore, these different results highlight that without modification of chitosan bulk concentration (i.e no dilution), the degree of coverage remains constant.

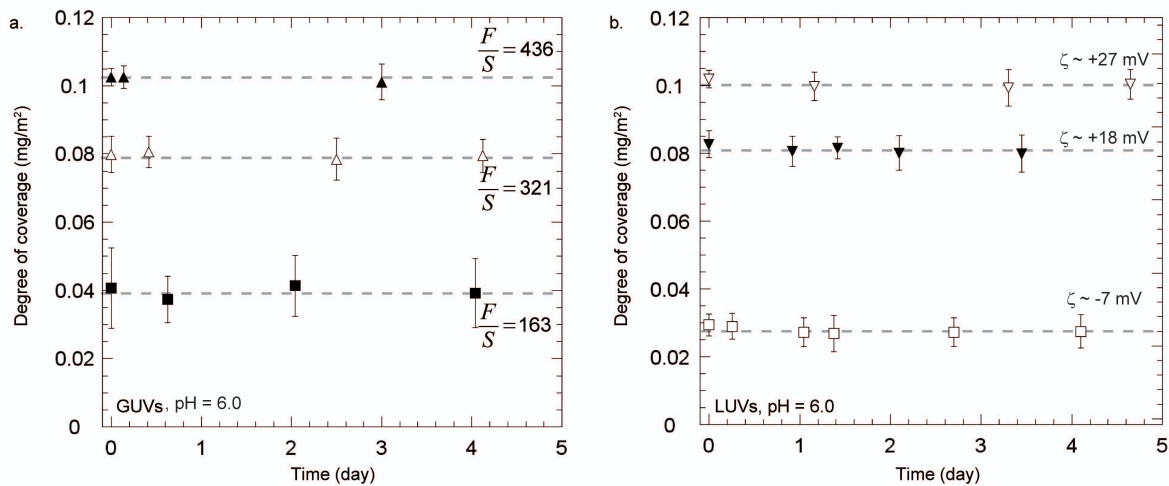


Figure 8.21: Time variation of the coverage degree for chitosan-coated vesicles incubated at $\text{pH} = 6.0$ with the three different molar ratio $R = [\text{NH}_3^+]_{\text{added}}/[\text{lipid out}]$ evaluated by (a) fluorescent microscopy observations on GUVs: $R = 0.14$ (solid squares), 0.42 (open triangles) and 1.72 (solid triangles) and (b) ζ -potential measurements on LUVs: $R = 0.03$ (open squares), 0.54 (solid triangles) and 1.91 (open triangles). Average values of the degrees of coverage are also indicated by the dashed line. We remind that the isoelectric point is obtained for $R = 0.18$ and corresponds to a coverage degree of 0.048 mg/m^2 .

We have then estimated the effect of dilution on the chitosan coating at fixed pH . GUVs are coated with chitosan at an added molar ratio $R_0 = [\text{NH}_3^+]/[\text{lipid out}] = 1.72$ and mixed to a sucrose solution to decrease the polymer concentrations to $R_0/2$, $R_0/5$ and $R_0/10$. Figure 8.22a shows the variation of the degree of coverage by fluorescence measurements on coated GUVs as a function of time for the different labeled polymer concentrations.

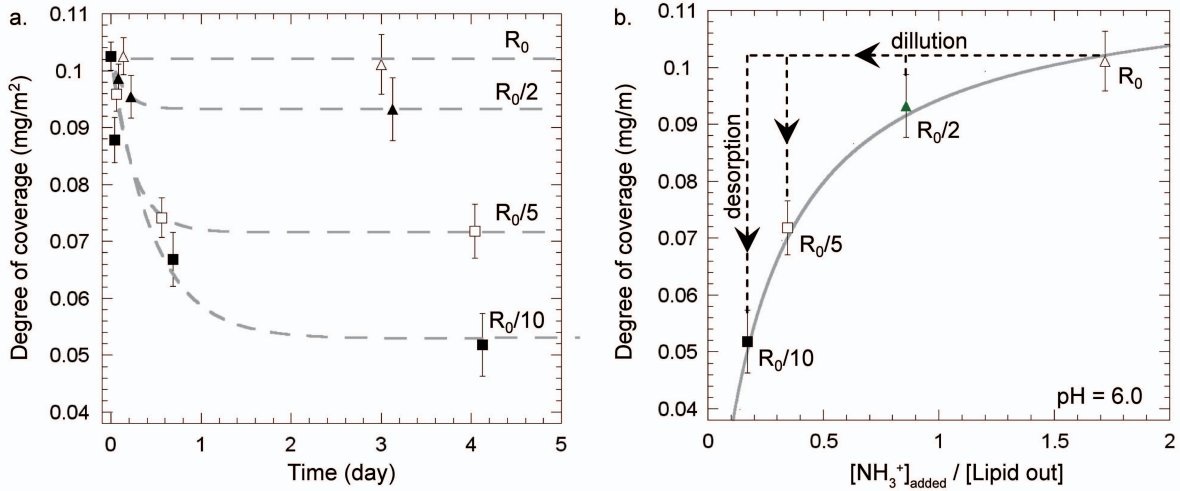


Figure 8.22: (a) Time variation of the degree of coverage for chitosan-coated GUVs initially incubated at $\text{pH} = 6.0$ with a molar ratio $[\text{NH}_3^+]/[\text{lipid out}] = 1.72$ (R_0 ; open triangles) and diluted at different molar ratio equal to 0.86 ($R_0/2$; solid triangles), 0.34 ($R_0/5$; open squares) and 0.17 ($R_0/10$; solid squares). The dashed lines represent exponential fits $\Lambda(t)/\Lambda_0 = \exp(-t/\tau_{off})^\beta$, where Λ_0 is the coverage degree at time $t = 0$ [Douglas et al., 1994]. (b) Degree of coverage evaluated 3 days (previous symbols) after the dilution compared with the adsorption curve (grey line) previously determined in the Figure 8.15b.

The chitosan desorption increases with dilution: higher the dilution, lower the resulting degree of coverage is. The quantification of the desorption kinetic is yet tricky due to the small number of presented measurements. Our data seem consistent with a first-order process (i.e. $\Lambda(t)/\Lambda_0 = \exp(-t/\tau_{off})^\beta$, where Λ_0 is the coverage degree at time $t = 0$) [Douglas et al., 1994] with a characteristic time τ_{off} of desorption around several hours (~ 5 to 12 hours depending of the dilution factor). This study does not allow to determine the process which limits desorption: the energetics of surface detachment ($\beta = 1$) or the diffusion ($\beta = 1/2$) [Sukhishvili and Granick, 1998]. Complementary experiments are thus required to conclude on the kinetic aspect.

At the equilibrium state, comparison of the coverage degrees reached 3 days after the dilution with the “adsorption isotherm” in Figure 8.15b, shows that desorption always leads to the degree of coverage reached by direct incubation of bare vesicles at the molar ratio $[\text{NH}_3^+]/[\text{lipid out}]$ expected after dilution (Figure 8.22b); chitosan adsorption is thus reversible in our experimental conditions (i.e. positive membrane and polyelectrolyte) and polyelectrolyte desorption will be considered with attention in the following where coated vesicles will be subjected to various stresses. We remark that higher dilutions (e.g. $R_0/50$ or $R_0/100$) will be interesting in order to probe chitosan-coated GUVs with negative ζ -potential and check if the desorption always follows the adsorption curve reported in Figure 8.15b.

Unfortunately, we do not have enough time to estimate the hyaluronan desorption in the same conditions. In the following we will thus assume that hyaluronan coating very likely exhibit the same behavior under dilution. It will also be interesting to estimate the adsorption

reversibility upon pH or salt variations.

As conclusion, fluorescence measurements evidence:

- The stability of the chitosan coating over few days when the polyelectrolyte concentration is remained constant.
- The reversibility of the chitosan adsorption when the polyelectrolyte concentration is decreased (upon dilution, the degree of coverage obtained at equilibrium, corresponds to the one expected by the incubation of bare vesicles at this polyelectrolyte concentration) in the range of positively charged chitosan-coated GUVs is obtained.

8.6.2 Effect of pH

Interaction polyelectrolyte-lipid membrane being mainly of electrostatic origin, the adsorption is modified when the respective charge signs and densities are changed by pH adjustments, as discussed earlier in section 8.2. In this section we wonder about the stability of the coating while the pH conditions are modified. We assume that the dilution effect discussed in the previous section is negligible in these experiments: observations are realized less than 1 hour after the beginning of the pH adjustment for small volume added.

Effect of pH on the ζ -potential of chitosan coated LUVs

We first observe the influence of pH on coated liposome ζ -potential (Figure 8.23) and compare with the results obtained previously on bare LUVs (see Figure 7.2). For this experiment, chitosan-coated LUVs are incubated at $\text{pH} = 6.0$ for an added molar ratio of $[\text{NH}_3^+]/[\text{lipid out}] \sim 3$ (see Figure 8.3). Then, the pH is adjusted by progressive addition of HCl or NaOH to cover the pH range from 2.0 to 12.0.

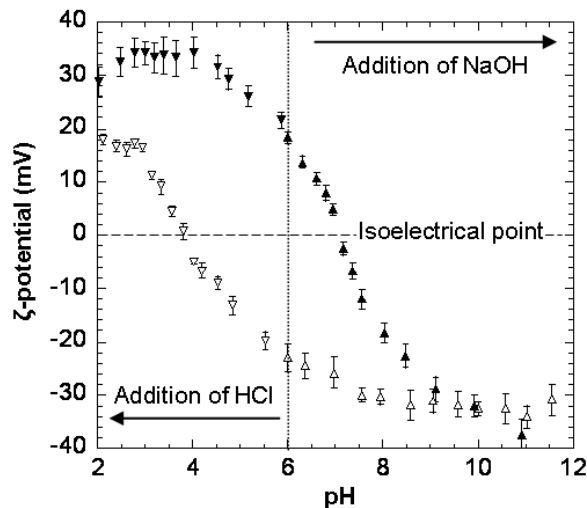


Figure 8.23: Variation of ζ -potential as a function of the measured pH for bare LUVs (open triangles) and for chitosan-coated LUVs (coating at $\text{pH} = 6.0$; solid triangles).

In acidic conditions, when pH decreases, ζ -potential passes through 0 at $\text{pH} \sim 4.0$, becomes positive before reaching a final value of around +16 mV for $\text{pH} < 3.0$ for bare liposomes. This variation reflects the repression of phosphate dissociation. Considering chitosan-coated LUVs, the trend is very different: at $\text{pH} = 6.0$, ζ -potential equals +18 mV (instead of -22 mV for bare vesicles) reaching a final constant value of +35 mV at $\text{pH} < 3.0$; this value results from conditions leading to fully protonated chitosan. ζ -potential is larger than that of bare vesicles in relationship with adsorption of positively charged chitosan. At pH in neutral to basic medium, ζ -potential variations of LUVs with or without chitosan are studied. For bare LUVs, the ζ -potential equals -22 mV at $\text{pH} = 6.0$ and decreases when the pH increases reaching a constant value of -32 mV at $\text{pH} \geq 7.5$. For coated vesicles, when pH is increased by addition of NaOH, the ζ -potential goes to zero at pH around 7.2 then becomes negative and finally reaches the value (-30 mV) of the bare LUVs at $\text{pH} = 9.0$. We stress that for $\text{pH} > 7.0$, negative contributions of the phosphate acid and of the carboxyl groups (produced by the apolar chain oxidation) in the phospholipids become predominant. In addition, for chitosan coated-LUVs, repression of the chitosan protonation occurs. Two hypotheses are conceivable, either desorption occurs or the chitosan remains adsorbed even when it is uncharged at $\text{pH} > 9.0$.

Confocal microscopy observation of polyelectrolyte coating stability on a broad range of pH

In order to directly prove the stability of both polyelectrolyte coatings over a broad range of pH, we observe coated GUVs by confocal microscopy. Vesicles are coated with chitosan at $\text{pH} = 6.0$ or with hyaluronan at $\text{pH} = 3.5$ (conditions in which polyelectrolyte and membrane exhibit an opposite net charge) and are subjected to pH shocks either down to $\text{pH} = 2.0$ or up to $\text{pH} = 10.0$ (Figure 8.24). The range of pH is chosen so that no significant osmotic deflation occurs upon the required additions of HCl or NaOH.

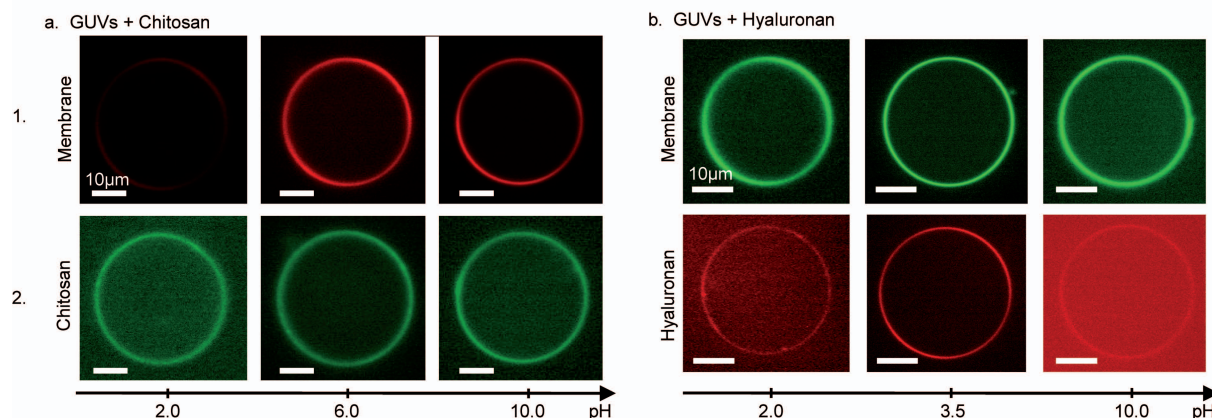


Figure 8.24: Confocal microscopy observation of GUVs of same sizes, coated with chitosan at $\text{pH} = 6.0$ (a) or with hyaluronan at $\text{pH} = 3.5$ (b) (column 2) and then subjected to pH shocks, either down to $\text{pH} = 2.0$ (column 1) or up to $\text{pH} = 10.0$ (column 3). We simultaneously visualize for each GUVs the lipid membrane (line 1) and the polyelectrolyte coating (line 2) for the three pH values. The scale bars represent $10 \mu\text{m}$.

8.7. COATING OF LIPID MEMBRANE BY MULTILAYER OF POLYELECTROLYTES¹²³

For the different values of pH, we visualize the lipid membrane and the polyelectrolyte coating (respectively lines 1 and 2 of Figure 8.24). We show that, in this range of pH, the membrane remains undamaged at the scale of observation and chitosan or hyaluronan remains adsorbed on it. We stress again that no quantitative comparison of coverage degrees is available from Figure 8.24 as explained above in the section 8.1.

As conclusion, these results show that:

- Chitosan and hyaluronan remain at least partially adsorbed over a broad range of pH (from 2.0 to 10.0) one hour after the pH adjustment, even when the polyelectrolytes become uncharged. Nevertheless no quantification of desorption could be carry out as a function of pH.
- Polyelectrolyte adsorption allows to tune the membrane charge as a function of pH.

8.7 Coating of lipid membrane by multilayer of polyelectrolytes

The adsorption of successive layers of positively charged and negatively charged polyelectrolytes on the membrane of liposomes is now investigated. Considering our previous data, the first polymer adsorbed was chitosan, followed by adsorption of hyaluronan to improve the stability. As presented in Chapter 3, Hyaluronan is a polysaccharide largely present in human tissues; it is chosen as an external layer to ensure an optimized compatibility in the body, in case of potential biomedical application [Vasiliu et al., 2005].

In order to characterize this polyelectrolyte complex formation on the lipid membrane, ζ -potential measurements are performed at three distinct and controlled pH values (pH = 3.5, 4.7, and 6.0). Before the addition of chitosan, we have controlled the charge of the lipid membrane for the different pH: the ζ -potential of the non-coated LUVs equals, respectively, -20 mV at pH = 6.0, -5 mV at pH = 4.7, and +5 mV at pH = 3.5. The membrane is thus negatively charged at pH = 6.0 and 4.7, while at pH = 3.5 it is positively charged, as shown in Chapter 7. Then the non-coated LUVs are first incubated in a chitosan solution at a molar ratio [repeat units]/[lipid out] ~ 5 to form the first layer of chitosan on the liposomes. This ratio corresponds to a significant degree of coating by chitosan with a low concentration of free polyelectrolyte in solution (monomeric concentration lower than 3×10^{-5} M, whatever the pH). After chitosan addition, the ζ -potential of the coated LUVs reach positive values, respectively, +11 mV at pH = 6.0, +22 mV at pH = 4.7, and +28 mV at pH = 3.5. Hyaluronan is then added to the chitosan-coated LUVs suspension.

Figure 8.25 shows variation of ζ -potential of the chitosan-coated LUVs as a function of the amount of hyaluronan added, represented by the molar ratio $[\text{COO}^-]/[\text{NH}_3^+]$, for the three different pH values.

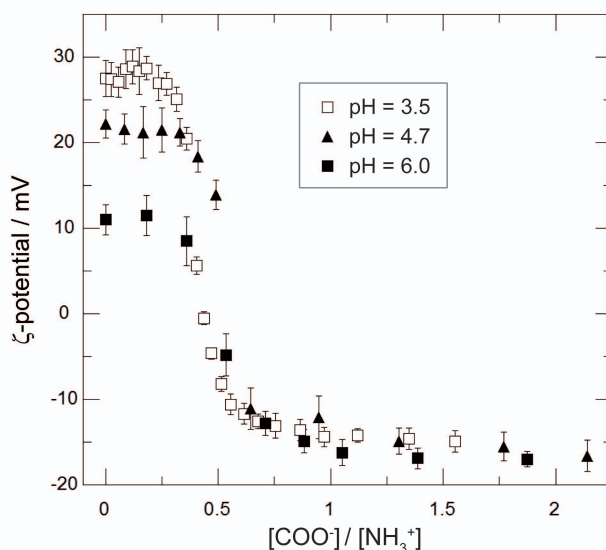


Figure 8.25: ζ -potentials of chitosan coated LUVs (chitosan: $M_w = 2.25 \times 10^5$, $DA = 5\%$) in the presence of hyaluronic acid (HA) ($M_w = 6.63 \times 10^5$) as a function of the molar ratio $[COO^-]/[NH_3^+]$ (amount of ionized HA carboxyl groups over the amount of chitosan protonated amino groups). The data were obtained at $pH = 3.5$ (open squares), $pH = 4.7$ (solid triangles) and at $pH = 6.0$ (solid squares) for chitosan-coated LUVs incubated at a molar ratio of chitosan monomer per accessible lipids of the membrane ~ 5 .

Upon addition of hyaluronan, we first observe that the ζ -potential remains nearly constant until approximately a ratio $[COO^-]/[NH_3^+] \sim 0.3$ and then decreases sharply to finally reach the same constant value of -16 mV for $[COO^-]/[NH_3^+] \sim 1$ for the three different pH. The initial positive plateau is explained by the formation of a complex between added hyaluronan and chitosan remaining free in solution (non-adsorbed on the liposomes). When the “neutralization” of the free chitosan is completed, added hyaluronan can adsorb on the chitosan-coated liposomes, leading to a decrease in ζ -potential before reaching a negative plateau.

In conclusion, we would like to stress that, whatever the pH and consequently the initial charge of the liposomes, chitosan adsorption gives positively charged composite systems, which upon addition of hyaluronan, give rise to negatively charged composite vesicles. The charge sign of these vesicles can be tuned in a controlled way by adsorption of successive polyelectrolyte layers leading to the modification of their interaction between artificial surface and living systems.

Complementary experiments of fluorescence microscopy on GUVs and EPR on LUVs could allow investigating the coating and the membrane state.

8.8 Conclusion

These studies performed on both LUVs and GUVs allow us to conclude that:

- **Chitosan and hyaluronan adsorb on DOPC membranes**, interactions are mainly of **electrostatic origin** and the **coverage degree** is **limited** by electrostatic phenomena
- Interactions of electrostatic origin, as shown from:
 - ✓ A stronger affinity when the polyelectrolyte and the membrane are of opposite charge signs
 - ✓ NaCl modifies this affinity, favoring the adsorption of polyelectrolytes on membranes of same charge sign or delaying the adsorption for oppositely charged membranes.
 - ✓ Addition of a hydrophobic interaction (alkylated chain) does not change the degree of coverage, but only delay the adsorption process. Our data seem to reveal that alkylated moieties do not interact directly with the lipid membrane.
- When the coverage degree is maximum in excess of polyelectrolyte, stable solutions of **isolated polyelectrolyte-coated vesicles** are obtained, allowing various characterization studies on single coated vesicles.
- **The polyelectrolyte conformation at the vesicle surface is controlled by both the persistence length and the polymer affinity for the solvent.** Chitosan chains are adsorbed flat at the membrane surface, while hyaluronan forms loops and build a 3D-layer made of trains interacting with the membrane and loops whose thickness increases with the molecular weight.
- **Study of the polyelectrolyte coating stability shows that:**
 - ✓ **Chitosan and hyaluronan remains adsorbed on DOPC membrane in a wide range of pH.**
 - ✓ **The polyelectrolyte adsorption seems reversible upon dilution.**
- **pH adjustment or adsorption of successive polyelectrolyte layers allows to tune the net charge** of coated vesicles.

Chapter 9

Study of chitosan- and hyaluronan-coated vesicles behaviors under external stresses

Ce chapitre est consacré à l'étude des vésicules décorées de chitosane ou d'acide hyaluronique soumises à des contraintes externes, soit en modifiant les interactions électrostatiques (pH, concentration ionique) soit en appliquant des contraintes mécaniques (pression osmotique, extrusion hydrodynamique de nanotube, compression entre deux surfaces). Nous observons les réponses des GUVs décorées à ces divers stimuli, nous comparons ces résultats à ceux obtenus pour des vésicules non-décorées ; enfin nous estimons l'effet de cette décoration sur les propriétés des membranes.

o o o o o o o o o o

This chapter is devoted to the study of chitosan or hyaluronan coated vesicles under external stresses, either playing on the electrostatic interactions (pH, ionic concentration) or induced by mechanical constraints (osmotic pressure, hydrodynamical tether extrusion, compression between two surfaces). We will observe polyelectrolyte-coated GUVs responses to these various stimuli, discuss these results in comparison with those obtained on bare vesicle and estimate the effect of the polyelectrolyte coating on the membrane properties.

In the following studies, 200 mM sucrose filled GUVs are coated either with chitosan at pH = 6.0, at a coverage degree of 0.11 mg/m² (i.e. an added molar ratio $[\text{NH}_3^+]/[\text{lipid out}] \sim 9$) or with hyaluronan at pH = 3.5, at a coverage degree of 0.65 mg/m² (i.e. an added molar ratio $[\text{COO}^-]/[\text{lipid out}] \sim 12$). These values correspond to the adsorption saturation (section 8.5) when membrane and polyelectrolyte are oppositely charged (strongest affinity). In these conditions, the maximum salt concentration in the solution remains of the order of 10⁻⁴ M. Furthermore, we consider that no polymer desorption occurs during the time scale of our differ-

ent experiments (~ 1 -2 hours) according to results reported in section 8.6.1.

We found, in a preliminary study (not reported in this manuscript) that, in the absence of glass treatment, chitosan and hyaluronan coated vesicles sediment, adhere on the glass surface and finally burst. After passivation of the surface with PEG (see section 6.3), they still exhibit some loose interactions with the glass plate, probably due to a weak adhesion, however they do not burst anymore. In the following experiments, this glass treatment of substrates has been systematically used.

9.1 Anisotropic depression: micropipette suction experiments

In order to determine the effect of chitosan adsorption on the membrane mechanical properties (i.e. bending and stretching moduli), we have first tried to perform micropipette aspiration experiments on coated vesicles, in the group of Carlos Marques (Institut Charles Sadron, Strasbourg). Unfortunately, we did not succeed in avoiding the adhesion of these modified vesicles on the glass pipette surface, neither by applying a PEG nor a Surfacil glass treatment [Campillo, 2007]. Moreover, the low membrane tension necessary to open pore in coated membranes, discussed in section 9.3.2, makes difficult aspiration experiments on such objects. Consequently, this method does not allow us the determination of the composite membrane properties (bending and stretching moduli).

9.2 Osmotic pressure

Then, we have investigated the influence of the polyelectrolyte coating on the morphological changes of GUVs under osmotic deflation. The osmotic shocks are induced by addition of solutions (glucose, NaCl ...) at different concentrations into the GUVs suspension as detailed in section 6.5.

We assume that vesicles can move upon a weak convective flow created by the solution addition without affecting their responses to the osmotic shocks (vesicle motions are estimated lower than one $\mu\text{m/s}$). In this study, the beginning of the deflation, indicated as $t = 0$, is assigned as soon as detectable vesicle deformation is observed.

The osmotic stress is imposed by difference between external and internal concentrations. The Reduced volume V_R value is calculated in a first approximation as the ratio of initial glucose concentration (200 mM) over the actual external glucose concentration.

9.2.1 Glucose shocks

Osmotic stress is first applied on chitosan-coated GUVs using glucose (non-charged specie).

Spherical deflation associated with tube ejections

The glucose concentration of the external solution is increased up to 250 mM, which corresponds to a reduced volume V_R around 0.8. Figure 9.1a shows the shape evolution of a chitosan-coated GUV under this osmotic stress. Upon the glucose shock, coated-GUVs shrink preserving their spherical shapes by spontaneously forming many tubular protrusions (of diameter lower than $1 \mu\text{m}$; tens of microns in length), without observable membrane fluctuations. It is demonstrated that these tubes are coated with fluorescent labeled chitosan as illustrated in Figure 9.1b; the comparison of the ratios of the fluorescence intensities ($R = I_{\text{chitosan}}/I_{\text{lipids}}$) in the coated GUV ($R = 0.78$) and in the tube ($R = 0.73$) shows no dramatic modification in the chitosan coverage degree of vesicles and membrane nanotubes. The final state is reached less than one minute after the beginning of the deflation, and, thereafter, we do not detect either shrink back of protrusions into the parental membrane or separation of daughter vesicles from the mother one.

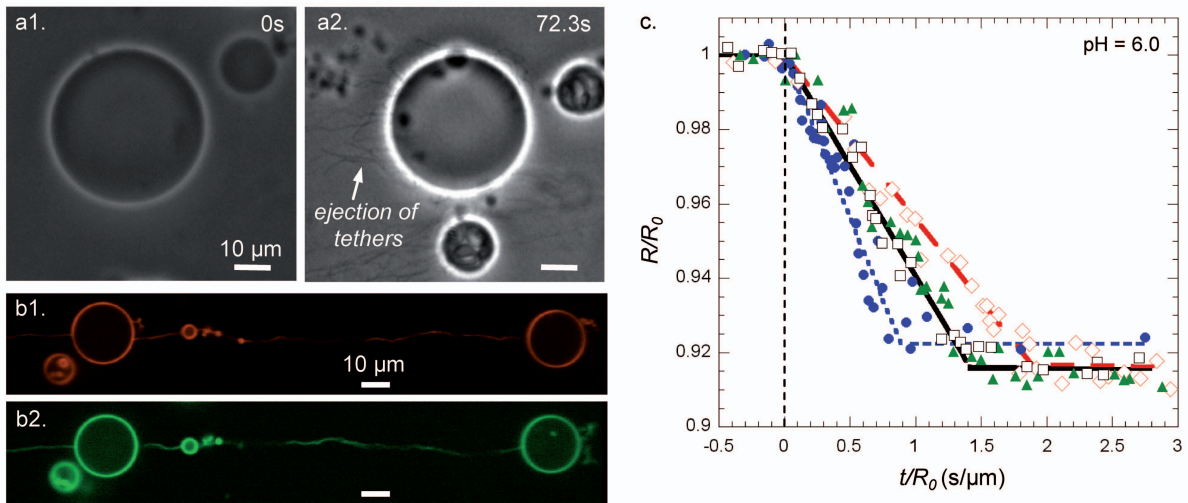


Figure 9.1: Osmotic deflation of chitosan-coated GUVs (coverage degree $\sim 0.11 \text{ mg}/\text{m}^2$) in contact with a hypertonic glucose solution at $\text{pH} = 6.0$: (a) Shape transformation: (a1) a coated GUVs in 200 mM glucose solution; (a2) same vesicle, 125 seconds after the controlled osmotic glucose shock with $\Delta c = 50 \text{ mM}$. (b) In the same conditions, the lipid membrane (b1) and the polyelectrolyte coating (b2) are successively visualized by fluorescence confocal observations. The scale bars represent $10 \mu\text{m}$. (c) Shrinkage dynamics of 4 chitosan-coated GUVs ($R = 22.4 \mu\text{m}$, blue solid circles; $R_0 = 16.8 \mu\text{m}$, black open squares; $R_0 = 16.7 \mu\text{m}$, green solid triangles and $R_0 = 19.0 \mu\text{m}$, red open diamonds) submitted to an osmotic stress ($\Delta c = 50 \text{ mM}$), R_0 is the initial radius of the vesicle at $t = 0$, R its radius at time t .

The striking point is that, contrary to bare DOPC vesicles which preferentially exhibit oblate or prolate-like shape at this reduced volume (see the ADE phase diagram in Figure 5.4), only spherical deflations with tube ejection are observed in the coated GUV suspension at $V_R = 0.8$. We attributed these obtained shapes to the spontaneous curvature c_0 induced by asymmetric binding of the polyelectrolyte on the DOPC membrane; c_0 being positive according to the ADE phase diagram.

This spontaneous ejection of tubes is interpreted within the model of tube formation, from membrane with c_0 , proposed by Kremer and Brochard-Wyart [Kremer, 2009] and detailed in the section 9.3.3. In our experiments, osmotic deflation provides a decrease of the membrane tension of the chitosan-coated GUVs. For even lower membrane tension $\sigma < \kappa c_0^2/2$, the extrusion force $f = 2\pi(\sqrt{2\kappa\sigma} - \kappa c_0)$ (Eq. 9.20) becomes negative, and tubes will grow spontaneously even without any external pulling force. We will go back in section 9.3.4 on the tube formation and the quantification of the spontaneous curvature.

We now focus on the spherical deflation mechanism. Figure 9.1c presents the shrinkage dynamics of different chitosan-coated GUVs submitted to the osmotic stress: a linear decrease of vesicles radius with time is found. Thirty chitosan-coated vesicles with different diameters have been considered and the R/R_0 variation ranges always in the domain limited by the two (A) and (B) dotted lines represented in Figure 9.1c.

This dynamic allows an easy estimation of the water permeability P of the chitosan-coated membrane as previously reported in [Boroske et al., 1981, Bernard et al., 2002]. We first assume that during shrinkage and tube ejection, the total area of the lipidic membrane remains constant and equal to $4\pi R_0^2$, with R_0 the initial radius.

The molar flux J of water through the membrane is related to the difference of molar concentrations Δc across the bilayer and the membrane permeability P , by $J = P\Delta c$. In addition, by integrating on the whole vesicle surface, we have:

$$\iint_{surface} \vec{J} \cdot d\vec{S} = -\frac{dn_{water}}{dt} \quad (9.1)$$

where n_{water} is the number of water molecules in the vesicle. Assuming that the water flux J is constant and perpendicular to the membrane surface, we obtain:

$$J = -\frac{1}{S(t)} \frac{d(V(t)/v_{water})}{dt} \quad (9.2)$$

where $V(t)$ is the volume encapsulated by the vesicle and v_{water} the water molar volume (18×10^{-6} m³/mol). We assume that the water exchange mainly occurs through the mother vesicle's surface of area $S(t) = 4\pi R(t)^2$.

$V(t)$ can be expressed as a function of the vesicle radius $R(t)$, the tube radius r (assumed to be constant), the tube length $L(t)$, and $N(t)$ the number of ejected tubes: $V(t) = \frac{4}{3}\pi R^3 - N(t)\pi r^2 L$. We define the adimensionalized variables $\alpha = R/R_0$ and $\beta = r/R$. The conservation of the membrane area leads to:

$$\frac{d\alpha}{dt}(1 - \beta) = -\frac{v_{water} P \Delta c}{R_0} \quad (9.3)$$

As ejected tubes always exhibit radius lower than $0.5 \mu\text{m}$ (i.e. $\beta = r/R \ll 1$), and consequently

we obtain:

$$\frac{R}{R_0} = 1 - \frac{v_{water} P \Delta c}{R_0} t \quad (9.4)$$

This linear behavior is well observed in Figure 9.1c and yields to an average permeability equals to $6.8 \pm 0.2 \times 10^{-5}$ m/s, estimated over thirty vesicles for $\Delta c = 50$ mM. This water permeability is similar to values obtained by different techniques for pure DOPC membranes (4 to 16×10^{-5} m/s) [Mathai et al., 2008]. This result highlights that the chitosan coating does not seem to modify the global membrane water permeability in these conditions.

Pearling of the tubes: formation of a necklace

More than 15 minutes after the glucose shock ($\Delta c = 50$ mM), we observe that the ejected coated tubes start to breakup into pearls (Figure 9.2). These pearls appear either at the end of the tether or randomly along it, as illustrated in the inset of Figure 9.2a, then they develop along the cylinder, and finally within 10 minutes, tubular structures are totally transformed into a periodic string of smaller vesicles connected by narrow necks (Figure 9.2b). This general phenomenon appears everywhere in the suspension and the pearl-necklace geometry is observed to be stable over few hours.

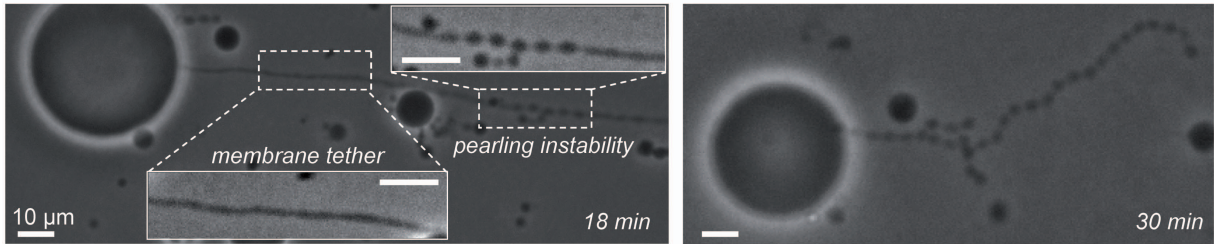


Figure 9.2: Pearling transformation of a chitosan-coated tube connected to the mother vesicle. The scale bars represent $10 \mu\text{m}$.

These shape changes are remarkably similar to the classical Rayleigh-Plateau instability in which a cylindrical fluid stream breaks into droplets [Plateau, 1873]. Indeed, tubular lipid membrane can also break up in this way, for example under the stimulus of anchoring amphiphilic polymers into the membrane outer leaflet [Tsafirir et al., 2003], which causes local spontaneous curvature, or under the tension of the membrane induced by optical tweezers [Bar-Ziv et al., 1998].

In our case, we attribute the pearling to spontaneous curvature due to the asymmetrical coating. Nevertheless no quantitative explanation is proposed at this time from these data. We notice that electrostatic interactions will probably have to be taken into account to describe the pearling instability observed with chitosan-coated vesicles. In particular, it will be interesting to check if the presence of salt can limit the pearling process as proposed by [Nguyen et al., 2005].

The glucose shock experiments highlight that:

- Chitosan-coated GUVs systematically exhibit spherical deflations associated with ejection of coated lipidic tubes. This shape is attributed to the spontaneous curvature c_0 induced by asymmetric association of the polyelectrolyte on the membrane.
- The tube formation is attributed to a negative extrusion force which appears when the membrane tension is decreased by osmotic deflation.
- Chitosan-coating does not seem to modify the membrane water permeability.

9.2.2 NaCl shocks

Membrane-chitosan interaction being mainly of electrostatic origin (see section 8.2), we have then applied the osmotic stress using NaCl, in order to add an electrostatic screening between the adsorbed charges during the deflation.

Figure 9.3 reports the results obtained for bare vesicles (line a), chitosan-coated GUVs (line b) and hyaluronan-coated GUVs (line c) in presence of NaCl shocks (from 0 to 10^{-3} M NaCl ($V_R \sim 0.99$) and from 10^{-3} to 10^{-2} M NaCl ($V_R \sim 0.91$)).

In all cases (coated and non-coated vesicles), up to 10^{-3} M NaCl, no modification is observed. Dealing with non-coated GUVs (Figure 9.3a), for NaCl concentration between 10^{-3} M and 10^{-2} M, we always observe large membrane fluctuations and bursting of all the vesicles after 2 minutes. This behaviour may be attributed to the salt effect on the lipid polar heads compaction in the external leaflet [Böckmann et al., 2003, Sachs et al., 2004] which modifies structural and dynamical properties of the zwitterionic membrane [Lee et al., 2008] leading to bursting. As far as isolated polyelectrolyte-coated GUVs (Figures 9.3b and 9.3c) are concerned, no bursting occurs up to 10^{-2} M NaCl but spherical deflation associated with invaginations is observed (formation of daughter vesicles inside the initial vesicles associated with the decrease of the initial vesicle diameter induced by the osmotic deflation).

In the hypothesis of the patch model, the bare domains of lipids are compacted in presence of salt excess, but compare with bare vesicles local interaction with polyelectrolyte makes the difference. Our results may be interpreted in term of transition from positive to negative spontaneous curvature contribution, according to the ADE phase diagram (Figure 5.4). From the mechanism proposed by [Kim and Sung, 2001] (Figure 9.3d), when salt is added, electrostatic repulsions are reduced in the adsorbed flexible polymer forming trains and loops. Intrachain electrostatic repulsion are repressed inducing the polymer collapse, causing a negative spontaneous curvature of the membrane and forming invaginations [Breidenich et al., 2005]. This mechanism fits well with our results obtained for hyaluronan (forming trains and loops at the membrane surface; see section 8.5.2). Concerning chitosan (adsorbed flat on the surface), screening of repulsion between highly positive patches, in addition of polar head compaction, cause a negative bending of the membrane. In both cases, polyelectrolyte coating prevents the disruption of the lipidic

membrane.

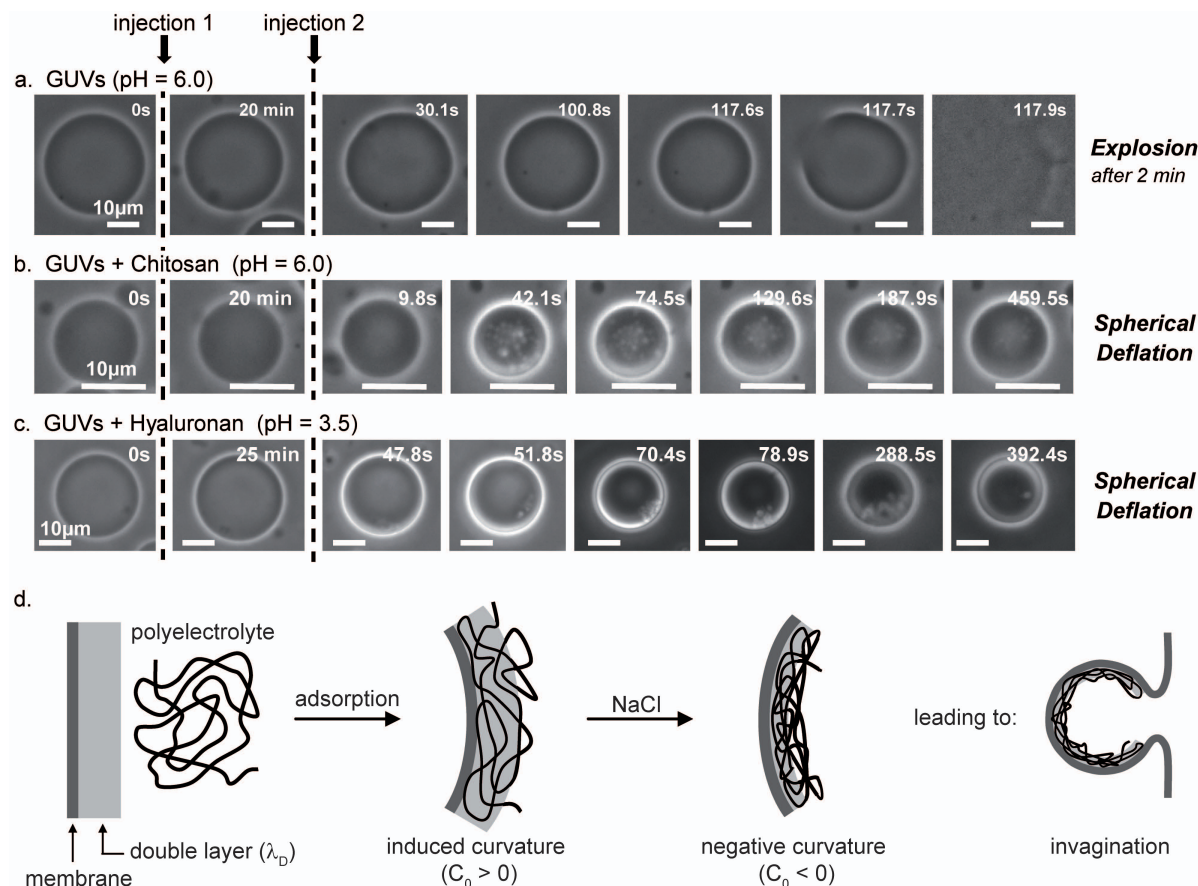


Figure 9.3: Observation of DOPC GUVs (a) and chitosan-coated GUVs (b) at $pH = 6.0$, and hyaluronan-coated GUVs (c) at $pH = 3.5$, for different NaCl concentrations (up to 10^{-2} M). Times series show the shape transformations of vesicles after NaCl injection (1) (to adjust at 10^{-3} M NaCl) and injection (2) (to adjust at 10^{-2} M NaCl). After injection (2), bare DOPC GUVs burst while polyelectrolyte-coated vesicles exhibit a spherical deflation with invaginations. The delay after each NaCl injection is indicated in the upper part of each picture. The scale bars represent $10 \mu\text{m}$. (d) Schematic figure of membrane bending (c_0) induced by flexible polyelectrolyte adsorption (e.g. hyaluronan) and formation of invagination upon addition of salt, as proposed by [Kim and Sung, 2001].

In addition, when polyelectrolyte-coated GUVs are initially close together, formation of GUVs aggregates is observed (Figure 9.4a and 9.4b1) as a function of the salt concentration. Cluster reorganizations are highlighted in these kinds of vesicle “foams”, which seems to indicate that the self association of polyelectrolyte-coated GUVs in presence of NaCl is controlled by a weak energy of attraction. These observations can be interpreted with the liposome association-dissociation mechanism previously reported in section 8.4, resulting from the balance between long-range electrostatic repulsion and short-range attractions. The coated membrane can be regarded as a patch-like (mosaic) structure, formed of domains of adsorbed polymer chains and of domains of bare membrane surface. In absence of salt, at this coverage degree ($[\text{NH}_3^+]_{\text{added}}/[\text{lipid out}] \sim 9$), vesicles are isolated due to the electrostatic repulsion (see Figure 8.11). In presence of NaCl, the long range repulsions are reduced, and consequently the short-range attractive potential between negatively and positively charged domains of the patch-like surfaces of two

separated vesicles leads to the formation of aggregates. Light scattering measurements on a coated LUVs suspension as a function of the salt concentration could confirm our interpretation.

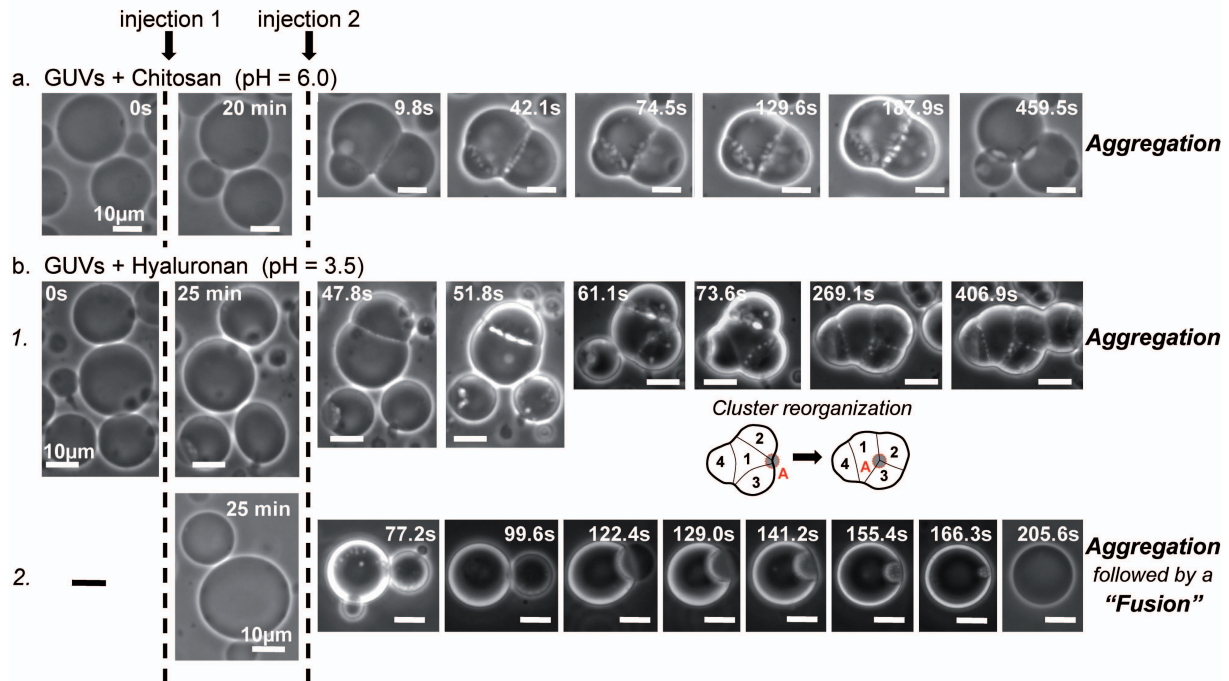


Figure 9.4: Formation of (a) chitosan or (b) hyaluronan-coated GUVs clusters by aggregation of initially vesicles closed together after NaCl injections (to adjust at 10^{-3} M NaCl and to adjust at 10^{-2} M NaCl), in addition to spherical deflation associated with invaginations. Reorganization of the vesicles in the aggregate is observed and illustrated in the inset sketch. (b2) Illustration of fusion between two aggregated hyaluronan coated vesicles (rare event). The time delay after each NaCl injection is indicated in the upper part of each picture. The scale bars represent $10 \mu\text{m}$.

In few rare cases, we observe fusion of coated GUVs as illustrated in Figure 9.4b2: the time sequence seems to indicate that the small vesicle comes in contact with a larger one, opens a pore (decrease of optical contrast of the inner medium) and reorganizes its membrane with that of the large vesicle in a multilamellar system (final diameter does not increase noticeably). This phenomenon is commonly reported and attributed to a strong polymer-lipid interaction destabilizing the vesicle and forcing the bilayer reorganization into multilamellar structure [Huebner et al., 1999, Rosa et al., 2007].

The salt shock experiments show that:

- Polyelectrolyte coating enhances the membrane resistance against salt shocks.
- Chitosan- and hyaluronan-coated GUVs systematically exhibit spherical deflations associated with invaginations. This shape is attributed to a negative spontaneous curvature induced by the screening of the electrostatic interactions in presence of salt.
- Aggregation of polyelectrolyte-coated GUVs close together is highlighted which, in few rare cases, leads to the formation of multilamellar vesicles.

9.2.3 HCl or NaOH shocks

We have previously shown the stability of the chitosan and hyaluronan coating in a wide range of pH (see section 8.6.2). We now focus on the behaviors of the polyelectrolyte-coated GUVs under pH shocks and compare them with bare vesicle in similar conditions. Bare GUVs experiments are realized at pH = 3.5 and 6.0; similar behaviors being observed in both cases, we only report here results obtained at pH = 6.0.

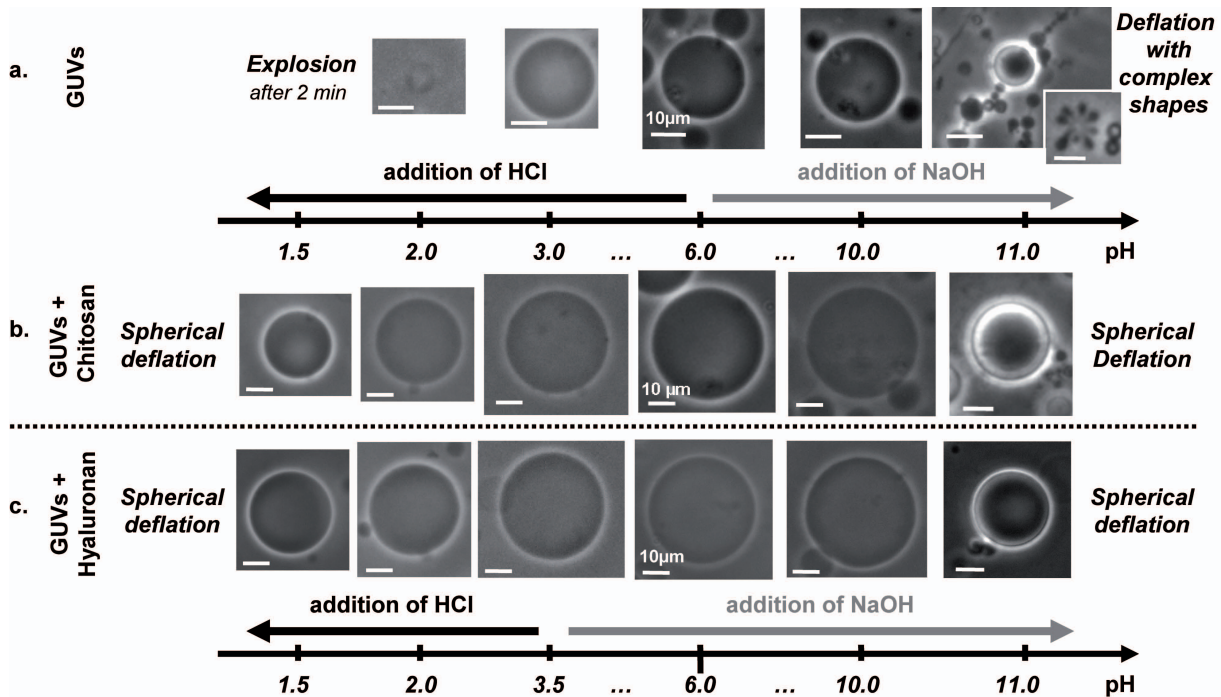


Figure 9.5: Behavior of non-coated GUVs (a) and chitosan (b) or hyaluronan (c) coated GUVs as a function of pH. The scale bars represent 10 μm .

Figure 9.5 sums up observations at the equilibrium state (~ 30 minutes after injection), obtained for non-coated GUVs (line a), chitosan-coated GUVs (line b) and hyaluronan-coated GUVs (line c) as a function of pH.

First of all, under basic conditions, for $\text{pH} > 10.0$, polyelectrolyte-coated GUVs remain stable and exhibit osmotic spherical deflation with tube ejection. Secondly, under acidic conditions, for pH between 2.0 and 1.5, a spherical deflation is also observed but it is not possible to clearly show evidence of tube ejection. On a contrary, bare GUVs burst quickly under acidic conditions for $2.0 < \text{pH} < 3.0$ or deflate to complex shapes (e.g budding previously reported by [Lee et al., 1999]) under basic conditions for $\text{pH} > 10.0$.

Therefore, chitosan or hyaluronan-coated vesicles are stable in extreme pH conditions and confirm that polyelectrolytes remains adsorbed on the membrane.

To sum up:

- Polyelectrolyte coating enhances GUVs resistance against pH shocks.
- Polyelectrolyte-coated GUVs always exhibit spherical deflation under osmotic pressure, with either ejection of membrane tubes (i.e. positive spontaneous curvature c_0) for glucose or pH shocks or by forming invaginations (i.e. negative spontaneous curvature) for NaCl gradient.

9.3 Point-acting force: hydrodynamic extrusion of tubes from chitosan-coated vesicles

In this part, we present results of hydrodynamic tether extrusion experiments on chitosan-coated GUVs (coverage degree of 0.11 mg/m^2) at $\text{pH} = 6.0$, to check how the polyelectrolyte coating changes the mechanical properties of the vesicles. These experiments have been realized by S. Kremer and C. Campillo, at the occasion of a collaboration with the group of Françoise Brochard-Wyart (Institut Curie, Paris) [Kremer et al., 2010].

9.3.1 Nanotether extrusion on bare DOPC GUVs

For bare DOPC vesicles, we get the results already describes in the literature by [Rossier et al., 2003, Borghi et al., 2003b] and presented in Figure 9.6: above a threshold flow velocity U_c , a membrane tube is extruded; the length $L(t)$ increases up to a stationary length L_∞ . Then, the flow is stopped, the tube retracts and $L(t)$ decreases to 0. This technique allows to study both membrane tube extrusion and retraction dynamics.

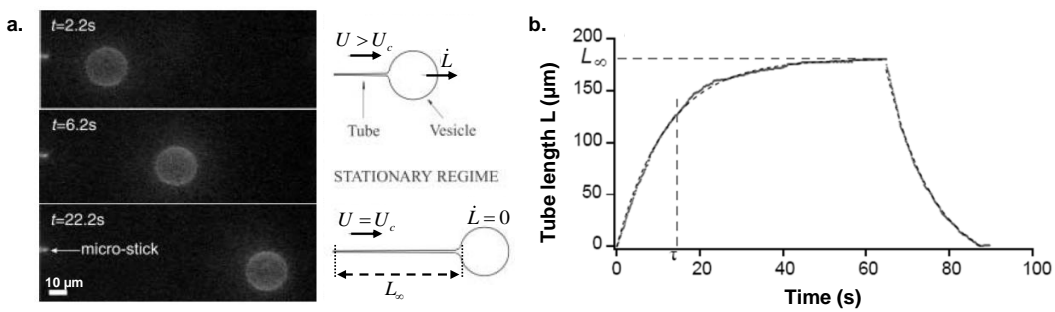


Figure 9.6: (a) Tube extrusion sequence under a hydrodynamical flow and typical sketch of the vesicle shape during the extrusion (adapted from [Borghi et al., 2003b]). (b) Tube extrusion and retraction dynamics on a bare DOPC vesicle. Extrusion and retraction are respectively fitted with Eq. (9.1) and (9.2) (adapted from [Borghi et al., 2003a]).

We now briefly review the main results of hydrodynamic tube extrusion from bare vesicles. The extrusion of a membrane nanotube can be seen as a first-order transition [Derenyi et al., 2002] at a threshold force $f = 2\pi\sqrt{2\kappa\sigma} = 2\pi\kappa/r$, where $\kappa \approx 4 \times 10^{-20} \text{ J}$ is the bending rigidity of the membrane, σ its tension and r the tube radius ($r = \sqrt{\kappa/2\sigma}$). Under a flow velocity U , the force

9.3. POINT-ACTING FORCE: HYDRODYNAMIC EXTRUSION OF TUBES FROM CHITOSAN-COATED

on the tethered vesicle of radius R is the Stokes friction $f_v = 6\pi\eta UR$ (η is the water viscosity). The equilibrium $f_v = f$ leads to the threshold velocity U_c given by:

$$U_c = \frac{\sqrt{2\kappa\sigma}}{3\eta R} = \frac{\kappa}{3\eta Rr} \quad (9.5)$$

The initial tension σ_0 is not imposed in our experiment, but is known to range between 10^{-7} to 10^{-5} N/m. From Eq. 9.5, σ_0 sets the initial threshold velocity U_{c0} . If $U > U_{c0}$, a tube is extruded at a velocity $\dot{L} = \frac{dL}{dt}$ given by the force balance equation:

$$U - \dot{L} = U_{c0} \quad (9.6)$$

As the tube grows, the excess surface area of the vesicle decreases, and the membrane tension σ increases. The relative area extension $\Delta A/A$ is related to the membrane tension σ by [Servuss et al., 1976]:

$$\frac{\Delta A}{A} = \frac{k_B T}{8\pi\kappa} \ln\left(\frac{\sigma}{\sigma_0}\right) \quad (9.7)$$

For a tube of length L and of radius r , $\Delta A = 2\pi Lr$ and $A = 4\pi R^2$. As L grows, σ increases and, according to Eq. 9.5, U_c increases until the growth stops when $U_c = U$. This fixes the membrane tension σ_∞ from Eq. 9.5. Inserting r and σ into Eq. 9.7 leads to:

$$L_\infty = \tau_0 U \ln\left(\frac{U}{U_{c0}}\right) \quad (9.8)$$

$$\frac{L}{L_\infty} = 1 - \exp\left(-\frac{t}{L_\infty} (U - U_{c0})\right) \quad (9.9)$$

where the characteristic time $\tau_0 = \frac{3k_B T R^3 \eta}{2\pi\kappa^2}$ strongly depends upon the size R and the curvature modulus κ of the vesicle. The extrusion time deduced from Eq. 9.9: $\tau = \frac{U - U_{c0}}{L_\infty} \simeq \tau_0 \left(1 + \ln \frac{U}{U_{c0}}\right)$ depends weakly upon U . When we stop the flow, the force balance equation becomes $\dot{L} = -U_c$ and leads to:

$$L = \tau_0 U \exp\left(-\frac{t}{\tau}\right) - \tau U_{c0} \quad (9.10)$$

This approximate solution describes well the retraction dynamics that starts at $L = L_\infty$ and $\dot{L} = -U$ and ends at $L = 0$ and $\dot{L} = -U_{c0}$ after a time $\tau_{retract} \approx \tau \ln(U/U_{c0})$. Experiments by [Borghini et al., 2003b], on nanotube extrusion from DOPC vesicles have confirmed the validity of Eq. 9.8, 9.9 and 9.10 which lead to a measurement of $\kappa \sim 10 k_B T$ for such bare vesicles.

9.3.2 Nanotether extrusion on chitosan-coated GUVs

As observed for bare vesicles, above a threshold flow velocity U_c , the extrusion of a lipidic tube is obtained from chitosan-coated GUVs. The variation of the extruded tube length L as a function of time is measured during hydrodynamic tube extrusion and retraction experiments.

Results show differences with respect to those got for bare vesicles.

First of all, while retraction curves follow the expected exponential behavior of Eq. 9.10 as illustrated in Figure 9.7, extraction regimes for applied forces higher than 5 pN are characterized by an erratic tube growth, which does not follow the expected exponential behavior obtained for bare vesicles (Eq. 9.9). This systematically observed phenomenon can be ascribed either to polymer accumulation at the neck of the tube or to transient pores induced by the increase of the membrane tension during tube extrusion.

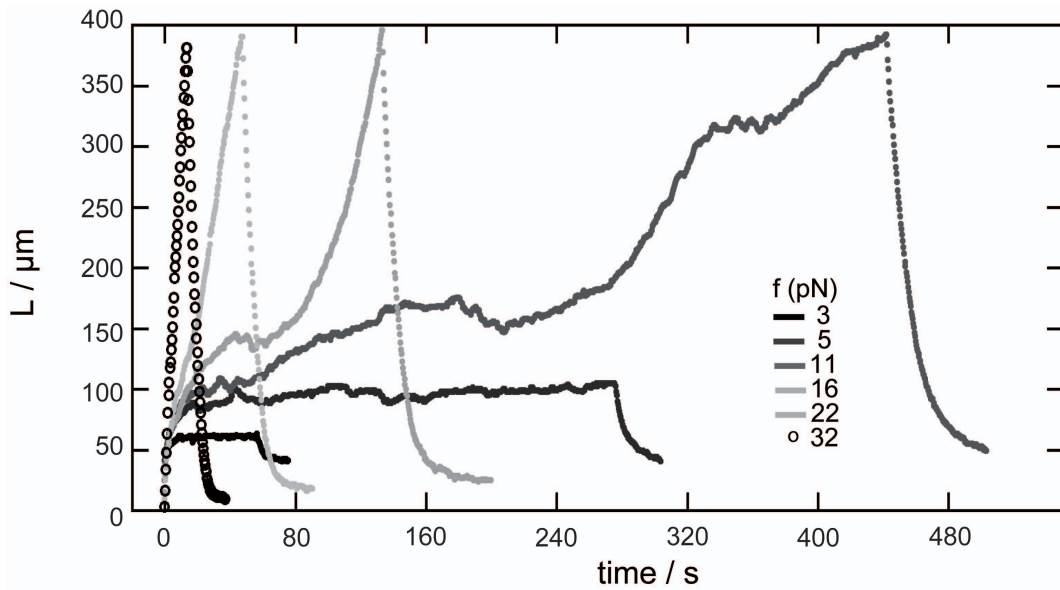


Figure 9.7: Tube extrusion and retraction dynamics from chitosan-coated GUVs for applied forces ranges from 3 to 32 pN (from the same GUV with an initial radius $R = 15 \mu\text{m}$). For extrusion forces superior to 5 pN, tube extrusion is stopped for a maximal tube length of 400 μm , which is simply the size of the camera field.

Betterton and Brenner have shown that for charged vesicles, electrostatic repulsion cause formation of transient pores [Betterton and Brenner, 1999]. Using their results, we estimate the electrostatic contribution to the surface tension for our chitosan-coated GUVs and found $\sigma \sim 2.10^{-5} \text{ N/m}$, with the Debye length $\lambda_D \sim 30 \text{ nm}$ (salt concentration in solution $\sim 10^{-4} \text{ M}$), the surface charge density $\Phi \approx \varepsilon\varepsilon_0\zeta/\lambda_D \sim 7.10^{-4} \text{ C/m}^2$ [Hunter, 1981] (ζ -potential $\sim +30 \text{ mV}$, see Figure 8.3a) and the permittivity of the external solution $\varepsilon\varepsilon_0$. Therefore, the increase of tension σ due to nanotube extrusion (of the order of 5.10^{-5} N/m for a tether length of 100 μm) at sufficiently high velocity contributes to decrease the barrier energy and to form a hole. Nevertheless, we have no direct evidence of these transient pores because of their milliseconds lifetime [Sandre et al., 1999].

Because the extrusion is erratic, we only consider the tube retraction (where no such effects can happen) to characterize the mechanical properties of the coated membrane (Figure 9.7). We measure the plateau value of the tether $L_\infty(U)$ while decreasing U step by step. As shown in Eq. 9.10 for the tube retraction, the asymptotical limit at infinite times provides a measurement

of the threshold extrusion velocity U_{c_0} . This parameter is calculated from the slope of $L(t)$ at the end of the retraction for different coated vesicles at different velocities. From the curves presented in Figure 9.7, we measure an average velocity $U_{c_0} = 0.34 \pm 0.15 \mu\text{m/s}$ corresponding to a Stokes force $f = 0.1 \pm 0.04 \text{ pN}$. So, the second difference with bare vesicles is that, for chitosan-coated vesicles, the values of U_{c_0} and consequently of f are dramatically lower than for bare vesicles ($f = 5 \text{ pN}$ reported by [Borghini et al., 2003b]); in other words, tubes of chitosan-coated vesicles are extruded at flow speeds of the order of a few $\mu\text{m/s}$ whereas for bare vesicles, the velocities are ten times larger.

Figure 9.8 shows the evolution of the tube length versus time for decreasing flow velocities. This allowed us to investigate the evolution of L_∞ versus flow velocity using classical theoretical framework. Fitting the curve $L_\infty(U)$ with Eq. 9.8 leads to the characteristic time associated to the relaxation $\tau_0 = 2.7 \text{ s}$ and $U_{c_0} = 9.2 \times 10^{-2} \mu\text{m/s}$. From U_{c_0} , we obtain a value of the initial membrane tension $\sigma_0 = 1.5 \times 10^{-10} \text{ N/m}$. We never observed large membrane fluctuations that should occur at such a low membrane tension. This clearly shows evidence that the model used for DOPC bare vesicles is not suitable to describe the behavior of chitosan-coated vesicles.

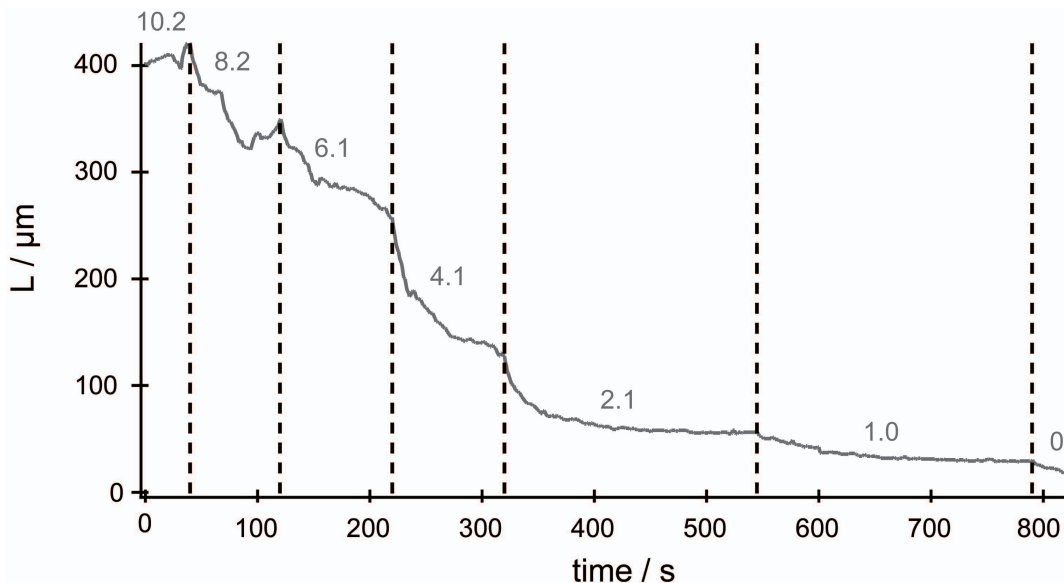


Figure 9.8: Tube length versus time for step-by-step decreasing forces: after a tube length of $400 \mu\text{m}$ is reached for a Stokes force of 10.2 pN , the fluid velocity is progressively reduced to observe the evolution of the stationary length for different Stokes forces (values in grey varying from 10.2 to 0 pN), $R = 15 \mu\text{m}$.

9.3.3 Proposed model to describe the tube extrusion from vesicles presenting a membrane asymmetry

The membrane of these modified vesicles is coated only on the external leaflet which interacts with the polyelectrolyte solution. This results in a membrane asymmetry, which induces a spontaneous curvature c_0 . Kremer and Brochard-Wyart have proposed an extension of the static model presented earlier to the dynamics of tube formation from membranes with a spontaneous curvature [Derenyi et al., 2007, Kremer, 2009] in order to describe the present results.

In the following, we assume that the extruded tube exhibits the same coverage degree that the whole coated vesicle as shown in section 9.2.1; chitosan desorption on the tube due to the change in curvature during the extrusion is in this study neglected.

With a spontaneous curvature term c_0 , the free energy of the vesicle F is given by:

$$\frac{F}{2\pi rL} = \frac{\kappa}{2} \left(\frac{1}{r} - c_0 \right)^2 + \sigma' = \frac{\kappa}{2r^2} - \frac{\kappa c_0}{r} + \sigma \quad (9.11)$$

where $\sigma = \sigma' + \kappa c_0^2/2$ is the global membrane tension. In a micropipette experiment, σ would be fixed by the aspiration pressure. σ' is the tension of the “bare” lipid membrane and corresponds to the energy required to maintain it flat. Derivation of free energy at constant volume $\Omega = 2\pi r^2 L$ provides an expression of the extrusion force:

$$f = \left(\frac{\partial F}{\partial L} \right)_{\Omega} = 2\pi \left(\frac{\kappa}{r} - \kappa c_0 \right) = 2\pi \left(\sqrt{2\kappa\sigma} - \kappa c_0 \right) \quad (9.12)$$

Thus, for $\sigma < \kappa c_0^2/2$, $f < 0$ and the vesicle spontaneously ejects tethers without being submitted to an external force as predicted previously [Derenyi et al., 2007] and observed during the osmotic deflation of chitosan-coated GUVs (see Figure 9.1). When $\sigma > \kappa c_0^2/2$, the tether extrusion requires the application of an external force. In this latter case, two situations can arise depending on the membrane tension $\sigma'_0 = \sigma'_{(t=0)}$ at the beginning of the extrusion experiment. When $\sigma'_0 \gg \kappa c_0^2/2$, the effect of spontaneous curvature can be neglected and the analysis presented above for membrane without spontaneous curvature is valid. When $\sigma'_0 \ll \kappa c_0^2/2$, the effect of spontaneous curvature has to be considered.

In the following, we assume that spontaneous curvature effect dominates at the beginning of extrusion ($\sigma = \sigma' + \kappa c_0^2/2$ with $\sigma'_0 \ll \kappa c_0^2/2$). The threshold extrusion velocity U_{c0} is given by the equality of extrusion and Stokes forces:

$$6\pi\eta R U_{c0} \cong 2\pi \frac{\sigma'_0}{c_0} \quad (9.13)$$

For $U > U_{c0}$, we consider two new cases according to whether σ'_∞ is small or large compared to $\kappa c_0^2/2$. In the first case ($\sigma'_\infty \ll \kappa c_0^2/2$), the equilibrium between extrusion force for $\sigma' = \sigma'_\infty$ (Eq. 9.12 with the square root term simplified) and Stokes force gives:

$$6\pi\eta R U \cong 2\pi \frac{\sigma'_\infty}{c_0} \quad (9.14)$$

Eq. 9.13 and 9.14 lead to:

$$\frac{\sigma'_\infty}{\sigma'_0} = \frac{U}{U_{c0}} \quad (9.15)$$

and tube radius r is given by:

$$\frac{1}{r} = c_0 + \frac{3\eta R U}{\kappa} \quad (9.16)$$

9.3. POINT-ACTING FORCE: HYDRODYNAMIC EXTRUSION OF TUBES FROM CHITOSAN-COATED

If we replace in the Helfrich relation, Eq. 9.7, σ'_∞/σ'_0 and the radius r by their respective expressions given by Eq. 9.15 and 9.16, we finally obtain

$$L_\infty = \frac{1}{2}\tau_0(U_c^* + U)\ln\left(\frac{U}{U_{c0}}\right) \quad (9.17)$$

where

$$U_c^* = \frac{\kappa c_0}{3\eta R} \quad (9.18)$$

and

$$\tau_0 = \frac{3k_B T R^3 \eta}{2\pi\kappa^2} \quad (9.19)$$

Eq. 9.17 is valid for $U < U_c^*$. $L_\infty(U)$ varies logarithmically with an inflexion point for $U = U_c^*$.

At large velocities ($U \gg U_c^*$), where $\sigma_\infty \gg \kappa c_0^2$, the expression of the extrusion force is approximately

$$f = 2\pi\sqrt{2\kappa\sigma_\infty} = 2\pi\frac{\kappa}{r} \quad (9.20)$$

Equilibrium between extrusion force and Stokes friction leads to:

$$\sigma_\infty = \frac{(3\eta R U)^2}{2\kappa} \quad (9.21)$$

and

$$\frac{1}{r} = \frac{3\eta R U}{\kappa} \quad (9.22)$$

From Eq. 9.14, always valid for $\sigma_0 = \kappa c_0^2/2$, we can determine σ_∞/σ_0 :

$$\frac{\sigma_\infty}{\sigma_0} = \frac{3\eta R U^2}{2\kappa c_0 U_{c0}} \quad (9.23)$$

Anew, replacing σ_∞/σ_0 and the tether radius r in the Helfrich relation, Eq. 9.7, by their respective expressions given by Eq. 9.22 and 9.23, we obtain finally:

$$L_\infty = \tau_0 U \ln\left(\frac{U}{\sqrt{2U_{c0}U_c^*}}\right) \quad (9.24)$$

At large velocities, the law for $L_\infty(U)$ is identical to the classical law (Eq. 4) with a renormalized threshold velocity $\tilde{U}_{c0} = \sqrt{2U_{c0}U_c^*}$.

To summarize, as a function of U , L_∞ is given by

$$L_\infty = \begin{cases} \frac{1}{2}\tau_0(U_c^* + U)\ln\left(\frac{U}{U_{c0}}\right) & \text{when } U_{c0} < U < U_c^* \\ \tau_0 U \ln\left(\frac{U}{\sqrt{2U_{c0}U_c^*}}\right) & \text{when } U > U_c^*. \end{cases}$$

where U_c^* corresponds to the inflexion point in the curve $L_\infty(U)$.

9.3.4 Interpretation of the experimental results with the membrane spontaneous curvature

We determine L_∞ as a function of flow velocities U , presented in Figure 9.9a for 4 different coated vesicles. The inflexion point of the curves estimated graphically gives the characteristic velocity $U_c^* = 11.8 \pm 2.6 \mu\text{m/s}$. The black line is an adjustment with Eq. 9.17 for one of the vesicles presented (vesicle 2). For $U > U_c^*$, the intersection between fit extrapolation (grey line) and axe $L_\infty=0$ corresponds to $\sqrt{2U_{c0}U_c^*}$.

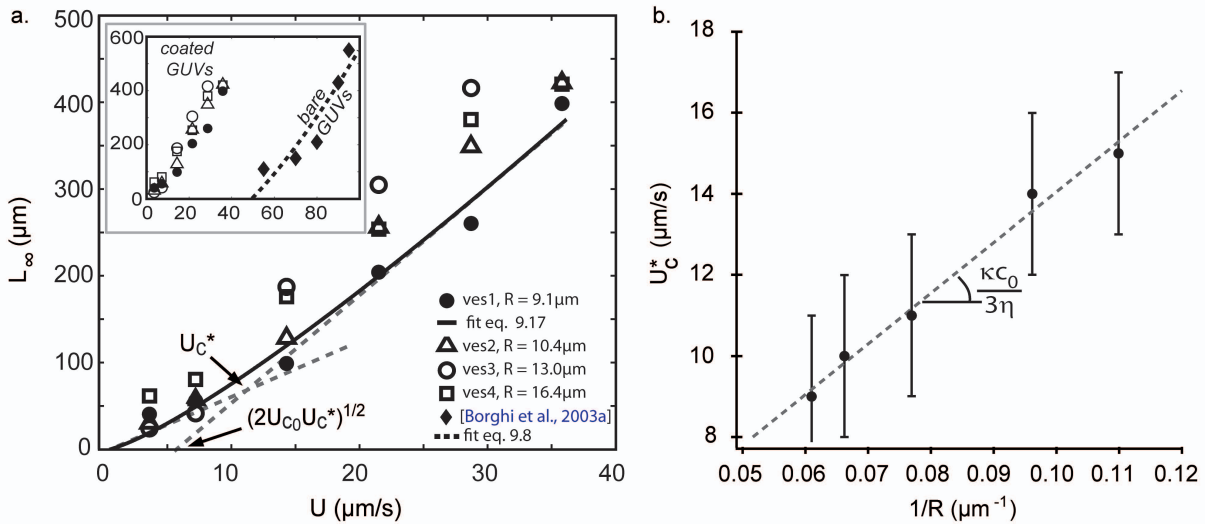


Figure 9.9: (a) Stationary length of the tube as a function of flow velocity (data from 4 different vesicles). From the inflexion point of the curve, we estimate the characteristic velocity U_c^* ($14 \mu\text{m/s}$ for vesicle #2: ves2), the intersection between fit extrapolation (grey dashed line) and axe $L_\infty=0$ corresponds to $\sqrt{2U_{c0}U_c^*}$ and gives the value of U_{c0} ($1.75 \mu\text{m/s}$ for ves2). Data of ves2 are fitted by Eq. 9.17 with the value of U_c^* and U_{c0} obtained previously, black line. Inset: $L_\infty(U)$ for chitosan-coated vesicles and for bare vesicles (solid diamonds, data from [Borghini et al., 2003b]) fitted by Eq. 9.8. (b) U_c^* versus $1/R$ curve gives a value for the spontaneous curvature $c_0 = 9.4 \pm 0.6 \mu\text{m}^{-1}$.

The spontaneous curvature c_0 is calculated from Eq. 9.18: the slope U_c^* versus $1/R$ curve (Figure 9.9b) gives a value for the spontaneous curvature $c_0 = 9.4 \pm 0.6 \times 10^{-3} \text{ nm}^{-1}$, assuming that $\kappa \approx 10 k_B T$. This allows the evaluation of the initial tension σ_0 and the threshold extrusion force f_0 from Eq. ?? and 9.13, for the different vesicles presented here; σ_0 lies between 0.8 and $3.7 \times 10^{-7} \text{ N/m}$ and f_0 between 0.4 and $3.4 \times 10^{-1} \text{ pN}$. The values of U_{c0} are coherent with values obtained at the end of retraction curves presented in Figure 9.7 (average value $0.34 \mu\text{m/s}$). The measurements of σ_0 are also in agreement with usual values of membrane tension. Finally, the values of the threshold extrusion force f_0 are much lower than for bare vesicles.

To sum up:

- Chitosan-coated vesicles show peculiar tether extrusion dynamics which can be attributed to the formation of membrane transient pores favored by electrostatic effects.

- Asymmetrical chitosan coating on the external vesicle surface (at pH = 6.0) induces a positive spontaneous curvature of the order of $9.4 \pm 0,6 \mu\text{m}^{-1}$

In the future, it will be interesting to probe in this way the effect of the coverage degree and of the salt concentration on the spontaneous curvature induced by polyelectrolyte coating. Moreover, checking if transient pores are indeed opened upon extrusion can be considered using chitosan-coated vesicles with higher internal viscosity leading to pores of larger sizes and longer life times.

9.4 Anisotropic compression: AFM experiments

Now chitosan-coated GUVs are submitted to an anisotropic compression using AFM in the colloid probe mode in order to study the effect of the chitosan coating on the mechanical properties of the vesicles. This technique commonly used to probe microcapsules or cells has never been employed at the best of our knowledge to study GUVs. These experiments have been realized in the group of Andreas Fery (University of Bayreuth, Germany) by Frédéric Dubreuil (CERMAV, Grenoble).

9.4.1 Force/deformation of chitosan-coated vesicles

Typical loading/unloading curves obtained for a chitosan-coated GUV are presented in Figure 9.10a. On these curves, a small hysteresis is noticed and interpreted partly in terms of small plastic deformation of the vesicle. Fluorescence pictures before (a) and after (b) the series of measurements confirm that there is no modification of the vesicle shape.

On the unloading curve slight adhesion between the bead and the chitosan from the coated surface can be evidenced via small jumps in the force curve corresponding to the desorption of some chain segments from the glass bead. Nevertheless, no modification of the vesicle mechanical response is induced since for successive deformations (around 10) on the same vesicle no change in the force curve is noticed, demonstrating that this force curve is perfectly reproducible as shown by the dotted line on Figure 9.10a.

These results are in pronounced difference to those obtained previously for lipidic LUVs in gel state [Delorme and Fery, 2006] or for crystalline catanionic aggregates of similar membrane structure [Delorme et al., 2006, Delorme et al., 2007]. In those systems, force-deformation data showed characteristic events, which could be explained by buckling instabilities of the membrane (see section 5.2.2). Such instabilities are not observed in the present case. This is consistent with the fluid nature of the membrane, which lowers the critical force for buckling so that it can no longer be detected.

We performed measurements on fifty vesicles with different diameters and we observe that the elastic response of the vesicle depends clearly on their radii which vary, in our experimental conditions, from 0.6 to 3.7 μm . Two examples are shown in Figure 9.10b: an increase of the

stiffness of the coated membrane is noticed when the radius of the vesicle increases.

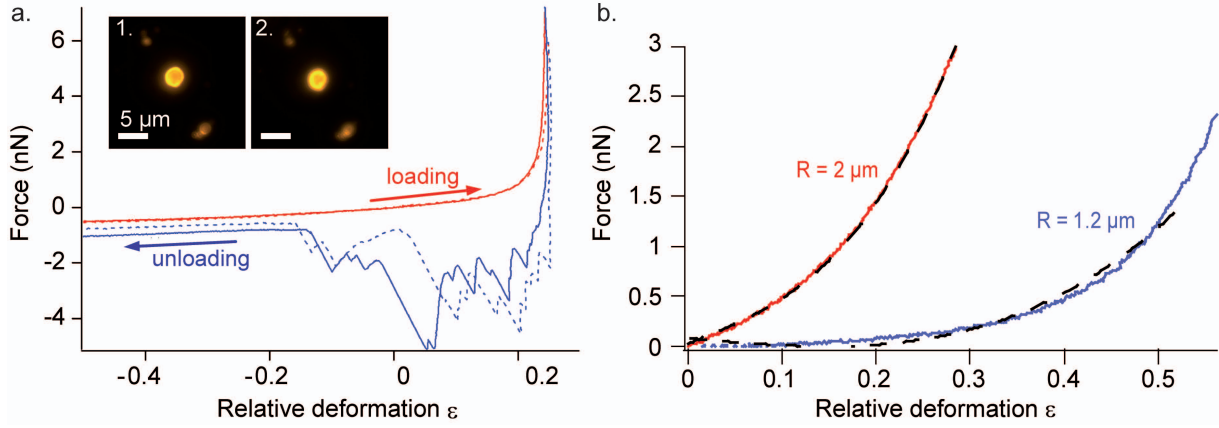


Figure 9.10: (a) Typical loading (red)/unloading (blue) curves on a 2 μm radius coated vesicle. Two successive curves (plain and dotted lines) are represented. Insets show the vesicle before (1) and after (2) the experiment. (b) Loading curve obtained for coated vesicles with two different radii (1.2 and 2 μm) at high degree of coverage. Dotted lines correspond to a fit of the force via a simple elasticity model described in the following (Eq. 9.27).

9.4.2 Model for result interpretation

Since the force/deformation hysteresis is small and since the vesicles are supposed to be impermeable at the AFM experiment time scale, we can, in a first approximation, neglect drainage of the water through the vesicle membrane and assume that the vesicle volume does not change during this experiment (i.e. less than 1 second is necessary to obtain the loading/unloading curve). Under this assumption, the simple model, which has been described by [Lulevich et al., 2004] for the deformation of impermeable elastic capsules, can be used. The coated membrane of these vesicles is regarded from a mechanical point of view as an homogeneous and isotropic material, modeled with an elastic surface [Feynman et al., 1966, Landau and Lifshitz, 1986].

In this model, the force response f of the system is expressed as the sum of two terms, one coming from the bending energy and the other one from the stretching energy of the elastic shell (section 5.3.1). Provided that the radius of the colloidal probe is much larger than the radius of the vesicle (which is always the case in practice), the force response of the coated vesicle is then:

$$f = \frac{\pi}{\sqrt{2}} Y_{2D} d \epsilon^{1/2} + 2\pi \frac{Y_{2D}}{1 - \nu_{2D}} R_0 \epsilon^3 \quad (9.25)$$

where d is the thickness, Y_{2D} the 2D Young modulus and ν_{2D} the 2D Poisson's ratio of the coated membrane.

Comparing the reaction forces due to bending (which scales as $\epsilon^{1/2}$) and stretching (which scales as ϵ^3), one can conclude that, for typical experimental values, where $d \sim 10$ nm (for the

membrane coated with a polyelectrolyte layer) [Leonenko et al., 2004, Kujawa et al., 2005] and $R_0 = 1 \mu\text{m}$, the bending contribution in Eq. 9.25 is negligibly small for relative deformations $\epsilon \geq 7.5 \times 10^{-2}$. Within our experimental conditions (a large range of deformation) this contribution was not observed. In this case the force response of the coated vesicle is dominated by the stretching term and can be expressed as:

$$f = 2\pi \frac{Y_{2D}}{1 - \nu_{2D}} R_0 \epsilon^3 \quad (9.26)$$

Since the 2D stretching modulus is generally used in the literature, we transform this expression using the relationship between the 2D Young modulus and the 2D stretching modulus ($\chi_{2D} = \frac{Y_{2D}}{2(1-\nu_{2D})}$; Appendix B), leading to:

$$f = 4\pi\chi_{2D}R_0\epsilon^3 \quad (9.27)$$

This expression adjusts well with the experimental data as shown on Figure 9.10b: the radius of the vesicle (R_0) is determined optically and the adjustment is realized with the stretching modulus χ_{2D} . In this case, the model predicts the dependence of the reaction force with the radius of the vesicle which is observed in our experiments. We underline that the Hertz model [Laney et al., 1997] usually used for this type of analysis [Liang et al., 2004] does not explain this radius dependency of the elasticity [Delorme and Fery, 2006].

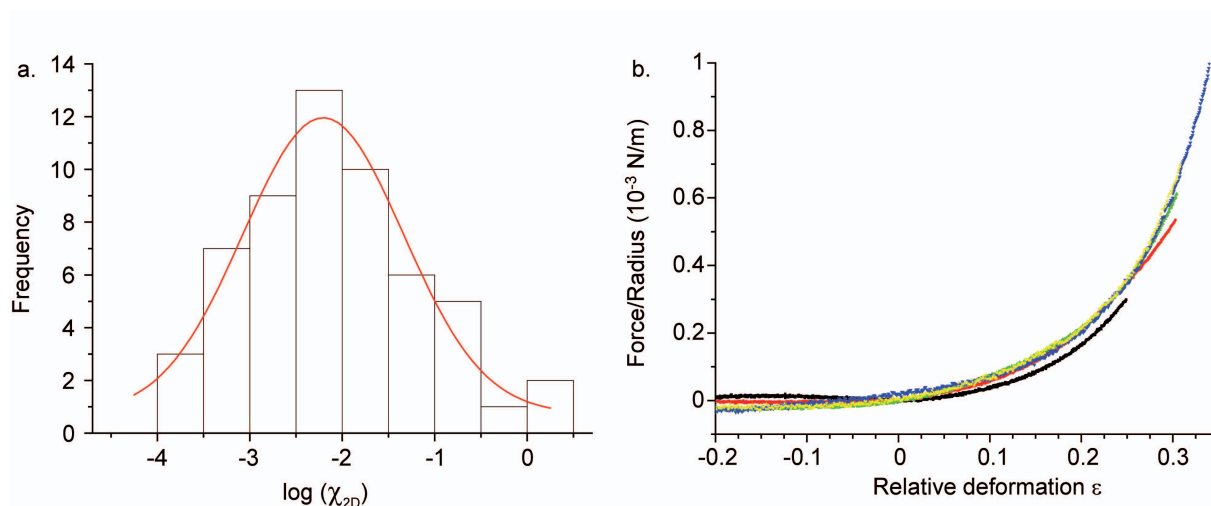


Figure 9.11: (a) Distribution of the Eh fitting parameters obtained on the different vesicles tested. (b) Normalized loading curve obtained for vesicles with different radius (from 0.9 to 3.1 μm) and same χ_{2D} equal to 6.3 mN/m .

An analysis of a large number of vesicles allows the establishment of a statistic of the fitting parameter χ_{2D} in order to deduce its most probable value. The distribution of the χ_{2D} parameter is presented in Figure 9.11a.

A Gaussian fit of the distribution of χ_{2D} among the fifty five chitosan-coated vesicles tested allows the determination a most probable value equals to 10 mN/m . From the width of the distribution, experimental values for χ_{2D} range from 1 to 45 mN/m . This dispersion may be

attributed to uncontrolled tension of the membrane due to interactions with the glass substrate despite the PEG treatment.

Taking into account vesicles with different radius (from 0.9 to 3.1 μm) but with the same $\chi_{2D} = 6.3 \text{ mN/m}$, we can draw in Figure 9.11b, a master curve representing the force-deformation normalized by the vesicle radius as predicted by Eq. 9.27.

Moreover, we assessed an estimate of the stretching modulus of $\sim 1 \text{ mN/m}$ for bare DOPC GUVs. We want to emphasize the increase of the stretching modulus due to the polyelectrolyte coating. Those results are in good agreement with recent measurements published for lipid monolayer in contact with chitosan [Pavinatto et al., 2010].

Complementary analysis of our data for the small deformation seems also interesting to probe the bending contribution.

Finally, to sum up,

- AFM compression experiments is demonstrated to be an interesting technique to probe global mechanical properties of GUVs.
- Reproducible and reversible force-deformation curves for individual chitosan-coated vesicles allows the determination of a stretching modulus of the order of 10 mN/m for chitosan-coated vesicles at the maximum coverage degree.

9.5 Conclusion

Studies of the behaviors of chitosan and hyaluronan coated GUVs under various applied constraints show that:

- **Polyelectrolyte coating strongly modifies the GUVs responses under stress, as:**
 - ✓ the enhancement of the GUVs **resistance against pH and salt shocks**.
 - ✓ **specific behaviors** attributed to the asymmetrical coating.
 - ✓ the absence of observable membrane fluctuations.
- **Electrostatic interactions control the observed behaviors:**
 - ✓ the electrostatic screening (*e.g.* with salt) allows a **transition from positive to negative membrane spontaneous curvature contribution**.
 - ✓ the electrostatic repulsions cause the **formation of membrane transient pores** in coated membrane for membrane tension two orders of magnitude lower than for bare ones.
- These studies under control stresses allow a first **determination of two mechanical parameters** of chitosan coated GUVs: the **membrane spontaneous curvature** and its **stretching modulus**.

In the future, it will be interesting to extend this study to the role of the coverage degree, of the polymer structure (e.g. hydrophobic polyelectrolyte derivatives) and of external parameters (e.g. pH or salt concentration) on the mechanical properties and the stability of coated GUVs. Measurements of the membrane fluctuation spectrum on such objects will be envisaged.

For the first time in this study, we have demonstrated that the AFM technique allows the determination of mechanical parameters of isolated GUVs, which open interesting perspectives in the characterization of composite vesicles.

observed plenty of vesicles in solution, an important reduction of the number of vesicles in solution has been observed upon temperature reduction. At 15°C, only few vesicles stay in solution and they always exhibited a poor optical contrast indicating compromised membrane integrity and imperfections such as membrane buds. Therefore, most of the vesicles were broken when lipid membrane is frozen at temperatures below T_m .

In fact, a loss of membrane surface area created by the ordering of the lipids occurs upon a temperature decrease, as reported in section 2.2. In our case, the loss of surface area leads to a decrease of the encapsulated volume; the vesicles water is ejected from the inner medium, which induces an increase of the inner sucrose concentration. Therefore, the bursting of vesicle may be due to the resulting increase in osmotic pressure.

10.1.1 Preparation of spherical DMPC GUVs with membrane in $P_{\beta'}$ gel phase at 15°C

To avoid the bursting of vesicles undergoing the transition between fluid and gel phase, we have controlled the external sucrose concentration in order to compensate the loss of surface ($\Delta A_{T-T'}$) induced by a decrease of temperature from the initial temperature T to the final temperature T' . The loss of volume ($\Delta V_{T-T'}$) is related to the loss of surface as:

$$\frac{\Delta V_{T-T'}}{V_T} = 1 - \left(\frac{A_{T'}}{A_T} \right)^{3/2} \quad (10.1)$$

Moreover, the relative volume variation is given in first approximation as the ratio of the concentrations $C_{initial}$ at the initial temperature and C_{final} at the final temperature:

$$\frac{\Delta V_{T-T'}}{V_T} \sim 1 - \frac{C_{initial}(T)}{C_{final}(T')} \quad (10.2)$$

We obtain finally the sucrose concentration necessary to compensate the loss of surface area:

$$C_{final}(T') = \frac{C_{initial}(T)}{\left(1 - \frac{\Delta A_{T-T'}}{A_T} \right)^{3/2}} \quad (10.3)$$

By applying this relationship to the results previously obtained by [Needham and Evans, 1988] (Figure 2.9a), we calculate the adjustment of concentration necessary to compensate the loss of surface as function of the temperature. Figure 10.1 shows this concentration adjustment for DMPC GUVs prepared at $T = 30^\circ\text{C}$ with $C_{initial} = 100$ mM.

Experimentally, to obtain GUVs with membrane in the rippled gel phase ($P_{\beta'}$) at 15 °C, the temperature is slowly decreased with a cooling rate of 0.05 °C/min and successive additions of a 200 mM sucrose solution are carried out each 0.5 °C steps in accordance with the adjustment of concentration reported in Figure 10.1, such as a final sucrose concentration of 164 mM is

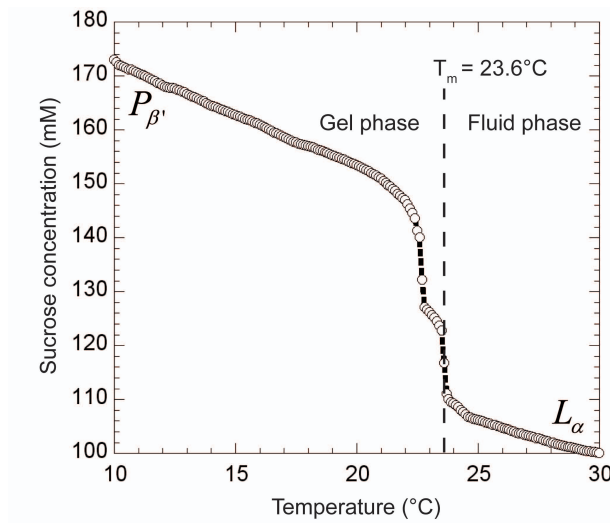


Figure 10.1: Adjustment of sucrose concentration necessary to compensate the loss of membrane surface area in DMPC vesicles filled with a 100 mM sucrose solution at 30°C, as function of the temperature, in order to obtain spherical vesicles with membrane in the $P_{\beta'}$ gel phase. This graph is obtained from the Figure 2.9a, by using the Eq. 10.3.

obtained at 15 °C. Vesicle suspension is finally stored at 15 °C in a 164 mM sucrose solution before use. Vesicles obtained with this protocol are spherical and present no observable defects in the membrane (see Figure 10.2 line (a)).

10.1.2 Deflation of gel phase GUVs associated with formation of depressions

Osmotic shocks are induced by addition of glucose solutions at different concentrations into the GUVs suspension at 15°C, as detailed in section 6.5. Upon the glucose shock, gel phase GUVs shrink forming concave faceted shapes as illustrated in Figure 10.2a. The final state is reached around 40 minutes after the beginning of the deflation, and, thereafter, no shape modification is observed over few hours, when temperature and osmotic pressure are kept constant.

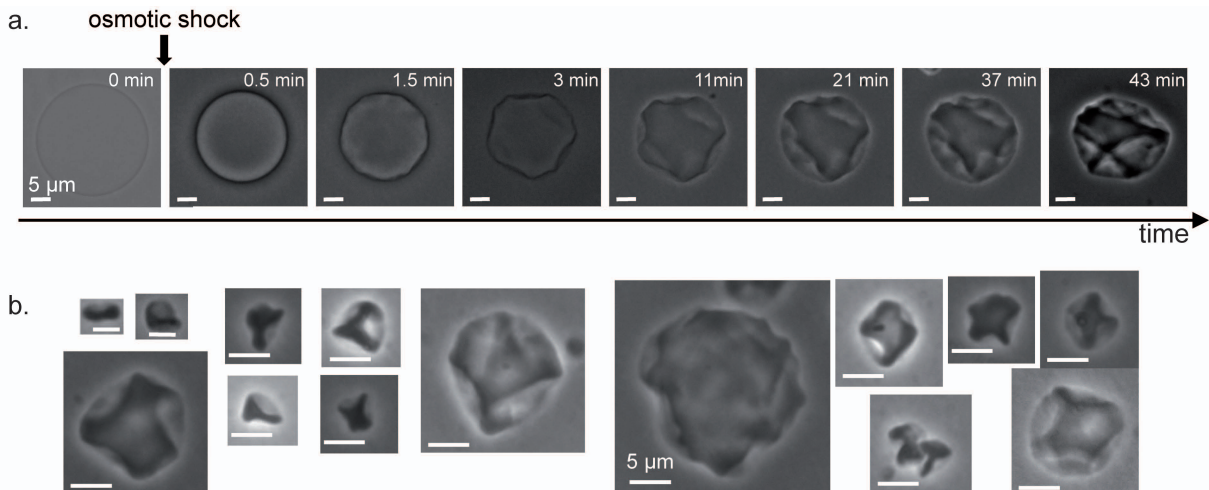


Figure 10.2: DMPC vesicles at 15°C under osmotic shocks. (a) Time sequence of a GUV deflation at a reduced volume $V_R = 0.45$ ($\Delta C = 200$ mM). (b) Equilibrium shapes observed for vesicles of different initial radius ($V_R = 0.6$; $\Delta C = 110$ mM). The scale bars represent 5 μm .

The shapes obtained (Figure 10.2b) are totally different from those observed with a fluid membrane (see the ADE shape phase diagram in Figure 5.4, [Döbereiner, 2000]). A large variety of morphologies is observed when vesicle size increases, from stomatocytes to concave polyhedra (*i.e.* sphere paved with depressions).

10.2 Numerical simulations of an elastic surface under an isotropic pressure

In order to quantitatively understand these specific shapes, we modeled the 2D solid-like gel phase membrane by a surface with mean curvature elasticity (bending modulus κ ¹) and in-plane Hookean deformation elasticity [Ben-Amar and Pomeau, 1997, Landau and Lifshitz, 1986] determined by two parameters such as 2D Young modulus Y_{2D} and 2D Poisson's ratio ν_{2D} (the relationships between the different elastic parameters ($\kappa, \mu, \chi, Y_{2D}, \nu_{2D}$) are detailed in Appendix B). The initial state is a spherical surface of radius R , enclosing the initial volume V_0 . We assume that the freezing of the $P_{\beta'}$ gel phase in the spherical conformation induces a spontaneous curvature of $2/R_0$ in the Helfrich energy [Helfrich, 1973], which corresponds to an initial unstrained surface.

Dimension analysis brings light onto three dimensionless parameters possibly controlling the shape at some volume $V < V_0$: the deflation $\frac{\Delta V}{V} = \frac{V_0 - V}{V_0} = 1 - V_R$ (V_R is the reduced volume), the Föppl-von Kármán number $\gamma = \frac{Y_{2D} R^2}{\kappa}$ [Lidmar et al., 2003], and the Poisson's ratio ν_{2D} (maximum value 1, for incompressible surfaces). Numerical study is then performed by decreasing the volume through small steps ($\approx 0.6\%$ of V_0), and searching for an equilibrium shape at each step by minimizing the integral of the surface energy using the finite element Surface Evolver software [Brakke, 1992]:

$$H_{elastic} = \iint_{surface} \left(\frac{\kappa}{2} \left(C - \frac{2}{R_0} \right)^2 + \frac{1}{2} \epsilon_{ij} K_{ijkl} \epsilon_{kl} \right) dS \quad (10.4)$$

where C is the mean curvature (everywhere equal to $2/R_0$ in the initial sphere), and the non-zero terms of the two-dimensional elasticity tensor are $K_{iiii} = \frac{1}{\nu_{2D}} K_{iijj} = \frac{1}{(1-\nu_{2D})} K_{ijij} = \frac{Y_{2D}}{1-\nu_{2D}^2}$ [Landau and Lifshitz, 1986]. The influence of the Gaussian curvature is neglected in our study.

Such quasi-static deflation was done for $\frac{\Delta V}{V} \in [0, 0.7]$, $\gamma \in [1.8, 2430]$, $\nu_{2D} \in [0, 0.98]$. The absolute minimum energy state which holds a single depression (see section 5.2.2) possibly wrinkled [Quilliet et al., 2008] is not of interested here, since experimental observations obviously report deflated GUVs with many depressions. Then, we focused on simulated shapes with many facets corresponding to metastable conformations.

¹Definitions of κ , as well as mean curvature, diverge between mathematicians and soft matter physicists. Here we use the latter's convention, where the energy of a spherical surface of zero spontaneous curvature is $8\pi\kappa$.

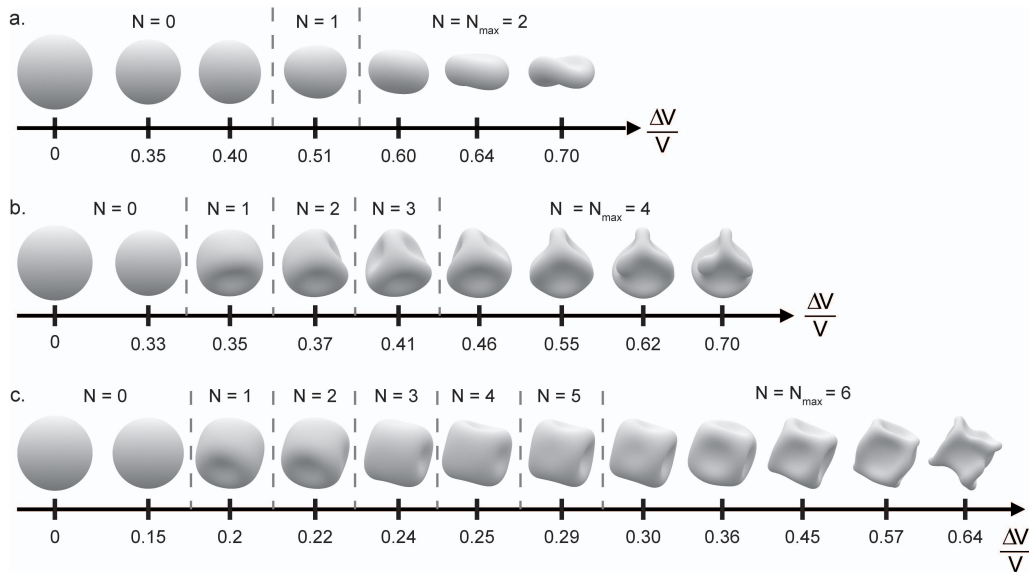


Figure 10.3: Sequences of shapes obtained by numerical simulations as a function of the deflation $\frac{\Delta V}{V_0}$. Simulation parameters: (a) Poisson's ratio $\nu_{2D} = 0.5$ and Föppl-von Karman number $\gamma = \frac{Y_{2D} R_0^2}{\kappa} = 51$; (b) $\nu_{2D} = 0.5$ and $\gamma = 135$; (c) $\nu_{2D} = 0.5$ and $\gamma = 259$. To each shape is attributed a number of depressions written between brackets; N corresponding to the maximum number of facets.

Figure 10.3 shows three examples of deflation sequences obtained by the numerical simulations. For small deflations, the surface first decreases keeping a spherical shape, then depressions (or concave faces) appear concomitantly and grow until paving the entire surface. For higher volume deflations, the shape evolves with a fixed number of depressions.

We notice that, coalescence of depressions does not occur in our simulations, i.e. no decrease of the depression number with the deflation is observed.

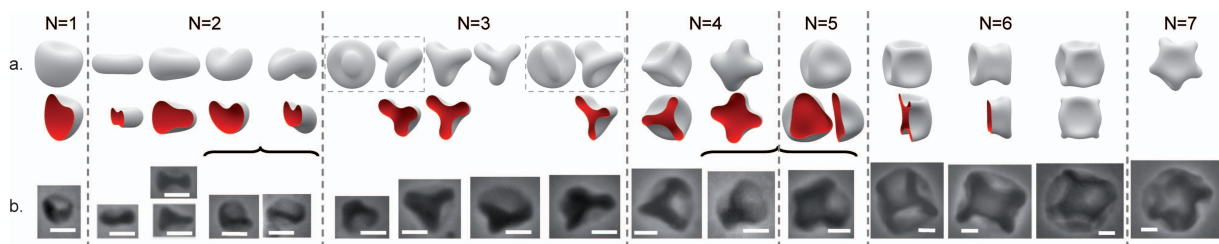


Figure 10.4: (a) Numerical simulations when either the Poisson's ratio ν_{2D} or the Föppl-von Karman number $\gamma = \frac{Y_{2D} R_0^2}{\kappa}$ increases (left to right). Each shape is characterized by an N which is the facet number of the nearest regular concave polyhedron. $N = 0$ (not shown here): sphere, oblate, untwined chestnut; $N = 1$: stomatocyte; $N = 2$: discocyte, asymmetric discocyte, bean, crisp; $N = 3$: nipple, 3-blades (or knizocyte), twisted 3-blades, bladed nipple; $N = 4$: tetrahedron, 4-blades. $N = 5$: dumbbell with triangular leg; $N = 6$: cube, dumbbell with square leg, bulged cube; $N = 7$: dumbbell with 5-star leg. (b) Experimental shapes for deflated gel phase GUVs ($V_R = 0.6$) when their radius increases. The scale bars represent $5 \mu\text{m}$.

Exploring the $(\frac{\Delta V}{V}, \gamma, \nu_{2D})$ phase diagram provided a great diversity of shapes, that for deflated enough surfaces (notion to be later clarified and illustrated in Figure 10.7) always take place within a reproducible succession, displayed on of Figure 10.4a. This succession provides a

way to quantify shapes: for some of them indeed (discocyte, 3-blades, tetrahedron, cube etc), it is possible to define the number N of depressions. When this notion becomes questionable (*e.g.* bean, nipple), an indirect attribution can be done by continuity in the succession. For $N > 6$, shapes resume to concave polyhedra, bulged (*i.e.* with a protuberance on the rims that separate two faces) or not. For N corresponding to the number of facets of regular polyhedra (6, 8, 12, 20), one retrieves quite regular shapes such as seen on biological objects like virus [Lidmar et al., 2003] and desiccated pollens [Katifori et al., 2010] (*e.g.* mahonia, ligustrum).

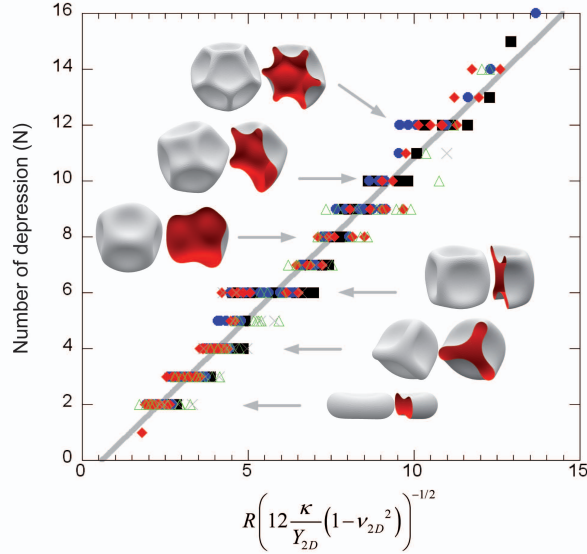


Figure 10.5: Surface Evolver simulations: generalized number of depressions N of the deflating spherical surface, as a function of its initial radius, normalized by $d_{eq} = \sqrt{12 \frac{\kappa}{Y_{2D}} (1 - \nu_{2D}^2)}$. Black solid squares: $\nu_{2D} = 0$ to 0.25 ; Blue disks: $\nu_{2D} = 0.3$ to 0.5 . Red solid diamonds: $\nu_{2D} = 0.55$ to 0.75 . Open green triangles: $\nu_{2D} = 0.8$ to 0.90 . Grey crosses: $\nu_{2D} = 0.92$ to 0.98 . Master curve: for $R > 0.59d_{eq}$, $N = 1.15 (R/d_{eq} - 0.59)$ (Grey line). For lowest values of N , the shapes are classified as indicated in Figure 10.4.

Quantitative shape description allows to study separate influences of γ and ν_{2D} on N . As shown on Figure 10.5, N gathers on a master curve, quasi-linear with $\left(\frac{\gamma}{1 - \nu_{2D}^2}\right)^{\frac{1}{2}}$, for ν_{2D} ranging between 0 and 0.98. This quantity can be considered as a reduced radius $\frac{R}{d_{eq}}$, where $d_{eq} = \sqrt{12(1 - \nu_{2D}^2) \frac{\kappa}{Y_{2D}}}$ appears as a characteristic length for the deformations of the surface. It is remarkable that nonzero shear energy causes emergence of a typical length for deformation, where in curvature-only systems (incompressible fluid vesicles) the only length scale is the vesicles's radius [Döbereiner, 2000].

Furthermore, this scaling of N can be understood within the frame of thin shells deformation theory [Landau and Lifshitz, 1986] for $\nu_{2D} < 0.5$. Indeed for thin shells of an isotropic material, the Poisson's ratio ν_{2D} of the model surface in the linear approximation equals to the material's 3D Poisson's ratio ν_{3D} [Komura et al., 2005, Quilliet et al., 2008], hence limited to the maximum value 0.5 of incompressible materials. For a thin shell of thickness d submitted to an uniform pressure, buckling is known to happen through reversion of a spherical cap of size $L = \sqrt{dR}$ [Landau and Lifshitz, 1986]. Depressions proliferate through volume reduction,

up to a total tiling of the sphere surface by $N \propto \frac{R^2}{L^2}$, or $\frac{R}{d}$, depressions. Linking 2D and 3D features with $d = \sqrt{12(1 - \nu_{2D}^2) \frac{\kappa}{Y_{2D}}}$ [Landau and Lifshitz, 1986] provides the numerical scaling obtained from Figure 10.5.

10.3 Comparison between experimental and simulated shapes

The comparison between experimental and numerical shapes (Figure 10.4) allows the estimation of the number of depressions from the phase contrast microscopy observations, compensating the lack of 3D information. Figure 10.6 shows a plot of the number of depressions measured this way as a function the initial GUV radius, and evaluated for different reduced volumes ($V_R = 0.6, 0.45$ and 0.35) over more than 1300 vesicles; this range is chosen such as N does not increase by further deflation. The variation of the number of depressions is consistent with the linear dependence on the radius previously obtained in Figure 10.5, leading to the determination of a typical elastic length $d_{eq} = \sqrt{12(1 - \nu_{2D}^2) \frac{\kappa}{Y_{2D}}} \sim 1.8 \mu\text{m}$. The micrometric value of d_{eq} is orders of magnitude higher than the bilayer thickness ($\sim 5 \text{ nm}$), or the ripple periodic undulations (amplitude $\sim 1 - 11 \text{ nm}$ and wavelength $\sim 15 - 55 \text{ nm}$) [Kaasgaard et al., 2003], emphasizing that despite of their weak relative thickness, solid vesicles cannot be considered as what is commonly called “thin shells” (shells of an isotropic bulk material with a thickness d much lower than its radius R) [Marmottant et al., 2010].

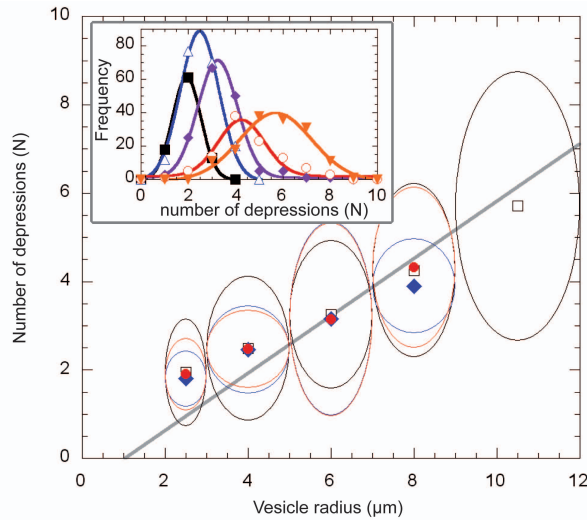


Figure 10.6: Number of depressions experimentally observed (through comparisons such as on Figure 10.4), as a function of the GUV radius. Inset shows the occurrence of facet number for each radius range (black solid squares: 2-3 μm ; blue open triangles: 3-5 μm ; violet solid diamonds: 5-7 μm ; red open circles: 7-9 μm ; orange solid triangles: 9-12 μm), at a reduced volume $V_R = 0.6$; solid lines are Gaussian fits to the data. R.m.s. of each size distribution are taken as vertical error bar in the main diagram. Black open squares: $V_R = 0.6$; blue solid diamonds: $V_R = 0.45$; red disks: $V_R = 0.35$. Curves at different reduced volume show no notable difference. Grey line is master curve of Figure 10.5 with $d_{eq} \sim 1.8 \mu\text{m}$.

This typical elastic length can be discussed taking into account previous published results on $P_{\beta'}$ gel phase DMPC vesicles, by rewriting it as $d_{eq} = \sqrt{6(1 + \nu_{2D}) \frac{\kappa}{\chi_{2D}}}$, where χ_{2D} is the

elastic area compressibility (or “stretching”) modulus. Taking $\kappa \sim 100 k_B T$ ², this leads $\chi_{2D} \approx 1 \mu\text{N}/\text{m}$. This value is very weak compared to 60 mN/m of [Needham and Evans, 1988], which was measured by micropipette aspiration technique on vesicles under very low tension, ironed except for ripples through preforming and temperature cycles. Osmotic deflation, inducing negative tension in the average membrane plane, is likely to induce fluctuations at a scale between ripples and vesicles. In the absence of a specific theory for the fluctuations of solid membranes, our study proposing a precise value for a characteristic length undoubtedly micrometric, provides a clue for a possible entropic, rather than elastic, origin of the area compressibility modulus.

Reduced volume data are considered in numerical phase diagrams of Figure 10.7, displayed as a function of $R/\sqrt{12 \frac{\kappa}{Y_{2D}} (1 - \nu_{2D}^2)}$ and $\frac{\Delta V}{V_0}$ at different Poisson’s ratio ν_{2D} (0, 0.5 and 0.8). Each shape diagram presents the number of facets $N_{transient}$, that increases with deflation (*i.e.* diminution of V_R), up to the plateau N which corresponds to the quite symmetrical shapes of Figure 10.4a. Comparison between numerical and experimental data, where the plateau in N is already reached at $V_R = 0.6$, indicate that the Poisson’s ratio ν_{2D} is very unlikely smaller than 0.8. On the other hand, a maximum limit is 0.95, where shapes begin to differ from the set displayed in Figure 10.4 (e.g. depressions are surrounded by spicules).

Such high Poisson’s ratio value confirms the fact that gel phase GUVs cannot be simply considered as thin shells of an isotropic bulk material [Landau and Lifshitz, 1986], where $\nu_{2D} = \nu_{3D} \leq 0.5$. The discrepancy between the lipidic membrane thickness d and the evaluated typical elasticity length d_{eq} may be understood by the anisotropic nature of the constitutive material, *i.e.* the rippled lipidic bilayer that obviously has different material properties in its average plane, and in the average perpendicular orientation of the lipids. The adequacy between experimental and numerical curves and shapes nevertheless shows the accuracy of a 2D elastic model with in-plane isotropy and shear energy to describe solid vesicles.

Of more general concern, simulations put into evidence a noticeable role of the Poisson’s ratio, often neglected in thin shell descriptions due to its limited range, which led to give the whole credit of the shape to Föppl-von Kármán number. Here we show that when Poisson’s ratio approaches 1, its value becomes crucial. This study, for the first time, explores the range of elastic parameters comprised between the surface model for thin shells of an isotropic material ($\nu_{2D} \leq 0.5$) and a surface with negligible shear elasticity (which is the case when $(1 - \nu_{2D}) \ll 1$), like fluid vesicles.

Besides allowing to give quantitative clues on the elastic features of gel phase lipid vesicles through mere observations, this study offers interesting insights to produce reproducible and stable structured shapes through the deformation of simple soft objects.

²In the P_β phase, $\kappa_{bilayer} = 75k_B T$ [Needham and Evans, 1988]. Even for a fluid membrane, such a value undergoes no significant logarithmic rescaling by fluctuations at the micronic scale. Locally, bending rigidification due to ripples (corrugated iron effect), calculated with geometric and elastic values of [Needham and Evans, 1988], cannot increase κ more than 180 $k_B T$ in the direction of the ripples. We thus propose, at the vesicle’s isotropic scale, 100 $k_B T$ as a sensible order of magnitude for κ .

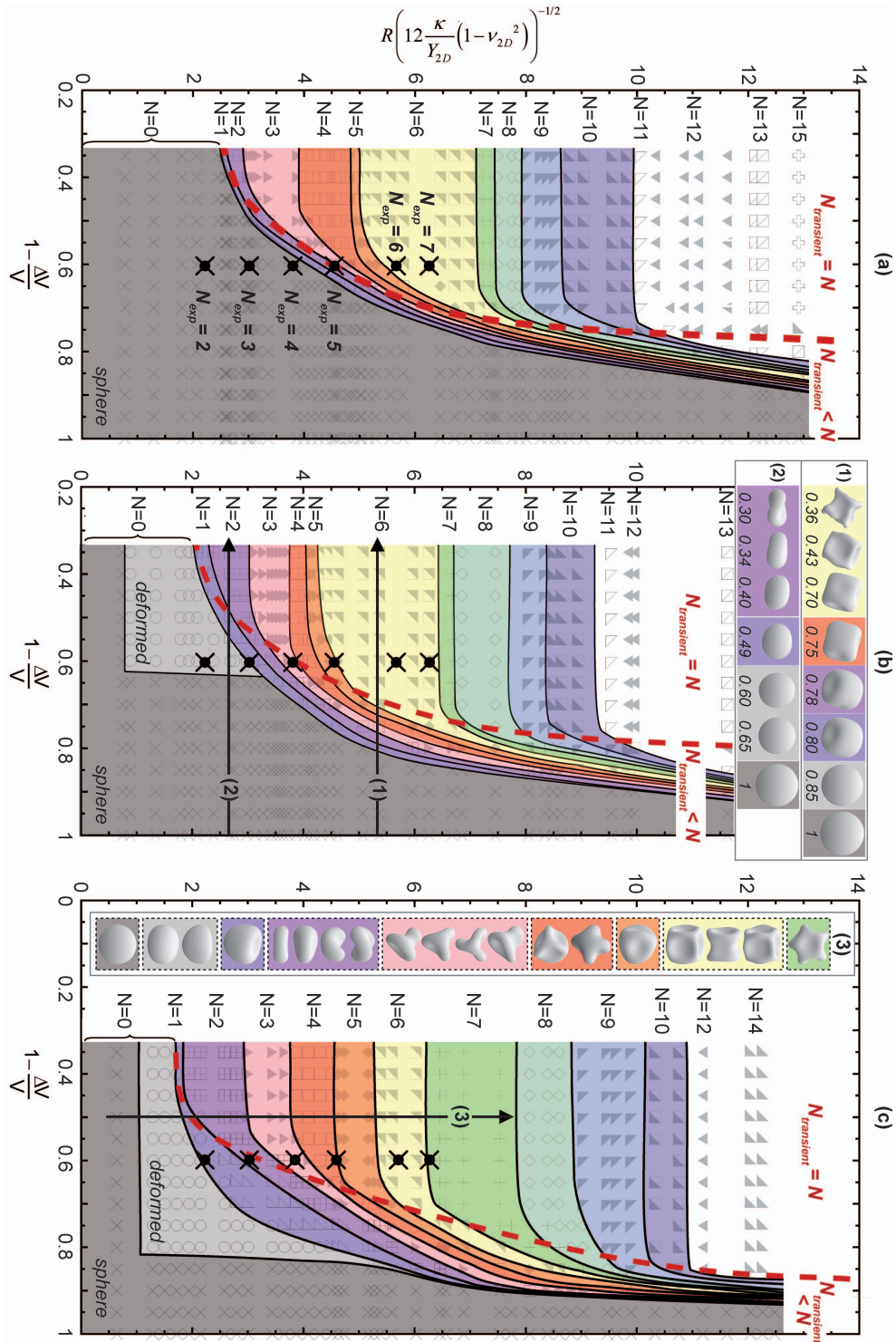


Figure 10.7: Shape phase diagrams established from Surface Evolver simulations: number of depressions $N_{\text{transient}}$ as a function of reduced volume $(V_R = 1 - \frac{\Delta V}{V_0})$ and initial radius normalized by typical elastic length d_{eq} , i.e. $R/\sqrt{12 \frac{\kappa}{Y_{2D}} (1 - \nu_{2D}^2)}$: (a) $\nu_{2D} = 0$ (b) $\nu_{2D} = 0.5$ and (c) $\nu_{2D} = 0.8$. Dark grey zones correspond to deflation with conservation of the spherical symmetry, light grey zones to non-spherical deformations without appearance of depressions and each colored zone to shapes with a given number of concave facets ($N > 0$). Red dotted lines delimit zones where the maximum number of depressions has been reached: $N_{\text{transient}} = N$. In such zones, the shape may evolve with $\frac{\Delta V}{V_0}$ like in the same sense than with γ or ν_{2D} : e.g. discocyte toward crisp (2), or cube toward bulged cube (1) presented in inset of (b), and the shape succession (3) reported in the inset of (c). Black crossed circles: experimental points obtained from the set of data at $V_R = 0.6$ of Figure 10.6; for this latter the vesicle radius is averaged for each N and non-dimensionalized by the d_{eq} obtained in Figure 10.4.

10.4 Conclusion

This chapter presents the osmotic deflation of DMPC vesicles with membrane in $P_{\beta'}$ ripple gel phase. Results obtained experimentally and numerically allow us to conclude that:

- The **deflated shapes of gel vesicles** are **facetted** (from discocyte to polyhedron-like shapes) and **stable** over few hours.
- The **number of depressions depends on the initial vesicle radius**.
- These **shape diversity** can be numerically retrieved through a **model of elastic surface** where an **in-plane elasticity** adds to the **out-of-plane bending** of vesicles in fluid phase.
- A **quantitative comparison between experiments and simulation** allows an estimation of the elastic features at the mesoscopic scale.

AFM compression experiments used on chitosan-decorated vesicles (section 9.4) would be interesting to probe buckling process (e.g. check if no plastic deformation takes place), and eventually estimate the bending and stretching modulus of these DMPC GUVs with membrane in $P_{\beta'}$ ripple gel phase.

Finally, we remark that these simulated shapes are retrieved for many biological objects such as red blood cells, virus, pollens or fruits as illustrated in Appendix C.

Chapter 11

Dynamical deformation of vesicles in fluid state under confined flows

Ce chapitre décrit le comportement de GUVs s'écoulant dans deux géométries confinées. Après une brève présentation des protocoles expérimentaux spécifiques à cette étude, nous rapportons des mesures de la déformation dynamique de vésicules et de la chute de pression associée à leur passage dans une constriction simple. Puis, nous étudions le comportement de vésicules entrant dans un canal présentant une série de constriction transversales périodiques (comparable à un rhéomètre à l'échelle de la vésicule).

o o o o o o o o o o

This chapter describes the behavior of DOPC GUVs flowing in close fitting channels. After presenting the experimental procedures specific to this study, we will report measurements of the dynamical deformation of vesicles and the pressure drop associated with their motion in a single constriction. Then, we will discuss vesicles flowing in a channel presenting a series of periodic variations of the cross-section (i.e. comparable to a vesicle-scale rheometer). These experiments have been realized with Magalie Faivre in the group of Pr. Howard A. Stone (Harvard University, USA).

11.1 Solution and experimental procedures

11.1.1 Sample Solutions

The vesicles are formed with the common technique of electroformation according to the protocol described in the section 6.1.2. The viscosity of the sucrose solution to be encapsulated is varied by addition of dextran ($M_w = 5 \times 10^5$) at various concentrations. Once formed, these viscous vesicles are suspended in a mixture of 220 mM glucose and dextran in order to respectively deflate them by osmotic shock (i.e reduced volume $V_R = 0.91$) and modify the outer medium viscosity (see Table 11.1); viscosities are measured with a cone/plate rheometer (ARES

Rheometer) at 25 °C.).

Internal media		External media		Viscosity contrast, λ
Dextran in 220mM sucrose solution (% w/w)	Viscosity (mPa.s)	Dextran in 220mM glucose solution (% w/w)	Viscosity (mPa.s)	
0	1.2	25	128.5	9×10^{-3}
2.5	3.6	25	128.5	27.5×10^{-3}
5	5.9	25	128.5	46×10^{-3}
0	1.2	10	16.6	72×10^{-3}
10	16.6	25	128.5	129×10^{-3}

Table 11.1: *Composition of the vesicles and viscosity of the internal and external medium. The corresponding viscosity contrast λ are also reported for each sample.*

11.1.2 Microfluidic devices and video-microscopy

The vesicles behavior is investigated in two different geometries: a simple long constriction and a succession of many short constrictions; the two geometries will be presented in detailed below. The microfluidic devices are manufactured using common soft-lithography techniques, as detailed in section 6.7.4 and the fluids are set into motion with a pressure driven flow approach presented earlier, leading to typical steady velocities of several cm.s^{-1} in the narrowest section of the channels.

Vesicles are observed by phase contrast microscopy. A high-speed camera (V5, Phantom) is used to follow the motion of the objects as they flow through the capillaries; typical frame rates ranging from 1000 to 5000 frame.s^{-1} .

11.1.3 Image Analysis

The image analysis of the movies is performed using a Matlab routine, which consists in detecting the vesicle outline and fitting it with an ellipse to evaluate the length of the major and minor axis ($2a$ and $2b$ respectively) and the position of the center of mass of the ellipse (x_0), as the vesicle travels through the channel as shown on the insert of Figure 11.1. In the following, we define the major and minor axis as initially along the x - and the y -direction respectively. We also define a_0 , the equivalent radius [Diaz and Barthès-Biesel, 2002] corresponding to the radius of the vesicle, as:

$$a_0 = (ab^2)^{1/3} \quad (11.1)$$

and the scalar object deformation parameter D , traducing the deformation state of the ellipsoid [Taylor, 1934], as:

$$D = \frac{a - b}{a + b} \quad (11.2)$$

11.2 Flow through a narrow capillary

11.2.1 Capillary geometry

The flow of vesicles in a capillary is investigated thanks to the differential manometer described in [Abkarian et al., 2006]. This microfluidic setup allows the simultaneous measurement of the dynamical deformation of the objects and the variation of the pressure drop associated with their motion in a constriction.

The typical dimensions of the device are defined in Figure 11.1: $w_1 = 20 \mu\text{m}$, the width of the channel before the constriction, $w_2 = 15 \mu\text{m}$, the width of the channel in the narrow region and $L = 490 \mu\text{m}$ the length of the constriction, have been adapted in order to deform significantly the vesicles. The height of the device, $h = 15 \mu\text{m}$ has been measured by profilometry. The pressure driven approach described in 6.7.4 is chosen ; typical pressure of 2.5 Psi is applied to the vesicles suspension. The Reynolds number associated with the experiments have been estimated around 6×10^{-2} .

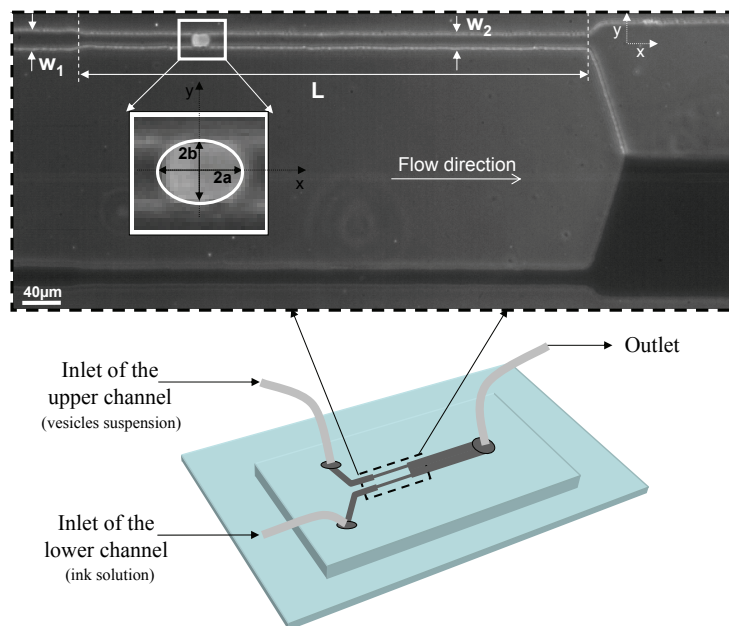


Figure 11.1: The device is composed of a test channel (upper one) where the vesicle's suspension is flown and a comparator channel filled with ink in order to visualize the interface of the co-flow. The dimensions of the constriction have been adapted in order to deform significantly the vesicles. The inset represents a typical image observed and illustrates the parameters extracted by the image analysis.

The principle of the differential manometer is rapidly reminded here. The device is composed of two identical channels: a test channel (upper channel of the picture, Figure 11.1) where the objects are flown and an identical control, or “comparator” channel (lower channel) where a solution of ink is injected. The two channels merge in the right part of the device and the ink allows the visualization of the co-flow's interface. In absence of object flowing in the upper channel,

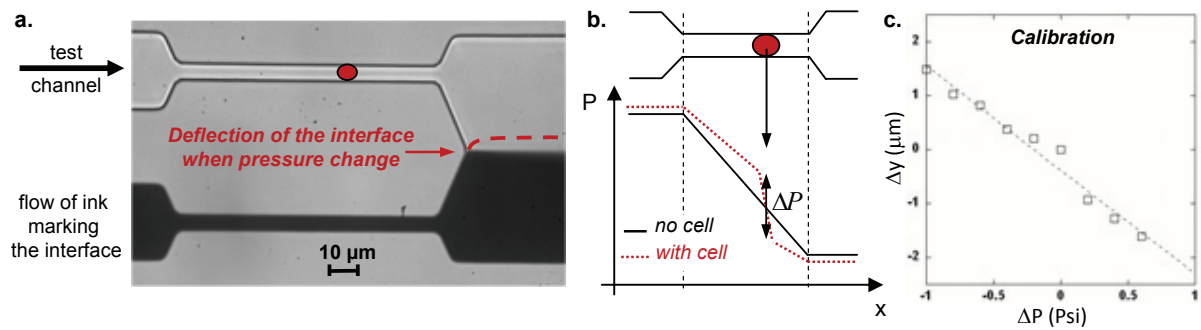


Figure 11.2: Principle of the measurement. a) As an object enters and obstructs the upper channel, the pressure profile locally changes in the channel inducing a change in flow rate in the right part of the channel ; consequently the interface of the co-flow moves [Abkarian et al., 2006]. b) Representation of the pressure profile associated with the channel in absence (solid line) and in presence of an object (dashed line) [Abkarian et al., 2008]. c) Thanks to an appropriate calibration, the interface displacements can be converted in pressure drop measurement [Abkarian et al., 2008].

the interface is centered, hence traducing the equilibrium between the pressures in the test and comparator channels (see picture Figure 11.2a). When a vesicle is flowing in the upper channel, its pressure profile changes slightly as shown with the dashed line on Figure 11.2b, triggering a change in flow rate in the right part of the device which leads to the deflation of the interface as sketched in Figure 11.2a. Thanks to an appropriate calibration (Figure 11.2c), the deflation of the interface can be converted in pressure drop measurements [Faivre, 2006].

11.2.2 General behavior

The Figure 11.3 presents the sequence of deformation of a vesicle with a diameter of the same order of magnitude than the constriction width ($2a_0/w_2 = 0.90$); it is shown entering, flowing through and exiting the narrow region of the channel. The vesicle gets stretched along the x-axis as it enters the narrowing. Once in the constriction, after a short entrance length, it adopts a stationary shape. As it approaches the exit of the narrow region, it gets compressed in the flow direction and then exits the constriction while being stretched in the y-direction by the extensional flow, which is produced by the sudden widening of the channel. Finally the vesicle relaxes slowly and reaches an equilibrium shape.

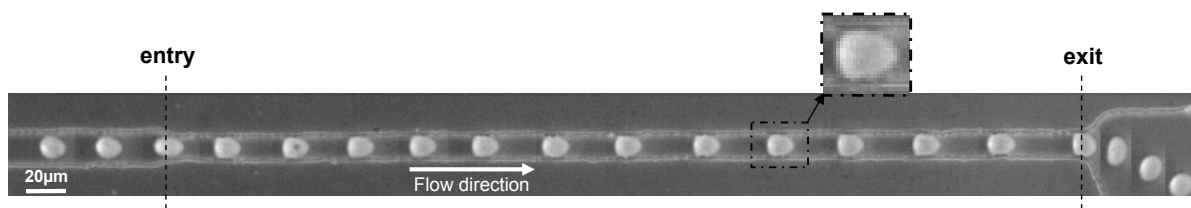


Figure 11.3: Sequence of deformation of a vesicle flowing in the constriction with a diameter $2a_0/w_2 = 0.90$ and a viscosity contrast $\lambda = 9 \times 10^{-3}$.

The dynamical study of the vesicles behavior and their time dependent deformation allows the determination of the velocity profile, the residence time - defined as the time spent by the

vesicle in the constriction - the transient equilibrium shape established in the capillary, the excess of pressure drop associated with the flow of vesicles in the close-fitting capillary and the evidence of the eventual membrane motion, as well as the influence of the different parameters of the system (the confinement $2a_0/w_2$, the viscosity contrast λ , etc. . .) on them.

11.2.3 Velocity profile and transit time of the vesicles

Velocity profile

We first investigate the variation of the vesicle's speed as it flows through the device. We report in Figure 11.4a, the evolution of the velocity V of the vesicle's center of mass normalized by the steady velocity \bar{V} adopted by the object as they flow through the constriction, for two objects of different size ($2a_0/w_2 = 0.53$ and 1.17) versus its non-dimensionalized displacement x_0/L . We emphasize that $x_0 = 0$ is chosen arbitrarily to be the entry of the constriction. We can see on the graph that, as the particles enter the narrowing, the speed increases slightly, reaches a plateau which traduces the steady average speed \bar{V} , before decreasing sharply during their exit of the constriction.

A small overshoot of the speed can be noticed as the particle enters the constriction; such as numerically predicted by [Diaz and Barthès-Biesel, 2002] for the motion of an elastic capsule in a cylindrical pore. We attribute this overshoot to the rapid elongation of the vesicle in the x-direction at the entrance in the pore, and we find the distance over which the velocity changes near the entrance to be roughly equal to twice the width of the constriction, as predicted for capsules.

We can remark that the small vesicle travels faster than the larger one, which is consistent considering that, in a Poiseuille flow, a small vesicle ($2a_0/w_2 < 1$) travels faster than the average speed of the fluid and that a larger vesicle ($2a_0/w_2 > 1$) moves slower than the fluid because it is obstructing the channel.

We also note that, before entering the constriction, the particles are flowing at a speed $V/\bar{V} = 0.8$. In a first approximation, let's consider that the vesicles are flowing at the average speed of the fluid; the conservation of the matter imposes:

$$\bar{V}_{liq_1} w_1 = \bar{V}_{liq_2} w_2, \quad (11.3)$$

where \bar{V}_{liq_1} et \bar{V}_{liq_2} are the average speed of the liquid in the section of the device of width w_1 and in the constriction of width w_2 , respectively.

Hence, from Equation 11.3, we find that

$$\frac{\bar{V}_{liq_1}}{\bar{V}_{liq_2}} = \frac{w_2}{w_1}, \quad (11.4)$$

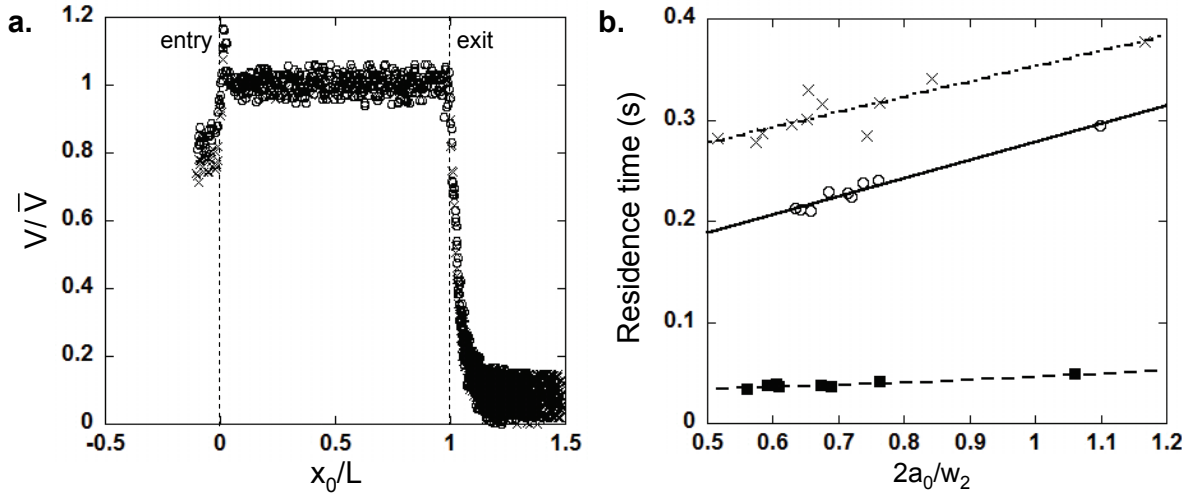


Figure 11.4: a) Velocity V normalized by the steady velocity \bar{V} in the constriction versus x_0/L , for two vesicles of different size: (crosses) $2a_0/w_2 = 0.53$, $\bar{V} = 1.97\text{mm/s}$; (open circles) $2a_0/w_2 = 1.17$, $\bar{V} = 1.29\text{mm/s}$, with the same viscosity contrast $\lambda = 46 \times 10^{-3}$. The origin of the position is chosen arbitrarily to be the entry of the narrowing. The entry and the exit of the channel are reported on the graph by the dashed lines. (b) Residence time versus the typical size of the vesicles $2a_0/w_2$ for three different viscosity conditions: (open circles) $\eta_{in} = 1.2\text{ mPa.s}$ and $\eta_{out} = 128.5\text{ mPa.s}$ ($\lambda = 9 \times 10^{-3}$), (crosses) $\eta_{in} = 5.9\text{ mPa.s}$ and $\eta_{out} = 128.5\text{ mPa.s}$ ($\lambda = 46 \times 10^{-3}$) and (solid squares) $\eta_{in} = 1.2\text{ mPa.s}$ and $\eta_{out} = 16.6\text{ mPa.s}$ ($\lambda = 72 \times 10^{-3}$).

$w_2/w_1 = 0.75$, consequently the ratio between the speed of the vesicles flowing in the region of the device of width w_1 and the steady speed inside the constriction is 0.75 which explains the value found from the graph in Figure 11.4a ($w_2/w_1 \approx 0.8$).

Residence time in the constriction

The residence time $t_{transit}$ of the vesicles, the time spent by the objects in the constriction, is also extracted from the steady speed measurements and defined as $t_{transit} = \frac{L}{\bar{V}}$, where L is the length of the constriction.

The Figure 11.4b, represents the transit time versus the typical size of the vesicles $2a_0/w_2$, for three viscosity ratio. The residence time appears to increase linearly with the vesicle's size, which is consistent with the idea that a large vesicle is going to block more the channel and therefore to travel slower than a smaller one. Moreover, the residence time does not seem to vary monotonically with the viscosity contrast, but seems to depend on both the inner and outer viscosities. Therefore, for two identical outer viscosities, we measure an increase in the residence time as the inner viscosity rises (see Figure 11.4b crosses and open circles). This method seems to be sensitive enough to probe the inner viscosity of objects flowing in close fitting channel. Moreover, we observe a drastic change in the transit time when the outer viscosity is decreased, the inner viscosity being fixed. This increase can be attributed to the fact that we apply a constant pressure ($P_{ves} = 2.5\text{ Psi}$) in order to set the fluids into motion instead of applying a given flow rate. This has for consequences to change the mean fluid velocity (and thus the vesicle

velocity) when changing the outer viscosity. Thus no direct conclusion can be drawn from that curve.

11.2.4 Vesicle's dynamic deformation

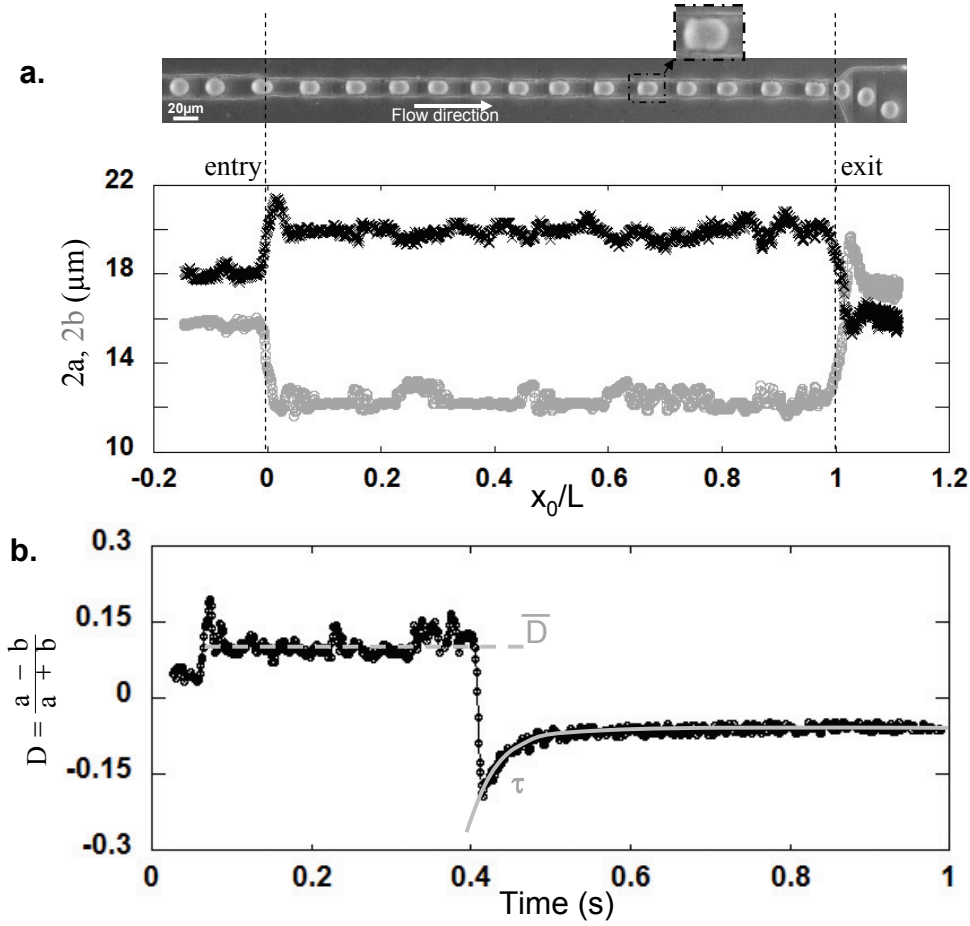


Figure 11.5: a) Variation of the major ($2a$; black crosses) and the minor axis ($2b$; grey circles) of a vesicle as it flows through the geometry, versus its non-dimensionalized displacement x_0/L , ($2a_0/w_2 = 0.90$ and $\lambda = 9 \times 10^{-3}$). The origin of the position is chosen arbitrarily to be the entry of the narrowing. The entry and the exit of the channel are reported on the graph by the dashed lines. The associated sequence of deformation is shown. b) Evolution of the deformation parameter $D = (a-b)/(a+b)$ versus time for the same object is presented. The origin of the time is taken arbitrarily as the beginning of the recording. \bar{D} is defined as the steady deformation state of the vesicle inside the constriction, and τ is the relaxation time as the vesicle exits the narrowing, obtained from the exponential fit $D(t) = m_1 + m_2 \times \exp(-t/\tau)$ (solid grey line), where m_1 and m_2 are constants.

Figure 11.5a presents a sequence of deformation and the evolution of the major ($2a$) and minor ($2b$) axis lengths of a vesicle ($2a_0/w_2 = 0.9$; $\lambda = 9 \times 10^{-3}$) flowing through the device, versus the non-dimensionalized position x_0/L . We retrieve the different regimes of deformation reported previously in the section 11.2.2:

- the stretching in the flow direction (increase of $2a$ and a decrease of $2b$) due to the entry

of the vesicle in the constriction,

- in the constriction, the evolution of the shape (decrease of $2a$ and increase of $2b$) towards the establishment of a steady shape (plateau in $2a$ and $2b$),
- the stretching orthogonally to the channel (length of the major axis - along the x -direction - drops and the length of the minor axis - along the y -direction - increases) because of the extensional flow, as the ellipsoid exits the constriction,
- the relaxation to an equilibrium shape while the particle exits the capillary.

We quantify the deformation of the object by plotting the evolution of the scalar deformation parameter D versus time, as presented in Figure 11.5b. Initially, D is close to zero and rapidly increases (stretching in the flow direction), indeed the front of the vesicles accelerates as it enters the narrowing - smaller section and therefore higher flow rate - whereas the back of the particles keeps moving at the same speed, hence resulting in the stretching of the object. Then, D decreases and reaches a plateau \bar{D} (establishment of a steady shape). The sharp and sudden decrease of D (stretching orthogonally to the flow) highlights the compression of the vesicles in the flow direction while exiting the constriction. Finally D relaxes to an equilibrium value.

From the representation of D versus time, we can extract several intrinsic parameters such as \bar{D} , the steady deformation parameter which corresponds to the equilibrium shape of the vesicle while being in the constriction, as illustrated on Figure 11.5b by a dashed grey line. We can also extract τ , the characteristic relaxation time of the vesicle extracted from the exponential fit $D(t) = m_1 + m_2 \times \exp(-t/\tau)$, reported on the graph with the solid grey line. Nevertheless this study, still under investigation, will be not reported in this manuscript.

Equilibrium state of deformation \bar{D}

We investigate the variation of the equilibrium state of deformation \bar{D} as a function of the confinement, for several contrasts of viscosity λ as presented in Figure 11.6a. Two regimes are observed around a critical value $2a_0/w_2 \sim 0.65$. For low confinement, \bar{D} is roughly constant, while for higher $2a_0/w_2$, it increases linearly. These observations are consistent with the view that deformation undergone by the vesicles can have two origins: the flow and the confinement. For small vesicles, the presence of the wall has a weak effect on \bar{D} and the deformation induced by the flow is dominant, while for larger vesicles, the effect of the confinement prevails. The threshold value of $2a_0/w_2 \sim 0.65$ will be discussed later, when dealing with the pressure drop measurements.

Moreover, it seems that more than the viscosity contrast, it is the outer viscosity which influences the steady deformation of the vesicle \bar{D} . In fact, for a high outer viscosity (solid circles and open squares), the steady deformation state follows the same trend whatever the viscosity of

the solution encapsulated in the vesicles. The dispersion of the data can be attributed to small discrepancy in the surface-to-volume ratio obtained after vesicles deflation. In the contrary, for a lower external viscosity (crosses), the vesicles are more deformed (\bar{D} higher). This can be explain by the same argument used previously for the residence time (see section 11.2.3): when the outer viscosity is decreased for a given applied pressure, the flow conditions are changed (the average speed of the fluid is increased) which will modify the deformation observed for the vesicles.

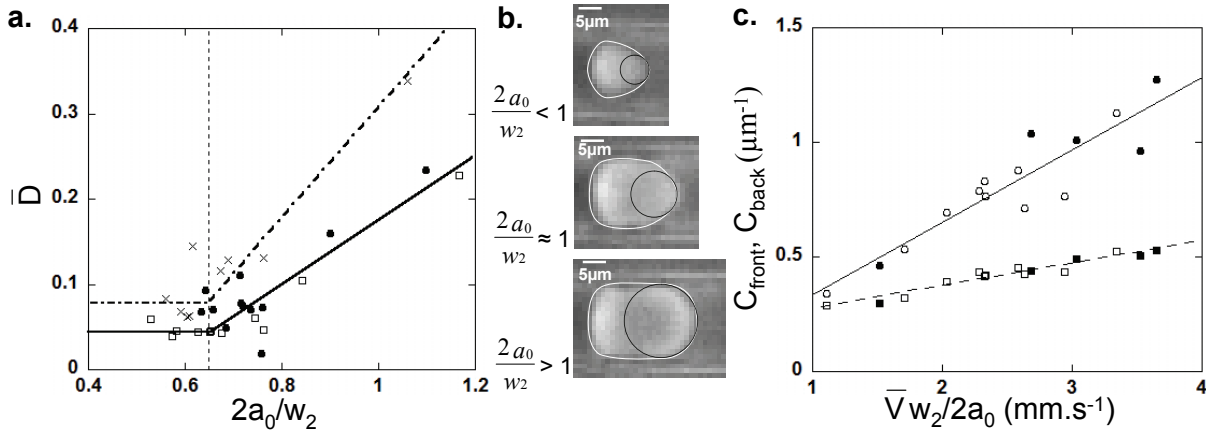


Figure 11.6: a) Variation of the steady state of deformation \bar{D} versus the non-dimensionalized vesicles size for three different viscosity contrasts: (solid circles) $\eta_{\text{in}} = 1.2 \text{ mPa} \cdot \text{s}$ and $\eta_{\text{out}} = 128.5 \text{ mPa} \cdot \text{s}$ ($\lambda = 9 \times 10^{-3}$), (open squares) $\eta_{\text{in}} = 5.9 \text{ mPa} \cdot \text{s}$ and $\eta_{\text{out}} = 128.5 \text{ mPa} \cdot \text{s}$ ($\lambda = 46 \times 10^{-3}$) and (crosses) $\eta_{\text{in}} = 1.2 \text{ mPa} \cdot \text{s}$ and $\eta_{\text{out}} = 16.6 \text{ mPa} \cdot \text{s}$ ($\lambda = 72 \times 10^{-3}$). The lines are a guide for the eyes and have no physical meanings. b) Stationnary shapes of three vesicles of different sizes: respectively $2a_0/w_2 = 0.63$, 0.95 and 1.20 from top to bottom, at a viscosity contrast $\lambda = 9 \times 10^{-3}$. The solid white lines represent the vesicles edge, whereas the black circles represent the vesicles front curvatures C_{front} . c) (circles) C_{front} and (squares) C_{back} , the front and back curvatures of the vesicle versus its steady velocity \bar{V} over the dimensionless size $2a_0/w_2$ for several vesicles with different internal viscosities (solid symbols) $\eta_{\text{in}} = 1.2 \text{ mPa} \cdot \text{s}$ and (open symbols) $\eta_{\text{in}} = 5.9 \text{ mPa} \cdot \text{s}$ but the same external one $\eta_{\text{out}} = 128.5 \text{ mPa} \cdot \text{s}$. The curvature is defined as $C = 2/R_{\text{curvature}}$, where $R_{\text{curvature}}$ is the radius of curvature.

We report on Figure 11.6b, pictures of the steady shapes of three vesicles of different sizes. We can see that the vesicles undergo a pointy front and a flat back, which are typical of the “bullet-like shape” described theoretically by [Noguchi and Gompper, 2005] and experimentally by [Vitkova et al., 2004]. It seems from Figure 11.6b that the smaller the vesicle is, relative to the constriction size, the smaller the curvature C ($C = 2/R_{\text{curvature}}$) of the front of the object appears.

Therefore, Figure 11.6c shows our measurements of C_{front} and C_{back} , the vesicles front and back curvatures respectively versus the particle’s steady speed \bar{V} over its dimensionless size $2a_0/w_2$. We can see that the curvatures depend on the particle’s speed as shown previously in the literature [Vitkova et al., 2004] and they are also inversely proportional to confinement. Although we present data from vesicles with different internal viscosities while exposed to the same external viscosity, the curvatures align in a single trend, hence showing that the front and

back curvatures are not imposed by the internal viscosity.

11.2.5 Excess of pressure drop associated with the flow of vesicles in a narrow capillary

We now investigate the excess of pressure drop created by the flow of a vesicle in the constriction. Figure 11.7 shows the sequence of deformation and the variation of ΔP , the excess of pressure drop associated with the flow of a vesicle in the narrow region of the device.

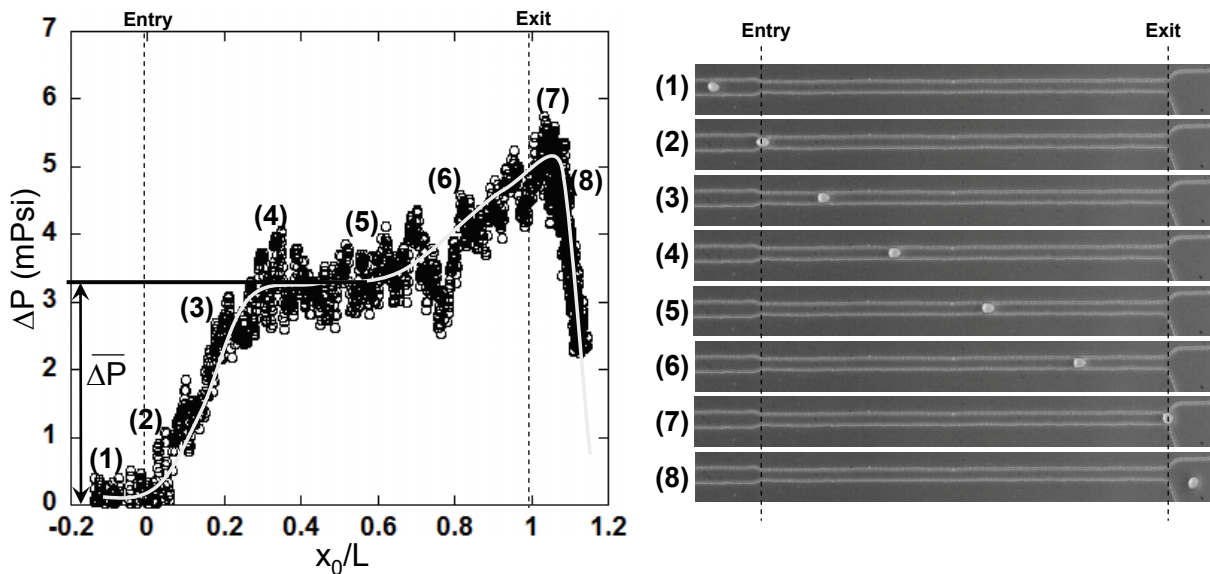


Figure 11.7: Variation of ΔP , the pressure drop associated with the flow of a vesicle in the constriction, as a function of its displacement x_0 normalized by the length of the narrowing L and the sequence of deformation associated; $2a_0/w_2 = 0.9$, $\lambda = 9 \times 10^{-3}$ and $P_{ves} = 2.5$ Psi. We decide to consider all the measurements of ΔP as positive numbers. The white curve is just a guide for the eyes and has no physical meaning. $\overline{\Delta P}$ represents the steady pressure drop corresponding to the plateau.

The pressure drop is arbitrarily set to be zero before the entry of the vesicle in the constriction as illustrated in Figure 11.7 (1). Then, as the vesicle enters the narrowing (2 and 3), P increases linearly before reaching a plateau value of 3.3 mPsi around $x_0/L = 0.3$ (4, 5 and 6). Finally, ΔP rises to a maximum ($\Delta P_{max} = 5.7$ mPsi) around $x_0/L = 1.02$, i.e. at the end of the constriction (7) and rapidly decreases back to the initial state (8) when the particle exits the constriction.

Such variation of the excess pressure drop caused by the entry of a deformable particle in a capillary has been studied numerically in the case of elastic capsule [Diaz and Barthès-Biesel, 2002]. They have predicted similar variation of δP as the object flows through a pore; however small differences arise. These discrepancies may be explained by the fact that the numerical results have been obtained for the entry of an elastic capsule in a circular pore with a sharp change in channel width (the object is not confined at all before entering the pore) whereas in our case the vesicle enters a square cross section constriction which typical size is not so different from

the channel width ($w_2/w_1 = 0.75$). We can also compare the maximum pressure drop ΔP_{max} obtained to measurements realized on red blood cells with the same geometry. Indeed previous published work [Abkarian et al., 2006] reports the maximum pressure drop associated with the flow of a red blood cell in a constriction, to be of the same order of magnitude (around 40 mPsi) for a typical cell size corresponding to $2a_0/w_2 = 1.1$.

Effect of viscosity contrast on ΔP

We now investigate the effect of λ , the viscosity contrast between the inner and outer solution, on the excess of pressure drop. Figure 11.8 displays the pressure drop data obtained for several vesicles of same size ($2a_0/w_2 \approx 1.1$) submitted to different viscosity contrasts ($\lambda = 72 \times 10^{-3}$ and 9×10^{-3}), symbolized respectively by the open circles and the crosses. The two curves are equivalent thus indicating no effect of the viscosity contrast on ΔP ; a result which is confirmed by the data obtained for smaller vesicles ($2a_0/w_2 \approx 0.9$). Similar conclusions were reported in numerical study of elastic capsules entering a cylindrical pore [Diaz and Barthès-Biesel, 2002].

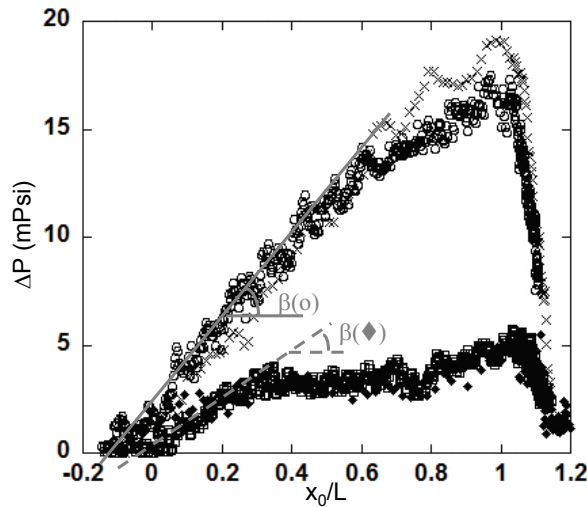


Figure 11.8: Effect of viscosity contrast and vesicle size. Excess of pressure ΔP versus the non-dimensionalized displacement x_0/L for several vesicles with different size and viscosity contrasts: (open circles) $2a_0/w_2 \approx 1.1$, $\lambda = 9 \times 10^{-3}$, (crosses) $2a_0/w_2 \approx 1.1$, $\lambda = 72 \times 10^{-3}$, (solid diamonds) $2a_0/w_2 \approx 0.9$, $\lambda = 46 \times 10^{-3}$ and (open squares) $2a_0/w_2 \approx 0.9$, $\lambda = 9 \times 10^{-3}$. In all cases, the applied pressure is $P_{ves} = 2.5$ Psi. β corresponds to the slope of the linear regime as illustrated by the grey lines.

Effect of the vesicle's size on ΔP

Finally we study the influence of the relative size of the particle $2a_0/w_2$ on the excess of pressure drop induced. Three major comments can be made. First, it can be seen from Figure 11.8 that in the case of a bigger vesicle ($2a_0/w_2 = 1.1$), the pressure drop measurement does not reach a plateau value before exiting the constriction, whereas it does for smaller objects

($2a_0/w_2 = 0.9$). Therefore it seems that the length necessary for the particle to induce the establishment of a constant pressure drop while flowing in a narrowing depends on the confinement.

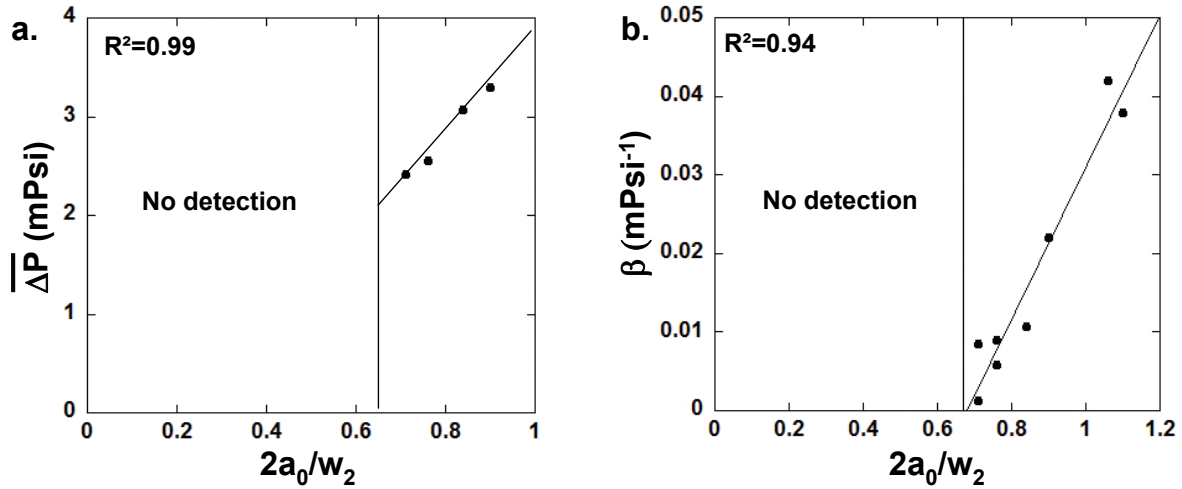


Figure 11.9: Effect of vesicle size ($2a_0/w_2$) on a) $\overline{\Delta P}$ the steady pressure drop and b) β the slope of the linear regime.

In order to quantify the effect of the vesicles relative size on the pressure drop measurements, we report on Figure 11.9a the plateau value $\overline{\Delta P}$ versus $2a_0/w_2$. We can first note that, below a critical vesicle size of $2a_0/w_2 \sim 0.65$, we are not able to measure the pressure drop associated with the vesicle's motion. We also show that the steady pressure drop $\overline{\Delta P}$ varies linearly with the confinement, hence allowing the discrimination of the particle's size.

Moreover β , the slope of the linear regime of ΔP versus the non-dimensionalized displacement x_0/L increases proportionally with $2a_0/w_2$. Therefore, there is no need to wait for the establishment of the plateau value $\overline{\Delta P}$ in order to discriminate the particle size.

These results open prospect on the development of a size measurement function completing the already existing microfluidic toolbox. Short channels associated with the simple design of the differential manometer allows to perform analysis on deformable objects suspension under flow.

11.2.6 What about the membrane's motion?

A small defect present on the vesicle - probably a lipid reservoir (highlighted by the black dot on the Figure) - allows the visualization of the membrane's motion as illustrated in 11.10a. Measurements of Δx , the defect's position relatively to the vesicle's center of mass is reported Figure 11.10b.

The graph reveals a slight increase in Δx around $x_0/L = 0$ which traduces the stretching of the vesicle along the x-axis as it enters the narrowing. For $0 < x_0/L < 0.8$, i.e. once the

steady shape established, Δx reaches a plateau traducing that the defect on the membrane stays approximately at the same position relatively to the center of mass. These data highlight the absence of motion of the membrane while the vesicle travels through the capillary. At the best of our knowledge, it is the first time that the behavior of the vesicle's membrane is highlighted, while flowing in a close-fitting channel. The sharp decrease of Δx indicates that the defect rotates on the membrane of the vesicle, from the front to the back, suggesting a tank-treading-like motion while flowing in the wider part of the channel.

To sum up, simultaneous measurements of the dynamical deformation of the vesicles and the

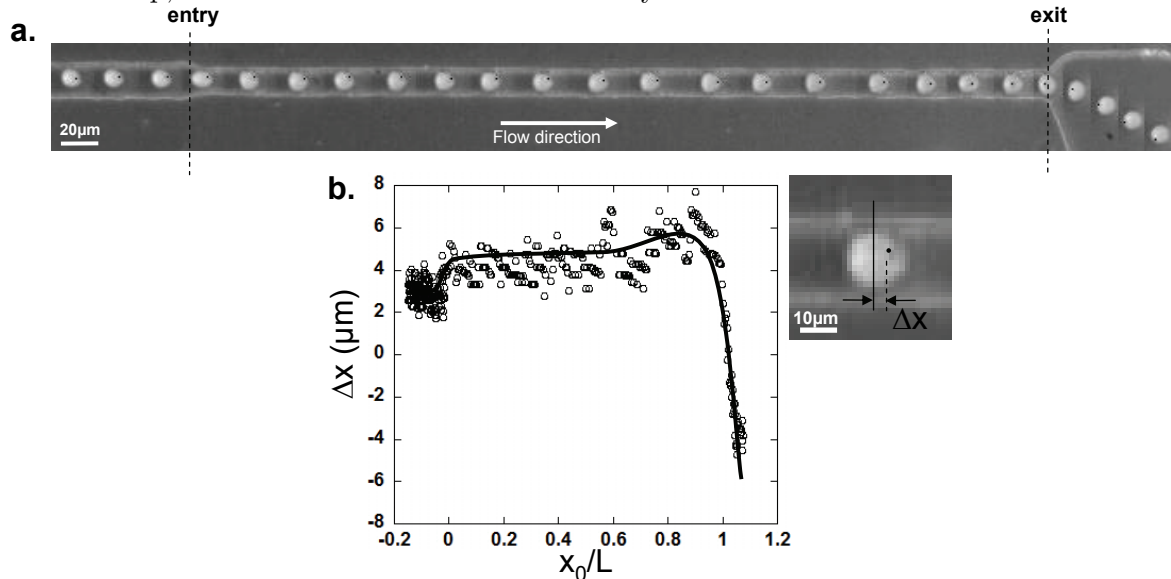


Figure 11.10: a) Sequence of deformation of a vesicle flowing in the constriction, with a viscosity contrast $\lambda = 9 \times 10^{-3}$ and a relative size $2a_0/w_2 = 0.76$; the pressure applied to the vesicle suspension is $P_{ves} = 2.5$ Psi. The presence of a small defect represented by the black dot highlights the motion of the vesicle's membrane. b) Variation of Δx (see picture), the small defect displacement relatively to the center of mass of the object versus its displacement x_0/L . The solid line is a guide for the eyes and has no physical meaning.

pressure drop produced by their motion in a close-fitting capillary with a square cross-section allow us to conclude that:

- The velocity profile of the vesicles is similar to that obtained by numerical simulations for elastic capsules flowing through a cylindrical pore.
- The vesicle's residence time increases linearly with the confinement of the particles $2a_0/w_2$ and depends on the internal viscosity for a given flow condition (mean fluid velocity imposed in our case by the external viscosity and the applied pressure).
- The equilibrium shape adopted by the vesicles in the constriction, depends on the vesicle's confinement ($2a_0/w_2$) and on their velocity.
- The excess of pressure drop associated with the flow of vesicles in a capillary is independent of the viscosity contrast and is linear to the confinement allowing a sensitive determination of the relative size of the object $2a_0/w_2$.

- The vesicle flowing through a close fitting channel does not present any membrane motion.

11.3 Flow through multiple periodic constrictions

We now investigate the flow of viscous vesicles in a periodic sequence of short constrictions. The vesicles are then submitted to a succession of large stretching and compressions whose spatial period is fixed but whose time period depends on the flow speed which is set independently. This geometry can be comparable to a vesicle-scale rheometer, allowing strong and regular solicitations of the objects mechanical properties in a controlled way.

Theoretical and experimental results on vesicles flowing in a sawtooth-shaped channel (confinement lower than 0.4 in the narrowest region) have been recently reported by [Noguchi et al., 2010]. This study highlights a transition from a state with orientational oscillations of a fixed shape to a state with periodically shape changes (from symmetric ellipsoid to bullet-like shape) with increasing flow velocity, and discuss the effect of the reduced volume on the vesicles shapes. In our study, we will focus on high flow speed experiments to study the shape change for highly confined vesicles (confinement ranging between 0.2 and 0.9).

11.3.1 Teeth-like geometry

The flow of vesicles through a channel with rapid, spatially periodic constrictions is investigated. These variations of the cross section have been chosen in order to induce rapid deformations of vesicles.

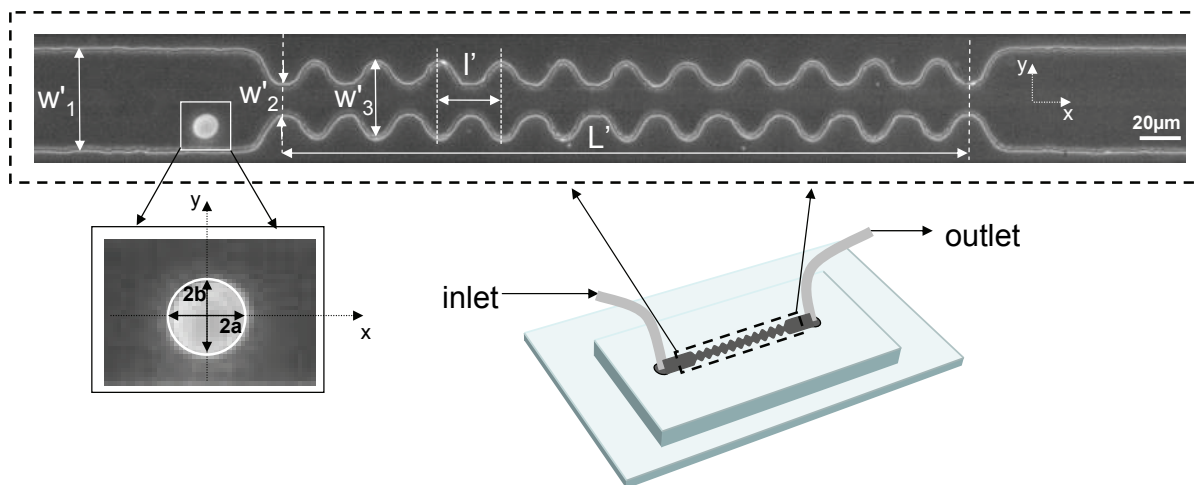


Figure 11.11: Geometry of the device and typical image observed. The dimensions of the constriction have been adapted in order to deform significantly the objects under study.

The typical dimensions of the device - $w'_1 = 60 \mu\text{m}$, the width of the channel before the multi-constriction, $w'_2 = 20 \mu\text{m}$, the width of the channel in the narrowest region, $w'_3 = 40 \mu\text{m}$, the width of the channel in the wider region, $l' = 35.5 \mu\text{m}$, the spatial period of the constrictions

and $L' = 425 \mu\text{m}$, the length of the channel - are defined Figure 11.11. The height of the device, $h' = 15 \mu\text{m}$ has been measured by profilometry. The pressure driven approach described in 6.7.4 is chosen ; typical pressure of 1.9 Psi is applied to the vesicles suspension. The Reynolds number associated with the experiments have been estimated at 8×10^{-2} .

11.3.2 General behavior

The Figure 11.12 presents the sequence of deformation of a vesicle ($2a_0/w_2' = 0.65$); the particle is shown entering, flowing through and exiting the multi-constriction channel. The vesicle gets stretched along the x-axis as it enters the narrowing, and then along the y-axis as it flows between two constrictions. As it exits the channel, it is stretched in the y-direction by the extensional flow, which is produced by the final widening of the channel. Finally, the vesicle relaxes slowly and reaches a quasi-circular equilibrium shape.

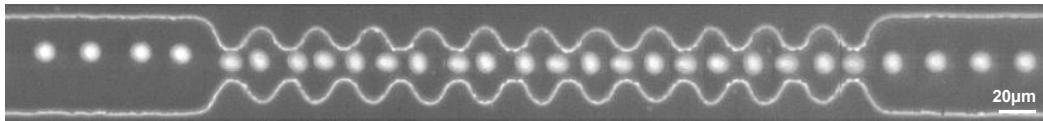


Figure 11.12: Sequence of deformation of a vesicle flowing through the multi-constriction device. The vesicle size is $2a_0/w_2' = 0.65$, the viscosity contrast $\lambda = 9 \times 10^{-3}$ and the pressure applied to push the vesicles solution $P_{ves} = 1.9 \text{ Psi}$.

The study of the time dependent behavior of the vesicles allows the determination of the velocity profile, the drift distance and their amplitude of deformation in the constrictions.

11.3.3 Drift of the vesicles

It can also be noticed from Figure 11.12, that the vesicle exits the multi-constriction channel further from the wall, i.e. closer to the center of the device, than when it enters. This transversal displacement of the deformable objects is emphasized by the graph in Figure 11.13. Indeed, the trajectories of three vesicles which have roughly the same diameter ($2a_0/w_2' = 0.42$) allow to highlight the drift across the streamlines undergone by the objects initially close to the wall.

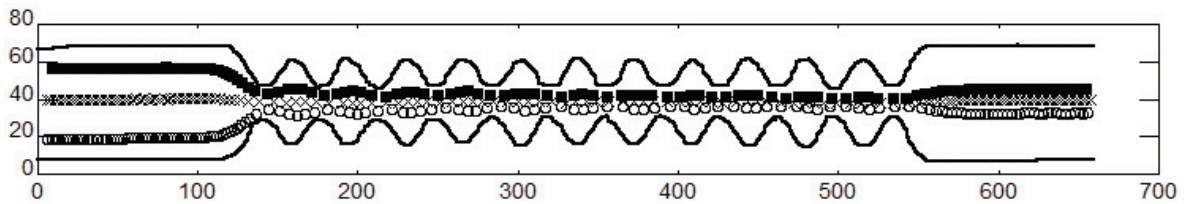


Figure 11.13: Trajectories of 3 vesicles of approximate same size ($2a_0/w_2' \approx 0.42$) flowing through the multi-constriction device with a viscosity contrast of $\lambda = 9 \times 10^{-3}$; the applied pressure is $P_{ves} = 1.9 \text{ Psi}$. Whatever their initial positions relative to the wall, the vesicles are centered when exiting the channel.

Various theoretical and experimental studies have explained this drift in terms of a lift force applied to the object (see section 5.4.1. In fact, deformable ellipsoidal particles - such as lipid vesicles - flowing near a wall are submitted to a lift force which tends to push them away from the wall. As illustrated on red blood cells [Faivre et al., 2006], the presence of a constriction in

a close fitting channel where a suspension of deformable objects is injected, increases locally the shear stress and leads to the increase of the drift undergone by the particles.

Effect of the vesicle's size on the drift

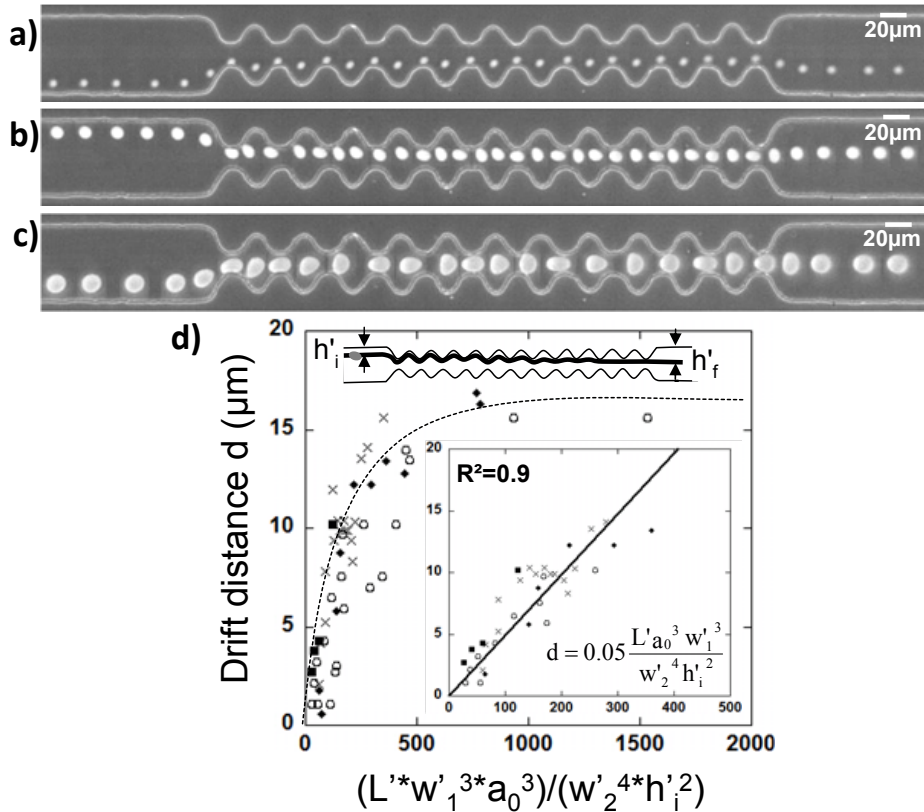


Figure 11.14: Sequence of displacement of 3 vesicles with different size (a) $2a_0/w_2' = 0.31$, (b) $2a_0/w_2' = 0.53$, (c) $2a_0/w_2' = 0.81$. (d) Drift distance d versus the equivalent volume a_0^3 of the vesicles for a given initial position relative to the wall h_i' and varying viscosity contrasts (open circles) $\lambda = 9 \times 10^{-3}$, (solid squares) $\lambda = 27.5 \times 10^{-3}$, (crosses) $\lambda = 72 \times 10^{-3}$ and (solid diamonds) $\lambda = 129 \times 10^{-3}$. The dashed line is a guide for the eyes, and has no physical meaning. The inset shows a close-up on the linear regime; the solid line represents a linear fit of the experimental data. The sketch defines h_i' and h_f' , the initial and final positions of the vesicles relative to the wall as well as the drift distance defined as $d = h_f' - h_i'$.

We now investigate the effect of the vesicles size on their displacement away from the wall. The Figures 11.14a, 11.14b and 11.14c present the displacement of three vesicles with different size respectively $2a_0/w_2' = 0.31$, $2a_0/w_2' = 0.53$ and $2a_0/w_2' = 0.81$. Although the three vesicles enter the multi-constriction roughly at the same position $h_i' \sim 10 \mu\text{m}$ (see the sketch of the Figure 11.14d), they exit at $h_f' = 18 \mu\text{m}$, $25 \mu\text{m}$ and $30 \mu\text{m}$ for the small, the medium and the large vesicles respectively. Hence, the vesicle size seem to influence the drift distance.

These results are coherent with the expression of the drift distance d - defined as $d = h_f' - h_i'$

- provided by [Faivre et al., 2006], in the case of a single long constriction:

$$d \approx 6K \frac{L' a_0^2 w_1'^3}{w_2'^4 h''^2} \quad (11.5)$$

where L' is the length of the constriction, a_0 is the equivalent radius of the particle, w_1' is the width of the channel before the narrowing, w_2' is the width of the narrowing, h'' is the distance of the particle to the wall in the constriction and K a dimensionless parameter dependent on the orientation of the particle and its shape, which in turns also depends on the viscosity ratio λ between the object and the suspending medium.

Because of the expansion, the spacing of the streamlines changes in the constriction by the geometric ratio w_2'/w_1' . Therefore, knowing the initial position h'_i as sketched in Figure 11.14d, we can estimate the distance h'' from the center of mass of the particle to the wall inside the narrowing:

$$h'' = h'_i w_2' / w_1' \quad (11.6)$$

From the equations 11.5 and 11.6, we study the variation of the drift distance d as a function of the parameter $(L' a_0^3 w_1'^3) / (w_2'^4 h_i'^2)$ for several vesicles with the same initial position h'_0 relative to the wall; the results are presented in Figure 11.14d. The drift distance is shown to vary linearly for small value of the $(L' a_0^3 w_1'^3) / (w_2'^4 h_i'^2)$, and then saturate to become constant at a drift distance of 16 μm .

We highlight that deformable objects flowing through multiple constrictions tend to get focalized in the channel ; the drift distance depends on the vesicle volume and the geometric parameters of the device. These results open prospect on the development of a centering function completing the already existing microfluidic toolbox available to perform lab-on-chip analysis on cells or deformable objects.

11.3.4 Velocity profile and transit time of the vesicles

Velocity profile

We have investigated the variation of the vesicle's velocity as it flows through the device. We report in Figure 11.15, the evolution of the speed v of the center of mass of the object, for two vesicles of different size ($2a_0/w_2 = 1.1$ and 2.1 , Figure 11.15a) versus the displacement x_0 of its center of mass, non-dimensionalized by l' the distance between two consecutive constrictions. We can note that $x_0 = 0$ indicates the entry of the multi-constriction channel.

We can see on the graph that, as the vesicle enters the multi-constrictions, the speed increases sharply, then it periodically increases and decreases back as the particle respectively enters and exits the successive constrictions. Finally, the velocities decrease sharply while the particles exit the teeth-like channel. The steady average speed \bar{V} is defined as the mean speed of the object

as it flows through the multi-constriction section of the device.

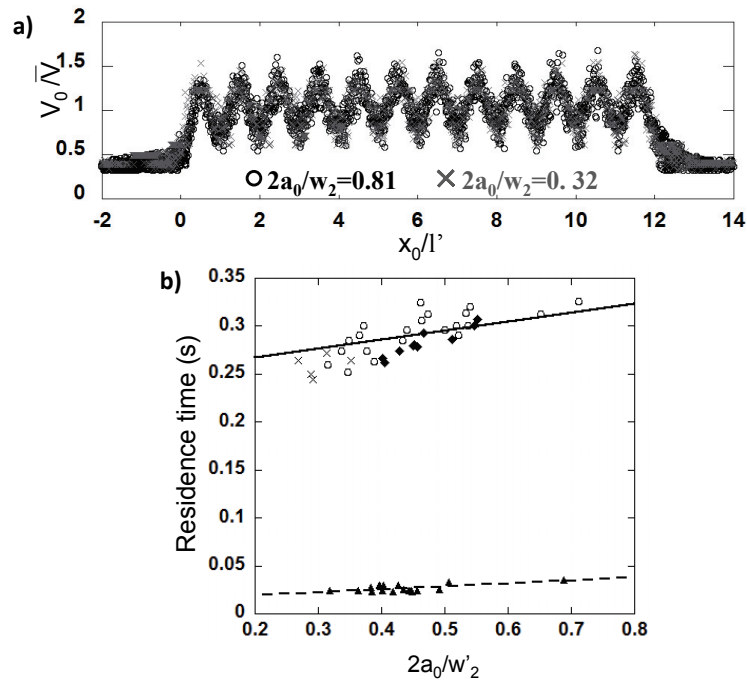


Figure 11.15: (a) Speed normalized by the mean speed \bar{V} versus the position of the center of mass of the particles, normalized by the distance between two consecutive constrictions, for two vesicles (crosses) $2a_0/w_2 = 0.32$ ($\bar{V} = 1.69 \text{ mm.s}^{-1}$) and (open circles) $2a_0/w_2 = 0.81$ ($\bar{V} = 1.19 \text{ mm.s}^{-1}$; $\lambda = 9 \times 10^{-3}$). \bar{V} is defined as the mean value of the object's speed when flowing through the multi-constriction section of the channel. (b) Residence time versus the typical size of the vesicles $2a_0/w_2$ for four viscosity contrasts (open circles) $\eta_{in} = 1.2 \text{ mPa.s}$ and $\eta_{out} = 128.5 \text{ mPa.s}$ ($\lambda = 9 \times 10^{-3}$), (crosses) $\eta_{in} = 3.6 \text{ mPa.s}$ and $\eta_{out} = 128.5 \text{ mPa.s}$ ($\lambda = 27.5 \times 10^{-3}$), (solid triangles) $\eta_{in} = 1.2 \text{ mPa.s}$ and $\eta_{out} = 16.6 \text{ mPa.s}$ ($\lambda = 72 \times 10^{-3}$) and (solid diamonds) $\eta_{in} = 16.6 \text{ mPa.s}$ and $\eta_{out} = 128.5 \text{ mPa.s}$ ($\lambda = 129 \times 10^{-3}$).

Residence time in the multiple constrictions

The residence time $t_{transit}$ of the vesicles in the multiple constrictions, defined as $t_{transit} = \frac{L'}{\bar{V}}$, where L' is the length of the multiple constrictions section, and \bar{V} , the mean speed of the objects.

The Figure 11.15b, represents the transit time versus the typical size of the vesicles $2a_0/w_2$, for four different viscosity ratios. The residence time appears to increase linearly with the confinement, as previously observed for the single constriction (see section 11.2.3), but now does not seem to depend on the inner viscosity. We always observe a drastic change in the transit time when the outer viscosity is decreased (solid triangles) and does not allow us direct comparison with the other data.

11.3.5 Vesicle's dynamic deformation

Dynamic deformation parameter

Figure 11.16 presents the sequence of deformation of a vesicle ($2a_0/w'_2 = 0.51$) flowing through the device and the evolution of the lengths of its major ($2a$) and minor ($2b$) axis, versus the non-dimensionalized position x_0/l' . The results shown here have been observed for many other vesicles and are therefore representative.

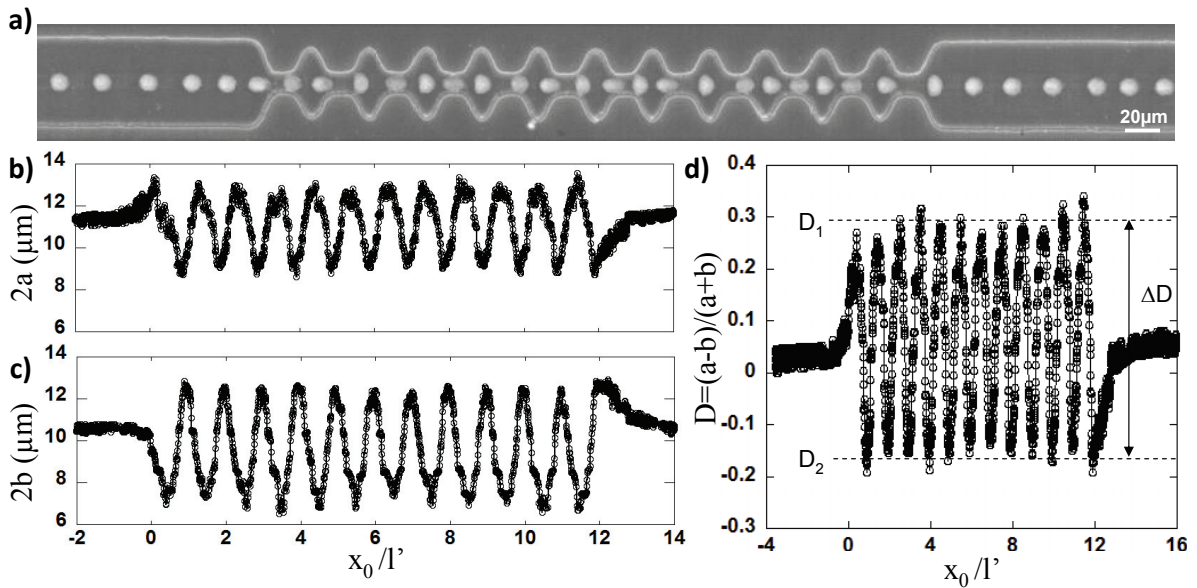


Figure 11.16: (a) Sequence of deformation of a vesicle flowing through the multi-constriction device. Variation of (b) the major and (c) the minor axis of the vesicle versus the non-dimensionalized position x_0/l' . (d) Variation of the deformation parameter D versus the vesicle's position x_0/l' . $2a_0/w'_2 = 0.55$ and $\lambda = 129 \times 10^{-3}$. D_1 and D_2 represent the mean of the maxima and the mean of the minima, respectively; ΔD , the amplitude of deformation is defined as $\Delta D = D_1 - D_2$.

As the vesicle approaches the entry of the constriction, it is stretched in the direction of the flow leading to an increase of $2a$ and a decrease of $2b$. Then, the shape evolves periodically as the object travels through the multi-constriction geometry (decrease of $2a$ and increase of $2b$ followed by a drop in $2a$ and a rise in $2b$). As the vesicle exits the constriction, it is stretched vertically because of the extensional flow; consequently, the length of the major axis (along the x -direction) drops and the length of the minor axis (along the y -direction) increases. Finally, both parameters $2a$ and $2b$ relax to constant values as the particle exits the channel and establishes an equilibrium shape.

We tried to quantify the deformation of the vesicle by plotting the evolution of the deformation parameter D versus the normalized position x_0/l' as presented in Figure 11.16d. Indeed, we can see that initially D is close to zero, the vesicle is hence already deformed before entering the multi-constriction section of the device; then D rapidly increases as the vesicle stretches to enter the narrowing. Then, the periodic oscillations of D show the response of the vesicle to

its passage through the multiple constrictions. Finally, the D increases traducing the relaxation of the particle's shape and the establishment of a steady shape. D_1 and D_2 are defined as the mean values of the maxima and the minima of the periodic oscillations of D respectively. The amplitude of deformation ΔD is defined as $\Delta D = D_1 - D_2$. It can be remarked on the Figure 11.16d, that ΔD is not exactly centered with respect to 0, which is coherent with the geometry.

Amplitude of deformation ΔD

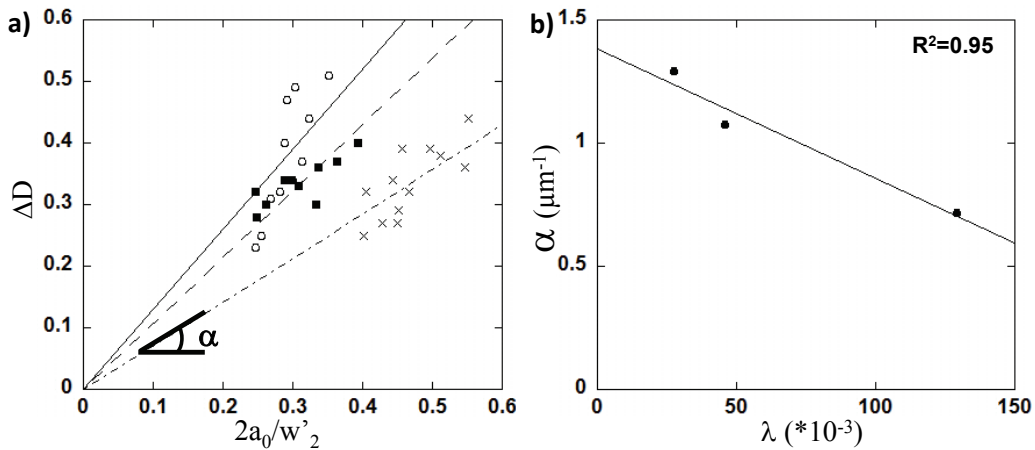


Figure 11.17: (a) Variation of the deformation amplitude ΔD versus the equivalent radius a_0 of the vesicles, for three different viscosity contrast (open circles) $\lambda = 27.5 \times 10^{-3}$, (crosses) $\lambda = 46 \times 10^{-3}$ and (solid squares) $\lambda = 129 \times 10^{-3}$. The lines are linear fits with a slope α . (b) Variation of the slope α , determined from (a), versus the viscosity contrast λ .

We now investigate the influence of the confinement and the viscosity contrast on ΔD , the amplitude of deformation of the vesicles. The Figure 11.17a shows the variation of ΔD as a function of the vesicle's equivalent radius, for three different viscosity contrasts. The amplitude of deformation increases linearly with the size of the object, as pointed out by the linear adjustments (see lines in Figure 11.17a).

From the fits, we obtain the slopes α of the different lines. The Figure 11.17b shows the evolution of α versus the contrast of viscosity. Although we need more data in order to conclude, the good agreement of the experimental data with the linear adjustment ($R^2 = 0.95$), seems to indicate that α decreases linearly as the viscosity contrast λ increases. Therefore, the amplitude of deformation ΔD depends on both relative vesicle size and viscosity contrast.

To sum up, measurements of the dynamical deformation of the vesicles in a teeth-like geometry allow us to conclude that:

- The flow of vesicles through multiple constrictions tends to focalize the objects in the channel. The drift distance depends on the vesicle volume and the geometric parameters of the device.

- The residence time of the vesicles increases with the size of the objects $2a_0/w_2$ and it seems independent of the inner viscosity.
- The amplitude of deformation varies linearly with the confinement such as the higher the viscosity contrast, the smaller the amplitude of deformation for a given vesicle size.

11.4 Conclusion

This chapter presents the behavior of DOPC GUVs flowing in two kinds of close fitting channels: a single constriction and a teeth-like geometry. Results allow to conclude that:

- **The confinement strongly affects the shape and the mobility of the fluid DOPC vesicles.**
- Both geometries complete the already existing microfluidic toolbox:
 - ✓ **Differential manometer** allows the **size measurement of individual objects**.
 - ✓ **Teeth-like geometry** allows the **focalization of deformable objects** in the outlet channel.

Additional measurements are required in order to characterize the vesicle deformation and mobility dependencies on the channel geometry (e.g. confinement, constriction length ...), the flow parameters (e.g. fluid velocity, fluid viscosity ...) and the vesicle properties (e.g. reduced volume, membrane and internal medium mechanical properties ...). This study will also be extended to the dynamics of composite vesicles described in the previous chapters and of red blood cells as initiated by [Abkarian et al., 2008].

Finally, these geometries open interesting perspectives for fast and reproducible measurements of the mechanical properties of deformable objects (e.g. vesicles, polyelectrolyte capsules or blood cells ...), and could be used to separate different components of a suspension by size or mechanical properties.

Chapter 12

Conclusion and prospects

Le but de ce travail était de développer des modèles mécaniques de cellules basés sur des vésicules lipidiques géantes unilamellaires (GUVs) et d'étudier les relations entre leurs paramètres mécaniques et leurs comportements sous contraintes.

Nous avons d'abord réussi à modifier les propriétés structurales et par conséquent mécaniques des membranes, soit en les décorant de polyélectrolytes (chitosane ou acide hyaluronique), soit en utilisant la transition de phase des lipides pour obtenir des membranes en phase gel.

Les vésicules constituées de DOPC et décorées de polyélectrolytes ont été largement caractérisées au cours de cette étude. Nous avons ainsi montré l'origine électrostatique de l'interaction entre les deux polyélectrolytes et la membrane de lipides zwitterioniques, en montrant le rôle de leurs densités de charges respectives sur la quantité de polymère adsorbé. Nous avons également prouvé que la structure chimique du polymère contrôle la conformation des chaînes adsorbées à la surface des vésicules : le chitosane s'adsorbe à plat alors que l'acide hyaluronique forme des boucles. Les paramètres clés sont la rigidité de la chaîne et l'affinité du polymère pour le solvant. Nous avons également mis en évidence une structure en patch des membranes décorées de polyélectrolytes, formée d'une alternance de domaines décorés et non-décorés. Cette structure hétérogène a permis de mieux comprendre le phénomène d'agrégation-dissociation observé pour les vésicules décorées en solution en fonction de la quantité de polyélectrolyte ajouté.

En outre, nous avons mis en évidence la possibilité d'ajuster de façon contrôlée la charge globale de ces vésicules en changeant la nature du polyélectrolyte ou la quantité adsorbée. Nous avons en particulier prouvé qu'il est possible d'alterner des couches de polyanion et de polycation à la surface d'une vésicule.

Concernant les GUVs à membrane en phase gel, nous avons proposé un protocole astucieux permettant de préserver la forme sphérique de GUVs lors de la diminution de température et de la transition entre la phase fluide et la phase gel $P_{\beta'}$.

Il est ensuite montré que la structure de la membrane influence fortement la valeur de ses paramètres mécaniques et change le comportement des GUVs complexes soumises à différentes contraintes (pression osmotique, chocs de pH et de sel, compression entre deux plans en utilisant

la microscopie à force atomique, ou force ponctuelle en extrudant un nanotube de membrane). Notre étude a été réalisée en aller-retour, soit en caractérisant les propriétés mécaniques de l'objet et en regardant leur influence sur son comportement, soit en appliquant une contrainte sur l'objet et en déterminant ses propriétés mécaniques à partir de son comportement.

Pour les vésicules décorées de polyélectrolyte, nous avons montré que leur décoration asymétrique induit une courbure spontanée dont le signe peut être simplement ajusté en modifiant l'écrantage électrostatique (c.-à-d. la force ionique de la solution).

De plus, nous avons prouvé à partir d'expériences originales de compression de GUVs décorée de chitosane par AFM, que l'adsorption d'un polyélectrolyte de charge opposée rigidifie les membranes, augmentant notamment leur module de compressibilité. Notre étude a également révélé que ces modifications de propriétés mécaniques induisaient des comportements originaux de ces vésicules sous contraintes externes. En particulier, sous pression osmotique, les vésicules décorées se dégonflent sphériquement en éjectant ou en invaginant des tubes selon l'écrantage électrostatique. Dans le cas des vésicules en phase gel, nous avons produit une grande variété de formes polyédriques concaves à partir des expériences de dégonflement. Ces diverses formes ont été numériquement retrouvées en utilisant un modèle élastique à 2 dimensions, et un diagramme de phase a été établi. En comparant quantitativement les formes expérimentales et simulées, nous avons pu évaluer les modules de compressibilité et cisaillement de membrane en phase gel $P_{\beta'}$.

Enfin, nous avons rapporté des résultats préliminaires sur des GUVs formées de DOPC s'écoulant dans deux géométries confinées différentes. Nous avons prouvé que le confinement affecte fortement la forme des GUVs et leur mobilité. L'étude du comportement des vésicules entrant dans la constriction simple permet de déterminer leur taille, tandis que leur écoulement dans des constriction multiples induit leur focalisation dans le canal et permet d'évaluer la viscosité de leur milieu interne. Bien que les paramètres mécaniques de la membrane n'aient pu être déterminés à l'heure actuelle à partir de ces données, de telles géométries devraient certainement permettre, à l'avenir, de caractériser rapidement et de façon reproductible les propriétés des vésicules.

Ces études offrent des perspectives intéressantes pour obtenir des formes plus ou moins structurées à partir de vésicules et proposent des techniques alternatives pour les caractériser. Plusieurs pistes s'ouvrent donc pour continuer dans ce domaine. Une première voie serait d'étudier les relations entre structure et propriétés mécaniques. Par exemple pour les membranes décorées de polyélectrolytes, nous pourrions étudier le rôle de différents paramètres sur les valeurs de paramètres mécaniques tel que le degré de couverture, la constitution chimique du polymère (chaînes alkylées) ou modifier les conditions externes tels que le pH ou la concentration en sel.

Une seconde piste consisterait à étudier le rôle des paramètres mécaniques sur le comportement de vésicules sous des contraintes biologiquement pertinentes, tels que l'écoulement dans les géométries confinées. Enfin, ces vésicules composites pourraient être intéressantes pour de futures applications telles que la vectorisation de médicaments (en raison de leur stabilité aux

chocs de pH et de sel - par exemple vésicules décorées de polyelectrolyte), ou comme modèle pour des objets biologiques plus complexes tels que les cellules, les virus ou les pollens.



The goal of this work was first to develop mechanical models of cells based on lipidic giant unilamellar vesicles (GUV) and then to investigate the relationship between mechanical parameters and behaviors under external stresses.

Firstly, we succeeded in modifying structural and consequently mechanical properties of membranes either by coating them in the fluid phase with polyelectrolytes (chitosan and hyaluronan) or by using the lipid phase transition to obtain membranes in the gel state.

The polyelectrolyte coated fluid DOPC vesicles have been extensively characterized. We have revealed the electrostatic origin of the interaction between polyelectrolytes and zwitterionic lipidic membrane, showing the role of their respective charge densities on the amount of adsorbed polymer. We have evidenced that the polymer chemical structure controls the adsorbed chain conformation at the vesicle surface: chitosan adsorbs flat while hyaluronan forms loops and trains. The key parameters are the chain rigidity and the polymer affinity for the solvent. We have also highlighted a patch-like structure of the polyelectrolyte coated membranes, consisting in the alternation of bare and polymer coated domains. This heterogeneous structure allows the pertinent description of the aggregation-dissociation phenomenon observed for coated vesicles in solution as a function of the amount of added polyelectrolyte.

Besides, the global charge of vesicles can be modified in a control way by changing either the adsorbed amount or the nature of the polyelectrolyte. We show in particular that it is possible to alternate layers of polyanion and polycation at the membrane surface.

Concerning DMPC GUVs with membrane in the gel state, we have developed a shrewd protocol to preserve the vesicles spherical shape upon cooling and transition from a fluid phase to the $P_{\beta'}$ gel phase.

Secondly, we have demonstrated that the membrane structure highly affects the value of the mechanical parameters and changes the behaviors of these complex vesicles under various applied constraints (e.g. osmotic pressure, pH and salt shocks, compression between two planes (using Atomic Force Microscopy) or point-acting force (by hydrodynamic membrane tether extrusion). Our study has been performed back and forth, either by characterizing the mechanical properties of the object and looking at their influence on the objects behavior, or by applying a stress to the object and trying to back up mechanical properties from their behavior.

For polyelectrolyte coated vesicles, we have highlighted that the asymmetric coating induces a spontaneous curvature which sign can be adjusted by changing the electrostatic screening.

Moreover, we have demonstrated from the original compression experiments of chitosan-coated GUVs with AFM that polyelectrolyte coating rigidifies lipid membranes, increasing among oth-

ers their stretching moduli.

Such studies have also underlined that those modified mechanical properties induce original behaviors of the composite vesicles under stress. In particular, under osmotic pressure, polyelectrolyte coated vesicles exhibit spherical deflation with either tube ejection or invaginations.

In the case of gel vesicles, we are able to produce a large panel of concave polyhedron-like shapes from the deflation experiments. These various shapes were numerically retrieved using a 2D elastic model and a shape phase diagram for such elastic surfaces has been established. By performing a quantitative comparison between experimental and simulated shapes, we have evaluated the stretching and the shear moduli of the membrane in the $P_{\beta'}$ gel state.

Finally, we reported preliminary results on bare GUVs flowing in two different geometries of close fitting channels. We have highlighted that confinement strongly affects the shape of GUVs and their mobility. Indeed, we found that the study of the behavior of vesicles flowing in the single constriction allows a determination of their size, whereas their flow through multiple constrictions induces their focalization in the outlet channel and allows an estimation of the internal medium viscosity. In spite of the fact that the membrane mechanical parameters are not determined from these data at the moment, such geometries open perspectives for fast and reproducible measurements of the GUV properties.

Altogether, these studies offer interesting insights for obtaining more or less structured shapes through composite vesicles and propose alternative techniques to study them. Several ways open themselves to continue this study further.

A first way would be to investigate the relationship between structure and mechanical properties. For example for polyelectrolyte coated membrane, we could evaluate the influence of different parameters on the mechanical parameters values. One could vary the coverage degree, the polymer chemical structure by using alkylated chains or by modifying external parameters such as pH or salt.

A second way would be to study the role of mechanical parameters on vesicles behavior under biologically relevant stresses, such as flow in confined geometries.

Finally, composite vesicles could be relevant for future applications in the domain of drug delivery, for example thanks to their stability against pH and salt shocks (e.g. polyelectrolyte coated vesicles) or as model for more complex biological objects such as cells, virus or pollen.

○ ○ ○ ○ ○ ○ ○ ○ ○ ○

Fazit

Das Ziel dieser Arbeit war es zunächst mechanische Modelle von Zellen basierend auf lipidischen "giant unilamellar vesicles" (GUV) [riesige einlamellige Vesikel] zu entwickeln und dann die Beziehung zwischen mechanischen Parametern und Verhaltensweisen unter äußeren Belastungen zu untersuchen.

Erstens gelang es uns strukturelle und folglich mechanische Eigenschaften von Membranen zu verändern, entweder durch Beschichtung der flüssigen Phase mit Polyelektrolyten (Chitosan und Hyaluronsäure) oder durch Nutzung des Lipid Phaseübergangs, um Membranen im Gel-Zustand zu erhalten.

Die mit Polyelektrolyt beschichteten flüssigen DOPC Vesikel, wurden umfassend charakterisiert. Wir haben den elektrostatischen Ursprung der Interaktion zwischen Polyelektrolyten und zwitterionischen lipidischen Membran aufdecken können, und so die Rolle der jeweiligen Ladungsdichten auf die Menge des adsorbierten Polymers gezeigt. Wir haben bewiesen, dass die polymerchemische Struktur die adsorbierten Kettenkonformation an der Vesikeloberfläche kontrolliert: Chitosan adsorbiert flach, während Hyaluronan Schlingen und Züge bildet. Die Schlüsselparameter sind die Kettensteifigkeit und die Lösungsmittelaffinität des Polymers. Wir haben auch eine fleckenähnliche Struktur der mit Polyelektrolyt beschichteten Membranen erkannt, welche aus dem Wechsel von nackten und mit Polymer bedeckten Domänen besteht. Diese heterogene Struktur ermöglicht eine Beschreibung des Aggregation-Dissoziation Phänomens, welches für die gelösten und beschichteten Vesikel als Funktion der dazugegebenen Menge der Polyelektrolyte beobachtet wird.

Außerdem kann die globale Ladung von Vesikeln in einer kontrollierten Weise geändert werden, indem entweder die adsorbierte Menge oder die Art der Polyelektrolyte geändert wird. Wir zeigen insbesondere, dass es möglich ist, Polyanion- und Polykationschichten an der Membranoberfläche abzuwechseln.

Was DMPC GUVs mit einer Membran im Gel-Zustand betrifft, haben wir ein geschicktes Protokoll entwickelt, welches die Erhaltung der Kugelform beim Abkühlen und beim Übergang des Vesikels von einer flüssigen Phase zur $P_{\beta'}$ Gelphase erhält.

Zweitens haben wir gezeigt, dass die Membran-Struktur den Wert der mechanischen Parameter stark beeinflusst und Änderungen in den Verhaltensweisen dieser komplexen Vesikel unter verschiedenen angewandten Einschränkungen hervorbringen kann (z. B. osmotischer Druck, pH- und Salz-Schocks, Kompression zwischen zwei Ebenen mittels Atomic Force Microscopy oder Punktkräfte durch hydrodynamische Membran-tether Bildung).

Unsere Studie wurde in zwei Richtungen durchgeführt, entweder durch die Charakterisierung der mechanischen Eigenschaften und deren Einfluss auf das Verhalten der Objekte, oder durch das Anlegen einer mechanischen Verspannung, um dann die mechanischen Eigenschaften aus dem Verhalten des Objektes abzuleiten.

Bei den Polyelektrolyt-beschichteten Vesikeln, haben wir gezeigt, dass die asymmetrische Beschichtung eine spontane Krümmung verursacht, deren Vorzeichen durch die Veränderung der elektrostatischen Abschirmung geregelt werden kann.

Darüber hinaus, haben wir bei den ursprünglichen Kompressions-Experimenten von Chitosan-beschichteten GUVs mit AFM gezeigt, dass eine Polyelektrolytbeschichtung die Lipidmembranen versteift, wodurch unter anderem eine Zunahme des Reckmodulus erreicht wird. Solche Studien

haben auch unterstrichen, dass diese veränderten mechanischen Eigenschaften das Verhalten der Verbund-Vesikel unter Stress erzeugen. Insbesondere unter osmotischem Druck, zeigen die mit Polyelektrolyten beschichteten Vesikel eine kugelförmige Entleerung mit entweder dem Auswurf oder der Einstülpung von Membranschläuchen.

Im Falle der Gel-Vesikeln, konnten wir eine große Gruppe von konkaven Polyeder-ähnliche Formen aus den Deflations-Experimenten erzeugen. Diese verschiedenen Formen wurden numerisch mit Hilfe eines 2D-elastischen Modelles reproduziert und ein Form-Phasendiagramm für solche elastischen Oberflächen wurde erstellt. Durch die Durchführung eines quantitativen Vergleiches zwischen experimentellen und simulierten Formen, haben wir sowohl die Reck- als auch die Schermodule der Membran in dem $P_{\beta'}$ Gel-Zustand ermitteln können.

Schliesslich, berichten wir über vorläufige Ergebnisse auf nackten GUVs, welche in zwei verschiedenen Geometrien durch enge Kanäle fließen. Wir haben beobachtet, dass diese geometrischen Beschränkung die Form und die Mobilität von GUVs stark beeinflusst. Tatsächlich fanden wir, dass die Untersuchung des Verhaltens von Vesikeln, welche in einzelne Engstellen fließen, eine Bestimmung der Vesikel-Größe ermöglicht, während ihre Strömung durch mehrere Engstellen die Fokussierung auf den Auslasskanal verursacht und so eine Abschätzung der inneren Lösungsviskosität erlaubt.

Trotz der Tatsache, dass momentan die mechanischen Parametern der Membran aus diesen Daten nicht eindeutig bestimmt werden, eröffnen solche Geometrien neue Perspektiven zur schnellen und reproduzierbaren Messungen der Eigenschaften von GUVs.

Insgesamt bieten diese Studien interessante Einblicke, um mehr oder weniger strukturierte Formen durch Composite-Vesikel zu erhalten und wir schlagen alternative Techniken vor, um diese zu studieren. Es eröffnen sich mehrere Möglichkeiten, um diese Studie weiter zu führen. Eine erste Möglichkeit wäre die Beziehung zwischen Struktur und mechanischen Eigenschaften zu untersuchen. Zum Beispiel, könnten wir für die Polyelektrolyt beschichtete Membran den Einfluss verschiedener Parameter auf die mechanischen Eigenschaften betrachten. Man könnte den Bedeckungsgrad variieren, indem man die polymer-chemische Struktur durch die Benutzung von alkylierten Ketten oder durch externe Parameter wie pH oder Salze verändert. Eine zweite Möglichkeit wäre, die Rolle der mechanischen Parameter auf das Vesikelverhalten unter biologisch relevanten Belastungen zu studieren, wie z.B. die Strömung in eingeschränkten Geometrien.

Schließlich, könnten die Composite-Vesikel für zukünftige Anwendungen im Bereich "Drug Delivery" relevant sein, zum Beispiel dank ihrer Stabilität gegenüber pH- und Salz-Schocks (z. B. Polyelektrolytbeschichtete Vesikel) oder als Modell für komplexere biologische Objekte wie Zellen, Viren oder Pollen.

Appendix A

Table units

We gather in the Table [A.1](#), the equivalence between the units of the quantities used in this manuscript.

Quantity	units
Pressure	$1.45 \times 10^{-4} \text{ Psi} \approx 1 \text{ Pa} \approx 1 \text{ N.m}^{-2} \approx 10^{-5} \text{ bar} \approx 9.87 \times 10^{-6} \text{ atm}$
Dynamic viscosity	$1 \text{ Pa.s} \approx 10^3 \text{ cP} \approx 1 \text{ kg.m}^{-1}.\text{s}^{-1}$
Energy	$1 k_B T \approx 4 \times 10^{-21} \text{ J}$ $1 \text{ erg} \approx 1 \text{ dyn.cm} \approx 10^{-7} \text{ J} \approx 10^{-7} \text{ N.m}$
Force	$1 \text{ N} \approx 10^5 \text{ dyn}$
Shear modulus	$1 \text{ N.m}^{-1} \approx 10^3 \text{ dyn.cm}^{-1}$
Surface shear viscosity	$1 \text{ N.s.m}^{-1} \approx 1 \text{ Pa.s.m} \approx 10^3 \text{ dyn.s.cm}^{-1} \approx 10^3 \text{ sp}$

Table A.1: *Equivalence between the units of diverse quantities used in the present manuscript.*

Appendix B

Link between isotropic material and 2D model elastic parameters

Mechanical parameters of the membrane - stretching χ , shear μ and bending κ moduli- can be related to the elastic parameters of a 3 dimensional material (3D Young modulus Y_{3D} , 3D Poisson ratio ν_{3D} sheet thickness d) thanks to the 2 dimensional elastic parameters (2D Young modulus Y_{2D} , 2D Poisson ratio ν_{2D}) when this material is considered as an infinitely thin elastic sheet [Landau and Lifshitz, 1986, Feynman et al., 1966]. Table B1 only reports the relationships between these various parameters in the case of in-plane material deformations.

Membranes parameters (3D)	Connections 2D / 3D for in-plane deformations	
	2D \rightarrow 3D:	3D \rightarrow 2D:
Bending modulus: $\kappa = \frac{Y_{3D} d^3}{12(1-\nu_{3D}^2)}$	3D poisson ratio: $\nu_{3D} = \nu_{2D}$	2D poisson ratio: $\nu_{2D} = \nu_{3D} = \frac{\chi_{2D} - \mu_{2D}}{\chi_{2D} + \mu_{2D}}$
Shear modulus: $\mu_{3D} = \frac{Y_{3D}}{2(1+\nu_{3D})}$	3D Young modulus: $Y_{3D} = \sqrt{\frac{Y_{2D}^3}{12\kappa(1-\nu_{2D})}}$	2D Young modulus: $Y_{2D} = Y_{3D} d$
Stretching modulus: $\chi_{3D} = \frac{Y_{3D}}{3(1-2\nu_{3D})}$	Sheet thickness: $d = \sqrt{12 \frac{\kappa}{Y_{2D}} (1-\nu_{2D}^2)} = \sqrt{6 \frac{\kappa}{\chi_{2D}} (1+\nu_{2D})}$	2D Shear modulus: $\mu_{2D} = \frac{Y_{3D} d}{2(1+\nu_{2D})}$
		2D Stretching modulus: $\chi_{2D} = \frac{Y_{3D} d}{2(1-\nu_{3D})}$

Table B.1: Relations between 2D and 3D parameters, evaluated from [Landau and Lifshitz, 1986].

Appendix C

Comparison simulations and biological objects

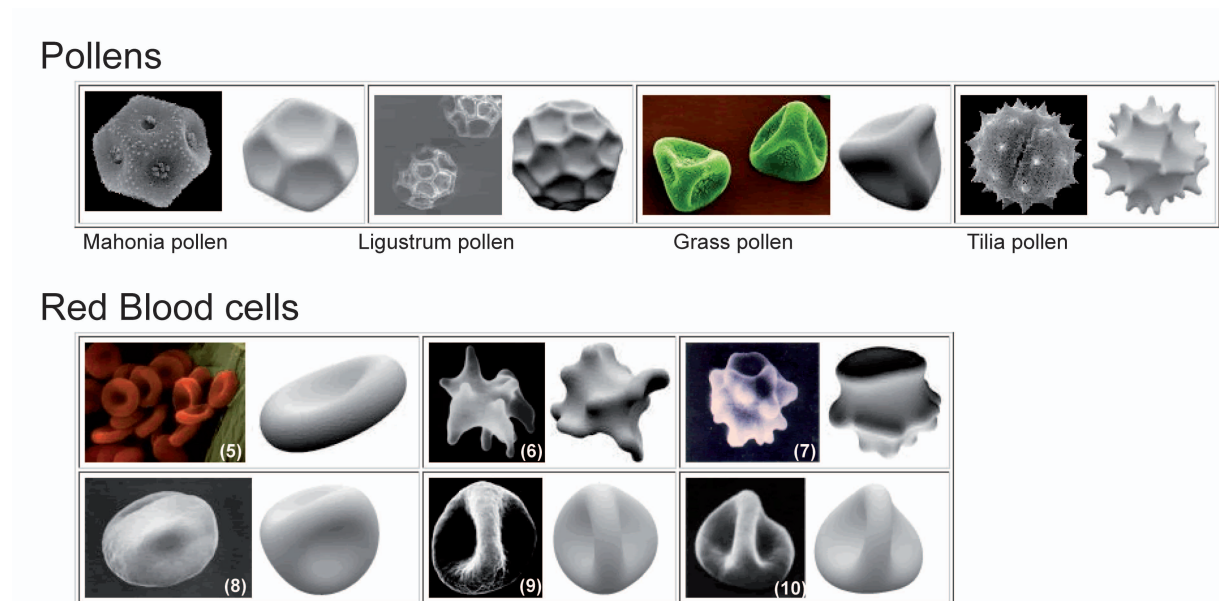


Figure C.1: Actual biological shapes on the left, and the corresponding Surface Evolver simulations on the right.

Bibliography

- [Abkarian et al., 2008] Abkarian, M., Faivre, M., Horton, R., Smistrup, K., Best-Popescu, C., and Stone, H. (2008). Cellular-scale hydrodynamics. *Biomed. Mater.*, 3:034011.
- [Abkarian et al., 2006] Abkarian, M., Faivre, M., and Stone, H. (2006). High-speed microfluidic differential manometer for cellular-scale hydrodynamics. *Proc. Natl. Acad. Sci. USA*, 103(3):538–542.
- [Abkarian et al., 2007] Abkarian, M., Faivre, M., and Viallat, A. (2007). Swinging of red blood cells under shear flow. *Phys. Rev. Lett.*, 98(18):188302.
- [Abkarian et al., 2002] Abkarian, M., Lartigue, C., and Viallat, A. (2002). Tank treading and unbinding of deformable vesicles in shear flow: determination of the lift force. *Phys. Rev. Lett.*, 88(6):068103–1 068103–4.
- [Abkarian and Viallat, 2005] Abkarian, M. and Viallat, A. (2005). Dynamics of vesicles in a wall-bounded shear flow. *Biophys. J.*, 89:1055–1066.
- [Alberts et al., 2002] Alberts, B., Johnson, A., Lewis, J., Raff, M., Roberts, K., and Walter, P. (2002). *Molecular Biology of the Cell. 4th revised edition*. Garland Science, New York.
- [Angelova and Dimitrov, 1987] Angelova, M. and Dimitrov, D. (1987). Liposome electroformation. *Faraday discussion of the chemical society*, 81:303–311.
- [Angelova and Tsoneva, 1999] Angelova, M. and Tsoneva, I. (1999). Interactions of dna with giant liposomes. *Chem. Phys. Lipids*, 101:123–137.
- [Antunes et al., 2009] Antunes, F., Marques, E., Miguel, M., and Lindman, B. (2009). Polymer-vesicle association. *Adv. Colloid Interface Sci.*, 147-148:18–35.
- [Arguelles-Monal et al., 2000] Arguelles-Monal, W., Cabrera, G., Peniche, C., and Rinaudo, M. (2000). Conductimetric study of the interpolyelectrolyte reaction between chitosan and polygalacturonic acid. *Polymer*, 41(7):2373–2378.
- [Babak et al., 1999] Babak, V., Lukina, I., Vikhoreva, G., Desbrieres, J., and Rinaudo, M. (1999). Interfacial properties of dynamic association between chitin derivatives and surfactants. *Colloids Surf A: Physicochem Eng Aspects*, 147:139–148.

- [Bagchi and Kalluri, 2009] Bagchi, P. and Kalluri, R. M. (2009). Dynamics of nonspherical capsules in shear flow. *Phys. Rev. E*, 80:016307.
- [Balaz, 2009] Balaz, S. (2009). Modeling kinetics of subcellular disposition of chemicals. *Chem. Rev.*, 109:1793–1899.
- [Bar-Ziv et al., 1998] Bar-Ziv, R., Moses, E., and Nelson, P. (1998). Dynamic excitations in membranes induced by optical tweezers. *Biophys. J.*, 75:294–320.
- [Barrat and Joanny, 1996] Barrat, J. and Joanny, J. (1996). Theory of polyelectrolyte solutions. *Adv. Chem. Phys.*, 94:1–66.
- [Ben-Amar and Pomeau, 1997] Ben-Amar, M. and Pomeau, Y. (1997). Crumpled paper. *Proc. R. Soc. London, Ser. A*, 453(8):729–755.
- [Bernard et al., 2002] Bernard, A.-L., Guedeau-Boudeville, M.-A., Jullien, L., and di Meglio, J.-M. (2002). Raspberry vesicles. *Biochimica et Biophysica Acta*, 1567(1-2):1–5.
- [Berriaud et al., 1998] Berriaud, N., Milas, M., and Rinaudo, M. (1998). *Polysaccharides: Structural Diversity and Functional Versatility*. Dekker, New York.
- [Berth and Dautzenberg, 2002] Berth, G. and Dautzenberg, H. (2002). The degree of acetylation of chitosan and its effect on the chain conformation in aqueous solution. *Carbohydr. Polym.*, 47:39–51.
- [Betterton and Brenner, 1999] Betterton, M. and Brenner, M. (1999). Electrostatic edge instability of lipid membranes. *Phys. Rev. Lett.*, 82:1598–1601.
- [Betticher et al., 1995] Betticher, D., Reinhart, W., and Geiser, J. (1995). Effect of RBC shape and deformability on pulmonary O₂ diffusing capacity and resistance to flow in rabbit lungs. *J. Appl. Physiol.*, 78:778–783.
- [Böckmann et al., 2003] Böckmann, R. A., Hac, A., Heimburg, T., and Grubmüller, H. (2003). Effect of sodium chloride on a lipid bilayer. *Biophys. J.*, 85:1647–1655.
- [Bonekamp et al., 1987] Bonekamp, B. C., Alvarez, R. H., Nieves, F. J. D., and Bijsterbosch, B. (1987). The effect of adsorbed charged polypeptides on the electrophoretic mobility of positively and negatively charged polystyrene lattices. *J. Colloid Interface Sci.*, 118(2):366–371.
- [Bordi et al., 2009] Bordi, F., Sennato, S., and Truzzolillo, D. (2009). Polyelectrolyte-induced aggregation of liposomes: a new cluster phase with interesting applications. *J. Phys.: Condens. Matter*, 21:203102–203128.
- [Borghi et al., 2003a] Borghi, N., Kremer, S., Askovic, V., and Brochard-Wyart, F. (2003a). Tube extrusion from permeabilized giant vesicles. *Europhys. Lett.*, 75(4):666–672.

- [Borghi et al., 2003b] Borghi, N., Rossier, O., and Brochard-Wyart, F. (2003b). Hydrodynamic extrusion of tubes from giant vesicles. *Europhys. Lett.*, 64(6):837–843.
- [Boroske et al., 1981] Boroske, E., Elwenspoek, M., and Helfrich, W. (1981). Osmotic shrinkage of giant egg-lecithin vesicles. *Biophys. J.*, 34:95–109.
- [Brakke, 1992] Brakke, K. (1992). The surface evolver. *Exp. Math.*, 1(2):141–165.
- [Breidenich et al., 2005] Breidenich, M., Netz, R., and Lipowsky, R. (2005). The influence of non-anchored polymers on the curvature of vesicles. *Mol. Phys.*, 103:3169–3183.
- [Brochard and Lennon, 1975] Brochard, F. and Lennon, J.-F. (1975). Frequency spectrum of the flicker phenomenon in erythrocytes. *J. Phys.*, 36:1035–1047.
- [Brooks et al., 1991] Brooks, J., Marques, C., and Cates, M. (1991). Role of adsorbed polymer in bilayer elasticity. *Europhys. Lett.*, 14(7):713–718.
- [Browicz, 1890] Browicz, E. (1890). Further observation of motion phenomena on red blood cells in pathological states. *Zbl. Med. Wiss.*, 28:625–627.
- [Brugnerotto et al., 2001] Brugnerotto, J., Desbrières, J., Roberts, G., and Rinaudo, M. (2001). Characterization of chitosan by steric exclusion chromatography. *Polymer*, 42:9921–9927.
- [Buhler and Boué, 2003] Buhler, E. and Boué, F. (2003). Persistence length for a model semi-rigid polyelectrolyte as seen by small angle neutron scattering: a relevant variation of the lower bound with ionic strength. *Eur. Phys. J. E.*, 10:89–92.
- [Callens et al., 2008] Callens, N., Minetti, C., Coupier, G., Mader, M.-A., Dubois, F., Misbah, C., and Podgorski, T. (2008). Hydrodynamic lift of vesicles under shear flow in microgravity. *Eur. Phys. Lett.*, 83(2):24002.
- [Cametti, 2008] Cametti, C. (2008). Polyion-induced aggregation of oppositely charged liposomes and charged colloidal particles: The many facets of complex formation in low-density colloidal systems. *Chem. Phys. Lipids*, 155:63–73.
- [Campillo, 2007] Campillo, C. (2007). *Développement et étude d'objets biomimétiques stimulables: Vésicules géantes encapsulant des systèmes visco-élastiques de poly(NIPAM)*. PhD thesis, University Joseph Fourier, Grenoble, France.
- [Campillo et al., 2009] Campillo, C., Schroder, A., Marques, C., and Pijépin-Donat, B. (2009). Composite gel-filled giant vesicles: Membrane homogeneity and mechanical properties. *B. Mater. Sci. Eng.*, 2:393–397.
- [Canham, 1970] Canham, P. B. (1970). The minimum energy of bending as a possible explanation of the biconcave shape of the human red blood cell. *J. Theor. Biol.*, 26:61–81.

- [Carvalho et al., 2008] Carvalho, K., Ramos, L., Roy, C., and Picart, C. (2008). Giant unilamellar vesicles containing phosphatidylinositol(4,5)bisphosphate: characterization and functionality. *Biophys. J.*, 95(9):4348–4360.
- [Cevc, 1990] Cevc, G. (1990). Membrane electrostatics. *Biochim. Biophys. Acta*, 1031:311–382.
- [Chang and Olbricht, 1993] Chang, K. and Olbricht, W. (1993). Experimental studies of the deformation and breakup of a synthetic capsule in steady and unsteady simple shear-flow. *J. Fluid Mech.*, 250:609–633.
- [Charitat et al., 2008] Charitat, T., Lecuyer, S., and Frangneto, G. (2008). fluctuations and destabilization of single phospholipid bilayers. *Biointerfaces*, 3(2):FB3–FB15.
- [Claessens et al., 2004] Claessens, M., van Oort, B., Leermakers, F., Hoekstra, F., and Stuart, M. C. (2004). Charged lipid vesicles: Effects of salts on bending rigidity, stability, and size. *Biophys. J.*, 87:3882–3893.
- [Clausen-Schaumann and Gaub, 1999] Clausen-Schaumann, H. and Gaub, H. (1999). Dna adsorption to laterally structured charged lipid membranes. *Langmuir*, 15:8246–8251.
- [Clément and Joanny, 1997] Clément, F. and Joanny, J.-F. (1997). Curvature elasticity of an adsorbed polymer layer. *J. Phys. II (France)*, 7:973.
- [Cohen-Stuart et al., 1980] Cohen-Stuart, C., Scheutjens, J., and Fleer, G. (1980). Polydispersity effects and the interpretation of polymer adsorption isotherms. *Polym. Sci., Part B: Polym. Phys.*, 18:559–573.
- [Coupier et al., 2008] Coupier, G., Kaoui, B., Podgorski, T., and Misbah, C. (2008). Noninertial lateral migration of vesicles in bounded poiseuille flow. *Phys. Fluids*, 20:111702.
- [Creuzet et al., 2006] Creuzet, C., Kadi, S., Rinaudo, M., and Auzely-Velty, R. (2006). New associative systems based on alkylated hyaluronic acid. synthesis and aqueous solution properties. *Polymer*, 47:2706–2713.
- [Cullis, 1976] Cullis, P. (1976). Lateral diffusion rates of phosphatidylcholine in vesicle membranes: effects of cholesterol and hydrocarbon phase transitions. *FEBS Lett.*, 70:223–228.
- [Dai and Sheetz, 1999] Dai, J. and Sheetz, M. (1999). Membrane tether formation from blebbing cells. *Biophys. J.*, 77:3363–3370.
- [Danker et al., 2009] Danker, G., Vlahovska, P., and Misbah, C. (2009). Vesicles in poiseuille flow. *Phys. Rev. Lett.*, 102:148102.
- [Davis, 1979] Davis, J. (1979). Deuterium magnetic-resonance study of the gel and liquid-crystalline phases of dipalmitoyl phosphatidylcholine. *Biophys. J.*, 27(3):339–358.
- [de Gennes, 1979] de Gennes, P. (1979). *Scaling concepts in polymer physics*. Cornell University Press, New York.

- [de Ven, 1994] de Ven, T. V. (1994). Kinetic aspects of polymer and polyelectrolyte adsorption on surfaces. *Adv. Colloid Interface Sci.*, 48:121–140.
- [de Vries et al., 2005] de Vries, A., Yefimov, S., Mark, A., and Marrink, S. (2005). Molecular structure of the lecithin ripple phase. *Proc. Natl. Acad. Sci. USA*, 102(15):5392–5396.
- [Decher, 1997] Decher, G. (1997). Fuzzy nanoassemblies : toward layered polymeric multicomposites. *Science*, 277:1232–1237.
- [Delorme et al., 2007] Delorme, N., Bardeau, J.-F., Carrière, D., Dubois, M., Gourbil, A., Möhwald, H., Zemb, T., and Fery, A. (2007). Experimental evidence of the electrostatic contribution to the bending rigidity of charged membranes. *J. Phys. Chem. B*, 11:2503–2505.
- [Delorme et al., 2006] Delorme, N., Dubois, M., Garnier, S., Laschewsky, A., Weinkamer, R., Zemb, T., and Fery, A. (2006). Surface immobilization and mechanical properties of cationic hollow faceted polyhedrons. *J. Phys. Chem. B*, 110:1752–1758.
- [Delorme and Fery, 2006] Delorme, N. and Fery, A. (2006). Direct method to study membrane rigidity of small vesicles based on atomic force microscope force spectroscopy. *Phys. Rev. E*, 74:030901.
- [Derenyi et al., 2002] Derenyi, I., Julicher, F., and Prost, J. (2002). Formation and interaction of membrane tubes. *Phys. Rev. Lett.*, 88:238101.
- [Derenyi et al., 2007] Derenyi, I., Koster, G., van Duijn, M., Czovek, A., Dogterom, M., and Prost, J. (2007). *Membrane Nanotubes*. Springer Berlin, Heidelberg.
- [Derzko and Jacobson, 1980] Derzko, Z. and Jacobson, K. (1980). Comparative lateral diffusion of lipid analogues in phospholipid multibilayers. *Biochemistry*, 19:6050–6057.
- [Desbrieres et al., 1996] Desbrieres, J., Martinez, C., and Rinaudo, M. (1996). Hydrophobic derivatives of chitosan: Characterization and rheological behaviour. *Int. J. Biol. Macromol.*, 19:21–28.
- [Desbrieres et al., 1997a] Desbrieres, J., Rinaudo, M., Babak, V., and Vikhoreva, V. (1997a). Surface activity of water soluble amphiphilic chitin derivatives. *Polym. Bull.*, 39:209–15.
- [Desbrieres et al., 1997b] Desbrieres, J., Rinaudo, M., and Chtcheglova, L. (1997b). Reversible thermothickening of aqueous solutions of polycations from natural origin. *Macromol. Symp.*, 113:135–149.
- [Deschamps et al., 2009] Deschamps, J., Kantsler, V., and Steinberg, V. (2009). Phase diagram of single vesicle dynamical states in shear flow. *Phys. Rev. Lett.*, 102:118105.
- [Dhont, 2002] Dhont, J., editor (2002). *33th IFF Spring School 2002 on Soft Matter, Complex Materials on mesoscopic scales*. Forschungszentrum Jülich GmbH, Jülich.

- [Diaz and Barthès-Biesel, 2002] Diaz, A. and Barthès-Biesel, D. (2002). Entrance of a bioartificial capsule in a pore. *CMES*, 3:321–337.
- [Diederich et al., 1998] Diederich, A., Bahr, G., and Winterhalter, M. (1998). Influence of surface charges on the rupture of black lipid membranes. *Phys. Rev. E*, 58(4):4883–4889.
- [Dijt et al., 1992] Dijt, J., Stuart, M. C., and Fleer, G. (1992). Kinetics of polymer adsorption and desorption in capillary flow. *Macromolecules*, 25:5416–5423.
- [Dijt et al., 1994] Dijt, J., Stuart, M. C., and Fleer, G. (1994). Competitive adsorption kinetics of polymers differing in length only. *Macromolecules*, 27:3219–3228.
- [Dimova et al., 2009] Dimova, R., Bezlyepkina, N., Jordö, M. D., Knorr, R., Riske, K., Staykova, M., Vlahovska, P., Yamamoto, T., Yang, P., and Lipowsky, R. (2009). Vesicles in electric fields: Some novel aspects of membrane behavior. 5:3201–3212.
- [Ding et al., 2007] Ding, W., Qi, X.-R., Fu, Q., and Piao, H.-S. (2007). Vesicles in electric fields: Some novel aspects of membrane behavior. 14(2):101–104.
- [Döbereiner, 2000] Döbereiner, H.-G. (2000). Properties of giant vesicles. *Curr. Opin. Colloid Interface Sci.*, 5:256–263.
- [Dobrynin et al., 2000] Dobrynin, A. V., Deshpikowski, A., and Rubinstein, M. (2000). Adsorption of polyelectrolytes at an oppositely charged surface. *Phys. Rev. Lett.*, 84:3101–3104.
- [Douglas et al., 1994] Douglas, J. F., Frantz, P., Johnson, H., Schneider, H., and Granick, S. (1994). Regimes of polymer adsorption-desorption kinetics. *Colloids Surf., A*, 86:251–254.
- [Dubreuil et al., 2003] Dubreuil, F., Elsner, N., and Fery, A. (2003). Elastic properties of polyelectrolyte capsules studied by atomic-force microscopy and rcm. *Eur. Phys. J. E*, 12:215–221.
- [Ducker et al., 1991] Ducker, W., Senden, T., and Pashley, R. (1991). Direct measurement of colloidal forces using an atomic force microscope. *Nature*, 353:239–241.
- [el Alaoui Faris, 2008] el Alaoui Faris, M. (2008). *Physique des membranes actives : Mesure de spectres de fluctuations*. PhD thesis, Thèse de doctorat de l’université Paris VI, Paris.
- [Elbert and Hubbell, 1996] Elbert, D. and Hubbell, J. (1996). Surface treatments of polymers for biocompatibility. *Annu. Rev. Mater. Sci.*, 26:365–394.
- [Eli et al., 1999] Eli, W., Chen, W., and Xue, Q. (1999). The association of anionic surfactants with β -cyclodextrins. an isothermal titration calorimeter study. *J. Chem. Thermodyn.*, 31:1283–1296.
- [Elsabee et al., 2009] Elsabee, M., Morsi, R., and Al-Sabagh, A. (2009). Surface active properties of chitosan and its derivatives. *Colloids Surf., B*, 74:1–16.

- [Ercelen et al., 2006] Ercelen, S., Zhang, X., Duportail, G., Grandfils, C., Desbrieres, J., Karaeva, S., Tikhonov, V., Mely, Y., and Babak, V. (2006). Physicochemical properties of low molecular weight alkylated chitosans: A new class of potential nonviral vectors for gene delivery. *Colloids Surf. B*, 51:140–148.
- [Erni et al., 2005] Erni, P., Fischer, P., and Windhab, E. (2005). Deformation of single emulsion drops covered with a viscoelastic adsorbed protein layer in simple shear flow. *Appl. Phys. Lett.*, 87:244104.
- [Evans and Needham, 1987] Evans, E. and Needham, D. (1987). Physical properties of surfactant bilayer membranes: Thermal transitions, elasticity, rigidity, cohesion, and colloidal interactions. *J. Phys. Chem.*, 91:4219–4228.
- [Evans and Rawicz, 1990] Evans, E. and Rawicz, W. (1990). Entropic-driven tension and bending elasticity in condensed-fluid membrane. *Phys. Rev. Lett.*, 64(17):2094–2097.
- [Evans and Yeung, 1994] Evans, E. and Yeung, A. (1994). Hidden dynamics in rapid changes of bilayer shape. *Chem. Phys. Lipids*, 73:39–56.
- [Fa, 2003] Fa, N. (2003). *Micro-rhéologie de vésicules géantes*. PhD thesis, Université Louis Pasteur, Strasbourg.
- [Faivre, 2006] Faivre, M. (2006). *Drops, vesicles and red blood cells: Deformability and behavior under flow*. PhD thesis, Université Joseph Fourier, Grenoble.
- [Faivre et al., 2006] Faivre, M., Campillo, C., Pepin-Donat, B., and Viallat, A. (2006). Reversible giant vesicles filled with poly(n-isopropylacrylamide) sols or gels. *Progr. Colloid. Polym. Sci.*, 133:41–44.
- [Fang and Chan, 2003] Fang, N. and Chan, V. (2003). Chitosan-induced restructuration of a mica-supported phospholipid bilayer: An atomic force microscopy study. *Biomacromolecules*, 4:1596–1604.
- [Fang et al., 2003] Fang, N., Lai, A.-K., Wan, K.-T., and Chan, V. (2003). Effect of acyl chain mismatch on the contact mechanics of two-component phospholipid vesicle during main phase transition. *Biophys. Chem.*, 104:141–153.
- [Feng et al., 2004] Feng, Z., Granick, S., and Gewirth, A. (2004). Modification of a supported lipid bilayer by polyelectrolyte adsorption. *Langmuir*, 20:8796–8804.
- [Fery and Weinkamer, 2007] Fery, A. and Weinkamer, R. (2007). Mechanical properties of micro- and nanocapsules: single capsule measurements. *Polymer*, 48:7221–7235.
- [Fettiplace and Haydon, 1980] Fettiplace, R. and Haydon, D. (1980). Water permeability of lipid-membrane. *Physiol. Rev.*, 60(2):510–550.

- [Feynman et al., 1966] Feynman, R., Leighton, R., and Sands, M. (1966). *The Feynman lectures on physics Volume II: Mainly electromagnetism and matter*. Addison Wesley, Massachusetts.
- [Filipovica-Grci et al., 2001] Filipovica-Grci, J., N.Skalko-Basnet, and Jalsenjaj, I. (2001). Mucoadhesive chitosan-coated liposomes: characteristics and stability. *J. Microencapsulation*, 18(1):3–12.
- [Fischer and Schmid-Schönbein, 1977] Fischer, T. and Schmid-Schönbein, H. (1977). Tank tread motion of red cell membranes in viscometric flow: behavior of intracellular and extracellular markers (with film). *Blood Cells*, 3:351–365.
- [Fleer et al., 1993] Fleer, J. L., Stuart, M. A. C., Scheutjens, J. M. H. M., Cosgrove, T., and Vincent, B. (1993). *Polymers at interfaces*. Chapman et Hall, London.
- [Flory, 1979] Flory, P. (1979). *Statistical mechanics of chain molecules*. Wiley, New York.
- [Fouissac, 1992] Fouissac, E. (1992). *Contribution à l'obtention d'acide hyaluronique par voie fermentaire et étude de ses propriétés physicochimiques*. PhD thesis, Thèse de doctorat de l'Université Joseph Fourier, Grenoble.
- [Gao et al., 2001] Gao, C., Donath, E., Moya, S., Dudnik, V., and Mohwald, H. (2001). Elasticity of hollow polyelectrolyte capsules prepared by the layer-by-layer technique. *Eur. Phys. J. E*, 5:21–27.
- [Garcia-Manyes et al., 2005] Garcia-Manyes, S., Oncins, G., and Sanz, F. (2005). Effect of ion-binding and chemical phospholipid structure on the nanomechanics of lipid bilayers studied by force spectroscopy. *Biophys. J.*, 89:1812–1826.
- [Geffroy et al., 2000] Geffroy, C., Labeau, M., Wong, K., Cabane, B., and Stuart, M. C. (2000). Kinetics of adsorption of polyvinylaniline onto cellulose. *Colloids Surf., A*, 172(1-3):47–56.
- [Girard, 2004] Girard, P. (2004). *Membranes hors d'équilibre: échanges et transport actif*. PhD thesis, Thèse de doctorat de l'Université de Paris VII, Paris.
- [Gregory, 1972] Gregory, J. (1972). Rates of flocculation of latex particles by cationic polymers. *J. Colloid Interface Sci.*, 42(2):448–456.
- [Gromer, 2007] Gromer, A. (2007). *Visualisation de la conformation de polyélectrolytes à l'interface solide-liquide par Microscopie à Force Atomique*. PhD thesis, Univerity Louis Pasteur, Strasbourg, France.
- [Guo et al., 2003] Guo, J., Ping, Q., Jiang, G., Huang, L., and Tonga, Y. (2003). Chitosan-coated liposomes: characterization and interaction with leuprolide. *Int. J. Pharm.*, 260:167–173.
- [Guo et al., 2009] Guo, K., Wang, J., Qiu, F., Zhang, H., and Yang, Y. (2009). Shapes of fluid vesicles anchored by polymer chains. *Soft Matter*, 5:1646–1655.

- [Haluska et al., 2008] Haluska, C., Schroder, A., Didier, P., Heissler, D., Duportail, G., Mely, Y., and Marques, C. (2008). Combining fluorescence lifetime and polarization microscopy to discriminate phase separated domains in giant unilamellar vesicles. *Biophys. J.*, 95:5737–5747.
- [Hara, 1993] Hara, M., editor (1993). *Polyelectrolytes: Science and technology*. Marcel Dekker, New York.
- [Haugland, 2005] Haugland, R. (2005). *The Handbook. A Guide to Fluorescent Probes and Labeling Technologies, 10th ed.* Invitrogen, San Diego.
- [Haxaire, 2000] Haxaire, K. (2000). *Conformation du hyaluronane et interactions en solution et à l'état solide*. PhD thesis, University Joseph Fourier, Grenoble, France.
- [Heimburg, 2000] Heimburg, T. (2000). A model for the lipid pretransition: coupling of ripple formation with the chain-melting transition. *Biophys. J.*, 78:1154–1165.
- [Heinrich and Waugh, 1996] Heinrich, V. and Waugh, R. (1996). A piconewton force transducer and its application to measurement of the bending stiffness of phospholipid membranes. *Ann. Biomed. Eng.*, 24:595–605.
- [Helfrich, 1973] Helfrich, W. (1973). Elastic properties of lipid bilayers: theory and possible experiments. *Z. Naturforsch. C*, 28:693–703.
- [Henriksen et al., 1994] Henriksen, I., Smistad, G., and Karlsen, J. (1994). Interactions between liposomes and chitosan. *Int. J. Pharm.*, 101(3):227–236.
- [Henriksen et al., 1997] Henriksen, I., Vhgen, S., Sande, S., Smistad, G., and Karlsen, J. (1997). Interactions between liposomes and chitosan ii: effect of selected parameters on aggregation and leakage. *Int. J. Pharm.*, 146:193–204.
- [Hesselink et al., 1971] Hesselink, F. T., Vrij, A., and Overbeek, J. T. G. (1971). Theory of stabilization of dispersions by adsorbed macromolecules .2. interaction between 2 flat particles. *J. Phys. Chem*, 75(14):2094–2103.
- [Hochmuth, 2000] Hochmuth, R. (2000). Micropipette aspiration of living cells. *J. Biomechanics*, 33:15–22.
- [Hoogeveen et al., 1996] Hoogeveen, N., Stuart, M. C., and Fleer, G. (1996). Polyelectrolyte adsorption on oxides ii. reversibility and exchange. *J. Colloid Interface Sci.*, 182:146–157.
- [Hope et al., 1985] Hope, M. J., Bally, M. B., Webb, G., and Cullis, P. R. (1985). Production of large unilamellar vesicles by a rapid extrusion procedure. characterization of size distribution, trapped volume and ability to maintain a membrane potential. *Biochim. Biophys. Acta*, 812:55–65.
- [Huang and Ingber, 1999] Huang, S. and Ingber, D. (1999). The structural and mechanical complexity of cell-growth control. *Nat. Cell Biol.*, 1(5):E131–E138.

- [Huebner et al., 1999] Huebner, S., Battersby, B., Grimm, R., and Cevc, G. (1999). Lipid-dna complex formation: Reorganization and rupture of lipid vesicles in the presence of dna as observed by cryoelectron microscopy. *Biophys. J.*, 76:3158–3166.
- [Hunter, 1981] Hunter, R. J. (1981). *Zeta potential in colloid science: Principles and applications*. Academic Press, London.
- [Hutter and Bechhoefer, 1993] Hutter, J. L. and Bechhoefer, J. (1993). Calibration of atomic-force microscope tips. *Rev. Sci. Instrum.*, 64(7):1868–1873.
- [Illum and Davis, 1994] Illum, L. and Davis, N. F. S. (1994). Chitosan as a novel nasal delivery system for peptide drugs. *Pharm. Res.*, 11:1186–1189.
- [Israelachvili, 1992] Israelachvili, J. (1992). *Intermolecular and surface forces*. Academic Press, London.
- [Janiak et al., 1979] Janiak, M., Small, D., and Shipley, G. (1979). Temperature and compositional dependence of the structure of hydrated dimyristoyl lecithin. *J. Biol. Chem.*, 254(13):6068–6078.
- [Jansen and Blume, 1995] Jansen, M. and Blume, A. (1995). A comparative study of diffusive and osmotic permeation across bilayers composed of phospholipids with different head groups and fatty acyl chains. *Biophys. J.*, 68(3):997–1008.
- [Jen et al., 2000] Jen, C., Jhiang, S.-J., and Chen, H.-I. (2000). Cellular responses to mechanical stress: invited review: effects of flow on vascular endothelial intracellular calcium signaling of rat aortas ex vivo. *J. App. Physiol.*, 89(4):1657–1662.
- [Jenkel and Rumbach, 1951] Jenkel, E. and Rumbach, B. (1951). Über die adsorption von hochmolekularen stoffen aus der losung. *Z. Elektrochem.*, 55(7):612–620.
- [Kaasgaard et al., 2003] Kaasgaard, T., Leidy, C., Crowe, J., Mouritsen, O., and Jørgensen, K. (2003). Temperature-controlled structure and kinetics of ripple phases in one- and two-component supported lipid bilayers. *Biophys. J.*, 85:350–360.
- [Kabanov, 2005] Kabanov, V. A. (2005). Polyelectrolyte complexes in solution and in bulk. *Russ. Chem. Rev.*, 74(1):3–20.
- [Kantsler and Steinberg, 2005] Kantsler, V. and Steinberg, V. (2005). Orientation and dynamics of a vesicle in tank-treading motion in shear flow. *Phys. Rev. Lett.*, 95:258101.
- [Kantsler and Steinberg, 2006] Kantsler, V. and Steinberg, V. (2006). Transition to tumbling and two regimes of tumbling motion of a vesicle in shear flow. *Phys. Rev. Lett.*, 96:036001.
- [Kaoui et al., 2009] Kaoui, B., Biro, G., and Misbah, C. (2009). Why do red blood cells have asymmetric shapes even in a symmetric flow? *Phys. Rev. Lett.*, 103:188101.

- [Kaoui et al., 2008] Kaoui, B., Ristow, G., Cantat, I., Misbah, C., and Zimmermann, W. (2008). Lateral migration of a two-dimensional vesicle in unbounded poiseuille flow. *Phys. Rev. E*, 77:021903.
- [Karlsson et al., 2001] Karlsson, M., Sott, K., A-S.Cans, Karlsson, A., Karlsson, R., and Orwar, O. (2001). Micropipet-assisted formation of microscopic networks of unilamellar lipid bilayer nanotubes and containers. *Langmuir*, 17(22):6754–6758.
- [Kas, 1997] Kas, H. (1997). Chitosan: Properties, preparations and application to microparticulate systems. *Microcapsules*, 14:689–711.
- [Käs and Sackmann, 1997] Käs, J. and Sackmann, E. (1997). Shape transitions and shape stability of giant phospholipid vesicles in pure water induced by area-to-volume changes. *Biophys. J.*, 60:825–844.
- [Katchalsky et al., 1954] Katchalsky, A., Sahvit, N., and H.Eisenberg (1954). Dissociation of weak polymeric acids and bases. *J. Polym. Sci.*, 13(68):69–84.
- [Katifori et al., 2010] Katifori, E., Alben, S., Cerda, E., Nelson, D. R., and Dumais, J. (2010). Foldable structures and the natural design of pollen grains. *Proc. Natl. Acad. Sci. USA*, 109:7635–7639.
- [K.Berndl et al., 1990] K.Berndl, Käs, J., Lipowsky, R., Sackmann, E., and Seifert, U. (1990). Shape transformations of giant vesicles: Extreme sensitivity to bilayer asymmetry. *Europhys. Lett.*, 13:659–664.
- [Keller and Skalak, 1982] Keller, S. and Skalak, R. (1982). A tank treading ellipsoidal particle in shear flow. *J. Fluid Mech.*, 120:27–47.
- [Kennedy et al., 2002a] Kennedy, J. F., Phillips, G. O., Williams, P. A., and Hascall, V. C., editors (2002a). *Hyaluronan, vol. 1: Chemical, biochemical and biological aspects*. Woodhead, Cambridge, UK.
- [Kennedy et al., 2002b] Kennedy, J. F., Phillips, G. O., Williams, P. A., and Hascall, V. C., editors (2002b). *Hyaluronan, vol. 2: Biomedical, Medical and Clinical Aspects*. Woodhead, Cambridge, UK.
- [Khor and Lim, 2003] Khor, E. and Lim, L. (2003). Implantable applications of chitin and chitosan. *Biomaterials*, 24:2339–2349.
- [Kim and Sung, 2001] Kim, Y. and Sung, W. (2001). Membrane curvature induced by polymer adsorption. *Phys. Rev. E*, 63:041910.
- [Kogan et al., 2007] Kogan, G., Soltés, L., Stern, R., and Gemeiner, P. (2007). Hyaluronic acid: a natural biopolymer with a broad range of biomedical and industrial applications. *Biotechnol. Lett.*, 29:17–25.

- [Komura et al., 2005] Komura, S., Tamura, K., and Kato, T. (2005). Buckling of spherical shells adhering onto a rigid substrate. *Eur. Phys. J. E*, 18:343–358.
- [Koynova and Caffrey, 1994] Koynova, R. and Caffrey, M. (1994). Phases and phase transitions of the phosphatidylethanolamines hydrated. *Chem. Phys. Lipids*, 69:1–34.
- [Koynova and Caffrey, 1998] Koynova, R. and Caffrey, M. (1998). Phases and phase transitions of the phosphatidylcholines. *Biochim. Biophys. Acta*, 1376:91–145.
- [Kratky and Porod, 1949] Kratky, O. and Porod, G. (1949). Röntgenuntersuchung gelöster fadenmoleküle. *Rec. Trav. Chem.*, 68:1106–1123.
- [Kratochvil and Suter, 1989] Kratochvil, P. and Suter, U. W. (1989). Definitions of terms relating to individual macromolecules, their assemblies, and dilute polymer-solutions. *Pure Appl. Chem.*, 61(2):211–241.
- [Kremer, 2009] Kremer, S. (2009). *Extrusion de nanotubes membranaires: de la vésicule à la cellule vivante*. PhD thesis, Université Paris 6, Paris.
- [Kremer et al., 2010] Kremer, S., Campillo, C., Quemeneur, F., Rinaudo, M., Pepin-Donat, B., and Brochard-Wyart, F. (2010). Nanotubes from asymmetrically decorated vesicles. *submitted*.
- [Kujawa et al., 2005] Kujawa, P., Moraille, P., Sanchez, J., Badia, A., and Winnik, F. (2005). Effect of molecular weight on the exponential growth and morphology of hyaluronan/chitosan multilayers: A surface plasmon resonance spectroscopy and atomic force microscopy investigation. *J. Am. Chem. Soc.*, 127(25):9224–9234.
- [Kwok and Evans, 1981] Kwok, R. and Evans, E. (1981). Thermoelasticity of large lecithin bilayer vesicles. *Biophys. J.*, 35(2):637–652.
- [Ladbury, 2004] Ladbury, J. (2004). Application of isothermal titration calorimetry in the biological sciences: Things are heating up! *BioTechniques*, 37(6):885–887.
- [Landau and Lifshitz, 1986] Landau, L. and Lifshitz, E. (1986). *Course of Statistical Physics, Vol. 7: Theory of Elasticity, 3rd edition*. Elsevier, Oxford.
- [Laney et al., 1997] Laney, D., Garcia, R., Parsons, S., and Hansma, H. (1997). Changes in the elastic properties of cholinergic synaptic vesicles as measured by atomic force microscopy. *Biophys. J.*, 72(2):806–813.
- [Langner and Kubica, 1999] Langner, M. and Kubica, K. (1999). The electrostatics of lipid surfaces. *Chem. Phys. Lipids*, 101(1):3–35.
- [Lee et al., 1999] Lee, J., Petrov, P., and Döbereiner, H.-G. (1999). Curvature of zwitterionic membranes in transverse pH gradients. *Langmuir*, 15:8543–8546.

- [Lee et al., 2006] Lee, J.-H., Agarwal, V., Bose, A., Payne, G., and Raghavan, S. (2006). Transition from unilamellar to bilamellar vesicles induced by an amphiphilic biopolymer. *Phys. Rev. Lett.*, 96:048102.
- [Lee et al., 2008] Lee, S.-J., Song, Y., and Baker, N. (2008). Molecular dynamics simulations of asymmetric NaCl and KCl solutions separated by phosphatidylcholine bilayers: potential drops and structural changes induced by strong Na⁺-lipid interactions and finite size effects. *Biophys. J.*, 94:3565–3576.
- [Lefebvre et al., 2008] Lefebvre, Y., Leclerc, E., Barthès-Biesel, D., Walter, J., and Edwards-Lévy, F. (2008). Flow of artificial microcapsules in microfluidic channels: A method for determining the elastic properties of the membrane. *J. Fluids*, 20:123102.
- [Leonenko et al., 2004] Leonenko, Z., Finot, E., Ma, H., Dahms, T., and Cramb, D. (2004). Investigation of temperature-induced phase transitions in dopc and dppc phospholipid bilayers using temperature-controlled scanning force microscopy. *Biophys. J.*, 86(6):3783–3793.
- [Liang et al., 2004] Liang, X., Mao, G., and Ng, S. (2004). Mechanical properties and stability measurement of cholesterol-containing liposome on mica by atomic force microscopy. *J. Colloid Interface Sci.*, 278(1):53–62.
- [Lidmar et al., 2003] Lidmar, J., Mirny, L., and Nelson, D. (2003). Virus shape and buckling transition in spherical shells. *Phys. Rev. E*, 68(5):051910.
- [Lifson and Katchalsky, 1954] Lifson, S. and Katchalsky, A. (1954). The electrostatic free energy of polyelectrolyte solutions. 2. fully stretched macromolecules. *J. Polymer Sci.*, 13(68):43–55.
- [Lim et al., 2006] Lim, C., Zhoua, E., and Quek, S. (2006). Mechanical models for living cells - a review. *J. Biomechanics*, 39:195–216.
- [Lim et al., 2002] Lim, G., Wortis, M., and Mukhopadhyay, R. (2002). Stomatocyte-discocyte-echinocyte sequence of the human red blood cell: Evidence for the bilayer-couple hypothesis from membrane mechanics. *Proc. Nat. Acad. Sci. U.S.A.*, 99(26):16766–16769.
- [Lim et al., 2008] Lim, G., Wortis, M., and Mukhopadhyay, R. (2008). *Soft Matter vol. 4: Lipid bilayers and red blood cells*. Wiley-VCH, Weinheim (Germany).
- [Lipowsky and Sackmann, 1995] Lipowsky, R. and Sackmann, E., editors (1995). *Structure and Dynamics of Membranes, Handbook of Biological Physics (Vol 1A and 1B)*. Elsevier Science, Amsterdam.
- [Liu and Fletcher, 2009] Liu, A. and Fletcher, D. (2009). Biology under construction: in vitro reconstitution of cellular function. *Nat. Rev. Mol. Cell Biol.*, 10:644–650.
- [Liu, 2006] Liu, K.-K. (2006). Deformation behaviour of soft particles: a review. *J. Phys. D: Appl. Phys.*, 39:R189–R199.

- [Luan and Ramos, 2007] Luan, Y. and Ramos, L. (2007). Real-time observation of polyelectrolyte-induced binding of charged bilayers. *J. Am. Chem. Soc.*, 129(47):14619–14624.
- [Luisi and Walde, 2000] Luisi, P. L. and Walde, P. (2000). *"Giant Vesicles", in Perspective in Supramolecular Chemistry*. John Wiley & Sons, Chichester, UK.
- [Lulevich et al., 2004] Lulevich, V., Andrienko, D., and Vinogradova, O. (2004). Elasticity of polyelectrolyte multilayer microcapsules. *J. Chem Phys.*, 120(8):3822–3826.
- [Luzzati and Husson, 1962] Luzzati, V. and Husson, F. (1962). The structure of the liquid-crystalline phases of lipid-water systems. *J. Cell Biol.*, 12(2):207–219.
- [Macdonald et al., 2000] Macdonald, P., Crowell, K., Franzin, C., Mitrakos, P., and Semchyschyn, D. (2000). ^2H NMR and polyelectrolyte-induced domains in lipid bilayers. *Solid State Nucl. Magn. Reson.*, 16:21–36.
- [MacKay, 1981] MacKay, A. (1981). A proton NMR moment study of the gel and liquid-crystalline phases of dipalmitoylphosphatidylcholine. *Biophys. J.*, 35(2):301–313.
- [Mader et al., 2006] Mader, M., Viktova, V., Abkarian, M., and et al. (2006). Dynamics of viscous vesicles in shear flow. *Eur. Phys. J.E.*, 19:389–397.
- [Mady et al., 2009] Mady, M., Darwish, M., Khalil, S., and Khalil, W. (2009). Biophysical studies on chitosan-coated liposomes. *Eur. Biophys. J.*, 38:1127–1133.
- [Majoros et al., 2005] Majoros, A. M. I., Patri, A., Baker, J., Holl, M., and Orr, B. (2005). Lipid bilayer disruption by polycationic polymers: The roles of size and chemical functional group. *Langmuir*, 21:10348–10354.
- [Malmsten, 2003] Malmsten, M. (2003). *Protein adsorption in intravenous drug delivery. In Biopolymers at Interfaces*. Dekker, New York.
- [Manning, 1969a] Manning, G. (1969a). Limiting laws and counterion condensation in polyelectrolyte solutions i. colligative properties. *J. Phys. Chem.*, 51(3):924–933.
- [Manning, 1969b] Manning, G. (1969b). Limiting laws and counterion condensation in polyelectrolyte solutions iii. an analysis based on the mayer ionic solution theory. *J. Phys. Chem.*, 51(8):3249–3252.
- [Marmottant et al., 2010] Marmottant, P., Bouakaz, A., de Jong, N., and Quilliet, C. (2010). Ultrasound-driven buckling of solid shell bubbles. *J. Acoust. Soc. Am.* submitted.
- [Marty and Tsapis, 2008] Marty, G. and Tsapis, N. (2008). Monitoring the buckling threshold of drying colloidal droplets using water-ethanol mixtures. *Eur. Phys. J. E*, 27(2):213–219.
- [Mathai et al., 2008] Mathai, J., Tristram-Nagle, S., Nagle, J., and Zeidel, M. (2008). Structural determinants of water permeability through the lipid membrane. *J. Gen. Physiol.*, 131(1):69–76.

- [Mazeau and Vergelati, 2002] Mazeau, K. and Vergelati, C. (2002). Atomistic modeling of the adsorption of benzophenone onto cellulosic surfaces. *Langmuir*, 18:1919–1927.
- [Mertins et al., 2009] Mertins, O., da Silveira, N., Pohlmann, A., Schrder, A., and Marques, C. (2009). Electroformation of giant vesicles from an inverse phase precursor. *Biophys. J.*, 96:2719–2726.
- [Mertins et al., 2008] Mertins, O., Lionzo, M., Micheletto, Y., Pohlmann, A., and da Silveira, N. (2008). Chitosan effect on the mesophase behavior of phosphatidylcholine supramolecular systems. *Mater. Sci. Eng., C*, 29:463–469.
- [Mertins et al., 2010] Mertins, O., Schneider, P., Pohlmann, A., and da Silveira, N. (2010). Interaction between phospholipids bilayer and chitosan in liposomes investigated by ^{31}P NMR spectroscopy. *Colloids Surf., B*, 75(1):294–299.
- [Messlinger et al., 2009] Messlinger, S., Schmidt, B., Noguchi, H., and Gompper, G. (2009). Dynamical regimes and hydrodynamic lift of viscous vesicles under shear. *Phys. Rev. E*, 80:011901.
- [Meyer, 1996] Meyer, H. (1996). Pretransition ripples in bilayers of dipalmitoylphosphatidylcholine: undulation or periodic segments? a freeze-fracture study. *Biochim. Biophys. Acta.*, 1302:138–144.
- [Miao et al., 1994] Miao, L., Seifert, U., Wortis, M., and Döbereiner, H. G. (1994). Budding transitions of fluid-bilayer vesicles: The effect of area-difference elasticity. *Phys. Rev. E*, 49(6):5389–5407.
- [Milas and Rinaudo, 1997] Milas, M. and Rinaudo, M. (1997). On the electrostatic interactions of ionic polysaccharides in solution. *Curr. Trends Polym. Sci.*, 2:47–67.
- [Mohandas and Evans, 1994] Mohandas, N. and Evans, E. (1994). Mechanical properties of the red cell membrane in relation to molecular structure and genetic defects. *Annu. Rev. Biophys. Biomol. Struct.*, 23:787–818.
- [Mui et al., 1995] Mui, B. L. S., Dberiner, H. G., Madden, T. D., and Cullis, P. R. (1995). Influence of transbilayer area asymmetry on the morphology of large unilamellar vesicles. *Biophys. J.*, 69:930–941.
- [Mukhopadhyay et al., 2002] Mukhopadhyay, R., Lim, G., and Wortis, M. (2002). Echinocyte shapes: Bending, stretching, and shear determine spicule shape and spacing. *Biophys. J.*, 82:1756–1772.
- [Muzzarelli, 1973] Muzzarelli, R. (1973). *Natural chelating polymers: alginic acid, chitin and chitosan*. Pergamon Press, New York.

- [Nayar et al., 1989] Nayar, R., Hope, M. J., and Cullis, P. R. (1989). Generation of large unilamellar vesicles from long-chain saturated phosphatidylcholines by extrusion technique. *Biochim. Biophys. Acta*, 986:200–206.
- [Needham and Evans, 1988] Needham, D. and Evans, E. (1988). Structure and mechanical properties of giant lipid (dmPC) vesicle bilayers from 20°C below to 10°C above the liquid crystalline phase transition at 24°C. *Biochemistry*, 27:8261–8269.
- [Netz and Andelman, 2003] Netz, R. and Andelman, D. (2003). Neutral and charged polymers at interfaces. *Physics Reports*, 380:1–95.
- [Nguyen et al., 2005] Nguyen, T., Gopal, A., Lee, K., and Witten, T. (2005). Surface charge relaxation and the pearling instability of charged surfactant tubes. *Phys. Rev. E*, 72:051930.
- [Noguchi and Gompper, 2005] Noguchi, H. and Gompper, G. (2005). Shape transitions of fluid vesicles and red blood cells in capillary flows. *Proc. Natl. Acad. Sci. USA*, 102(40):12159–14164.
- [Noguchi et al., 2010] Noguchi, H., Gompper, G., Schmid, L., Wixforth, A., and Franke, T. (2010). Dynamics of fluid vesicles in flow through structured microchannels. *Eur. Phys. Lett.*, 89:28002–6.
- [Nylander et al., 2006] Nylander, T., Samoshina, Y., and Lindman, B. (2006). Formation of polyelectrolyte-surfactant complexes on surfaces. *Adv. Colloid Interface Sci.*, 123-126:105–123.
- [Odijk, 1977] Odijk, T. (1977). Polyelectrolytes near rod limit. *J. Polym. Sci., Polym. Phys.*, 15(3):477–483.
- [Odijk, 1979a] Odijk, T. (1979a). On the ionic-strength dependence of the intrinsic viscosity of DNA. *Biopolymers*, 18:3111–3113.
- [Odijk, 1979b] Odijk, T. (1979b). Possible scaling relations for semidilute polyelectrolyte solutions. *Macromolecules*, 12(4):688–693.
- [Odijk and Houwaart, 1978] Odijk, T. and Houwaart, A. (1978). Theory of excluded-volume effect of a polyelectrolyte in a 1-1 electrolyte solution. *J. Polym. Sci., Polym. Phys.*, 16(4):627–639.
- [Ohki, 1982] Ohki, S. (1982). A mechanism of divalent ion-induced phosphatidylserine membrane-fusion. *Biochim. Biophys. Acta*, 689(1):1–11.
- [Ohtani et al., 1989] Ohtani, Y., Irie, T., Uekama, K., Fukunaga, K., and Pitha, J. (1989). Differential effects of α -, β - and γ -cyclodextrins on human erythrocytes. *Eur. J. Biochem.*, 186:17–22.

- [Olbrich et al., 2000] Olbrich, K., Rawicz, W., Needham, D., and et al. (2000). Water permeability and mechanical strength of polyunsaturated lipid bilayers. *Biophys. J.*, 79(1):321–327.
- [Olla, 1997a] Olla, P. (1997a). The lift on a tank-treading ellipsoidal cell in a shear flow. *J. Phys. A*, 30:317–329.
- [Olla, 1997b] Olla, P. (1997b). The role of tank-treading motions in the transverse migration of a spheroidal vesicle in a shear flow. *J. Phys. France II*, 7:1533–1540.
- [O’Shaughnessy and Vavylonis, 2005] O’Shaughnessy, B. and Vavylonis, D. (2005). Non-equilibrium in adsorbed polymer layers. *J. Phys.: Condens. Matter*, 17:R63–R99.
- [Pabst et al., 2007] Pabst, G., Hodzic, A., Strancar, J., Danner, S., Rappolt, M., and Laggner, P. (2007). Rigidification of neutral lipid bilayers in the presence of salts. *Biophys. J.*, 93:2688–2696.
- [Parfitt and Rochester, 1983] Parfitt, G. and Rochester, C. (1983). *Adsorption from solution at the solid/liquid interface*. Academic Press, New York.
- [Pauchard and Allain, 2003] Pauchard, L. and Allain, C. (2003). Stable and unstable surface evolution during the drying of a polymer solution drop. *Phys. Rev. E*, 68:052801.
- [Pauchard and Couder, 2004] Pauchard, L. and Couder, Y. (2004). Invagination during the collapse of an inhomogeneous spheroidal shell. *Europhys. Lett.*, 66(5):667–673.
- [Pavinatto et al., 2010] Pavinatto, A., Pavinatto, F., Barros-Timmons, A., and Jr., O. O. (2010). Electrostatic interactions are not sufficient to account for chitosan bioactivity. *ACS Appl. Mater. Interfaces*, 2:246–251.
- [Pefferkorn, 1995] Pefferkorn, E. (1995). The role of polyelectrolytes in the stabilization and destabilization of colloids. *Adv. Colloid Interface Sci.*, 56:33–104.
- [Pefferkorn et al., 1985] Pefferkorn, E., Carroy, A., and Varoqui, R. (1985). Dynamic behavior of flexible polymers at a solid/liquid interface. *J. Polym. Sci., Part B: Polym. Phys.*, 23:1997–2008.
- [Peniche and Arguelles-Monal, 2001] Peniche, C. and Arguelles-Monal, W. (2001). Chitosan based polyelectrolyte complexes. *Macromol. Symp.*, 168:103–116.
- [Perkel and Ullman, 1961] Perkel, R. and Ullman, R. (1961). The adsorption of polydimethylsiloxanes from solution. *J. Polymer Sci.*, 54(159):127–148.
- [Perugini et al., 2000] Perugini, P., Genta, I., Pavanetto, F., Conti, B., Scalia, S., and Baruffini, A. (2000). Study on glycolic acid delivery by liposomes and microspheres. *Int. J. Pharm.*, 196(1):51–61.
- [Petelska and Figaszewski, 2000] Petelska, A. and Figaszewski, Z. (2000). Effect of pH on the interfacial tension of lipid bilayer membrane. *Biophys. J.*, 78:812–817.

- [Petrache et al., 2004] Petrache, H., Tristram-Nagle, S., Gawrisch, K., Harries, D., Parsegian, V., and Nagle, J. (2004). Structure and fluctuations of charged phosphatidylserine bilayers in the absence of salt. *Biophys. J.*, 86:1574–1586.
- [Philippova et al., 2001] Philippova, O., Volkov, E., Sitnikova, N., and Khokhlov, A. (2001). Two types of hydrophobic aggregates in aqueous solutions of chitosan and its hydrophobic derivative. *Biomacromolecules*, 2:483–490.
- [Plateau, 1873] Plateau, J. (1873). *Statique expérimentale et théorique des liquides soumis aux seules forces moléculaires*.
- [Portet et al., 2009] Portet, T., Febrer, F., Escoffre, J.-M., Favard, C., Rols, M.-P., and Dean, D. (2009). Visualization of membrane loss during the shrinkage of giant vesicles under electropulsation. *Biophys. J.*, 96(10):4109–4121.
- [Pospieszny et al., 1994] Pospieszny, H., Struszczyk, H., Chirkov, S. N., and Atabekov, J. G. (1994). *New applications of chitosan in agriculture*. Bremerhaven, Wirtschafsverlag NW, Germany.
- [Quéguiner and Barthès-Biesel, 1997] Quéguiner, C. and Barthès-Biesel, D. (1997). Axisymmetric motion of capsules through cylindrical channels. *J. Fluid Mech.*, 348:349–376.
- [Quemeneur et al., 2008] Quemeneur, F., Rinaudo, M., and Pépin-Donat, B. (2008). Influence of polyelectrolyte chemical structure on their interaction with lipid membrane of zwitterionic liposomes. *Biomacromolecules*, 9:2237–2243.
- [Quilliet et al., 2008] Quilliet, C., Zoldesi, C., Riera, C., van Blaaderen, A., and Imhof, A. (2008). Anisotropic colloids through non-trivial buckling. *Eur. Phys. J. E*, 27:13–20. and erratum.
- [Rappolt et al., 2000] Rappolt, M., Pabst, G., Rapp, G., Kriechbaum, M., Amenitsch, H., Krenn, C., Bernstorff, S., and Laggner, P. (2000). New evidence for gel-liquid crystalline phase coexistence in the ripple phase of phosphatidylcholines. *Eur. Biophys. J.*, 29:125–133.
- [Rawicz et al., 2000] Rawicz, W., Olbrich, K., McIntosh, T., and et al. (2000). Effect of chain length and unsaturation on elasticity of lipid bilayers. *Biophys. J.*, 79(1):328–339.
- [Reed, 1994] Reed, W. (1994). *Macro-ion characterization from dilute solutions to complex fluids*. ACS symposium series N° 548. American Chemical Society, Washington.
- [Rhazi et al., 2002] Rhazi, M., Desbrieres, J., Tolaimate, A., Rinaudo, M., Vottero, P., Alagui, A., and el Meray, M. (2002). Influence of the nature of the metal ions on the complexation with chitosan. application to the treatment of liquide waste. *Eur. Polym. J.*, 38:1523–1530.
- [Rinaudo, 1974] Rinaudo, M. (1974). *Polyelectrolytes*. D. Reidel Publishing Compagny, Dordrecht-Holland.

- [Rinaudo, 2006] Rinaudo, M. (2006). Chitin and chitosan: Properties and applications. *Prog. Polym. Sci.*, 31(7):603–632.
- [Rinaudo, 2008] Rinaudo, M. (2008). Main properties and current applications of some polysaccharides as biomaterials. *Polym. Int.*, 57(3):397–430.
- [Rinaudo, 2009] Rinaudo, M. (2009). Polyelectrolyte properties of a plant and animal polysaccharide. *Struct. Chem.*, 20(2):277–289.
- [Rinaudo et al., 2005] Rinaudo, M., Auzely, R., Vallin, C., and Mullagaliev, I. (2005). Specific interactions in modified chitosan systems. *Biomacromolecules*, 6:2396–2407.
- [Rinaudo et al., 1992] Rinaudo, M., Dung, P. L., Gey, C., and Milas, M. (1992). Substituent distribution on o, n-carboxymethylchitosans by ^1H and ^{13}C nmr. *Int J Biol Macromol*, 14:122–128.
- [Rinaudo et al., 1999a] Rinaudo, M., Pavlov, G., and Desbrieres, J. (1999a). Influence of acetic acid concentration on the solubilization of chitosan. *polymer*, 40:7029–7032.
- [Rinaudo et al., 1999b] Rinaudo, M., Pavlov, G., and Desbrieres, J. (1999b). Solubilization of chitosan in strong acid medium. *Int. J. Polym. Anal. Charac.*, 5:267–276.
- [Rinaudo et al., 1997] Rinaudo, M., Roure, I., Milas, M., and Malovikova, A. (1997). Electrostatic interactions in aqueous solutions of ionic polysaccharides. *Int. J. Polym. Anal. Charac.*, 4(1):57–69.
- [Risso et al., 2006] Risso, F., Collé-Paillot, F., and Zagzoule, M. (2006). Experimental investigation of a bioartificial capsule flowing in a narrow tube. *J. Fluid Mech.*, 547:149–173.
- [Rosa et al., 2007] Rosa, M., Miguel, M., and Lindman, B. (2007). DNA encapsulation by biocompatible cationic vesicles. *J. Colloid Interface Sci.*, 312(1):87–97.
- [Rossier et al., 2003] Rossier, O., Cuvelier, D., Borghi, N., Puech, P., Derényi, I., Buguin, A., Nassoy, P., and Brochard-Wyart, F. (2003). Giant vesicles under flows: extrusion and retraction of tubes. *Langmuir*, 19:575–584.
- [Rothman and Dawidowicz, 1975] Rothman, J. and Dawidowicz, E. A. (1975). Asymmetric exchange of vesicle phospholipids catalyzed by the phosphatidylcholine exchange protein. measurement of inside-outside transitions. *Biochemistry*, 14(13):2809–2816.
- [Rüppel and Sackmann, 1983] Rüppel, D. and Sackmann, E. (1983). On defects in different phases of two-dimensional lipid bilayers. *J. Physique*, 44:1025–1034.
- [Rusu-Balaita et al., 2003] Rusu-Balaita, L., Desbrières, J., and Rinaudo, M. (2003). Formation of a biocompatible polyelectrolyte complex: chitosan-hyaluronan complex stability. *Polym. Bull.*, 50:91–98.

- [Sabin et al., 2006] Sabin, J., Prieto, G., Ruso, J. M., Hidalgo-Alvarez, R., and Sarmiento, F. (2006). Size and stability of liposomes: A possible role of hydration and osmotic forces. *Eur. Phys. J. E*, 20:401–408.
- [Sabin et al., 2007] Sabin, J., Ruso, J. M., and Sarmiento, F. (2007). Fractal aggregates induced by liposome-liposome interaction in the presence of Ca^{2+} . *Eur. Phys. J. E*, 24:201–210.
- [Sachs et al., 2004] Sachs, J. N., Nanda, H., Petrache, H. I., and Woolf, T. B. (2004). Changes in phosphatidylcholine headgroup tilt and water order induced by monovalent salts: molecular dynamics simulations. *Biophys. J.*, 86:3772–3782.
- [Samoshina et al., 2005] Samoshina, Y., Nylander, T., Shubin, V., Bauer, R., and Eskilsson, K. (2005). Equilibrium aspects of polycation adsorption on silica surface: How the adsorbed layer responds to changes in bulk solution. *Langmuir*, 21:5872–5881.
- [Sandre, 2000] Sandre, O. (2000). *Pores transitoires, adhésion et fusion des vésicules géantes*. PhD thesis, Thèse de doctorat de l’université Paris 6, Paris.
- [Sandre et al., 1999] Sandre, O., Moreaux, L., and Brochard-Wyart, F. (1999). Dynamics of transient pores in stretched vesicles. *Proc. Natl. Acad. Sci. USA*, 96:10591–10596.
- [Saxton and Jacobson, 1997] Saxton, M. J. and Jacobson, K. (1997). Single-particle tracking: Applications to membrane dynamics. *Annu. Rev. Biophys. Biomol. Struct.*, 26:373–399.
- [Schneider et al., 1996] Schneider, H. M., Frantz, P., and Granick, S. (1996). The bimodal energy landscape at polymer-solid interfaces. *Langmuir*, 12:994–996.
- [Secomb, 2003] Secomb, T. (2003). *Modeling and Simulation of Capsules and Biological Cells*. Chapman & Hall, London.
- [Secomb et al., 1986] Secomb, T., Skalak, R., Özkaya, N., and Gross, J. (1986). Flow of axisymmetric red blood cells in narrow capillaries. *J. Fluid Mech.*, 163:405–423.
- [Secomb et al., 2007] Secomb, T., Styp-Rekowska, B., and Pries, A. (2007). Two-dimensional simulation of red blood cell deformation and lateral migration in microvessels. *Ann. Biomed. Eng.*, 35(5):755–765.
- [Seelig et al., 1987] Seelig, J., Macdonald, P., and Scherer, P. (1987). Phospholipid head groups as sensors of electric charge in membranes. *Biochemistry*, 26:7535–7541.
- [Seifert et al., 1991] Seifert, U., Berndt, K., and Lipowsky, R. (1991). Shape transformations of vesicles: Phase diagram for spontaneous curvature and bilayer-coupling models. *Phys. Rev. A*, 44(2):1182–1202.
- [Servuss et al., 1976] Servuss, R., Harbich, V., and Helfrich, W. (1976). Measurement of the curvature-elastic modulus of egg lecithin bilayers. *Biochim. Biophys. Acta*, 436:900–903.

- [Shafir and Andelman, 2007] Shafir, A. and Andelman, D. (2007). Bending moduli of charged membranes immersed in polyelectrolyte solutions. *Soft Matter*, 3:644–650.
- [Shelby et al., 2003] Shelby, J., White, J., Ganesan, K., Rathod, P., and Chiu, D. (2003). A microfluidic model for single-cell capillary obstruction by plasmodium falciparum infected erythrocytes. *Proc. Natl. Acad. Sci. USA*, 100:14618–14622.
- [Shoemaker and Vanderlick, 2002] Shoemaker, S. and Vanderlick, T. (2002). Intramembrane electrostatic interactions destabilize lipid vesicles. *Biophys. J.*, 83(4):2007–2014.
- [Skalak and Branemark, 1969] Skalak, R. and Branemark, P. I. (1969). Deformation of red blood cells in capillaries. *Science*, 164:717–719.
- [Skolnick and Fixman, 1977] Skolnick, J. and Fixman, M. (1977). Electrostatic persistence length of a wormlike polyelectrolyte. *Macromolecules*, 10(5):944–948.
- [Skotheim and Secomb, 2007] Skotheim, J. M. and Secomb, T. (2007). Red blood cells and other nonspherical capsules in shear flow: Oscillatory dynamics and the tank-treading-to-tumbling transition. *Phys. Rev. Lett.*, 98:078301.
- [S.P. Sutura, 1993] S.P. Sutura, R. S. (1993). The history of poiseuille’s law. *Annu. Rev. Fluid Mech.*, 25:1–19.
- [Sukhishvili and Granick, 1998] Sukhishvili, S. and Granick, S. (1998). Kinetic regimes of polyelectrolyte exchange between the adsorbed state and free solution. *J. Chem. Phys.*, 109(16):6869–6878.
- [Sun et al., 1996] Sun, W., Tristram-Nagle, S., Suter, R., and Nagle, J. (1996). Structure of the ripple phase in lecithin bilayers. *Proc. Natl. Acad. Sci. USA*, 93(14):7008–7012.
- [Taglienti et al., 2006] Taglienti, A., Cellesi, F., Crescenzi, V., Sequi, P., Valentini, M., and Tire, N. (2006). Investigating the interactions of hyaluronan derivatives with biomolecules. the use of diffusional nmr techniques. *Macromol. Biosci.*, 6:611–622.
- [Tanaka et al., 2002] Tanaka, T., Tamba, Y., Masum, S. M., Yamashita, Y., and Yamazaki, M. (2002). La^{3+} and Gd^{3+} induce shape change of giant unilamellar vesicles of phosphatidylcholine. *Biochim. Biophys. Acta*, 1564:173–182.
- [Tardieu et al., 1973] Tardieu, A., Luzzati, V., and Reman, F. (1973). Structure and polymorphism of hydrocarbon chains of lipids - study of lecithin-water phases. *J. Mol. Biol.*, 75:711–733.
- [Taylor, 1934] Taylor, G. (1934). The formation of emulsions in definable fields of flow. *Proc. Roy. Soc.*, 146(858):501–523.
- [Thongborisute et al., 2006] Thongborisute, J., Takeuchi, H., Yamamoto, H., and Kawashima, Y. (2006). Visualization of the penetrative and mucoadhesive properties of chitosan and chitosan-coated liposomes through the rat intestine. *J. Liposome Res.*, 16:127–141.

- [Tribet and Vial, 2008] Tribet, C. and Vial, F. (2008). Flexible macromolecules attached to lipid bilayers: impact on fluidity, curvature, permeability and stability on the membranes. *Soft Matter*, 4:68–81.
- [Tsafrir et al., 2003] Tsafrir, I., Caspi, Y., Guedeau-Boudeville, M.-A., Arzi, T., and Stavans, J. (2003). Budding and tubulation in highly oblate vesicles by anchored amphiphilic molecules. *Phys. Rev. Lett.*, 91(13):138102.
- [Tsapis et al., 2005] Tsapis, N., Dufresne, E., Sinha, S., Riera, C., Hutchinson, J., Mahadevan, L., and Weitz, D. (2005). Onset of buckling in drying droplets of colloidal suspensions. *Phys. Rev. Lett.*, 94:018302.
- [Tsuchida and Hatta, 1988] Tsuchida, K. and Hatta, I. (1988). ESR studies on the ripple phase in multilamellar phospholipid bilayers. *Biochim. Biophys. Acta*, 945:73–80.
- [Varoqui, 1982] Varoqui, R. (1982). Effect of polymer adsorption on the electrophoretic mobility of colloids. *New J. Chem.*, 6(4):187–189.
- [Vasiliu et al., 2005] Vasiliu, S., Popa, M., and Rinaudo, M. (2005). Polyelectrolyte capsules made of two biocompatible natural polymers. *Eur. Polym. J. EPL*, 41(5):923–932.
- [Velegol and Thwar, 1984] Velegol, D. and Thwar, P. (1984). Analytical model for the effect of surface charge nonuniformity on colloidal interactions. *Langmuir*, 17:7687–7693.
- [Vial et al., 2005] Vial, F., Rabhi, S., and Tribet, C. (2005). Association of octyl-modified poly(acrylic acid) onto unilamellar vesicles of lipids and kinetics of vesicle disruption. *Langmuir*, 21:853–862.
- [Vinogradova, 2004] Vinogradova, O. (2004). Mechanical properties of polyelectrolyte multilayer microcapsules. *J. Phys.: Condens. Matter*, 16:R1105–R1134.
- [Vitkova et al., 2004] Vitkova, V., Mader, M., and Podgorski, T. (2004). Deformation of vesicles flowing through capillaries. *Europhys. Lett.*, 68(3):398–404.
- [Volodkin et al., 2007] Volodkin, D., Ball, V., Schaaf, P., Voegel, J.-C., and Mohwald, H. (2007). Complexation of phosphocholine liposomes with polylysine. stabilization by surface coverage versus aggregation. *Biochim. Biophys. Acta*, 1768:280–290.
- [Walde et al., 2010] Walde, P., Cosentino, K., Engel, H., and Stanod, P. (2010). Giant vesicles: Preparations and applications. *ChemBioChem*, 11(7):848–865.
- [Walter et al., 2001] Walter, A., Rehage, H., and Leonhard, H. (2001). Shear induced deformation of microcapsules: shape oscillations and membrane folding. *Colloids and surfaces A: Physicochem. Eng. Aspects*, 123:183–185.
- [Wang et al., 1995] Wang, H., Ip, W., Boissy, R., and Grood, E. (1995). Cell orientation response to cyclically deformed substrates: experimental validation of a cell model. *J. Biomech.*, 28(12):1543–1552.

- [Wang et al., 2005] Wang, J., Guo, K., Qiu, F., Zhang, H., and Yang, Y. (2005). Predicting shapes of polymer-chain-anchored fluid vesicles. *Phys. Rev. E*, 71:041908.
- [Waugh et al., 1992] Waugh, R., Song, J., Svetina, S., and Zeks, B. (1992). Local and nonlocal curvature elasticity in bilayer membranes by tether formation from lecithin vesicles. *Biophys. J.*, 61(4):974–982.
- [Waught and Agre, 1982] Waught, R. and Agre, P. (1982). Surface viscosity measurements from large bilayer vesicle tether formation. i. analysis. *Biophys. J.*, 38:29–37.
- [Winiski et al., 1986] Winiski, A., McLaughlin, A., McDaniel, R., Eisenberg, M., and McLaughlin, S. (1986). An experimental test of the discreteness of charge effect in positive and negative lipid bilayers. *Biochemistry*, 25(25):8206–8214.
- [Winterhalter and Helfrich, 1992] Winterhalter, M. and Helfrich, W. (1992). Bending elasticity of electrically charged bilayers: coupled monolayers, neutral surfaces and balancing stresses. *J. Phys. Chem.*, 96:327–330.
- [Wintz et al., 1996] Wintz, W., Döbereiner, H.-G., and Seifert, U. (1996). Starfish vesicles. *Europhys. Lett.*, 33:403–408.
- [Yaroslavov et al., 2009] Yaroslavov, A., Sitnikova, T., Rakhnyanskaya, A., Yaroslavova, E., Davydov, D., Burova, T., Grinberg, V., Shi, L., and Menger, F. (2009). Biomembrane sensitivity to structural changes in bound polymers. *J. Am. Chem. Soc.*, 131:1666–1667.
- [Zhang and Wang, 2009] Zhang, J. and Wang, S. (2009). Topical use of coenzyme Q(10)-loaded liposomes coated with trimethylchitosan: Tolerance, precorneal retention and anti-cataract effect. *Int. J. Pharm.*, 372(1-2):66–75.
- [Zhang et al., 1998] Zhang, M. Q., Desai, T., and Ferrari, M. (1998). Proteins and cells on peg immobilized silicon surfaces. *Biomaterials*, 19(10):953–960.
- [Zhelev et al., 1994] Zhelev, D., Needham, D., and Hochmuth, R. (1994). A novel micropipet method for measuring the bending modulus of vesicle membranes. *Biophys. J.*, 67(2):720–727.
- [Zoldesi, 2006] Zoldesi, C. (2006). *Hollow colloidal particles by emulsion templating: from synthesis to self-assembly*. PhD thesis, Utrecht University, Utrecht, The Netherlands.

Résumé général

Le but de ce travail était de développer des modèles mécaniques de cellules basés sur les vésicules lipidiques géantes unilamellaires (GUVs) et d'étudier les relations entre paramètres mécaniques et comportements sous contraintes.

Nous avons tout d'abord réussi à modifier les propriétés structurales des membranes soit en les décorant de polyélectrolytes (chitosane ou acide hyaluronique), soit en utilisant la transition de phase des lipides pour obtenir des membranes en phase gel.

La caractérisation des membranes décorées a montré l'origine électrostatique de l'interaction polyélectrolyte/membrane, et a mis en évidence le rôle de la structure chimique des polymères sur leur conformation à la surface des vésicules. Concernant les membranes en phase gel, nous proposons un protocole astucieux permettant de préserver la forme sphérique de GUVs lors de la diminution de température.

Nous avons ensuite montré que la structure de la membrane influence fortement la valeur des paramètres mécaniques et le comportement des GUVs complexes soumises à différentes contraintes (pression osmotique, chocs de pH et de sel, compression entre deux plans (microscopie à force atomique) ou force ponctuelle (extrusion de nanotubes de membrane)). Les expériences d'AFM ont révélées que la décoration rigidifie les membranes, augmentant notamment leur module de compressibilité. Le dégonflement osmotique de GUVs en phase gel a mis en évidence une grande variété de formes polyédriques, que nous avons pu retrouver numériquement en utilisant un modèle 2D élastique adapté.

Nous avons enfin proposé une technique originale pour caractériser les vésicules en étudiant leur écoulement dans des géométries confinées.

General summary

The goal of this work was to develop mechanical models of cells based on lipidic giant unilamellar vesicles (GUVs) and to investigate the relationship between mechanical parameters and behaviors under external stresses.

Firstly, we succeeded in modifying structural properties of membranes either by coating fluid phase bilayers with polyelectrolytes (chitosan or hyaluronan) or by using the lipid phase transition to obtain membranes in the gel state.

The characterization of the coated membrane has revealed the electrostatic origin of the interaction between DOPC bilayers and polyelectrolytes, and that the adsorbed chain conformation at the vesicle surface is controlled by the polymer chemical structure. Concerning membranes in the gel state, a shrewd protocol was proposed to preserve the DMPC GUVs spherical shape upon cooling and transition from the fluid to the gel phase.

Secondly, we have demonstrated that the membrane structure highly affects the value of the mechanical parameters and changes the behaviors of these complex GUVs under various applied constraints (e.g. osmotic pressure, pH and salt shocks, compression between two planes (Atomic Force Microscopy) or point-acting force (hydrodynamic membrane tether extrusion)). In particular, AFM experiments have demonstrated that polyelectrolyte coating rigidifies lipid membranes, increasing among others their stretching moduli. As well, the osmotic deflation of gel GUVs have lead to a large panel of concave polyhedron-like shapes, numerically retrieved using a relevant 2D elastic model.

Finally, we have proposed an original technique to characterize vesicles by studying their flow in confined geometries.

Allgemeine Zusammenfassung

Das Ziel dieser Arbeit war es zunächst mechanische Modelle von Zellen basierend auf lipidischen "giant unilamellar vesicles" (GUV) [riesige einlamellige Vesikel] zu entwickeln und dann die Beziehung zwischen mechanischen Parametern und Verhaltensweisen unter äußeren Belastungen zu untersuchen.

Erstens gelang es uns, strukturelle Eigenschaften von Membranen zu verändern, entweder durch Beschichtung der flüssigen Phase der Lipid-Doppelschicht mit Polyelektrolyten (Chitosan oder Hyaluronsäure) oder durch Nutzung des Lipidphasenübergangs, um Membranen im Gel-Zustand zu erhalten.

Die Charakterisierung der beschichteten Membran hat nicht nur die elektrostatische Herkunft der Interaktion zwischen DOPC Doppelschichten und Polyelektrolyten deutlich gemacht, sondern auch dass die adsorbierte Kettenkonformation an der Vesikeloberfläche durch eine polymer-chemische Struktur gesteuert wird. Was Membranen im Gel-Zustand betrifft, wird ein ausgeklügeltes Protokoll vorgeschlagen, um die Kugelform der DMPC GUVs beim Abkühlen und dem Flüssigkeits-Gel Phasenübergang zu bewahren.

Zweitens haben wir gezeigt, dass die Membran-Struktur den Wert der mechanischen Parameter stark beeinflusst und Änderungen in den Verhaltensweisen dieser komplexen GUVs unter verschiedenen angelegten Einschränkungen hervorbringen kann (z. B. osmotischer Druck, pH- und Salz-Schocks, Kompression zwischen zwei Ebenen mittels Atomic Force Microscopy oder Punktkräfte durch hydrodynamische Membran-tether Bildung). Insbesondere haben AFM Experimente gezeigt, dass eine Polyelektrolytbeschichtung die Lipidmembranen versteift, wodurch unter anderem eine Zunahme des Reckmodulus erreicht wird. Ebenso, hat die osmotische Entleerung der gelartigen GUVs zu einer großen Gruppe von konkaven polyeder-ähnliche Formen geführt, die numerisch mit Hilfe eines entsprechenden 2D-elastischen Modelles reproduziert wurde.

Schließlich haben wir eine originelle Technik entwickelt, um Vesikel durch das Studium ihrer Strömung in eingeschränkten Geometrien zu charakterisieren.